

**ULTRAFAST DYNAMICS OF CARBON DIOXIDE
IN IMIDAZOLIUM IONIC LIQUIDS**

by

Thomas Brinzer

B.A. Chemistry, Franklin & Marshall College, 2003

D.C., Palmer College of Chiropractic, 2007

Submitted to the Graduate Faculty of
the Kenneth P. Dietrich School of Arts and Sciences in partial
fulfillment

of the requirements for the degree of

Doctor of Philosophy

University of Pittsburgh

2018

UNIVERSITY OF PITTSBURGH
KENNETH P. DIETRICH SCHOOL OF ARTS AND SCIENCES

This dissertation was presented

by

Thomas Brinzer

It was defended on

December 5, 2017

and approved by

Sean Garrett-Roe, Assistant Professor, Chemistry

Sunil Saxena, Professor, Chemistry

David Waldeck, Professor, Chemistry

Steve Corcelli, Professor, Department of Chemistry, University of Notre Dame

Dissertation Director: Sean Garrett-Roe, Assistant Professor, Chemistry

Copyright © by Thomas Brinzer
2018

ULTRAFAST DYNAMICS OF CARBON DIOXIDE IN IMIDAZOLIUM IONIC LIQUIDS

Thomas Brinzer, PhD

University of Pittsburgh, 2018

The ultrafast vibrational dynamics of carbon dioxide (CO_2) were studied in a series of physiosorbing ionic liquids using two-dimensional infrared (2D-IR) spectroscopy. The microscopic dynamics reported by CO_2 were found to depend strongly on the choice of anion. The timescales of spectral diffusion are attributed to the breakup of a local solvent shell (ion cage) around CO_2 , and to correlate with the bulk viscosity in 1-alkyl-3-methylimidazolium ionic liquids. This correlation breaks for novel ionic liquid mixture with short alkyl sidechains and non-imidazolium head groups; however, the timescales of spectral diffusion are consistent with trends in ion transport (conductivity).

A semi-empirical spectroscopic map, developed from ab initio calculations, allowed comparison of experimental observables with molecular dynamics simulations. The observed and calculated frequency and reorientational dynamics of CO_2 were compared, finding good correspondence. Both frequency and reorientational dynamics show multi-exponential behavior, indicating complex dynamics. Decomposition of the calculated frequency fluctuation correlation function (FFCF) into contributions from structural components of the ions confirms that the longest timescale is dominated by interactions of the anion and CO_2 ; however, there are substantial contributions from inertial motions involving the cation's charged head group.

Temperature-dependent 2D-IR of thiocyanate ($[\text{SCN}]^-$) and CO_2 in 1-alkyl-3-imidazolium bistriflimide ($[\text{Im}_{n,1}][\text{Tf}_2\text{N}]$, $n = 2, 4, 6$) ionic liquids interrogated the energetic barriers to motions around the probe molecules and the effect of increasing ionic liquid heterogeneity

on the observed dynamics. Both $[\text{SCN}]^-$ and CO_2 show a strong correlation of microscopic dynamics with viscosity in each ionic liquid studied; however, the spectral diffusion of $[\text{SCN}]^-$ in $[\text{Im}_{2,1}][\text{Tf}_2\text{N}]$ is offset from those of $[\text{SCN}]^-$ in the longer chain ionic liquids, potentially because of rotational motions. Additionally, both $[\text{SCN}]^-$ and CO_2 show activated behavior in their spectral diffusion, with the activation barrier being dominated by the slowest resolved relaxation processes. The calculated barriers for both CO_2 and $[\text{SCN}]^-$ correspond broadly to those for ion self-diffusion from MD and NMR studies. $[\text{SCN}]^-$ shows a decrease in E_a for $n = 6$, possibly because of increasing nanoscopic polar-apolar segregation. The calculated barriers for CO_2 do not show this dependence on alkyl chain length, consistent with molecular modeling of the CO_2 frequency.

TABLE OF CONTENTS

PREFACE	xv
1.0 INTRODUCTION	1
1.1 2D-IR	3
1.1.1 Spectroscopic Maps	6
1.1.2 Ultrafast spectroscopy of carbon dioxide	8
1.2 IONIC LIQUIDS	8
2.0 MULTIDIMENSIONAL INFRARED SPECTROSCOPY THEORY	12
2.1 NONLINEAR OPTICAL RESPONSE FUNCTIONS <i>AB INITIO</i>	12
2.2 LINESHAPE THEORY	21
2.2.1 Homogeneous Dephasing	21
2.2.2 Non-homogeneous Dephasing	25
3.0 METHODS	36
3.1 EXPERIMENTAL METHODS	36
3.1.1 Laser System and Timings	36
3.1.1.1 Modifications to Operation of the Laser System	38
3.1.2 Optical Parametric Amplifier and 2D-IR Systems	39
3.1.3 Detectors	42
3.1.4 2D-IR Data Acquisition	42
3.1.5 Nitrogen Purge	45
3.1.6 Sample Temperature Control	46
3.1.7 Polarizer / Waveplate Combo	48
3.1.8 Ionic Liquids	49

3.1.8.1	Drying ILs	49
3.1.8.2	Loading an Ionic Liquid with Carbon Dioxide	50
3.2	DATA ANALYSIS AND FITTING METHODS	51
3.2.1	Averaging During Post-Processing	51
3.2.2	Graphical Correlation Fitting Methods	52
3.2.2.1	Ellipticity	54
3.2.2.2	Centerline Slope	55
3.2.3	Global Fitting of Spectra	56
3.2.4	Correlation Function Fitting	57
4.0	ANION DEPENDENCE	58
4.1	CHAPTER SUMMARY	58
4.2	INTRODUCTION	59
4.3	METHODS	64
4.3.1	Materials	64
4.3.2	FTIR	65
4.3.3	2D-IR	65
4.3.3.1	Generation of femtosecond mid-IR pulses	65
4.3.3.2	2D Spectrometer	65
4.3.4	Global Fitting and Bootstrapping	66
4.3.5	Computational Details	66
4.4	RESULTS AND DISCUSSION	67
4.4.1	Linear IR Spectroscopy Results	67
4.4.2	Vibrational Frequency Calculations	71
4.4.3	Frequency, Geometry, and Charge Transfer Discussion	74
4.4.4	2D-IR Spectroscopy Overview	79
4.4.5	2D-IR Shoulders and Cross-Peaks	80
4.4.6	Peak Assignment	83
4.4.7	Modelling of Main Band	88
4.4.8	Modelling of Shoulders and Cross-Peaks	93
4.5	MOLECULAR INTERPRETATION	96

4.6	CONCLUSIONS	100
5.0	EUTECTIC IL MIXTURES AND THEIR EFFECT ON CO₂	102
5.1	CHAPTER SUMMARY	102
5.2	INTRODUCTION	103
5.3	EXPERIMENTAL	105
5.3.1	Synthetic Details	105
5.4	RESULTS AND DISCUSSION	106
5.4.1	Melting behavior	106
5.4.2	Viscosity	108
5.4.3	CO ₂ Uptake and Density	108
5.4.4	Heat Capacity	109
5.4.5	Conductivity	109
5.4.6	Molecular insights via 2D-IR spectroscopy	111
5.5	CONCLUSIONS	115
5.6	ACKNOWLEDGMENTS	115
6.0	SPECTROSCOPIC MAP	116
6.1	INTRODUCTION	116
6.2	METHODS	119
6.2.1	Experimental Methods	119
6.2.2	Simulation Methods	120
6.2.2.1	MD Simulations	120
6.2.2.2	Vibrational Frequency Calculations	120
6.3	RESULTS AND DISCUSSION	121
6.3.1	Linear Spectrum	121
6.3.2	Orientalional and Population Dynamics	124
6.3.3	Frequency Fluctuation Dynamics	130
6.3.4	FFCF Decomposition	136
6.4	CONCLUSIONS	139
6.5	ACKNOWLEDGEMENTS	140
7.0	THIOCYANATE T-DEPENDENT 2D-IR	141

7.1	CHAPTER SUMMARY	141
7.2	INTRODUCTION	142
7.3	METHODS	145
7.4	RESULTS AND DISCUSSION	146
7.4.1	Linear spectroscopy	146
7.4.2	Nonlinear spectroscopy	149
7.4.3	Spectral density and multimode Brownian oscillator description	154
7.4.4	Arrhenius analysis	156
7.4.5	Dynamics on a rugged energy landscape	159
7.5	CONCLUSIONS	162
7.6	ACKNOWLEDGMENTS	165
8.0	CARBON DIOXIDE T-DEPENDENT 2D-IR	166
8.1	INTRODUCTION	166
8.2	EXPERIMENTAL METHODS	166
8.3	RESULTS AND DISCUSSION	167
8.3.1	Linear Spectroscopy	167
8.3.2	Nonlinear Spectroscopy	168
8.3.3	Arrhenius Analysis	171
8.4	CONCLUSIONS	176
9.0	CONCLUSIONS	177
9.1	CO ₂ 'S LOW FREQUENCY SHOULDER AND THERMALLY EXCITED BENDING MODE	177
9.2	FIFTH-ORDER SIGNAL	179
9.3	CO ₂ AND THE IONIC LIQUID ENVIRONMENT	179
	APPENDIX. SUPPORTING INFORMATION	184
A.1	ANION DEPENDENCE	184
A.1.1	Comparison of Global Fitting with Center Line Slope	184
A.1.2	2D IR Spectra	186
A.1.3	Computational Results	186
A.2	NOVEL EUTECTIC IONIC LIQUID MIXTURE	190

A.2.1	Viscosity	190
A.2.2	Density	190
A.2.3	Water Content	190
A.2.4	DSC Melting Point	190
A.2.5	DSC Heat Capacity	191
A.2.6	Conductivity	191
A.2.7	TGA Thermal Stability	192
A.2.8	IR Spectroscopy	192
A.2.9	Data	194
A.3	THIOCYANATE TEMPERATURE DEPENDENT 2D-IR	196
	BIBLIOGRAPHY	198

LIST OF TABLES

1	Thermocouple calibration	47
2	Experimental and calculated antisymmetric stretch vibrational frequencies . .	75
3	Carbon dioxide frequency parameters	77
4	Assignment of CO ₂ features to 3rd or 5th order	89
5	Best fit correlation function parameters, by ionic liquid	93
6	Data summary for eutectic IL samples compared to [Im _{6,1}][Tf ₂ N].	108
7	Best global fit lineshape parameters of CO ₂ in synthesized and reference ionic liquids	114
8	CO ₂ FTIR parameters in [Im _{4,1}][PF ₆]	122
9	Anisotropy ($\alpha = 0.4C_2$) fitting results (experiment).	128
10	Orientalional correlation function (C_2)fitting results (simulation).	129
11	Magic angle polarization FFCF of CO ₂ in [Im _{4,1}][PF ₆]	133
12	Frequency fluctuation correlation function (c_2)fitting results (simulation). . .	134
13	T-dependent FTIR peak parameters	147
14	Thiocyanate T-dependent correlation function fitting results	152
15	Thiocyanate Arrhenius fitting results	158
16	FFCF analysis of carbon dioxide in ILs	172
17	Arrhenius analysis of carbon dioxide in ILs	174
18	Geometries optimized allowing charge transfer.	188
19	Geometries optimized without allowing charge transfer.	189
20	TGA Data.	194
21	MDSC Data (second heat at 2 °C min ⁻¹)	195

22	Novel IL Water Content	195
23	Activation barrier heights and prefactors for SCN^- without fast components .	196
24	Arrhenius fits for the intermediate and long time constants in each ionic liquid.	196
25	Correlation times for SCN^- with short time component omitted	197

LIST OF FIGURES

1	2D-IR pulse sequence	3
2	Double sided Feynman diagrams for the paths through Liouville space	19
3	Components of 2D-IR signal	24
4	2D-IR Lineshape Comparison	29
5	Motional narrowing	31
6	Spectral diffusion in a 2D spectrum	33
7	2D-IR experimental layout	37
8	Spectral averaging	53
9	Linear and 2D-IR of Carbon Dioxide in Water	63
10	FTIR of carbon dioxide in ionic liquids	68
11	T-dependent FTIR of carbon dioxide in 1-butyl-3-methylimidazolium triflate	70
12	ALMO decomposition of carbon dioxide frequency	76
13	2D-IR spectra of carbon dioxide in ionic liquids	81
14	Bending mode kinetics	82
15	Double sided Feynman diagrams for 3rd and 5th order signals	87
16	Experimental 2D-IR spectra of CO ₂ in [Im _{4,1}][X]	90
17	Example of global fitting of 2D-IR spectra	92
18	Stochastic simulation spectrum	95
19	τ_c -viscosity correlation with differing ionic liquid anion	98
20	Components of the synthesized novel ionic liquids	104
21	DSC heating curves and melting points for IL mixtures	107
22	Carbon dioxide sorption of synthesized and reference ionic liquids	110

23	Heat capacities for synthesized and reference ionic liquids	111
24	2D-IR spectra of CO ₂ in synthesized and reference ionic liquids	113
25	FTIR spectrum of CO ₂ in [Im _{4,1}][PF ₆]	123
26	IR pump-IR probe spectra of CO ₂ in [Im _{4,1}][PF ₆]	125
27	Isotropic pump-probe spectrum amplitude for CO ₂ in [Im _{4,1}][PF ₆]	127
28	CO ₂ anisotropy decay in [Im _{4,1}][PF ₆]	127
29	Magic angle 2D-IR spectra of CO ₂ in [Im _{4,1}][PF ₆]	132
30	Experimental and computed FFCF of CO ₂ in [Im _{4,1}][PF ₆]	135
31	CO ₂ FFCF decomposition into components from the anion and cation	137
32	1-alkyl-3-methylimidazolium bistriflimide line structure	145
33	T-dependent FTIR of the CN stretching mode in [Im _{4,1}][Tf ₂ N]	147
34	Thiocyanate T-dependent 2D-IR	148
35	Thiocyanate T-dependent FFCF.	153
36	Relationship between thiocyanate's T-dependent τ_{corr} and viscosity	154
37	Calculated low frequency spectral density for [SCN] ⁻ from experimental FFCFs	156
38	Arrhenius plots showing the temperature-dependence of τ_{corr} in [Im _{n,1}][Tf ₂ N]	158
39	Rough energy landscape model	163
40	T-dependent FTIR of CO ₂ in [Im _{n,1}][Tf ₂ N]	168
41	Temperature-dependent 2D-IR of CO ₂ in [Im _{n,1}][Tf ₂ N]	170
42	Temperature-dependent FFCF of CO ₂ in [Im _{n,1}][Tf ₂ N]	171
43	Correlation between CO ₂ 's temperature-dependent τ_{corr} and the viscosity of the ionic liquid	173
44	Arrhenius analysis of CO ₂ in [Im _{n,1}][Tf ₂ N]	174
45	CLS overlaid on the 2D spectrum of CO ₂ in [Im _{4,1}][TFA]	185
46	CLS fitting of CO ₂ ν_3 2D spectrum from [Im _{4,1}][TFA]	185
47	2D-IR spectra of CO ₂ ν_3 in [Im _{4,1} ⁺] (A) [PF ₆] ⁻ , (B) [Tf ₂ N] ⁻ , and (C) [DCA] ⁻ , showing the range of timescales for spectral diffusion in ν_3	186

PREFACE

The journey from first contemplating a return to school to a completed dissertation has not been a quiet one. It has rather been an odyssey, full of both unexpected challenges and unhopd-for joys. That I have reached the stage of a dissertation is a testament to tremendous support by family, friends, and the Pitt chemistry community. If I thanked here all of those who have helped me, the list could run for many pages and still be incomplete. There are, however, a few people who I wish to single out because of my special gratitude towards them.

First, I would like to thank my thesis advisor, Prof. Sean Garrett-Roe, without whom none of this work would have been possible. His persistent scientific curiosity has inspired and challenged me through the process of developing my project and my scientific thinking to their current levels. His seemingly inexhaustible patience has comforted me at low points in the journey, and has given me as a model to emulate during tough times. Finally, his passion for teaching has allowed me to develop an understanding of the theoretical underpinnings of non-linear spectroscopy, on which this entire thesis is based.

There are several other people at the University to whom I would like to extend a special thanks. Prof. Sunil Saxena taught my first spectroscopy course, and helped me to overcoming the challenge of returning to course work after eight years. All of the members of the stellar Garrett-Roe research group deserve my thanks, but I want to extend it particularly to Mr. Zhe Ren (任哲) for perpetually insightful discussions on my research topics, and for assistance with optics. Similarly, Mr. Ali Sinan Sağlam has been a true friend. He has elucidated numerous mathematical concepts, and greatly assisted my introductory studies of quantum mechanics. Finally, the support staff at Pitt's excellent shops, especially Mr. Thomas Gasmire, who taught me the basics of machining, and Mr. Jeff Sicher, who assisted

in design of the temperature-control hardware, deserve my thanks.

Finally, I never would have made it through this process without the support of my amazing family and friends. Through every step of this journey, they have been there with helping hands and listening ears. Most especially, I want to thank my amazing wife, Becky Whalen, who has always been there to motivate me and buoy my spirits whenever I felt discouraged in my progress, no matter how challenging her own circumstances have been, and our new daughter Evelyn, who has consistently and effortlessly inspired me during these last few months.

1.0 INTRODUCTION

The goal of this work is to better understand the local solvent structure and dynamics around physically absorbed carbon dioxide in ionic liquids, using two-dimensional infrared (2D-IR) spectroscopy. Ionic liquids are promising material components of second and third generation carbon capture technologies, which must be developed and implemented to mitigate anthropogenic climate change.

The equilibrium solvent structure around carbon dioxide depends on the energetic interactions of carbon dioxide with its solvent, and thus (combined with the neat solvent structure) determines the enthalpy, entropy, and free energy of solvation of CO_2 , which are major factors that affect the efficiency of carbon capture and storage applications. The free energy of solvation determines the equilibrium capacity of an ionic liquid to dissolve CO_2 . Decomposition of this free energy into enthalpic and entropic components can allow the calculation of the energy penalty associated with regenerating the solvent after it has been used to capture CO_2 , one of the major contributions of the parasitic load on that post-combustion carbon capture technologies impose on power plants.¹ The thermodynamic picture alone does not solely determine the efficiency of a carbon capture system, however.²

Every chemical process has both thermodynamic and kinetic components that must be considered in any application, and carbon capture is no exception to this rule. The rate of carbon dioxide absorption and desorption depend strongly on mass transport of CO_2 ,^{3,4} which is intimately bound up with the dynamics of CO_2 in its local environment. The lifetime of a solvent shell around CO_2 in the condensed phase acts as a lower bound on its translation diffusion through the liquid environment. Depending on the heterogeneity of the liquid, and the effects of this heterogeneity on the frequency of the molecule, it is likely that the longest dynamical processes observed in 2D-IR spectroscopy will relate to complete

breakup of a first (or second) solvent shell, and could give insight into important effects such as mass transport of CO₂.

By understanding both the structure *and* dynamics around CO₂, it is possible to gain an intimate understanding of the relationships between the two. The hope is that such an understanding will lead to the development of improved materials for carbon capture and storage, and can, in a small way, help to advance the state of carbon capture technologies.

The practical implications of understanding “how” carbon dioxide is dissolved in ionic liquids is unambiguous, and would independently be enough to spur investigation into this area. The question of how ionic liquids solvate small molecules such as carbon dioxide, however, is also interesting from a fundamental perspective. Ionic liquids are complex liquids with heterogeneous polar and nonpolar domain structures and may show heterogeneous dynamics.⁵⁻⁷ They are typically composed of asymmetric soft cations and bulky soft anions, which leads to substantial solvent entropy. Contributions to the *enthalpy* of solvation are also complicated. At a minimum, factors such as charge-charge interaction from self-interaction of the solvent ions, dipolar interactions, and van der Waals interactions (from the alkyl tails typically found on cations) must be considered.⁸⁻¹⁰ How these interactions between the anion and the cation balance with those between the anion, cation, and CO₂ and the changes of configurational entropy on mixing is a deep and subtle question. Indeed, there is substantial debate in the literature as to the specific interactions with anion and cation, and even more with the polar and nonpolar regions of the ionic liquid.¹¹⁻¹⁴ The molecular origin of the selectivity of ionic liquids for carbon dioxide over nitrogen is similarly debated,¹⁵⁻¹⁸ and has not yet been fully explained.

Dynamics in the condensed phase are driven by thermal energy, and thus are related strongly to not only the enthalpy, but also the entropy of solvation. The combination of these entropic effects with the complex enthalpic considerations described above lead to inhomogeneous disorder in the condensed phase, and can lead to heterogeneous microenvironments that mix on a timescale defined by the timescale of solvent shell relaxation.^{19,20}

Disentangling these effects experimentally requires a technique that provides observables commensurate in distance-dependence to the size of the solvent shell of CO₂, and in time dependence to the timescale of solvent shell randomization. Two-dimensional infrared

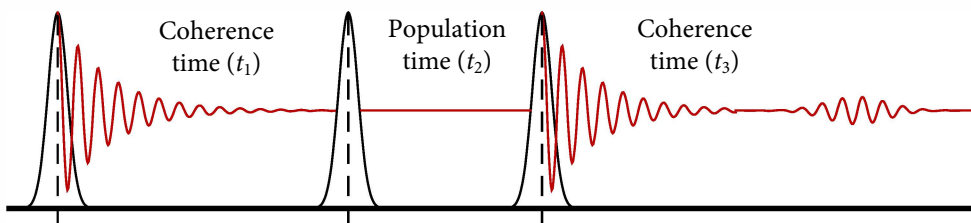


Figure 1: 2D-IR pulse sequence. The interaction of three ultrafast optical pulses with a sample generate two coherences, separated by a variable population time.

spectroscopy is a technique that meets this stringent requirement. The vibrational frequency of a small molecule such as CO_2 depend on local environmental effects that decay over the first one or two solvation shells around it; furthermore, the vibrational frequency fluctuates on the timescale of environmental fluctuations. Therefore, the frequency fluctuation correlation function (a principle observable of 2D-IR spectroscopy) provides direct insight into the local environment and its fluctuations, which are the variables of interest in this case.

1.1 TWO-DIMENSIONAL INFRARED SPECTROSCOPY

Two-dimensional infrared (2D-IR) spectroscopy is a coherent third-order optical spectroscopy, where the time-dependent frequency response of a vibrational mode provides information about the local environment of a molecule. A 2D-IR experiment is an optical three pulse experiment (Figure 1). The first pulse creates a vibrational coherence, whose time evolution (t_1 , with free induction decay until the second laser pulse) contributes to the absorption lineshape in initial frequency (ω_1). The second pulse generates a phase-labeled population state. The vibrational frequency is stochastically modulated by interaction with the bath, until the third optical pulse creates a second coherence, which is detected after t_3 . The experiment thus creates a signal that resolves population time dependent initial (ω_1) and final (ω_3) vibrational frequencies (Section 2.1).

2D-IR spectroscopy is a vibrational analog of multidimensional nuclear magnetic resonance (NMR) techniques such as homonuclear correlation spectroscopy (COSY) and nuclear Overhauser enhancement spectroscopy (NOESY). While 2D-IR spectroscopy does not generally provide the atomistic structures available through NMR methods, the ultrafast time resolution allows the observation of molecular processes that would be averaged away in a typical 2D-NMR experiment.

The main peak for a 0–1 transition on a 2D-IR will be centered on the $\omega_1 = \omega_3$ diagonal. The number of diagonal peaks thus give information on the number of distinct chemical environments for the probed vibrational modes. Similar to 2D-NMR spectroscopy, the 2D spectrum of two *coupled* vibrational modes will show off-diagonal cross-peaks for the two main peaks. Since the strength of coupling depends on both the orientation of the vibrations’ transition dipoles, and on the distance between them, the positions and intensity of cross-peaks give structural information about molecular geometries in the condensed phase.

Cross-peaks can also result from dynamic exchange of individual vibrations between distinct chemical environments. 2D-IR spectroscopy can thus be used to examine, for example, ultrafast complexation (and de-complexation) at equilibrium.^{21,22} While the positions of cross-peaks are similar to those from vibrational coupling, these mechanisms of cross-peak formation can be distinguished by the relative kinetics observed through the peak volume.

Even for a single oscillator, the IR spectral lineshape contains a wealth of information. The shape of the 2D-IR peak for a single oscillator depends on the local environment around the vibration. This stochastic frequency fluctuation is reflected in the IR lineshape; however, it is buried in a static linewidth in FTIR (first-order) spectroscopy. The resolution of a second frequency axis, combined with the exquisite time resolution of 2D-IR spectroscopy allows one to quantify these changes. Changes in the peak shape with increasing population time (t_2) reflect changes in the local environment (Section 2.2), and thus can give the timescale of inter- or intramolecular motions, such as hydrogen bond switching.

Much of the seminal literature on ultrafast multidimensional spectroscopy (2D-IR or 3D-IR) focused on either protein structure^{23–28} or water^{29–33} dynamics using two chromophores: the amide I (or amide I’) band of polypeptides, and the O–H (or O–D) stretching modes of liquid water.

The focus on polypeptides through the amide I mode is readily understandable. The amide I mode of polypeptides is a strong vibrational chromophore; furthermore, adjacent (in the tertiary structure) carbonyl modes in a polypeptide can couple together, causing delocalization of the vibrational modes, and consequent evolution of cross-peaks on the 2D-IR spectrum. Thus, the 2D-IR spectrum contains information on the tertiary structure (since cross-peaks depend on the coupling and orientation of vibrational chromophores) of polypeptides. The distribution of polypeptide structures and their vibrational motions determine the shapes and frequencies of the diagonal peaks and cross-peaks; therefore, the 2D-IR spectrum contains not only structural but also dynamical information. Of course, multidimensional NMR spectroscopy also contains such information through a similar mechanism (and clever EPR experiments can access it); however, the sub-picosecond time resolution of infrared spectroscopy makes it a method of choice, especially for determining sub-microsecond conformational changes in polypeptides. Additionally, cross-peaks from chemical exchange have been used to study transitions between conformational substates, as in transient conformational changes.^{34–40}

In addition to studies of protein and peptide conformation, 2D-IR spectroscopy has been applied to a number of other biochemical problems. It has been used to distinguish the substates of neuropeptides,⁴¹ and to determine structural and dynamical information for such diverse systems as amyloid fibrils,^{42,43} photoswitchable proteins,^{44,45} villin,⁴⁶ and myoglobin.^{47,48} and even transmembrane helix dimers.⁴⁹ Significant effort has also been put into studying the effects of ultrafast solvent and substrate motions on the activities of enzyme active sites,^{50–54} with sometimes controversial results. Finally, studies of ultrafast events in drug binding^{55,56} have given new insights into the role of water in facilitating binding of drugs at active sites on influenza and HIV reverse transcriptase.

The structure and dynamics of the water hydrogen bonding has been an area of ongoing research for many years, and numerous 2D (and 3D) IR spectroscopy experiments have attempted to shed light on this issue through resolving ultrafast hydrogen bonding dynamics. The appeal of the area is obvious. The self-interactions with water, and how these change when solutes are present, are of paramount importance for any aqueous system, including (but not limited to) nearly every biochemical system of interest. Given the importance of

such systems in human health, such interest is not surprising (see above); however, even the solvation of ions has led to significant research, with ultrafast infrared spectroscopy shedding light on the specific interactions and changes in dynamics brought on by, for example, kosmotropes and chaotropes in water.⁵⁷ Similarly, extensive studies of water in the pore regions of membrane-bound ion channels have been carried out, with the goal of better understanding the mechanisms that govern these proteins.

Even neat water is itself a difficult system to study, behaving non-ideally in many respects. Numerous studies have attempted to disentangle the hydrogen bonding networks in water.^{33,58–70} The difficulty of the problem has led to extension of ultrafast techniques from two dimensions to three dimensions,^{71–73} and to continue new techniques such as two-dimensional Raman-terahertz spectroscopy.⁷⁴

While less commonly utilized than amide I and O–H stretching modes, 2D-IR spectroscopy has also been extended to the study of other vibrational modes in the condensed phase. Nitriles (or cyanates),^{75–81} azido-compounds (or azides),^{50,82–84} and metal carbonyl complexes,^{85–88} have all been used to study condensed phase systems.

1.1.1 Spectroscopic Maps

The desire to invert a 2D-IR lineshape to obtain local dynamics from diagonal peaks, as well as dynamical structural information from cross-peaks, has led to a close association between 2D-IR spectroscopy methods and computational and theoretical methods aimed at interpreting those spectra. One of the most important computational methods commonly used to gain physical insight into the molecular environment from the 2D-IR lineshape involves semi-empirical spectroscopic maps for IR vibrations. 2D-IR spectra (and the related frequency fluctuation correlation functions) can be calculated directly from the time-dependent frequency trajectory of a molecule. Obtaining the vibrational frequency at each time step could require solving the many body Schrödinger equation at each time step of the trajectory, which is untenable for large condensed phase systems over long trajectories, due to the computational cost.ⁱ

ⁱThe treatment of quantum dynamics in the condensed phase is itself an enormous field, and no attempt is made to discuss it in depth here. There are numerous approaches, ranging from the semiclassical initial value

Semi-empirical spectroscopic maps (hereafter: spectroscopic maps) allow the calculation of long ($> 1 \mu\text{s}$) frequency trajectories, using a mixed classical-quantum method. Briefly, quantum chemistry calculations are used to calculate the anharmonic frequency of a vibrational mode at points across its potential energy surface for a number of molecular dynamics snapshots. The quantum calculations are used to parameterize an empirical map, that approximates the vibrational frequency based on classical observables, such as local electric fields or Lennard-Jones forces.

After validating the map against an independent number of quantum chemistry calculations, it can then be applied to a full MD trajectory. The resulting instantaneous vibrational frequency trajectory can be used to calculate spectroscopic observables, using a response function formalism (Chapter 2). The spectroscopic observables are validated against experiment. They can then be compared with other observables from MD, such as time-dependent distribution functions or time correlation functions. Physical insight into the system can then be gleaned from decomposition of these MD observables into contributions from specific types of atoms or molecules in the simulation (Chapter 6), or even electrostatic or Lennard-Jones contributions.

A number of spectroscopic maps have been developed, including for amides in N-methylacetamide^{94,95} and proteins^{96,97}, for O–H in liquid water,^{59,60,98,99} for azides,¹⁰⁰ and for nitriles^{101–106}. Direct comparison of simulation with experiment can, in the best cases, allow determination of atomistic details that would be impossible to resolve spectroscopically, as in the case of liquid water.⁷³

Chapter 6 details the application of a new spectroscopic map for CO_2 in ionic liquids to calculate frequency trajectories that are directly compared with experimental results. The map was collaboratively developed for this work,^{10,107} as there were no previously developed spectroscopic maps for CO_2 , either in ionic liquids or in other solvents.

representation,⁸⁹ and the semiclassical stochastic Liouville equation,⁹⁰ to ring-polymer molecular dynamics and other methods of approximating nuclear dynamics,^{91,92} and even explicit time-dependent quantum mechanics calculations.⁹³

1.1.2 Ultrafast spectroscopy of carbon dioxide

Gas phase CO₂ has been studied for its role in atmospheric chemistry;^{108–111} however, CO₂ dissolved in soft condensed phase materials was only occasionally used for spectroscopic investigations of interactions with materials^{112–114}. In time-resolved ultrafast spectroscopy, CO₂ was largely ignored. In liquid water, the line is highly narrowed, and only shows very slight inhomogeneity associated with hydrogen bond switching. It is almost completely in the homogeneous limit, and therefore, little could be learned from its dynamics.¹¹⁵ CO₂ was used as a test case for the development of new infrared techniques^{71,115} due to its high oscillator strength.

It was therefore plausible that in a different condensed phase environment (either with strong electric fields or with relatively slow solvent motions) CO₂ would not be in the motional narrowing limit, but would report dynamics that reflected the time-evolution of the local solvent structure.

The homogeneous limit, after all, depends on both the timescale of motions in its local environment and on the magnitude of its frequency fluctuations in that environment (Section 2.2.2). The second factor in particular explains why time-resolved electronic (UV-Vis) spectroscopies (*e.g.*, time-resolve Stokes shifts), can resolve rapid inertial motions, such as inertial motions, that are in the homogeneous limit for infrared spectroscopy.^{116–118}

1.2 IONIC LIQUIDS

Ionic liquids are complex solvents, composed of anions and cations, which can have heterogeneous polar and nonpolar domains. They have been proposed as components in carbon capture and storage technologies. The diversity of local environments, and the slow dynamics exhibited by ionic liquids (due to high solvent friction from electrostatic interactions between the anion and cation), causes CO₂ dissolved in these liquids *not* to be motionally narrowed. While the band is still narrow ($< 7\text{ cm}^{-1}$), it reports on local structure and dynamics through its 2D lineshape. Determining this fact, combined with understanding

the structure of the 2D-IR spectrum of CO₂ in ionic liquids, was one of the main goals of the initial work (Chapter 4).

Room temperature ionic liquids (commonly referred to simply as ionic liquids) are salts with melting points below 100 °C. The melting point depression, compared with, for example NaCl that melts at 801 °C is due to several factors. Anions and cations are often bulky organic structures, with significant amounts of charge delocalization. Cations also often have asymmetric alkyl tails attached, which serve to disrupt packing of the crystal lattice. Addition of an asymmetric butyl tail, for example, depresses the melting point by approximately 50 °C from 1,3-dimethylimidazolium chloride to 1-butyl-3-methylimidazolium chloride. Replacing the chloride anion with bistriflimide ([Tf₂N]⁻) depresses the melting point further by 75 °C, resulting in a liquid salt with a melting point (-5 °C) below that of liquid water.

Ionic liquids have attracted significant attention for a variety of applications in recent years because of their useful properties. Specifically, the combination of negligible vapor pressure, high thermal and electrochemical stability, good conductivity and non-flammability with widely tunable chemical properties (generally through chemical modification of the cation or anion), makes them attractive targets for a number of processes.¹¹⁹ While early ionic liquids, such as haloaluminates¹²⁰ exhibited excellent electrochemical and reactivity properties, they were hydrolytically unstable, making them unsuitable for a number of applications. Most modern room temperature ionic liquids, on the other hand, show good to excellent hydrolytic stability, which enables their use in applications, such as post-combustion carbon capture,^{17,121–126} where exposure to water vapor is inevitable. Indeed, in addition to carbon capture, non-haloaluminate ionic liquids are being developed for biochemical,¹²⁷ electrochemical,^{128–133} synthetic,^{134–137}, and numerous other applications.^{17,138–142} Additionally, it is possible to tailor specific ionic liquid-solvent interactions by covalent modification of the anion or cation (so-called “task-specific” ionic liquids), opening the door to a number applications.^{16,121,143,144}

Despite the rapidly expanding number of ionic liquid publications and patents,¹³⁹ fundamental questions about ionic liquids remain unanswered. The molecular origin of viscosity^{81,145} and transport properties³ in ionic liquids remains open to debate.

The concept of “ionicity” attempts to describe the degree to which anions and cations in ionic liquids behave as ions, as opposed to neutral species. It is deeply related to self-transport properties in ionic liquids, which are of interest for many applications. Ionicity is often related to deviation of the conductivity and viscosity of an ionic liquid from the Walden rule, which describes a linear proportionality between the two.^{146,147} In the case where NMR diffusion measurements are present, ionicity can be assessed by the Nernst-Einstein equation. Deviations from ideality have been interpreted either as evidence of partial charge transfer between the anion and cation, or as evidence of long lived anion-cation pairs in the liquid.^{4,13} The existence of long-lived ion pairs^{148–150} in a pure liquid phase seems counter-intuitive, and has been seemingly contradicted by experimental and computational work.^{151–153} Nevertheless, the concept has remarkable persistence in the literature.

Structural and dynamical heterogeneity^{7,154,155} are a huge area of investigation for ionic liquids. The equilibrium liquid structure of ionic liquids is dependent on a hierarchy of energetic interactions between the liquid’s components. To a good approximation, the three components of most ionic liquids are the negatively charged anions, the positively charged cation head groups, and the mostly nonpolar alkyl tails. The most basic organization in an ionic liquid (as it is in all salts) is charge alternation between the anions and the cation head groups. Nonpolar alkyl tails, which can have favorable dispersion interactions with the liquid, arrange themselves to maximize these interactions with minimal disruption of charge ordering.

In ionic liquids with longer alkyl tails (typically with $n \geq 6$), it is widely accepted that the tails will aggregate to form nonpolar domains, which intercalate between the more polar charged domains.¹⁵⁶ The primary evidence of these mesoscopic domains comes from X-ray scattering, which shows the evolution of a sharp low q peak (indicating alternating structures on a several nanometer length scale) with increasing alkyl chain length.^{157–161} Similar effects have been observed in computational simulations of ionic liquids.^{160,162–164} There is some spectroscopic evidence of clustering effects of alkyl tails, even with short ($n = 2$) lengths;¹⁶⁵ These clusters lack, however, the sharply defined low q scattering peaks seen on X-ray scattering of longer chain ionic liquids.

At least one neutron scattering study agreed with the appearance of a low q peak with

increasing alkyl tail length, but disagreed with the attribution of these features to a lattice or pseudomicellar structure, instead arguing that it was a pure space filling effect, with cations displaced from each other by alkyl tails.¹¹ Such a picture is not inconsistent with work on mixtures of hydrogen-bonding molecular liquids showing local structural heterogeneity without long range structural correlations.^{166–168} Recent dispersion corrected *ab initio* molecular dynamics studies showed a substantial decrease in the microheterogeneity of ionic liquids when a dispersion correction was applied, due a combination of increased anion–side chain and cation–cation interactions.¹⁴ The same work also saw ion self-diffusion values correct towards experimental behavior compared with previous computational studies.

Likewise, the degree to which cooperativity between the anion and cation contributes to the liquid structure and dynamics is not fully understood.^{8,169–171}

The addition of solutes, which disturbs the liquid structure, further complicates matters. The degree to which nascent solvent cavities,¹⁷² interactions with the cation and anion,¹⁵ and effects such as enthalpy/entropy compensation¹⁷³ contribute to the ability of ionic liquids to solvate small molecules is an open question. Furthermore, some experimental and computational work suggests that diffusion of small molecules in ionic liquids is limited not by alkyl tail domains, but rather by transient density fluctuations of the polar regions.^{174–176} There have also been suggestions of heterogeneous solute dynamics in ionic liquids, which is consistent with the previous picture.⁵

Solvation of large dye molecules has been studied using electronic spectroscopy, with excellent time resolution of frequency and rotational dynamics^{177,178}; however, some computational work indicates these molecules alter the solvent structure significantly, in part due to shape-based (packing) effects.¹⁷⁹

In part because of the interest in carbon capture and storage applications, there has been considerable effort made to understand the local environment of carbon dioxide in ionic liquids.^{12,15,18,173,180–195} Nevertheless, experimentally validated insight into the inhomogeneity of local structures, and the timescales they interconvert on has been lacking. Such insight could both lead to fundamental insights into how ionic liquids solvate small, uncharged molecules, and could help to improve carbon capture efforts with ionic liquids.

2.0 MULTIDIMENSIONAL INFRARED SPECTROSCOPY THEORY

2.1 NONLINEAR OPTICAL RESPONSE FUNCTIONS *AB INITIO*

The goal of spectroscopy is to deeply understand the interaction of light and matter, and in so doing to gain physical insights into the systems being studied. The most complete treatment thereof would include a quantum mechanical description of both the molecular system and the electromagnetic radiation, and would require solving coupled systems of the equations of quantum electrodynamics and the time-dependent Schrödinger equation.

In order to ameliorate the treatment of this difficult problem, a semiclassical approach, where the electromagnetic field is treated classically and only the molecular energy levels are treated quantum mechanically, is often employed. Such a treatment is sufficient to describe ultrafast infrared spectroscopy, and is used throughout this work.

In a pulsed laser spectroscopy experiment, the driving electric field can be treated as a wavepacket

$$\begin{aligned}\vec{E}(t) &= \vec{E}'(t) \cos(\vec{k} \cdot \vec{r} - \omega t + \phi) \\ &= \vec{E}'(t) \frac{(e^{i\vec{k} \cdot \vec{r} - i\omega t + i\phi} + e^{-i\vec{k} \cdot \vec{r} + i\omega t - i\phi})}{2} \\ &\equiv E(t) + E^*(t)\end{aligned}\tag{2.1}$$

with envelope $\vec{E}'(t)$ that includes the optical polarization of the pulse. The wave propagates along the direction of its wavevector \vec{k} , with a central frequency ω and a phase ϕ .

The starting point for the description of molecular energy levels and their time evolution is the time-dependent Schrödinger equationⁱ

$$\frac{\partial}{\partial t} |\psi(t)\rangle = -\frac{i}{\hbar} \hat{H}(t) |\psi(t)\rangle \quad (2.2)$$

The interaction with a driving weak electric field ($\hat{H}' \ll \hat{H}_0$) can be treated as a time-dependent perturbation of the system, modifying the time-independent molecular Hamiltonian

$$\hat{H}(t) = \hat{H}_0 + \hat{H}'(t) \quad (2.3)$$

where the energy is the interaction energy between the molecular dipole and the driving field

$$\hat{H}'(t) = -\hat{\mu} \cdot \vec{E}(t) \quad (2.4)$$

where $\hat{\mu}$ is the dipole operator and $\vec{E}(t)$ is the time-dependent driving electric field.

Since multidimensional infrared spectroscopy experiments typically involve condensed phase environments that are not pure states, it is convenient to use a density operator formalism. For a pure state, the density operator is the outer product of state vectors

$$\hat{\rho}(t) = |\psi_k(t)\rangle \langle \psi_k(t)| = \sum_m \sum_n c_n(t) c_m^*(t) |\phi_n\rangle \langle \phi_m| \quad (2.5)$$

which can be expanded in an arbitrary orthonormal basis $|\psi\rangle = \sum_k c_k |\phi_k\rangle$. A mixed state density operator can be described as a superposition of pure state density operators

$$\hat{\rho}(t) = \sum_k P_k |\psi_k(t)\rangle \langle \psi_k(t)| \quad (2.6)$$

where P_k is the probability of the system to be in state $|\psi_k(t)\rangle$.ⁱⁱ Diagonal elements of the density matrix represent *populations* in the ensemble, while off-diagonal elements represent *coherences*, or linear combinations of eigenstates with the same initial phase.

ⁱGiven here in Dirac notation, which is used whenever possible throughout this work. Note that $\langle \psi|$ and $|\psi\rangle$ are Hermitian conjugates of each other.

ⁱⁱThe expectation value of an operator acting on a wavefunction is $\langle \hat{O} \rangle = \langle \psi(t) | \hat{O} | \psi(t) \rangle$. Starting at this point, it is relatively straightforward to derive that the expectation value of an operator acting on the density matrix is $\langle \hat{O} \rangle = \sum_{m,n} \hat{O}_{mn} \hat{\rho}_{nm} \equiv \text{Tr}(\hat{O} \hat{\rho})$.

The time evolution of the density matrix can be derived by substituting the time-dependent Schrödinger equation into the time derivative of the density matrix of a pure state. This treatment yields the Liouville-Von Neumann equation

$$\frac{\partial \hat{\rho}}{\partial t} = -\frac{i}{\hbar} [\hat{H}, \hat{\rho}] \quad (2.7)$$

This equation holds for any density operator (including those for mixed states), because a mixed state density operator is a linear combination of pure state density operators (Equation 2.6).¹⁹⁶

The time dependent perturbation of the density matrix can then be derived by a perturbative expansion. It is convenient to use the interaction picture (Dirac picture) of quantum mechanics, where both operators and state vectors carry the time dependence, for this derivation. The Dirac picture allows separation of the system's time evolution into components from the perturbation and from free evolution of the system between perturbations.

$$|\psi_I(t)\rangle = e^{\frac{i}{\hbar}\hat{H}_0(t-t_0)} |\psi(t)\rangle \quad (2.8a)$$

$$\hat{O}_I(t) = e^{\frac{i}{\hbar}\hat{H}_0(t-t_0)} \hat{O}(t) e^{-\frac{i}{\hbar}\hat{H}_0(t-t_0)} \quad (2.8b)$$

For a wavefunction, its time dependence is equal to the time-dependent perturbation operating on the freely evolving system

$$\frac{d}{dt} |\psi_I(t)\rangle = -\frac{i}{\hbar} \hat{H}'_I(t) |\psi_I(t)\rangle \quad (2.9)$$

Integrating this equation, followed by iterative substitution of the result into itself leads to the well-known Dyson series (given here in the Schrödinger picture)¹⁹⁷

$$|\psi(t)\rangle = |\psi^{(0)}(t)\rangle + \sum_{n=1}^{\infty} \left(\frac{i}{\hbar}\right)^n \prod_{j=1}^n \left\{ \int_{t_0}^{\tau_{j+1}} d\tau_j e^{-\frac{i}{\hbar}\hat{H}_0(\tau_{j+1}-\tau_j)} \hat{H}'(\tau_j) \right\} e^{-\frac{i}{\hbar}\hat{H}_0(\tau_1-t_0)} |\psi(t_0)\rangle \quad (2.10)$$

where $\tau_{n+1} \equiv t$. This gives the wavefunction in terms of a power expansion of the weak perturbative term H' . Each perturbative term has an associated τ_j , or absolute time where the interaction occurs.

A similar treatment using the density operator is straightforward, however, the commutator in the Liouville-Von Neumann equation generates a series of nested commutators in the

result. The fundamental character; however, is still that of a power series in the perturbation

$$\hat{\rho}(t) = \hat{\rho}^{(0)} + \sum_{n=1}^{\infty} \hat{\rho}^{(n)}(t) \quad (2.11)$$

Where $\hat{\rho}^{(n)}(t)$ is the n th-order density operator, ordered in powers of the perturbation, and $\hat{\rho}^{(0)}$ is the zeroth-order (unperturbed) density matrix.

$$\hat{\rho}^{(n)}(t) = - \left(\frac{i}{\hbar} \right)^n \prod_{j=1}^n \int_{t_0}^{\tau_{j+1}} d\tau_j [\hat{H}'_I(\tau_n), [\hat{H}'_I(\tau_{n-1}), \dots [\hat{H}'_I(\tau_1), \hat{\rho}_I(t_0)] \dots]] \quad (2.12)$$

again where $\tau_{j+1} \equiv t$.

The experimentally observable macroscopic polarization is the expectation value of the dipole operator

$$P(t) = \langle \hat{\mu} \rangle = \text{Tr} (\hat{\mu} \hat{\rho}(t)) \quad (2.13)$$

The n th-order polarization can be obtained by substituting the n th order density operator and the specific perturbation (Equations 2.12 and 2.4). Since the n th-order polarization depends on the delays between pulses, rather than their absolute times (stationarity), we also move from absolute time to time intervals ($t_n = \tau_{n+1} - \tau_n$), and set $0 = \tau_1$ (the first interaction is considered to occur at $t = 0$).

$$P^{(n)}(t) = \prod_{j=1}^n \int_0^{\infty} dt_j E_j(t - \sum_{k=j}^n t_k) R^{(n)}(t_n, \dots, t_1) \quad (2.14)$$

where E_j is the j th driving electric field, and $R^{(n)}$ is the molecular response, which is defined by

$$R^{(n)}(t_n, \dots, t_1) = - \left(-\frac{i}{\hbar} \right)^n \text{Tr} \left\{ \hat{\mu} \left(\sum_{l=1}^n t_l \right) \left[\hat{\mu} \left(\sum_{m=1}^{n-1} t_m \right), \dots [\hat{\mu}(0), \hat{\rho}(-\infty)] \dots \right] \right\} \quad (2.15)$$

The transition dipole operator $\hat{\mu}$ is a matrix consisting of off-diagonal elements that give the probability of transitions between states.¹⁹⁷ In the harmonic approximation, only transitions between adjacent states are allowed. The transition dipole operator is then proportional to

the sum of raising and lowering operators, times the magnitude of the 0–1 transition dipole moment.

$$\hat{\mu} = |\mu_{01}|(\hat{a} + \hat{a}^\dagger) = |\mu_{01}| \begin{bmatrix} 0 & 1 & & & \\ 1 & 0 & \sqrt{2} & & \\ & \sqrt{2} & 0 & \sqrt{3} & \\ & & \sqrt{3} & 0 & \ddots \\ & & & \ddots & \ddots \end{bmatrix} \quad (2.16)$$

In the harmonic case, this is a sparse matrix; however, with anharmonicity, additional transitions (e.g. overtones) become possible, and the matrix must be calculated explicitly.

Assuming that there is no molecular response before the first interaction, Equation 2.14 shows that the observed n th-order polarization is a convolution of the molecular response with the driving laser pulses (electric fields). In the limit as the envelope of the pulses becomes much shorter than the timescale of the molecular response, the n th order polarization is directly proportional to the molecular response.

When the driving field is on resonance, the dipole operator shifts density from diagonal to off-diagonal elements (generating coherences between adjacent states, $\hat{\rho}_{nm} = c_n c_m^*$), and from off-diagonal to diagonal elements (generating a population from a coherence, $\hat{\rho}_{nn} = c_n c_n^*$). The frequency of the coherence depends on the difference in energy between the two states ($(E_n - E_m)/\hbar$), and creates an oscillating dipole at the resonant frequency between the two states

$$\hat{\rho}_{10} = i \langle c_1(t) c_0^*(t) \rangle = i c_1 c_0 e^{-i\omega_{01}t} \quad (2.17)$$

Hermiticity of the density matrix ($\rho_{ij} = \rho_{ji}^*$) implies that ρ_{01} will rotate through the complex plane with the same frequency, but in the opposite direction, as ρ_{10} .

It is then straightforward to show that the first order response (neglecting dephasing, orientational, and lifetime effects) is given by

$$R^{(1)}(t_1) = \frac{i}{\hbar} \text{Tr} \left(\hat{\mu}(t_1) [\hat{\mu}(0), \hat{\rho}(-\infty)] \right) \quad (2.18a)$$

$$= \frac{i}{\hbar} \text{Tr} \left(\hat{\mu}(t_1) \hat{\mu}(0) \rho \right) - \frac{i}{\hbar} \text{Tr} \left(\hat{\rho}(-\infty) \hat{\mu}(0) \hat{\mu}(t_1) \right) \quad (2.18b)$$

$$\equiv R_1^{(1)}(t_1) + R_1^{*(1)}(t_1) \quad (2.18c)$$

$$= \frac{i}{\hbar} \mu_{01}^2 (e^{-i\omega_{01}t_1} - e^{+i\omega_{01}t_1}) \propto \mu_{01}^2 \sin(\omega_{01}t_1) \quad (2.18d)$$

The two terms that arise from expanding the commutator are complex conjugates of each other, due to the invariance of a trace under cyclic permutation. Since $R^{(1)}$ and $R^{*(1)}$ do not vary in their real components (what a square-law IR detector measures), it is conventional to express response functions purely in terms of their R_n and neglect R_n^* .

The first-order polarization depends on the convolution of the driving electric field with the first-order response (omitting for the moment the wavevectors and phases in the electric field, as they make the equations more cumbersome)

$$\begin{aligned} P^{(1)}(t) &= \frac{i\mu_{01}^2}{\hbar} \int_0^\infty dt_1 (E(t-t_1) + E^*(t-t_1)) (e^{-i\omega_{01}t_1} - e^{+i\omega_{01}t_1}) \\ &= \frac{i\mu_{01}^2}{2\hbar} \int_0^\infty dt_1 \vec{E}'(t-t_1) (e^{-i\omega(t-t_1)} + e^{+i\omega(t-t_1)}) (e^{-i\omega_{01}t_1} - e^{+i\omega_{01}t_1}) \end{aligned} \quad (2.19)$$

Since each term in the response can interact with either E or E^* , there are four possible terms contributing to the macroscopic first-order polarization. Assuming, however, that the system is on-resonance, and $\omega = \omega_{01}$, we can simplify this by applying the rotating wave approximation (RWA). Multiplying the exponentials and collecting the terms in t_1 , we keep only those terms that contain the difference of frequencies ($\omega - \omega_{01} = 0$). The terms containing the sum of frequencies ($\omega + \omega_{01} = 2\omega_{01}$) are highly oscillatory, and their integral can be neglected when on resonance.

$$\begin{aligned} P^{(1)}(t) &= \frac{i\mu_{01}^2}{2\hbar} \left\{ e^{-i\omega t} \int_0^\infty dt_1 \vec{E}'(t-t_1) (e^{i(\omega-\omega_{01})t_1} + e^{i(\omega+\omega_{01})t_1}) \right. \\ &\quad \left. - e^{i\omega t} \int_0^\infty dt_1 \vec{E}'(t-t_1) (e^{-i(\omega+\omega_{01})t_1} + e^{-i(\omega-\omega_{01})t_1}) \right\} \\ &\approx \frac{i\mu_{01}^2}{2\hbar} \left\{ e^{-i\omega t} \int_0^\infty dt_1 \vec{E}'(t-t_1) - e^{i\omega t} \int_0^\infty dt_1 \vec{E}'(t-t_1) \right\} \end{aligned} \quad (2.20)$$

In the limit where incident optical pulses are short compared with the timescale of the system's response, but long compared to the oscillation period of the light, we can approximate the pulse envelope as a Dirac delta function, but retain frequency, phase, and wavevector information.

$$E(t) = \delta(t) e^{i(\vec{k}\cdot\vec{r}-\omega t+\phi)} \quad (2.21a)$$

$$E^*(t) = \delta(t) e^{-i(\vec{k}\cdot\vec{r}-\omega t+\phi)} \quad (2.21b)$$

This semi-impulsive limit greatly simplifies the calculation of n th-order spectra, as the convolutions in Equation 2.14 disappear.

Including phase and wavevector information, and in the semi-impulsive limit, we find that the macroscopic polarization generated by a coherence is an oscillating electric field at the resonant frequency of the transition.

$$\begin{aligned} P^{(1)}(t) &\approx \frac{i\mu_{01}^2}{2\hbar} \left(e^{i(\vec{k}\cdot\vec{r}-\omega t+\phi)} - e^{-i(\vec{k}\cdot\vec{r}-\omega t+\phi)} \right) \\ &= \frac{\mu_{01}^2}{\hbar} \sin(\vec{k}\cdot\vec{r}-\omega t+\phi) \end{aligned} \quad (2.22)$$

The electric fields imprint a wavevector and phase on the polarization, which is emitted in the direction of the optical pulse. In the far field, there is an additional phase lag of 90° because the sample acts as a sheet of oscillating dipoles.¹⁹⁸ This phase lag causes the induced field to cancel the driving field at the detector.

The third-order response (necessary for the description of 2D-IR spectroscopy) contains eight terms from expanding the nested commutatorⁱⁱⁱ

$$\begin{aligned} R^{(3)}(t_1, t_2, t_3) = & - \left(-\frac{i}{\hbar} \right)^3 \text{Tr} \left(\hat{\mu}_3 \hat{\mu}_2 \hat{\mu}_1 \hat{\mu}_0 \hat{\rho} - \hat{\mu}_3 \hat{\mu}_2 \hat{\mu}_1 \hat{\rho} \hat{\mu}_0 - \hat{\mu}_3 \hat{\mu}_2 \hat{\mu}_0 \hat{\rho} \hat{\mu}_1 + \hat{\mu}_3 \hat{\mu}_2 \hat{\rho} \hat{\mu}_1 \hat{\mu}_0 \right. \\ & \left. - \hat{\mu}_3 \hat{\mu}_1 \hat{\mu}_0 \hat{\rho} \hat{\mu}_2 + \hat{\mu}_3 \hat{\mu}_1 \hat{\rho} \hat{\mu}_0 \hat{\mu}_2 + \hat{\mu}_3 \hat{\mu}_0 \hat{\rho} \hat{\mu}_1 \hat{\mu}_2 - \hat{\mu}_3 \hat{\rho} \hat{\mu}_0 \hat{\mu}_1 \hat{\mu}_2 \right) \end{aligned} \quad (2.23)$$

where $\hat{\rho} \equiv \hat{\rho}(-\infty)$ and $\hat{\mu}_n \equiv \hat{\mu}(\sum_{j=1}^n t_j)$.

After convoluting with the electric field, there are 64 terms. Of these, 12 survive the rotating wave approximation, and 6 represent unique combinations of coherences and populations ($R_1^{(3)}$ through $R_6^{(3)}$). The other 6 terms are their complex conjugates ($R_1^{*(3)}$ through $R_6^{*(3)}$), and do not contain additional information.

It is tedious to work out all combinations and determine which survive the RWA by hand (in part because some of the terms in Equation 2.23 contribute to multiple pathways, due to the invariance of the trace to cyclic permutation, combined with different electric field interactions). Because of this, and the need to keep track of more complicated systems (e.g. 5th-order spectroscopies or 3rd-order spectroscopies with coupled oscillators), it is common to use double-sided Feynman diagrams (a graphical perturbation theory) to keep track of the various pathways through Liouville space that survive the RWA (Figure 2).^{196,197}

ⁱⁱⁱExpanding a nested commutator will yield 2^n terms, where n is the number of commutations.

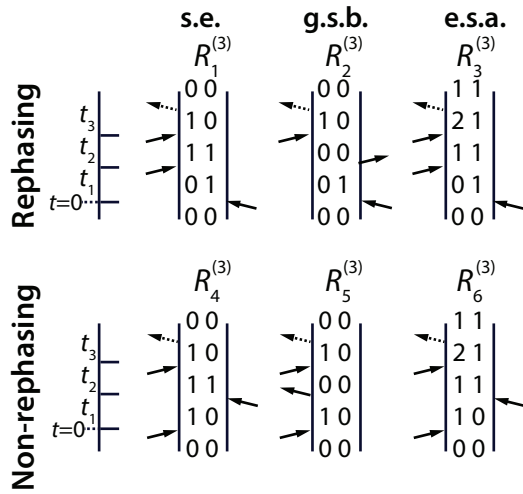


Figure 2: Double sided Feynman diagrams for the paths through Liouville space (in the harmonic and rotating wave approximations). The top row shows rephasing diagrams, where the coherences in t_1 and t_3 have opposite signs. The bottom row shows non-rephasing pathways. Each diagram represents a single term in the expansion of the nested commutator for the macroscopic polarization of the sample.

Each diagram represents a specific term in the n th-order macroscopic polarization, and gives (1) the coherences (in Dirac notation, which implicitly includes the direction of the frequency) (2) the population states (3) the electric field term (E or E^*) that generates each coherence and (4) the sign of the specific term in the molecular response (neglecting the prefactor of i^n). By convention, only terms with emission from the *ket* (left) side are plotted. Corresponding terms with emission from the *bra* (right) side are complex conjugates of those plotted.

After collecting terms by frequencies during ω_1 and ω_3 (the coherences during t_1 and t_3), two types of diagrams survive the RWA. They are grouped based on the direction in which they are emitted, which depends on the wavevectors of the driving electric fields that are imparted to them.

$$R_{1,2,3}^{(3)} \equiv \sum_{n=1}^3 R_n^{(3)}(t_1, t_2, t_3) = -\frac{i2\mu_{01}^4}{\hbar^3} \left(e^{-i\omega_{01}(t_3-t_1)} - e^{-i((\omega_{01}-\Delta_{anh})t_3-\omega_{01}t_1)} \right) \quad (2.24a)$$

$$R_{4,5,6}^{(3)} \equiv \sum_{n=4}^6 R_n^{(3)}(t_1, t_2, t_3) = -\frac{i2\mu_{01}^4}{\hbar^3} \left(e^{-i\omega_{01}(t_3+t_1)} - e^{-i((\omega_{01}-\Delta_{anh})t_3+\omega_{01}t_1)} \right) \quad (2.24b)$$

Here, Δ_{anh} is the anharmonic shift for the excited state coherence ($\omega_{12} = \omega_{01} - \Delta_{anh}$). Note that this treatment assumes the harmonic scaling of transition dipole moments, and neglects any effects from Stokes shifts on the frequency of stimulated emission.

The first three terms are rephasing pathways (Equation 2.24a), where the sign of the coherence is flipped between t_1 and t_3 . They are emitted in the direction $\vec{k}_s = -\vec{k}_1 + \vec{k}_2 + \vec{k}_3$ (where k_n are the wavevectors of the successive optical pulses). These pathways are responsible for the appearance of a photon echo during t_3 . The second three pathways are non-rephasing pathways (Equation 2.24b), where the sign of the coherence does not change between t_1 and t_3 . They are emitted in the direction $\vec{k}_s = \vec{k}_1 - \vec{k}_2 + \vec{k}_3$. In a ‘‘pump-probe’’ experimental geometry, where the first two pulses are collinear and $\vec{k}_1 = \vec{k}_2$, both signal are emitted in the direction of the third pulse (\vec{k}_3).

The treatment to this point in the chapter neglects effects such as dephasing, vibrational relaxation, and molecular reorientation, which are essential to understanding the lineshape of an infrared spectrum. The next sections gradually introduce these concepts, fleshing out

a more complete response function, and its physical implications, on the skeleton derived from quantum mechanical principles in this introduction.

2.2 LINESHAPE THEORY

The response function developed so far, which contains only oscillatory frequencies, would result in a spectrum that consists of a Dirac δ function at each resonant frequency; however, the IR spectrum, even of a single oscillator, has a natural linewidth. This linewidth results from effects such as the finite lifetime of a coherence (lifetime broadening), rotations of the molecule (orientational broadening), and dephasing effects. We will begin by considering the case of homogeneous dephasing, and we will progress to more advanced cases from there.

2.2.1 Homogeneous Dephasing

Homogeneous dephasing, the loss of the initial phase of the coherence, is modeled phenomenologically as a sum of first order rates for pure dephasing (T_2^*), caused by fluctuations in the environment, population relaxation (T_1), and orientational relaxation (T_{or}).

$$\frac{1}{T_2} = \frac{1}{T_2^*} + \frac{1}{2T_1} + \frac{1}{T_{or}} \quad (2.25)$$

Dephasing can only occur during a coherence, and gives an exponential decay of the signal intensity. It can be phenomenologically included in the response function by multiplication with an exponential decay over each coherence time. For the first order response, including dephasing, $R_1^{(1)}$ is then given by

$$R_1^{(1)}(t_1) = \frac{i\mu_{01}^2}{\hbar} e^{-i\omega_{01}t_1} e^{-t_1/T_2} \quad (2.26)$$

The Fourier transform (power spectrum) of this signal is a convolution of real Lorentzian and imaginary dispersive lineshapes with the first-order response (a δ function at a single

resonant frequency) developed so far, giving a “natural linewidth” to the peak.

$$S(\omega) = 2 \int_0^\infty dt e^{i\omega t} iR^{(1)}(t) \quad (2.27a)$$

$$\propto \mu_{01}^2 \frac{1}{i(\omega - \omega_{01}) - \Gamma} \quad (2.27b)$$

where ω_{01} is the central frequency of the vibration and $\Gamma \equiv 1/T_2$. The observed power spectrum after self-heterodyning with the optical pulse (since the field is emitted in the \vec{k}_3 direction) is equal to the real portion, that is a Lorentzian peak shape

$$A(\omega) = \Re(S(\omega)) \propto \mu_{01}^2 \frac{\Gamma}{(\omega - \omega_{01})^2 + \Gamma^2} \quad (2.28)$$

The imaginary part of the signal (which we cannot measure using a square law detector) gives the dispersive part of the lineshape

$$D(\omega) = \Im(S(\omega)) \propto -\mu_{01}^2 \frac{\omega - \omega_{01}}{(\omega - \omega_{01})^2 + \Gamma^2} \quad (2.29)$$

For a two-dimensional infrared spectrum, assuming harmonic scaling of the transition dipole moment and equal homogeneous dephasing times for the 0–1 and 1–2 transitions, the response function (Equations 2.24a and 2.24b) is relatively simple to modify, as it is simply multiplied by dephasing components for t_1 and t_3 .

$$\begin{aligned} R_{1,2,3}^{(3)} &= R_{1,2,3}^{(3)} e^{-\Gamma(t_1+t_3)} \\ R_{4,5,6}^{(3)} &= R_{4,5,6}^{(3)} e^{-\Gamma(t_1+t_3)} \end{aligned} \quad (2.30)$$

The two-dimensional spectrum may then be calculated by a two-dimensional Fourier transform after heterodyning with a local oscillator that provides phase information.^{iv}

$$S(\omega_1, \omega_3; t_2) = \int_0^\infty \int_0^\infty dt_1 dt_3 \sum_n iR_n(t_1, t_2, t_3) e^{i\omega t_1} e^{i\omega t_3} \quad (2.31)$$

After Fourier transform, it is possible to find an analytic form for the spectra, which is the product of two one dimensional peak shapes. Rephasing spectra can be distinguished from

^{iv}In a pump-probe experimental geometry, the rephasing and non-rephasing signal, which are emitted along \vec{k}_3 (Section 2.1), are self-heterodyned by the third pulse.

non-rephasing spectra by the factor of $\omega_n + \omega_{10}$ in their denominator, which arises from the reversed sign of the coherence during t_1 .

$$\begin{aligned}
R_{1,2}^{(3)}(\omega_1, \omega_3) &\propto \mu_{01}^4 \frac{1}{i(\omega_1 + \omega_{01}) - \Gamma} \cdot \frac{1}{i(\omega_3 - \omega_{01}) - \Gamma} \\
R_3^{(3)}(\omega_1, \omega_3) &\propto \mu_{01}^4 \frac{1}{i(\omega_1 + \omega_{01}) - \Gamma} \cdot \frac{1}{i(\omega_3 - \omega_{12}) - \Gamma} \\
R_{4,5}^{(3)}(\omega_1, \omega_3) &\propto \mu_{01}^4 \frac{1}{i(\omega_1 - \omega_{01}) - \Gamma} \cdot \frac{1}{i(\omega_3 - \omega_{01}) - \Gamma} \\
R_6^{(3)}(\omega_1, \omega_3) &\propto \mu_{01}^4 \frac{1}{i(\omega_1 - \omega_{01}) - \Gamma} \cdot \frac{1}{i(\omega_3 - \omega_{12}) - \Gamma}
\end{aligned} \tag{2.32}$$

These two-dimensional peak shapes contain phase twists that cannot be removed by simply taking the real portion of the spectrum, unlike the first-order case, in which the real component was purely absorptive. The phase twists arise because both the dispersive and absorptive components are split between the real and imaginary parts of the peak (Figure 3). It is possible to calculate an absolute value spectrum, which removes the spectral phase, however, this broadens the peak and can lead to complicated interferences in cases with multiple peaks.

The dispersive components of the rephasing and non-rephasing diagrams, however, have opposite phase twists because they lie in different quadrants of the spectrum due to the difference in sign of ω_1 (non-rephasing spectra are in quadrant I while rephasing spectra are in quadrant II). It is therefore extremely common to calculate purely absorptive spectra by taking the real part of the sum of the non-rephasing and rephasing spectra (rephasing spectra are plotted so that $\omega_1 = -\omega_1$). The purely absorptive spectra remove interferences from overlapping peaks, and give higher frequency resolution of individual peaks. Finally (unlike absolute value spectra) they preserve the sign of the response function, which can be invaluable in identifying the origins of spectral peaks (see Section 4.4.6 for one example).

There are practical challenges in measuring a purely absorptive spectrum in a non-collinear geometry, largely related to determination of the absolute phase of each signal. In a collinear (“pump-probe”) geometry, however, both rephasing and non-rephasing signals are emitting in the same direction, and so a purely absorptive spectrum is natively collected.

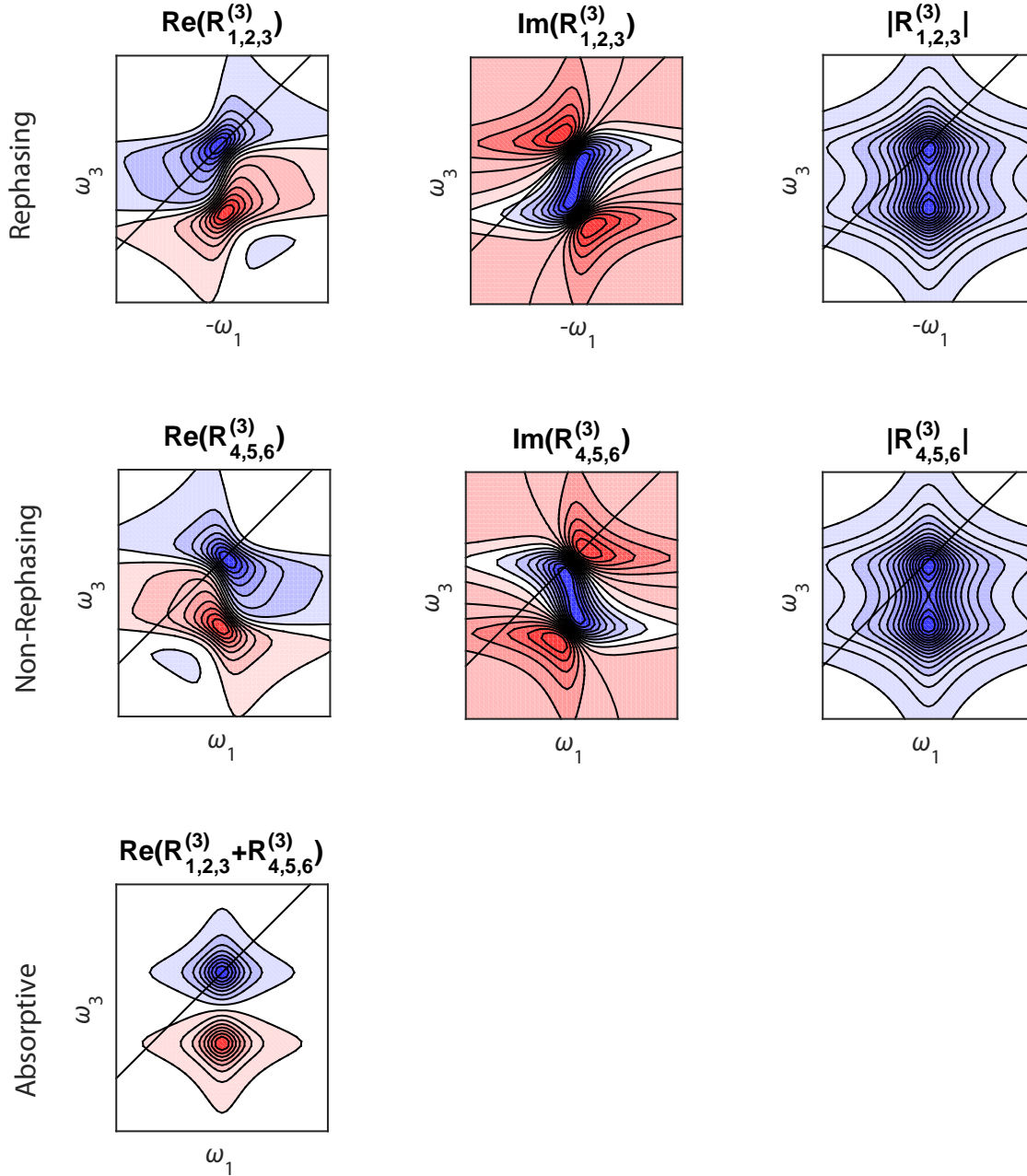


Figure 3: The real, imaginary, and absolute value spectra of an anharmonic oscillator with a lineshape from pure dephasing. Blue peaks have negative values while red peaks are positive. Both rephasing and non-rephasing spectra contain phase twists in their real values, making interpretation difficult. The absolute value removes the spectral phase, but broadens the peak compared with the purely absorptive spectra, which is the real portion of $R_{1,2,3}^{(3)}(-\omega_1, \omega_3; t_2) + R_{4,5,6}^{(3)}(\omega_1, \omega_3)$.

2.2.2 Non-homogeneous Dephasing

In the limit of homogeneous dephasing just described, the absorptive lineshape of the 2D spectrum is a two-dimensional Lorentzian that does not change as a function of the delay between the second and third perturbations (the population time, t_2). This model is a good description if there is only a single resonant transition frequency, or if (as will be described herein) the time-dependent changes in oscillatory frequency are relatively small in amplitude and rapid compared with the timescale of the molecular response.

Most 2D-IR spectra, even of single vibrational modes, show a spectral lineshape that changes with increasing population time. Such a change in lineshape cannot be described by a phenomenological damping term (T_2), and require a more complete treatment. The stochastic lineshape theory used is adapted from Kubo's famous treatment of dephasing in NMR spectra.

A vibrational mode can be treated as an anharmonic oscillator, the frequency of which depends on the shape of its multi-dimensional potential energy surface. The curvature of this surface depends on the coupling of the vibrational mode to its local environment. Environmental effects such as electric fields and field gradients, charge transfer, dispersion, and even exchange repulsion interactions can change the curvature of the potential energy surface, and thus the energies of stationary states of the oscillator. Even a one-dimensional harmonic oscillator will show these effects, since the energy levels depend on the spring constant of the bond, which determines the curvature of the potential energy surface

$$\hat{V} = \frac{1}{2}k\hat{q}^2 \tag{2.33a}$$

$$E_v = \hbar\sqrt{\frac{k}{\mu}}\left(v + \frac{1}{2}\right) \tag{2.33b}$$

$$\frac{E_2 - E_1}{\hbar} = \sqrt{\frac{k}{\mu}} \tag{2.33c}$$

where \hat{V} is the potential energy operator, k is the spring constant of the bond, \hat{q} is the position operator, μ is the reduced mass, and v is the vibrational quantum number.

As the local environment changes around the vibration, its instantaneous frequency will change as its instantaneous potential energy surface changes. This stochastic walk through

frequency space is referred to as spectral diffusion and, if it occurs on the appropriate timescale (typically hundreds of femtoseconds to picoseconds), it can cause population time dependent changes in the spectral lineshape. The timescale of this spectral diffusion, and the total frequency width sampled, depends on the timescale of molecular motions in the condensed phase, and the magnitude of the coupling between the high frequency vibrational mode and the bath degrees of freedom (the low frequency spectral density). Such coupling is typically treated semi-classically, with the high frequency vibration treated quantum mechanically and the bath treated classically.

Of course, a high frequency vibration can also couple to other high frequency vibrational modes (either directly or anharmonically), and these couplings will cause characteristic changes in the spectral lineshape, especially the evolution of cross-peaks. They are not typically considered, however, in the treatment of non-homogeneous dephasing, and so they are neglected in this discussion.

The time dependent fluctuation in the vibrational frequency is treated using an ensemble average of the elements of the density matrix. The fluctuating frequency approximation is then invoked, assuming that there is a time-independent average frequency and a time-dependent fluctuation about that average value.

$$\omega_{01}(t) = \langle \omega_{01} \rangle + \delta\omega_{01}(t) \quad (2.34a)$$

$$\langle \delta\omega_{01}(t) \rangle = 0 \quad (2.34b)$$

where $\langle \omega_{01} \rangle$ is the time-independent ensemble average frequency, and $\delta\omega_{01}(t_1)$ is a time-dependent frequency fluctuation. The first-order response function then includes both the ensemble average and the response function

$$R_1^{(1)}(t_1) = ie^{-i\langle \omega_{01} \rangle t_1} \left\langle \mu_{01}(0)\mu_{01}(t_1)e^{-i\int_0^{t_1} d\tau \delta\omega_{01}(\tau)} \right\rangle \quad (2.35)$$

or in the third-order case

$$R_{1,2}^{(3)}(t_1, t_2, t_3) = -\frac{2i}{\hbar^3} e^{i\langle\omega_{01}\rangle t_1 - i\langle\omega_{01}\rangle t_3} \dots \times \left\langle \prod_{j=1}^4 \left\{ \mu_{01} \left(\sum_{k=0}^{j-1} t_k \right) \right\} \exp \left[i \int_0^{t_1} d\tau \delta\omega(\tau) - i \int_{t_1+t_2}^{t_1+t_2+t_3} d\tau \delta\omega(\tau) \right] \right\rangle \quad (2.36a)$$

$$R_{4,5}^{(3)}(t_1, t_2, t_3) = -\frac{2i}{\hbar^3} e^{-i\langle\omega_{01}\rangle t_1 - i\langle\omega_{01}\rangle t_3} \dots \times \left\langle \prod_{j=1}^4 \left\{ \mu_{01} \left(\sum_{k=0}^{j-1} t_k \right) \right\} \exp \left[-i \int_0^{t_1} d\tau \delta\omega(\tau) - i \int_{t_1+t_2}^{t_1+t_2+t_3} d\tau \delta\omega(\tau) \right] \right\rangle \quad (2.36b)$$

where $t_0 \equiv 0$. In the Condon approximation, that the transition dipole moment does not depend on the molecule's vibrational frequency (and thus is time independent), the transition dipole moments can be factored from the ensemble average to the prefactor.

This slowly converging oscillatory ensemble average can be evaluated computationally from a frequency trajectory; however, it is often treated with a perturbative power expansion to allow analysis with functions^{196,197}

$$\begin{aligned} \left\langle \exp \left[-i \int_0^t d\tau \delta\omega_{01}(\tau) \right] \right\rangle &= 1 - i \int_0^t d\tau \langle \delta\omega_{01}(\tau) \rangle \dots \\ &\quad - \frac{1}{2} \int_0^t d\tau_2 \int_0^{\tau_2} d\tau_1 \langle \delta(\omega_{01}(\tau_1) \delta\omega_{01}(\tau_2)) \rangle + \dots \quad (2.37a) \\ &\equiv e^{-g(t)} = 1 - g(t) - \frac{1}{2} g^2(t) + \dots \end{aligned}$$

The linear term vanishes, since it is the ensemble average of $\delta\omega(t)$ (Equation 2.34a), and the leading term in the series is then the lineshape function

$$g(t) = \int_0^t d\tau_1 \int_0^{\tau_1} d\tau_2 \langle \delta\omega_{01}(\tau_2) \delta\omega_{01}(0) \rangle \quad (2.38)$$

The cumulant expansion is normally truncated at second order, which is exact when the distribution of frequency fluctuations is Gaussian. Substituting the lineshape function into the first-order and third-order responses gives straightforward expressions for each.¹⁹⁶

$$R_1^{(1)}(t_1) = \frac{i\mu_{01}^2}{\hbar} e^{-i\langle\omega_{01}\rangle t_1} e^{-g(t_1)} \quad (2.39a)$$

$$R_{1,2}^{(3)}(t_1, t_2, t_3) = -\frac{2i\mu_{01}^4}{\hbar^3} e^{i\langle\omega_{01}\rangle t_1 - i\langle\omega_{01}\rangle t_3} e^{-g(t_1) + g(t_2) - g(t_3) - g(t_1+t_2) - g(t_2+t_3) + g(t_1+t_2+t_3)} \quad (2.39b)$$

$$R_{4,5}^{(3)}(t_1, t_2, t_3) = -\frac{2i\mu_{01}^4}{\hbar^3} e^{-i\langle\omega_{01}\rangle t_1 - i\langle\omega_{01}\rangle t_3} e^{-g(t_1) - g(t_2) - g(t_3) + g(t_1+t_2) + g(t_2+t_3) - g(t_1+t_2+t_3)} \quad (2.39c)$$

The lineshape function itself is the double time integral of the two-point frequency fluctuation correlation function (FFCF).

$$C(\tau_1) = \langle \delta\omega(\tau_1)\delta\omega(0) \rangle \quad (2.40)$$

The FFCF contains substantial information about characteristic timescales of local dynamics around a vibration, and thus is the observable of interest when attempting to understand, for example, the dynamics of a solvent shell around a molecule. The Fourier transform of the frequency fluctuation correlation function is the spectral density ($\tilde{C}(\omega)$), weighted by the magnitude of coupling of bath modes into the high frequency observed mode.

The behavior of the correlation function depends on the damping of the system. Underdamped (high frequency / low friction) modes show oscillations in their correlation functions. With zero solvent friction, the oscillator shows coherent motion. With low, but finite, friction, the correlation function shows damped oscillations. Overdamped (low frequency / high friction) modes typically show an exponential decrease in correlation.¹⁹⁶

The FFCF of a high frequency mode coupled to an overdamped bath can be approximated using Kubo’s exponential ansatz¹⁹⁹

$$\langle \delta\omega(\tau)\delta\omega(0) \rangle = \Delta^2 e^{-\frac{|\tau|}{\tau_c}} \quad (2.41)$$

which includes terms that describe the variance in frequency fluctuations (Δ^2) and the characteristic timescale of the chromophore’s frequency fluctuations (τ_c). Integrating this correlation function twice generates a Kubo lineshape function

$$g(t) = \Delta^2 \tau_c^2 \left[e^{-\frac{|t|}{\tau_c}} + \frac{t}{\tau_c} - 1 \right] \quad (2.42)$$

A Kubo lineshape is related to commonly employed lineshapes for fitting FTIR (and other spectra); however, it might not be apparent at first glance. The Lorentzian and Gaussian peak shapes can be derived from the fast and slow modulation limits of the Kubo lineshape respectively (Figure 4). The Voigt profile approximates bimodal dynamics by combining the results from both limiting cases of the Kubo lineshape. In certain cases, these cases can be good approximations to the experimental lineshape; however, often a Kubo lineshape provides a more accurate physical description of the dynamics.

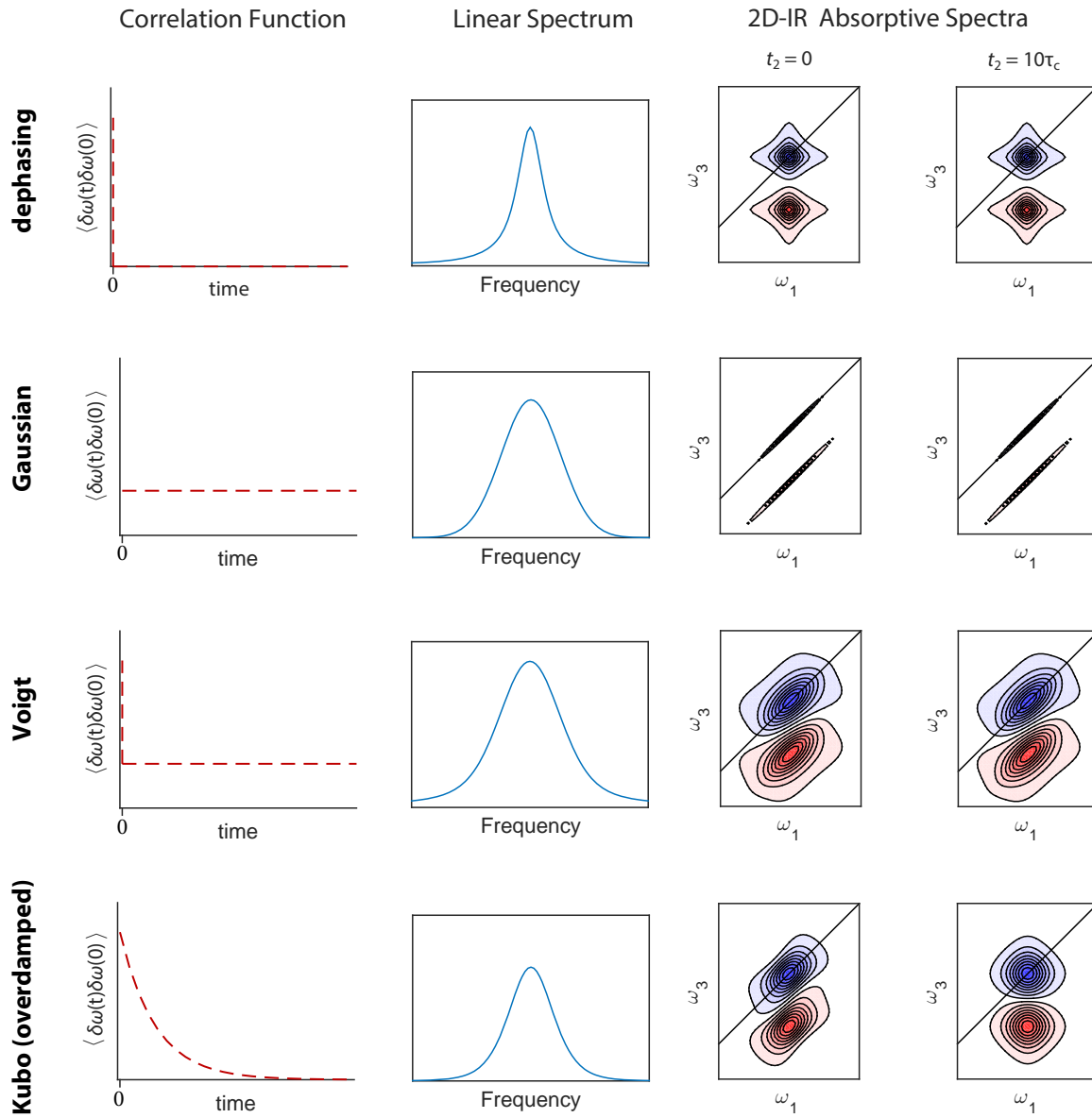


Figure 4: Correlation functions, first-order IR spectra, and 2D-IR absorptive spectra for Lorentzian, Gaussian, Voigt, and Kubo lineshapes. The Voigt lineshape, which approximates the dynamics of a two-component system with fast inertial and slow diffusive components, does not capture spectral diffusion in the 2D lineshape, although it can approximate the linear spectrum well for most transitions.

The first limiting case is the fast modulation limit (or homogeneous limit). In this case, there are frequency fluctuations that are very small in amplitude, or correlation times that are very short. The determining factor is the product of the frequency distribution and the correlation time ($\Delta\tau$). When $\Delta\tau_c \ll 1$, the system is in the fast modulation limit. The value of $g(t)$ is dominated by the second term (t/τ_c),

$$\lim_{\Delta\tau \rightarrow 0} (g(t)) = \Delta^2 \tau_c t \equiv \frac{t}{T_2^*} \quad (2.43)$$

and leads to a lineshape term from pure dephasing (T_2^*). As seen earlier, the exponential decay in the lineshape function leads to a Lorentzian peak shape. The rate ($T_2^* \equiv (\Delta^2 \tau_c)^{-1}$) of this dephasing process leads to motional narrowing of the lineshape (Figure 5), where the peak width ($1/(\pi T_2^*)$) is significantly less than the width of the instantaneous frequency distribution. Similar phenomena result in both the narrow Lorentzian shape of peaks on NMR, and in coalescence of peaks from quickly exchanging spins environments on NMR. In both cases, the frequency of molecules fluctuates quickly enough that only the average frequency is observed. The associated frequency fluctuation correlation function is a δ -function in time $\langle \delta\omega(\tau)\delta\omega(0) \rangle = \delta(t)/T_2^*$, which approximates loss of initial frequency correlation on a timescale that cannot be resolved in the lineshape of the vibration (often assumed to be inertial dynamics in the case of 2D-IR).

The second limiting case is the slow modulation limit (or inhomogeneous limit). In this case, there are either frequency fluctuations that are very large in amplitude, or correlation times that are very long. Again, the determining factor is the magnitude of $\Delta\tau_c$. When $\Delta\tau \gg 1$, the system is in the slow modulation limit. The lineshape function $g(t)$ becomes independent of the correlation time, as can be readily shown by substitution of the short time limit ($t \ll \tau_c$) of $\exp(-t/\tau_c) \approx 1 - t/\tau_c + t^2/(2\tau_c^2) + \dots$ into Equation 2.42

$$\begin{aligned} \lim_{\Delta\tau \rightarrow \infty} (g(t)) &= \Delta^2 \tau_c^2 \left[1 - \frac{t}{\tau_c} + \frac{t^2}{2\tau_c^2} + \frac{t}{\tau_c} - 1 \right] \\ &= \frac{\Delta^2 t^2}{2} \end{aligned} \quad (2.44)$$

When substituted into the molecular response, this term gives a Gaussian in the time domain. The absorptive lineshape is a Gaussian in frequency with a standard deviation in frequency

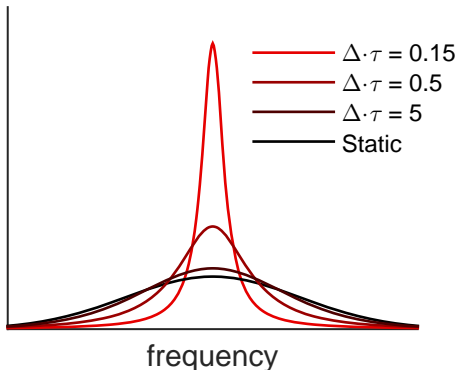


Figure 5: Linear spectrum transitioning from the slow modulation limit ($\Delta\tau_c \gg 1$) to the fast modulation limit ($\Delta\tau_c \ll 1$). Spectra are calculated using a Kubo lineshape, with the width of the frequency distribution Δ held constant (1.6 rad ps^{-1}), while varying the correlation time τ_c . As $\Delta\tau_c$ decreases, the peak becomes motionally narrowed, taking on a Lorentzian character, with a FWHM that is significantly smaller than that of the distribution.

of Δ (the underlying frequency distribution). This limit assumes that the frequencies of molecules do not vary on the timescale of vibrational relaxation, indicating that there is a quasi-static distribution of local environments. The associated frequency fluctuation correlation function is simply the variance of the frequency distribution $\langle \delta\omega(\tau)\delta\omega(0) \rangle = \Delta^2$, and does not vary with time.

The Voigt peak shape (Voigt profile) is the convolution of a Gaussian and Lorentzian peak shape. It is often used for empirically fitting IR absorption bands, with the phenomenological justification that it applies the natural linewidth at each point in the static Gaussian frequency distribution (thus accounting for both homogeneous and inhomogeneous dynamics). The implied time correlation function gives a coarse-grained biexponential dynamics

$$\langle \delta\omega(\tau)\delta\omega(0) \rangle = \frac{\delta(t)}{T_2^*} + \Delta^2 \quad (2.45)$$

$$g(t) = \frac{t}{T_2^*} + \frac{\Delta^2 t^2}{2} \quad (2.46)$$

with the δ function approximating inertial dynamics and the quasi-static component giving a Gaussian frequency distribution. The lineshape function is then the sum of exponential and Gaussian decays. Since the lineshape function is substituted into an exponential in the response function ($R_1^{(3)} \propto e^{-g(t)}$), the dephasing and Gaussian lineshapes are multiplied together in the frequency domain. Fourier transforming convolutes their lineshapes in the frequency domain, according to the convolution theorem

$$\mathcal{F}(f \cdot g) = \mathcal{F}(f) \otimes \mathcal{F}(g) \tag{2.47}$$

where \mathcal{F} is the Fourier transform, f and g are functions, and \otimes indicates a convolution.

The correlation functions implied by a Voigt profile (“Bloch dynamics”) and a Kubo lineshape (“spectral diffusion”) differ in the timescale of implied dynamics over the vibrational lifetime (Figure 4). With a first-order IR spectrum, however, it is nearly impossible to distinguish these spectra within the limitation of experimental noise.

A two-dimensional infrared spectrum, however, contains sufficient information to distinguish these two cases. Spectral diffusion causes changes in the peak shape with increasing population time, due to loss of correlation in initial and final frequencies of the oscillators. Most molecules in condensed phase samples do show population time dependent changes in their 2D-IR spectral lineshapes, and therefore Lorentzian, Gaussian, and Voigt profiles are not appropriate lineshapes to describe their dynamics.

At early population times, before local environment randomizes and the oscillator’s “memory” of its environment during the first coherence time (t_1) is lost, the 2D spectrum appears stretched along the $\omega_1 = \omega_3$ diagonal. This effect results from line narrowing of the rephasing spectrum in the antidiagonal direction at early times with non-homogeneous dephasing. As the system loses memory of its initial condition, the absorptive spectrum becomes more rounded, indicating there is no longer correlation between the initial and final frequencies of the oscillators (Figure 6). There are a variety of methods that are used to either fit the response function directly from the 2D-IR spectra (e.g. global fitting in Section 3.2.3) or use shape-based methods to extract correlation information from 2D-IR spectra (Section 3.2.2). The frequency fluctuation correlation function, of course, need not experience a mo-

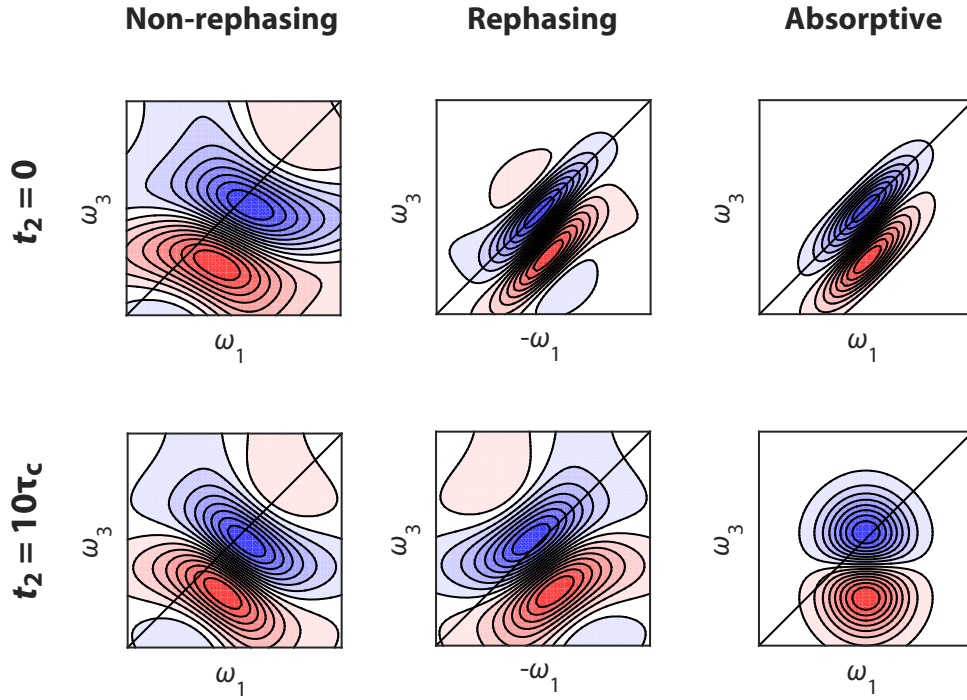


Figure 6: Real components of rephasing, non-rephasing, and purely absorptive 2D-IR spectra for a transition undergoing spectral diffusion (a Kubo lineshape with $\Delta = 1 \text{ rad ps}^{-1}$ and $\tau_c = 1.5 \text{ ps}$). At early population times ($t_2 = 0$, first row), the rephasing spectrum is narrowed in the antidiagonal direction, which causes the absorptive spectrum to be stretched along the diagonal. At late population times ($t_2 = 10\tau_c$), spectral diffusion in both the rephasing and non-rephasing spectra cause the absorptive spectrum to become rounded.

noexponential decay. The FFCF is the inverse Fourier transform of the spectral density

$$C(t) = \mathcal{F}^{-1}(\tilde{C}(\omega)) \tag{2.48}$$

and the (low frequency) spectral density is determined by the intermolecular degrees of freedom of the system. Even only considering the first two solvation shells around a vibrational mode leads to a $6N$ -dimensional (N being the number of particles) phase space. There is no *ab initio* reason why there is a single timescale that describes the “average motions” that cause frequency fluctuations in a chromophore. Indeed, even in single component systems, one often expects at least an inertial time component (from ballistic motions such as librations), and a slower diffusive component that decays exponentially. Heterogeneous systems, such as amphiphiles (e.g. ionic liquids or certain polymer systems), liquid crystals, colloidal dispersions, or membrane bound proteins can have even more complicated dynamics.

The starting point for modeling the dynamics of such a system will often be a linear combination of Kubo lineshapes. Often, one term in the sum will be in the motional narrowing limit (to capture inertial timescales)

$$\langle \delta\omega(t)\delta\omega(0) \rangle = \sum_{i=1}^n \Delta^2 e^{-\frac{|t|}{\tau_c}} \tag{2.49a}$$

$$\approx \frac{\delta(t)}{T_2^*} + \sum_{i=1}^{n-1} \Delta^2 e^{-\frac{|t|}{\tau_c}} \tag{2.49b}$$

When comparing to experimental data, it is not easy to separate the pure dephasing contribution (from motionally narrowed frequency fluctuations) from contributions to homogeneous dephasing from lifetime and orientational effects. One naturally measures a homogeneous dephasing time the orientational and population effects also lead to loss of signal during the coherence times. If the reorientation time (T_{or}) and vibrational lifetime (T_1) are determined from polarization controlled experiments, it is possible to calculate T_2^* using Equation 2.25. A constant offset in the correlation function represents some motions in the system in the slow modulation limit, and broadens the final peaks shape along the diagonal. Complete randomization of the local environment back to the ensemble occurs on a timescale of the longest time constant in the exponential.

Multiple dynamical processes with distinct timescales can contribute to any component of a n -term exponential fit (which coarse grains the dimensionality of the phase space for $6N$ to n). When applying a multiexponential FFCF, we are approximating that there are types of intermolecular motions (that affect the vibrational mode of the chromophore) on distinct timescales. In general, the time constants of a multiexponential Kubo FFCF should each be separated by about an order of magnitude if they are to be clearly resolved.

It is possible for molecular rotations of the molecule to affect the infrared lineshape, through coupling of the molecular orientation into the frequency fluctuation correlation function (especially in a slowly evolving liquid or at an interface). This leads to so-called reorientation-induced spectral diffusion, and is an active area of theoretical development in ultrafast spectroscopies. [200–203](#)

3.0 METHODS

3.1 EXPERIMENTAL METHODS

A schematic of the experimental setup for the lasers and signal delay generator (SDG), optical parametric amplifier (OPA) and 2D-IR spectrometer, as well as detectors and computer-controlled data acquisition shows the main conceptual components of the 2D-IR experiment (Figure 7).

3.1.1 Laser System and Timings

The commercial chirped pulse amplification system (Coherent Legend Elite) comprises an oscillator, an optical stretcher, an amplifier, and an optical compressor.

The solid state Ti:Sapphire oscillator (Vitesse) generates an 80 MHz train of sub-100 fs pulses with a wavelength of 805 nm when it is mode locked (average power around 330 to 340 mW, approximately 4.2 nJ per pulse). It is pumped by a solid state frequency-double Nd:YVO₄ laser (Verdi). Initial mode locking of the oscillator is typically accomplished by a piezoelectric that jitters the laser cavity's back mirror. The mode locked oscillator pulses have a frequency bandwidth ≥ 10 nm.

The 80 MHz pulse train is detected by a photodiode placed after a beam sampler, and the resulting signal is passed through an electronic filter to remove high frequency components. The filtered signal gives an 80 MHz radio frequency (RF) signal that is sent to a signal delay generator (SDG) and used to control the all additional timing in the experiment, including timings for the pump laser and amplifier, and also timings of detectors and opto-electronic elements further down the beam path.

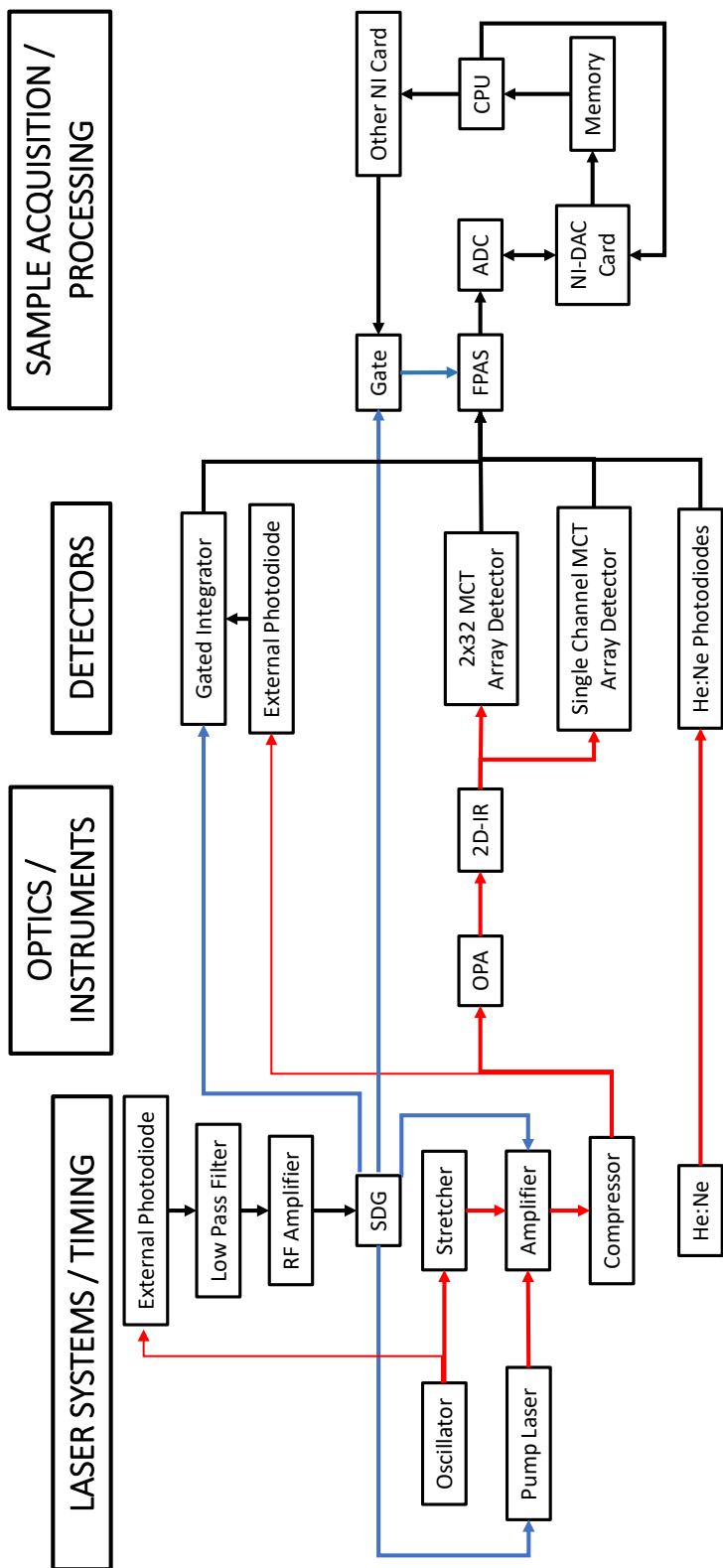


Figure 7: 2D-IR experimental layout. Red lines represent optical pulses, blue lines represent triggers from the signal delay generator (SDG), and black lines represent other electrical signals.

Prior to amplification, pulses are chirped by an optical “stretcher” where different frequencies travel slightly different path lengths after being dispersed by a grating. Stretching the pulse allows amplification without damaging the lasing medium. An internal photodiode in the stretcher is positioned behind one of the mirrors near its edge to detect the stretched pulse. Since the CW (non-mode locked) Ti:Sapphire output has significantly lower bandwidth than the mode locked pulse, it is not dispersed as significantly in the stretcher, and will not trigger the photodiode. Failure to trigger this photodiode will cause a bandwidth error (BWD on the SDG) that prevents laser operation, and is a sign that the oscillator is not properly mode locked.

The amplifier cavity contains a Ti:Sapphire rod that is optically pumped by a frequency-doubled Nd:YVO₄ pump laser (Evolution). Frequency doubling is accomplished by a lithium triborate (LiB₃O₅) crystal, which is temperature-controlled. Timing of the pump laser is controlled by the SDG.

A pair of Pockels cells controls the timing to allow oscillator pulses to enter and exit the amplifier cavity. The frequency of the Pockels cells is variable; however, for all of these experiments, it was set to 5 kHz. The frequency and timing of the Pockels cells are both controlled by the SDG (and thus indirectly by the RF signal from the oscillator). The first Pockels cell controls injection timing, while the second controls ejection timing. The difference between their timings controls the number of round trips a pulse will make in the cavity. Timing of the second Pockels cell in particular has a significant impact on the noise in the laser output, and thus on nonlinear optical processes in the optical parametric amplifier (OPA).

Following pulse ejection, the pulse is optically compressed using a set of gratings and mirrors (essentially the reverse of the optical stretcher described above). Amplification increases the energy per pulse by approximately five orders of magnitude (around 4 W average power and 0.8 mJ per pulse).

3.1.1.1 Modifications to Operation of the Laser System The electronics board of the oscillator has experienced some difficulty with keeping the correct voltages on the circuits involved in (1) measuring the power of the Vitesse, (2) determining if the Vitesse is mode

locked, and (3) running the internal photodiode. The first two caused the `Auto Modelock` feature of the oscillator to constantly run, jittering the back mirror of the cavity and causing spectral modulation that propagated through the system and resulted in a sinusoidal modulation of the intensity of the OPA output at approximately 60 Hz. The third caused a low amplitude radio frequency signal, the amplitude of which (~ 100 mV) was not sufficient to run the timing circuit in the SDG. The low RF signal caused the SDG to “miss” cycles in the 80 MHz RF signal, which caused mis-firing of the Pockels cells, giving rise to dropped pulses down the table. Since all of these problems related back to the electronic board, and all came on around the same time, it was very difficult to chase down the cause of the apparent large fluctuations in the OPA’s mid-IR output.

To ameliorate these difficulties, the following modifications and protocols were put in place.

First, the `Auto Modelock` feature of the oscillator should not be left on during operation. Rather, after a short warm-up period, the `Auto Modelock` feature can be briefly enabled to cause the oscillator to mode lock. Mode locking can be confirmed by examining the average power and bandwidth of the oscillator output. Average power can be detected with the thermopile power meter, and should be above 320 mW. The spectrum of the oscillator can be determined using an external fiber optic spectrometer (Ocean Optics). The full width at half maximum of the peak should be higher than 10 nm, and there should not be significant modulation of the frequency by eye.

Second, the internal photodiode was replaced with an external photodiode (ThorLabs) placed after the first turning mirror outside of the oscillator. The signal from this photodiode is filtered with a lowpass filter, and then amplified using an RF amplifier to obtain an amplitude of slight less than 1 V before being passed to the SDG.

3.1.2 Optical Parametric Amplifier and 2D-IR Systems

The optical parametric amplifier design by Hamm, Kaindl, and Stenger leads to suppression of random laser noise, yielding pulse energy fluctuations as low as 0.2%,²⁰⁴ and allows the downconversion of 805 nm optical pulses from the laser into tunable mid-infrared pulses with

a bandwidth of approximately 200 cm^{-1} . Approximately 1 W of output from the Legend (200 μJ per pulse) is used to run the OPA. The nonlinear optical processes

Less than 3% of this energy is used for continuum white light generation by focusing onto a sapphire filament, after being split off with a beam sampler. The polarization of the NIR light used for white light generation is first rotated by 90° from horizontal to vertical using a half waveplate / polarizer combo.

The white light is used to seed a type II β -barium borate (BBO) crystal, which is optically pumped by NIR light (approximately 2% of the total input), and then re-pumped (after returning from a concave mirror) by the remainder of the NIR light, yielding between 60 and 70 μJ of signal (amplified white light) and idler (at the difference frequency between signal and the pump light). The central frequency of the signal, or the frequency of white light that is amplified, is controlled by tuning the phase matching angle of the BBO crystal.

Signal and idler are then separated using a dichroic mirror, and spatially and temporally overlapped in a type I silver thiogallate (AgGaS_2) crystal, which downconverts the wavelength through difference frequency mixing. The resulting mid-infrared pulses have a tunable wavelength from 2 to 10 μm and an energy from 1 to 2 μJ . Higher frequency outputs, including signal and idler, are filtered out using a longpass filter before entry into the 2D-IR spectrometer.

Temporal overlap of the first two pumps and white light in the BBO crystal, and of signal and idler in the AgGaS_2 crystal, is controlled using three independent translational stages. Since the spatial length of a 100 fs wavepacket is only around 30 μm , it is necessary to have stages that can be controlled to the micron to ensure pulse overlap.

The 2D-IR spectrometer design by Helbing and Hamm²⁰⁵ utilizes a pump-probe design. A wedged calcium fluoride window immediately after the OPA creates two back reflections that serve as probe (third pulse) and reference pulses, while allowing transmission of the majority of the OPA output to a Mach-Zehnder interferometer.

The beam encounters two beam splitters in the interferometer. The first serves to split the beam into two pump pulses. The second splits off a portion of each pump pulse that is sent to a single channel MCT detector. This single channel detector allows the collection of a pump pulse interferogram for each scan of the interferometer, and thus provides phase

information for the spectrum. The remainder of the pump light travels collinearly to the sample, where it is spatially overlapped with the probe pulse.

The probe and reference beams are focused to the sample by an off-axis parabolic mirror (which also focus the pump light to the same position as the probe), while a second serves to re-collimate the beam after the sample (a telescope). Assuming the pump pulses are collinear ($\Delta\vec{k}_{12} = 0$), both rephasing and non-rephasing signals are emitted along the direction of the probe pulse (Chapter 2). The signal field is thus self-heterodyned by the probe pulse, and there is therefore no independent local oscillator. The probe, now also containing third order signal, and reference beams are directed to a single monochromator, which disperse them onto a 2×32 mercury cadmium telluride (MCT) array detector (Section 3.1.3).

The Mach-Zehnder interferometer is continuously scanned during data acquisition, and the delay time is tracked by the interference of a He:Ne laser, which also travels through the interferometer, approximately 2 cm above the infrared beam (Section 3.1.4). The He:Ne beam is initially linearly polarized, and may be treated as the addition of two components ($|x\rangle$ and $|y\rangle$), each at 45° to the initial linear polarization and normal to the wavevector.

$$\vec{E}(\vec{x}, t, \phi) = \frac{1}{\sqrt{2}}|x\rangle E(\vec{k} \cdot \vec{x} - \omega t + \phi) + \frac{1}{\sqrt{2}}|y\rangle E(\vec{k} \cdot \vec{x} - \omega t + \phi) \quad (3.1)$$

The He:Ne beam in the stationary arm converted to circularly polarized light using a quarter-wave plate, which induces a 90° phase shift in the y component (the component parallel to the extraordinary axis of the waveplate). After exiting the Mach-Zehnder, the collinear He:Ne beams are separated using a polarization cube set at 45° , which separates the light into its x and y components. Each polarization of light from the mobile arm interferes with the same polarization from the stationary arm. Since the y -polarized light from the stationary arm has been retarded by 90° , there is a 90° phase shift in the interferogram. Conceptually, if one considers the interference of x -polarized light with itself to trace a cosine function with a period equal to the 2.11 fs, then the interference of y -polarized light with itself is a sine function. Combined, the two trace a circle in the xy -plane with a period of 2.11 fs.

3.1.3 Detectors

Measurement of a 2D-IR spectrum using the current spectrometer design²⁰⁵ requires the measurement of (1) the probe and reference signals on the 2×32 channel mercury cadmium telluride (MCT) array detector, (2) the interference of the two pump pulses on a single channel MCT detector to determine spectral phase, and (3) the interference of a He:Ne beam with itself using fast photodiodes to track the position of the Mach-Zehnder interferometer mirrors.

The MCT detectors (InfraRed Associates, Inc.) are cooled with liquid nitrogen (77 K) to reduce noise due to thermally excited electrons generating current. The detectors are run in photoresistive mode. A bias voltage is required to operate the detector. Infrared light on the detector causes promotion of electrons into the conduction band, and thus generates a small current that is detected by the femtosecond pulse acquisition system (FPAS, Section 3.1.4). Despite the femtosecond pulse duration, the electrical response of the MCT detector occurs on a few microsecond time scale.

3.1.4 2D-IR Data Acquisition

Spectrometer software hand coded in MATLAB controls data acquisition by interfacing with the detector hardware and delay stage motors in the 2D-IR spectrometer (Figure 7).

A femtosecond pulse acquisition system (FPAS, InfraRed Systems, Inc.) has both gated integration and sample hold circuits, as well as an analog to digital converter (ADC). The FPAS has 80 input channels, each of which is capable of integrating a signal, and then holding the value until it is passed to further electronics. Timing of FPAS signal acquisition is controlled by delay 4 from the SDG.

The FPAS interfaces with a National Instruments Data Acquisition Card (DAC) through an analog to digital converter. The DAC interfaces with the memory on the computer, and thus provides the direct bridge from data acquisition at the FPAS to data storage and analysis by the MATLAB software.

There is also a hardware gate that can be closed to prevent the FPAS from receiving triggers from the SDG. Opening and closing this gate is controlled by the CPU through a

National Instruments USB-6501 card.

Data acquisition begins with a command from the CPU to close the gate before the FPAS. This initial step is relatively non-critical with the current experimental setup; however, it becomes more important as additional detectors and electronics are included in experiments, since it ensures that all electronics trigger from the same signal from the SDG.

The CPU then configures the DAC, by telling it the number of shots (based on input parameters in the MATLAB software) to prepare for. After the DAC is ready, the CPU tells it to start acquisition, and then sends a command to open the gate. The CPU then sends a command to move the Mach-Zehnder interferometer motor between its starting and ending positions. Once the motor has finished moving, the sampler is read out, and the gate is closed. The next acquisition task is then started (starting with the command for DAC acquisition), and the previous scan is analyzed as the current scan is being acquired by the DAC.

Sample processing takes place in five steps: sorting the data, subtracting the background, averaging the data, storing the result, and analyzing the noise.

Raw experimental data for each scan contains the value of each channel on the FPAS for each trigger (each laser shot). In order to calculate a 2D spectrum (or even analyze the time-dependent data), this data must be sorted and reordered based on the time between laser pulses.

Sorting shots is accomplished by sorting the data for each shot into 2.11 fs bins, based on the interference pattern of the He:Ne with itself (Section 3.1.2). The inputs from the photodiodes serve as (x, y) coordinates, and as the interferometer moves, the “position” of the He:Ne traces a circle in the xy -plane. After subtracting the mean x and y values to center the circle at zero, the software checks for crossings between quadrants II and I by comparing the previous two x values when $y \geq 0$. Each crossing from II to I adds 1 to the bin number, while each crossing from I to II (on the return run of the mobile arm) subtracts 1 from the bin number. This process provides an index of bin numbers for each shot. For each channel, each bin is populated by averaging the shots with that bin number assigned.

The binned data is then sorted into a pump interferogram vector and a probe & reference matrix based on channel numbers. After removing the background, there is a time-dependent

signal at each pixel, for both probe and reference. These are used to calculate a time-dependent change in absorbance for each signal:

$$S(t) = 10^3 \log_{10} \frac{I^{(\text{probe})}}{I^{(\text{ref})}} \quad (3.2)$$

Assuming that $I^{(\text{ref})}$ is equal to a constant times the unpumped intensity of the probe light, this equation can be rewritten as:

$$S(t) = 10^3 \log_{10} \frac{I^{(\text{probe})}}{kI_0^{(\text{probe})}} = 10^3 (\Delta A - \log_{10} k) \quad (3.3)$$

Since the constant term will not vary with position of the Mach-Zehnder interferometer (and should vary only with low frequency), it is removed from the spectrum during the Fourier transform.¹

Before Fourier transforming the time-dependent signal at each pixel, however, it is necessary to determine the spectral phase by examining the pump light interferogram. The spectral phase depends on the difference between t_0 , as determined by the interferogram, and the real t_0 . The exact difference depends on the error from discretization of the signal into 2.11 fs bins, or how far off t_0 is from the position of the zero bin. After finding the zero-bin by taking the `max` of the interferogram, the spectrometer software then analyzes the phase of the spectrum by fitting the frequency-dependent spectral phase $\phi(\omega)$ and finding its slope $\partial\phi/\partial\omega$.

A time-shifted wavepacket can be written as the convolution of the wavepacket with a time-shifted Dirac delta function,

$$f(t) = (e^{i\omega_0 t} A(t)) \otimes \delta(t - t') \quad (3.4)$$

where ω_0 is the carrier frequency, $A(t)$ is the pulse envelope, and \otimes represents a convolution. Convolution of the wavepacket with the shifted Dirac delta function shifts the wavepacket to its new position t' . After Fourier transform, this equation gives the spectral peak multiplied by an oscillatory component in frequency.

$$F(\omega) = \left(\tilde{A}(\omega) \otimes \delta(\omega - \omega_0) \right) e^{i\omega t'} \quad (3.5)$$

¹For a pump-probe spectrum (which utilizes a mechanical chopper on the pump arm), this term is removed by subtracting the pumped and unpumped spectra.

This frequency-shifted component may be conceived as a frequency-dependent phase offset

$$e^{i\omega t'} = e^{i\phi(\omega)} \quad (3.6)$$

showing that the slope of the spectral phase is equal to the time-shift of the wavepacket

$$\frac{\partial\phi(\omega)}{\partial\omega} = t' \quad (3.7)$$

Thus the slope of the spectral phase of the pump pulses can be used to accurately determine the difference between the position of the t_0 bin and the true t_0 necessary for accurate spectral calculation.

Calculation of the fully absorptive 2D frequency spectrum from the time-dependent signal ($PP(t_1, \omega_3; t_2)$) at each pixel is then straightforward. The amplitudes of time points before the t_0 bin, which contain a mixture of different population times, are set to zero and circularly shifted to the end of the vector. The signal is Fourier transformed after averaging the first and last time points' amplitudes (which helps to remove baseline artifacts from having a discontinuous function) and then zeropadding to twice the number of bins. The resulting 2D frequency spectrum ($R(\omega_1, \omega_3; t_2)$) is then corrected for the spectral phase by multiplying by $e^{-i\phi}$ (Equations 3.5 and 3.6).

Spectral averaging occurs in the time domain, where each bin continues to accumulate signal over the course of the experiment. After each scan, the resulting accumulated data, included the Fourier transformed 2D-IR spectrum, are saved in a temp file for future analysis.

3.1.5 Nitrogen Purge

The 2D-IR and FTIR spectrometer systems were purged with dry nitrogen gas from liquid nitrogen boil off.

For the 2D spectrometer, a nitrogen purge line was run to the Horiba monochromator, as well as to the 2D spectrometer and the OPA. The 2D spectrometer itself is surprisingly sensitive to the flow rate of nitrogen gas, and therefore it is impossible to run at a high flow rate while maintaining acceptable noise levels (<50 μ OD per 500 shots). The spectrometer

was therefore purged at a high flow rate for approximately one hour before measurements began.

Following this initial high flow purge, the nitrogen flow rate was decreased to around 30 standard cubic feet per hour (SCFH), and the quality of the purge was determined by looking for a CO₂ absorbance on the IR power spectrum of the array detector. The shape of the pump light interferogram on the single channel detector served as a secondary test of the quality of the purge, since the atmospheric CO₂ band causes the evolution of two lobes on the sides of the IR interferogram.

Generally, if the spectrometer was closed and sealed with lab tape, a flow rate of 30 SCFH nitrogen was sufficient to maintain the purge over several hours, once it had been established. The initial hard purge is simply to reduce the time from sealing the spectrometer to data acquisition.

3.1.6 Sample Temperature Control

The temperature of the sample was monitored by measuring the temperature at the front face of the 1 mm thick calcium fluoride optical window, using a J-type thermocouple (National Instruments, model NI USB-TC01). The thermocouple was held in place with a small nylon-tipped screw that was threaded into the wall of the brass cell. A small amount of Thermalcote Thermal Joint Compound was placed on the tip of the thermocouple to improve thermal contact with the window. Calibration of the thermocouple was testing using a dry well (Fluke 624 Temperature Calibrator, Field Metrology Well).

This data is fit excellently ($R^2 = 1.00$) by a linear relationship

$$T_{\text{measured}} = mT_{\text{set}} + b \quad (3.8)$$

where $m = 1.0052 \pm 0.0004$ and $b = 0.25 \pm 0.02$.

Samples for FTIR and 2D-IR were temperature controlled using a Fisher Isotemp250LCU recirculating heater/chiller. For both systems, the sample temperature control was accomplished using an anodized aluminum sample cell holder, that was designed to be in thermal contact with the front face and sides of the brass sample cell.

Table 1: Thermocouple calibration

Dry well set point (°C)	Measured temperature (°C)
10.00	10.3
25.00	25.4
40.00	40.5
55.00	55.5
70.00	70.6
85.00	85.7
100.00	100.8

Temperature-dependent FTIR studies were performed using a modified Nicolet 6700 FTIR spectrometer that allowed temperature control of the cell holder using a recirculating chiller. The temperature-dependent 2D-IR apparatus was hard-plumbed to avoid damaging the electronics in the event of a leak or line failure. Both FTIR and 2D-IR temperature modifications went through several iterations before a working design was obtained. The recirculating water was originally run through 1/8 in. (3.175 mm) internal diameter stainless steel tubing, as this was able to be easily cut and bent by hand, and we erroneously assumed that the pressure drop in a system was mostly determined by the narrowest tubing the water had to flow through (in this case, the anodized aluminum sample cell holder). The proper way to treat this system, however, is by calculating the cumulative pressure drop from each element, as each element will result in some additional pressure drop.

The Darcy-Weisbach equation²⁰⁶ allows the calculation of pressure drop of a flowing fluid due to wall friction within a straight length of pipe, and gives a qualitative understanding of the pressure drop due to our pipes, and how this varies with internal pipe diameter.

$$\Delta P = f_D \rho v^2 L / (2D_H) \quad (3.9)$$

ΔP is the pressure drop, f_D is the Darcy friction factor, ρ is the density of the fluid, v is the linear velocity, L is the length of pipe, and D_H is the diameter of the pipe. Since we are

flowing in a closed system, the pressure drop from net change in height is zero.

For a fixed volumetric flow rate (Q) in a circular pipe, the linear velocity is approximately equal to the volumetric flow rate divided by the cross sectional area of the pipe (this treatment neglects differences in velocity across the pipe). Substituting the volumetric flow rate and cross sectional area for the linear velocity in equation 3.9 shows that the pressure drop in a pipe is approximately proportional to D^{-5} , and suggested that increasing the pipe diameter was the easiest way to alleviate the flow problems in our system. Increasing the internal diameter of the pipe from 1/8 in. (3.175 mm) to 1/2 in. (12.7 mm) significantly increased the flow rate in the system, and improved both heating and cooling at the sample cell.

3.1.7 Polarizer / Waveplate Combo

Polarization control for the pump arm of the 2D spectrometer (necessary for polarization controlled pump-probe measurement and for magic angle 2D-IR measurements in Chapter 6) was accomplished using a $\lambda/2$ waveplate / wire grid polarizer combination. The waveplate rotates the optical polarization of the IR pump pulses, and the polarizer then removes undesired linear or elliptically polarized light.

Both the waveplate and polarizer were mounted in rotational mounts to control their angle. The polarizer was mounted in a computer controlled motorized rotation mount (Thor-Labs) with a DC servo motor. The positions for parallel and perpendicular polarizations was set by finding extinction of the perpendicularly polarized light without the waveplate in place. Leakthrough of the non-rotated optical pulse at extinction was estimated to be less than 1% using a liquid nitrogen cool MCT single channel detector that was placed in line with the pump light after a OD 2 neutral density filter.

For polarization control of pump-probe measurements, the polarization of the outgoing light was controlled with the angle of the polarizer. The waveplate was angle tuned to ensure equal amplitude of the parallel and perpendicular polarizations (that is, to 45° rotation of the optical polarization) using the same single channel MCT detector. Overlap of both polarizations of pump light with the probe pulse was also confirmed using a pinhole at the focal plane of the measurement. During spectral acquisition, spectra for each population

time were collected in the all parallel and crossed polarizations by alternating the polarizer between 0 and 90° for each run.

Magic angle 2D-IR spectra (54.74° rotation between the pump and probe pulses) were collected directly at this polarization, rather than collecting all parallel (ZZZZ) and crossed (ZZXX) polarizations and then calculating an isotropic spectrum. This choice was made in order to decrease the time of data acquisition and help to remove artifacts from gradual detuning of the OPA and from correlated noise sources such as purge and laser drift.

3.1.8 Ionic Liquids

Ionic liquids, with the exception of the short chain ionic liquid mixtures synthesized by A. Ivanova at Carnegie Mellon University (Chapter 5), were obtained from IoLiTec, Inc. They were used without further purification; however, the alkyimidazolium ionic liquids were dried prior to use.

Most experiments required small volumes (<100 μ L of dried ionic liquid for spectroscopic analysis; however, it was difficult to dry, CO₂-load, and handle such small volume. We therefore used a 1 mL reservoir of ionic liquid, which could be dried, and loaded with CO₂ in a single glass vial.

The glass vials were custom-made by Lori Neu at the university's Glass Shop. The design consists of a small reservoir in which a liquid sample can be placed. An access port, covered with a rubber septum, allows liquid to be placed in the chamber. A three-way glass stopcock allows the sample to be isolated from ambient air, and can be opened either to dry the sample under vacuum, or to load the sample with CO₂. Samples were stirred with a PTFE-coated magnetic stir bar both during drying to prevent bumping, and during CO₂ loading to increase the rate of CO₂ sorption.

3.1.8.1 Drying ILs Ionic liquids were dried using a 10 μ Torr rotary vane pump with a liquid nitrogen cooled vacuum trap. The rate of water desorption was facilitated by gently heating the samples (to around 80°C) and stirring rapidly during drying. Stirring and heating the ionic liquid set up convection currents in the liquid, which move water more

rapidly to the interface than would be accomplished by diffusion alone. Stirring similarly helps with the rate of CO₂ addition to ionic liquids. Anecdotally, NMR experiments involving loading CO₂ under pressure into an ionic liquid in an NMR tube were reputed to take days. By stirring the ionic liquid, we are able to lower this time to minutes (see below).

For hydrophobic ionic liquids, such as [Im_{*n*,1}][Tf₂N], this resulted in drying to less than 100 ppm water, verified by FTIR.ⁱⁱ More hydrophilic ionic liquids, such as [Im_{4,1}][SCN] and [Im_{4,1}][TFA] were unable to be dried to as low of water content using this method, mainly due to the strength of the vacuum pump.

3.1.8.2 Loading an Ionic Liquid with Carbon Dioxide Ionic liquid samples were kept isolated from the ambient air to avoid the ionic liquid absorbing atmospheric water. After drying, they were heated using a hot plate set at 100 °C and stirred for approximately 10 minutes. The increased temperature was determined empirically to result in appropriate optical densities (around 0.3 O.D.) of CO₂ in ionic liquid samples studied. Loading at lower temperatures using current equipment resulted in frequent “overshooting” of the desired CO₂ concentration, which then necessitated placing the IL back under vacuum and re-loading with CO₂.

CO₂ (99.8% purity, Matheson TRIGAS) was allowed to flow at a low rate through flexible Tygon tubing for 2 minutes to remove as much residual water vapor as possible before loading. The Tygon tubing was then connected the horizontal inlet on the glass vial as the rubber septum was vented with a 18G×1.5 needle and the stopcock was opened (“down”) position. This setup resulted in a constant flow of dry CO₂ above the ionic liquid, and positive pressure helped to limit water contamination. The CO₂ was allowed to load for approximately 5 minutes with rapid stirring, after which the stopcock was closed as the venting needle was removed.

After loading the ionic liquid sample with CO₂, the vial was transferred to a modified glove bag, which was purged with nitrogen. The glove bag was modified by cutting off the gloves to allow increased dexterity while assembling samples. Empirically, filling and

ⁱⁱWhile Karl Fischer titration is generally considered the gold standard for water determination in ionic liquids, the mid-IR symmetric and antisymmetric stretching bands of liquid water in ionic liquids provides equivalent information to below 100 ppm water.⁸¹

emptying the glove bag three times with N_2 after moving the vial in seemed to prevent significant water contamination. With nitrogen still flowing (to create a slight positive pressure) a small amount of ionic liquid was then drawn out of the vial through the septum, using a 1 mL syringe with an 18G needle. A single drop of this sample was placed on a calcium fluoride window in the brass sample. As quickly as possible, the IL drop was covered with the other window, and covered with the cover of the brass cell. The cell was then removed from the glove bag and was assembled using four screws.

Total CO_2 and water content were confirmed by taking an FTIR of the sample and examining the OH stretch region (for water) and the antisymmetric stretching region (for CO_2).

3.2 DATA ANALYSIS AND FITTING METHODS

3.2.1 Averaging During Post-Processing

2D-IR spectral averaging occurs on the fly for each scan during data acquisition (Section 3.1.4); however, there are some experimental reasons to average during post-processing instead. Specifically when working with CO_2 spectroscopy, the necessity of nitrogen-purging the system introduces potential drift in the noise stability of the system, and in the intensity of pump light. Over an experimental timeframe of 5-10 hours per sample, drift in stability due to the purge, as well as laser and OPA drift, can cause correlation and non-Gaussian (over the timescale of a run) noise patterns that do not average out and cause difference in the spectral shape of spectra accumulated far apart in lab time.

One way to deal with this problem is to randomize the order of data collection, so that this correlated noise will hopefully be moderated over the course of an experiment; however, long t_2 data points (where $t_2 \gg T_1$) necessitate large numbers of accumulation, and often account for a significant fraction of the experimental time. One possible solution to this problem is to break up the runs for long data points into multiple shorter acquisitions, which are then scattered randomly over the course of the experiment (Figure 8). Breaking

the runs up this way causes small increases in the total experimental time, due to having to run the population time’s translation stage multiple times; however, the total time added is short compared with the duration of the experiments (around 30 seconds per scan for CO₂, based on the total t_1 time of 10.5 ps and the Mach-Zehnder speed of 0.8 ps s⁻¹).

Since t_0 bins are not completely consistent between spectra, and since the ω_1 spacing depends on the total t_1 length, $PP(t_1, \omega_3; t_2)$ is first truncated to the shortest length in t_1 . The resulting spectra are then Fourier transformed along ω_1 using the same procedure as in spectral accumulation (Section 3.1.4). The spectra are then averaged in the frequency domain. Spectra are averaged in the frequency domain, rather than the time domain, to account for the small differences in phase over the course of an experiment.

In practice, running with a randomized time order and spectral averaging of shorter scans over multiple repetitions seems to increase consistency in the results from spectral fitting, and results well-behaved spectra over the course of the experiment, at the cost of some additional time per experiment. If the run is broken into multiple repetitions, it also has the advantages that (1) in a low S/N case, it may be possible to re-optimize the OPA between repetitions, and (2) a single (albeit lower S/N) set of spectra is accumulated much more quickly than previously, and can be used for on the fly analysis to change spectral parameters during the course of an experiment. It is probably essential when working with the current purge system, and is very beneficial even in cases that do not require a nitrogen purge.

3.2.2 Graphical Correlation Fitting Methods

A number of shape-based fitting methods have been developed to attempt to graphically extract the value of the frequency fluctuation correlation function from 2D-IR spectra.²⁰⁷ Each of these methods can relate the spectral lineshape with the two-point frequency fluctuation correlation function, although they uniformly cannot determine dynamics near the motionally narrowed limit, and they vary in their susceptibility to artifacts from backgrounds, phase errors, and apodization. In this work, the two of the more robust methods were used when graphically analyzing spectra: ellipticity²⁰⁸ and centerline slope.²⁰⁹⁻²¹¹

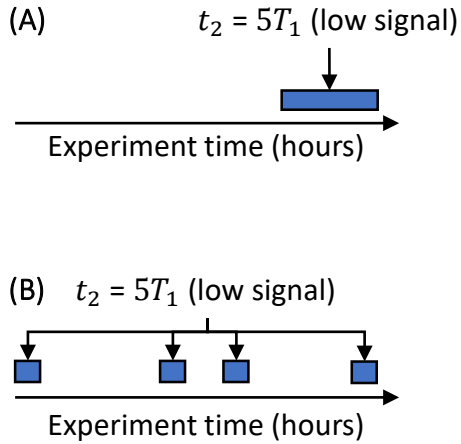


Figure 8: Post-processing averaging allows for the accumulation of multiple shorter spectra over the course of the experiment, which can help control for correlation noise processes, slow laser and OPA drift, and drift in the quality of the nitrogen purge for CO_2 experiments. In case (A), a spectrum with low signal-to-noise (e.g. a long t_2 spectrum requiring > 100 spectra) taken in a single run. In case (B), the same number of spectral scans is broken into four separate runs, and distributed randomly over the total experimental time. In a normal experiment, laser drift or other correlated / non-Gaussian noise processes will have a bigger effect on the spectra in case (A) than case (B).

Uniformly, the spectra were fitted using a nonlinear least squares analysis (`fit` MATLAB), typically with upper and lower bounds on the fitting parameters (although fits were allowed to freely vary in those bounds, and fits were typically tested by starting at multiple initial values to avoid being trapped in a local minimum).

Individual points for fits were weighted by the inverse of their variance. In the case (as in centerline slope especially) where the fitting results must serve as inputs for subsequent fits, uncertainties in the fits were treated as standard deviations on the values. Uncertainties in the fitting results were propagated through each step, using the standard methods for uncorrelated errors for a function of multiple variables $R(x_1, x_2, \dots, x_i)$ with standard deviations of the independent variables $(\sigma_1, \sigma_2, \dots, \sigma_i)$ that are much smaller than the mean value of their associated variables:²¹²

$$\sigma_R = \sqrt{\sum_i \left(\frac{\partial R}{\partial x_i} \right)^2 \sigma_i^2} \quad (3.10)$$

3.2.2.1 Ellipticity The ellipticity of a 2D-IR spectrum is defined as the ratio of the difference in diagonal and antidiagonal linewidths (σ_D and σ_A) of the 2D-IR peak shape, divided by the total linewidth²⁰⁸

$$\epsilon = \frac{\sigma_D^2 - \sigma_A^2}{\sigma_D^2 + \sigma_A^2} \quad (3.11)$$

In the limit of totally uncorrelated frequencies, this quantity is equal to zero. In the limit of totally correlated initial and final frequencies, this quantity is equal to 1 (the 2D-IR spectrum would be a line stretched along the $\omega_1 = \omega_3$ diagonal). In practice, even at the earliest t_2 times, lifetime, orientational, and fast dynamical effects cause some broadening along the antidiagonal, and thus the ellipticity values start at a value < 1 and then decay to zero over the population time.

Ellipticity was calculated by fitting each 2D-IR spectrum to a two-dimensional Gaussian function. The general form of an elliptical function with unequal standard deviations along its dimensions ($\omega_x \neq \omega_y$) is:

$$\exp \left[- \left(\frac{(x - \mu_x)^2}{2\sigma_x^2} + \frac{(y - \mu_y)^2}{2\sigma_y^2} \right) \right] \quad (3.12)$$

The natural basis for the two-dimensional Gaussian is along the diagonal ($\omega_1 = \omega_3$) and antidiagonal ($\omega_1 = -\omega_3$) axes; however, the basis for of the 2D-IR spectrum is along ω_1 and ω_3 . Rotating the basis by 45° clockwise, and including a fixed amplitude as well as a second peak separated in ω_3 by the anharmonicity gives the functional form used in this work:

$$A \left(\exp \left[- \left(\frac{(\omega_1 - \mu_{\omega_1} + \omega_3 - \mu_{\omega_3})^2}{2\sigma_D^2} + \frac{(\omega_1 - \mu_{\omega_1} - \omega_3 + \mu_{\omega_3})^2}{2\sigma_A^2} \right) \right] + \exp \left[- \left(\frac{(\omega_1 - \mu_{\omega_1} + \omega_3 - \mu_{\omega_3} + \Delta_{anh})^2}{2\sigma_D^2} + \frac{(\omega_1 - \mu_{\omega_1} - \omega_3 + \mu_{\omega_3} - \Delta_{anh})^2}{2\sigma_A^2} \right) \right] \right) \quad (3.13)$$

where A is the amplitude, μ_{ω_n} is the center frequency in ω_n , σ_D and σ_A are the diagonal and antidiagonal standard deviations, and Δ_{anh} is the difference in frequency between the 0–1 and 1–2 transitions (the anharmonicity). Inaccuracy in the values of σ_D and σ_A due to the loss of the expected factor of $\frac{1}{\sqrt{2}}$ from the rotation cancels in the calculation of ellipticity.

There are several lineshape assumptions in this treatment. Specifically, the peak shapes (σ_A and σ_D) and amplitudes of the 0–1 and 1–2 transitions are assumed to be identical. For many transitions, these assumptions would be poor, due to for example, deviations of transition dipole moment magnitude from the harmonic model or differences in population relaxation between the bands. For thiocyanate ion in an ionic liquid solvent, however, they are relatively good assumptions, and lead to stable fits.

3.2.2.2 Centerline Slope The centerline slope (CLS) method^{209–211} provides an alternative to ellipticity for shape-based fitting of 2D-IR spectra. A CLS analysis involves calculating the slope of the line connecting the peak positions of one-dimensional cuts parallel to one of the frequency axes. Depending on whether slices are taken parallel to ω_3 (sometimes ω_m) or ω_1 (sometimes ω_τ), the correlation value is either equal to the slope or its inverse respectively.

Like ellipticity, CLS provides a method to graphically extract correlation values from 2D-IR spectra. Unlike ellipticity, however, CLS does not rely on the assumption of a Gaussian lineshape; it is more capable of dealing with vibrational lines close to the motional narrowing limit.²⁰⁹

In this work, slices were taken parallel to ω_3 . The method employed would be called CLS_{ω_3} (CLS_{ω_m}), hereafter referred to simply as CLS. This specific method is less sensitive to distortions from peak overlap than taking slices parallel to ω_1 . In this work specifically, however, it was chosen because the narrowness of the CO_2 line limits the number of points in the FWHM (where the CLS is closest to a straight line). Taking slices parallel to ω_3 allows interpolation along ω_1 by additional zeropadding of the time-dependent signal before Fourier transforming, which gives enough points to fit a straight line with reasonable confidence intervals. For all cases tested, the calculated values of the centerline slope do not change with interpolation along ω_1 , but the confidence intervals improve significantly.

Peak positions of one-dimensional slices of the 2D spectrum were found here by fitting to the sum of two Voigt profiles, one positive and one negative, separated by the anharmonicity of the transition. Uncertainties in the center frequency were propagated into the fit for the centerline slope fit.

3.2.3 Global Fitting of Spectra

An alternative to shape-based fitting of 2D-IR spectra is global fitting to calculated spectra. This method has the advantage of being able to treat spectra that are closer to the homogeneous broadening limit than graphical methods, and can also potentially account for more complicated lineshapes and vibrational couplings or chemical exchange processes where the peaks are not fully resolved. Additionally, for narrow bands, such as $\text{CO}_2 \nu_3$ (FWHM $\approx 6\text{cm}^{-1}$), there may be statistical benefits due to fitting the entire spectral window, rather than just a slice of the spectrum, as in the CLS method.

Briefly, 2D spectra are calculated using a density matrix (Liouville space) response function formalism, in the semi-impulsive limit, utilizing the fluctuating frequency and rotating wave approximations. The ensemble average of frequency fluctuations is evaluated using the cumulant expansion truncated at second order (which is exact when the distribution of frequency fluctuations is Gaussian), which allows for the use of analytical forms of the correlation and lineshape functions (Section 2.2).

The starting point for the correlation function (and its double time integral, the lines-

hape function) is generally Kubo’s exponential decay ansatz (Equation 2.41), which includes a terms that describes the variance in frequency fluctuations and the correlation time of the chromophore’s frequency fluctuations. Homogeneous (fast) dynamics that contribute to the lineshape through dephasing are approximated by including a Dirac delta function which leads to convolution of the Kubo lineshape with a two-dimensional Lorentzian in the frequency domain. Quasi-static dynamics can be approximated by including a static offset in the total correlation function.

For multiexponential dynamics, the total lineshape function can be assumed to be a sum of Kubo lineshapes, and the homogeneous and inhomogeneous contributions can be considered limiting cases of these Kubo components (Section 2.2). The total number of components needed to approximate the dynamics can be ambiguous; however, time constants must normally be separated by approximately an order of magnitude to be distinguished.

Spectra are calculated t_2 point, with equal frequency spacing to the experimental spectra. Each point in the resulting calculated spectrum is then subtracted from the corresponding point in the experimental spectrum, and the sum of squared residuals is calculated as a metric of goodness of fit. Lineshape parameters, including time constants (τ_i), linewidths (Δ_i), anharmonicity (Δ_{anh}), center frequency (ω_0), and spectral phase (ϕ) were then obtained using a constrained nonlinear optimization algorithm (`fmincon` MATLAB) to minimize the sum of squared residuals.

3.2.4 Correlation Function Fitting

Graphical 2D-IR spectral fitting methods (Section 3.2.2) provide an estimate of the frequency fluctuation correlation value at each t_2 time. The resulting FFCF plots were fitted using a bounded nonlinear least squares analysis in MATLAB.

In the case of global fitting, the correlation function was not fitted directly. Rather, lineshape of the spectrum at each t_2 time was optimized using a lineshape function that was the double time integral of a correlation function.

4.0 CARBON CAPTURE FROM CARBON DIOXIDE'S POINT-OF-VIEW

The text in this chapter has been adapted from Brinzer T.; Berquist E. J.; Ren, Z.; Dutta, S.; Johnson C. A.; Krisher, C. S.; Lambrecht, D. S.; Garrett-Roe, S. *J. Chem. Phys.* **2015**, *142*, 212425, and its erratum T.; Berquist E. J.; Ren, Z.; Dutta, S.; Johnson C. A.; Krisher, C. S.; Lambrecht, D. S.; Garrett-Roe, S. *J. Chem. Phys.* **2017**, *147*, 049901. The author's contribution to the work included choosing the system of study, designing and performing all FTIR and two-dimensional infrared spectroscopy experiments and analysis (including power measurements and assignment of fifth-order signal), performing the kinetic Monte Carlo simulations, and writing the text of the manuscript, excepting the computational section, which he revised.

4.1 CHAPTER SUMMARY

The CO₂ ν_3 asymmetric stretching mode is established as a vibrational chromophore for ultrafast two-dimensional infrared (2D-IR) spectroscopic studies of local structure and dynamics in ionic liquids, which are of interest for carbon capture applications. CO₂ is dissolved in a series of 1-butyl-3-methylimidazolium-based ionic liquids ([Im_{4,1}][X]), where [X]⁻ is the anion from the series hexafluorophosphate (PF₆⁻), tetrafluoroborate (BF₄⁻), bis-(trifluoromethylsulfonyl)imide (Tf₂N⁻), triflate (TfO⁻), trifluoroacetate (TFA⁻), dicyanamide (DCA⁻), and thiocyanate (SCN⁻). In the ionic liquids studied, the ν_3 center frequency is sensitive to the local solvation environment and reports on the timescales for local structural relaxation. Density functional theory calculations predict charge transfer from the anion to the CO₂ and from CO₂ to the cation. The charge transfer drives geometrical distortion of

CO₂, which in turn changes the ν_3 frequency. The observed structural relaxation timescales vary by up to an order of magnitude between ionic liquids. Shoulders in the 2D-IR spectra arise from anharmonic coupling of the ν_2 and ν_3 normal modes of CO₂. Thermal fluctuations in the ν_2 population stochastically modulate the ν_3 frequency and generate dynamic cross-peaks. These timescales are attributed to the breakup of ion cages that create a well-defined local environment for CO₂. The results suggest that the picosecond dynamics of CO₂ are gated by local diffusion of anions and cations.

4.2 INTRODUCTION

There is a pressing need to develop next-generation materials to capture CO₂ from fossil-fuel burning power plants. Commercial carbon capture technologies are inefficient and greatly increase the cost of energy¹. Novel materials, including metal-organic frameworks,^{213,214} polymers,^{215,216} and ionic liquids,^{17,121,122} have been proposed as transformational technologies. In each case, however, a lack of tools to interrogate at a molecular scale how CO₂ interacts with the sorbents, what local structures it forms, and for how long those structures persist has limited the ability to optimize these materials for this important task.

Our strategy to investigate the local environment of CO₂ is to use a vibration of the CO₂ itself. We hypothesized that the antisymmetric stretching vibration of CO₂, the ν_3 mode, could be a sensitive probe of the carbon capture process and that ultrafast two-dimensional vibrational spectroscopy (2D-IR) could give new insight into the local structure and dynamics around the CO₂. The central goal of this report is to establish the ν_3 mode of CO₂ as a viable platform for ultrafast multidimensional spectroscopy of carbon capture in ionic liquids.

Ionic liquids, sometimes called room temperature molten salts, excite particular interest for carbon capture due to their chemical tunability. Ionic liquids are organic salts that are molten at or below 100 °C. Each formula unit consists of an anion-cation pair without a surrounding solvent. The physical and chemical properties of ionic liquids can be manipulated by changing the specific anion and cation pair, which provides tremendous flexibility. The chemical space spanned by possible ionic liquids is estimated at 10¹⁸ anion-cation com-

binations, including binary and ternary mixtures,²¹⁷ only a tiny fraction of which has been explored.

Even without optimization, many ionic liquids have CO₂ solubility and selectivity comparable to molecular solvents,^{218,219} and chemical modification can improve these properties further.^{124,220} Ionic liquids exhibit negligible vapor pressure and are generally thermally and hydrolytically stable at the operating temperature (~ 50 °C) of post-combustion carbon capture.

The promise of chemical tunability of ionic liquid properties has spurred efforts to design improved ionic liquids, both synthetically^{121,124,125,220–223} and *in silico*.^{224,225} Additionally, other strategies, such as creating mixtures of multiple ionic liquids,^{226,227} or mixtures of ionic liquids with molecular solvents^{228,229} show promise. Despite the progress that has been made, there remains a lack of fundamental understanding of the local solute-solvent interactions between CO₂ and the ionic liquid sorbents.

Molecular modelling provides valuable insights but faces challenges due to the time- and length-scale mismatches between the simulations and bulk thermodynamic experiments. Electronic structure theory can predict CO₂ binding motifs and energies,^{185,230–232} molecular dynamics simulations of CO₂ in ionic liquids can provide atomistic detail of local structure and dynamics in the condensed phase,^{12,171–173,184,233} and Monte Carlo simulations can calculate important thermodynamic properties.^{173,234–238} However, it remains a challenge to directly compare these results to macroscopic experimental observables such as viscosity or CO₂ solubility.

Ultrafast spectroscopy naturally provides observables that are compatible with the time- and length-scales of molecular modelling. Ultrafast two-dimensional infrared spectroscopy (2D-IR), a coherent third-order spectroscopy, can investigate femtosecond to picosecond molecular dynamics in the condensed phase at equilibrium.^{22,197,239,240}

A 2D-IR experiment, in essence, measures the distribution of vibrational frequencies in an ensemble of molecules at two points in time, separated by a controllable delay. When the delay is short, the local environment does not have time to reorganize, causing correlation of initial and final frequencies, and stretching the 2D-IR peak along the frequency diagonal. As the delay time is increased, the system loses memory of its initial configuration and the

peaks become rounder. Thus, 2D-IR spectra encode the two-point frequency fluctuation correlation function through the change in their shape with the population time, t_2 , of the experiment

$$c_2(t_2) = \langle \delta\omega(t_2)\delta\omega(0) \rangle \quad (4.1)$$

where $\delta\omega(t)$ is the offset of the instantaneous vibrational frequency $\omega(t)$ from the average $\langle\omega\rangle$

$$\delta\omega(t) = \omega(t) - \langle\omega\rangle \quad (4.2)$$

This time-correlation function is the essential information content of any specific peak in 2D-IR spectroscopy, which can be compared with the available time-correlation functions from molecular simulations.

Cross-peaks in 2D-IR also contain valuable information. Vibrational coupling of modes, population transfer, and chemical exchange can all generate cross-peaks in a 2D-IR spectrum. These mechanisms can be distinguished by their spectral kinetics. Vibrational coupling, or mixing of the local modes, causes cross-peaks that are seen even at the earliest population times, because they result from direct vibrational transitions, for example the coupling of the symmetric and antisymmetric stretching modes of water.²⁴¹ Coherence transfer between bright modes can additionally create beat frequencies in both their diagonal and cross-peaks.²⁴¹ Population transfer arises from the exchange of excited state population during t_2 , for example, that of the Amide I modes of small peptides.²⁴² Chemical exchange results from the change in frequency of a single molecule as it moves between different local environments, for example, the exchange of free and complexed phenol-benzene.²² Both population transfer and chemical exchange give rise to dynamic cross-peaks, whose relative intensity shows an early minimum, increasing with population time.

Linear spectroscopies can provide insight into structure and dynamics in ionic liquids. For example, Raman spectroscopy has been used to study CO₂ in [Im_{4,1}][TFA],²⁴³ or the effects of ionic liquid water content on CO₂ solubility.²²⁸ Similarly, NMR spectroscopy has been used to probe the solvation of CO₂ in imidazolium ionic liquids at high pressures.^{18,195}

A number of studies have also examined structure and dynamics in ionic liquids on an ultrafast timescale using various chromophores, including IR pump-probe measurements of small anions in ionic liquids,²⁴⁴ 2D-IR studies of water²⁴¹ and thiocyanate⁸¹ in imidazolium

ionic liquids, electronic spectroscopy of solvated laser dyes,^{178,245} and optical Kerr effect spectroscopies.^{165,246–248} Each of these spectroscopies is sensitive to the spectral density of low frequency vibrations (i.e., the Fourier transform of $c_2(t)$), but they differ in the coupling of their respective chromophores to the low frequency modes.

The difficulty for most ultrast spectroscopies lies in connecting the average solvent dynamics to the dynamics specifically around the CO₂. Time-dependent Stokes shift and fluorescence upconversion experiments¹⁷⁸ can measure dynamics over a broad range of timescales; however, it is an open question how relevant the dynamics of a comparatively large laser dye are to those of a small molecule such as CO₂. Optical Kerr effect spectroscopies^{165,249} are sensitive to the many body Raman polarizability tensor, which is difficult to connect to specific motions around a solute in most cases. In our approach, our spectroscopic probe is guaranteed to access the solvation environment of CO₂ (because it *is* CO₂) and is guaranteed to be local to the CO₂ (because it is an isolated vibration of the CO₂). On the other hand, the observed solvation dynamics will arise from only those local motions which most strongly couple into the ν_3 mode; there is no guarantee that the accessible solvent motions are important. This report explores what information this otherwise optimal probe provides.

For our present purposes, a good spectroscopic probe should have the following properties: a high transition dipole moment ($\epsilon \sim 800$ to $1000 \text{ M}^{-1} \text{ cm}^{-1}$); a fundamental frequency in a spectral region that is free of fundamentals or strong combination bands (for most ionic liquids from 1600 to 2600 cm^{-1}); sensitivity to the local environment; a lifetime, T_1 , that is long enough to measure dynamics on a tens of picoseconds timescale; and, finally, a lineshape at least partially inhomogeneously broadened, so that motional narrowing (homogeneous broadening) does not average away the embedded information.

Given these requirements, the ν_3 band of CO₂ is a natural choice. Nonlinear spectroscopy on the ν_3 band ($\epsilon \sim 1000 \text{ M}^{-1} \text{ cm}^{-1}$) has been demonstrated in water,^{250,251} where the T_1 time is ~ 10 ps. In addition, the mode absorbs in a free spectroscopic window of most ionic liquids ($\sim 2350 \text{ cm}^{-1}$).

The remaining question is how sensitively CO₂ reports on structural relaxation of its local environment in ionic liquids. CO₂ in water is an important point of reference because, in water, CO₂ is insensitive to its environment. The CO₂ ν_3 frequency shift from the gas phase

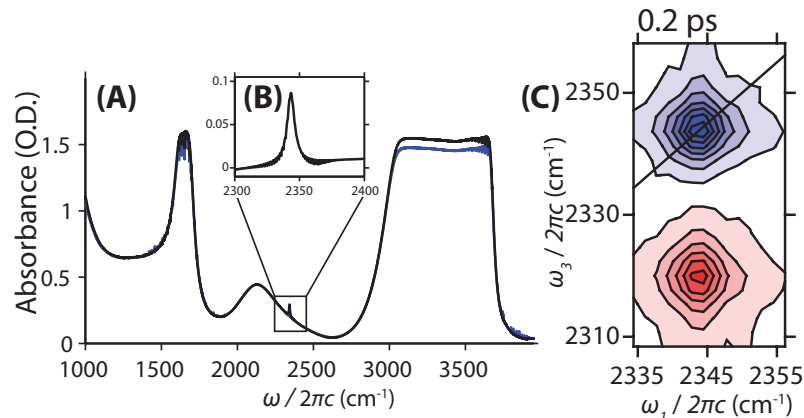


Figure 9: (A) FTIR spectrum of H₂O with (blue line) and without (black line) CO₂ dissolved in it. CO₂ ν_3 lies in the overtones and combinations bands from H₂O librational modes. (B) Inset of ν_3 with water background subtracted shows the Lorentzian character of the peak. (C) Purely absorptive 2D-IR spectrum of ν_3 in H₂O with $t_2 = 0.2$ ps shows that, in water, the line is nearly completely in the limit of homogeneous dynamics.

to the condensed phase is very small, which indicates low sensitivity to the condensed phase local environment. In addition, the CO₂ ν_3 line is narrow and Lorentzian (Figure 9). Even at early population times, the 2D spectra show almost no diagonal character (Figure 9C), indicating that peak shape is determined by dephasing time, T_2 , and that a deeper analysis of the frequency fluctuations (Equation 4.1) is not possible. This finding is consistent with previous three pulse photon echo peak shift (3PEPS) experiments.²⁵⁰ In ionic liquids, the timescales of solvent motion are expected to be slower than in water, and the coupling to the environment may well be larger. Both of these effects would increase the ability to observe dynamics around CO₂.

The other vibrational modes of CO₂, the symmetric stretch, ν_1 , and the doubly degenerate bend, ν_2 and $\bar{\nu}_2$, present distinct challenges for vibrational spectroscopy. The ν_2 modes are sensitive to the chemical environment of the CO₂,^{113,114} but are located in the crowded fingerprint region. The Raman active ν_1 is readily measured, but the lineshape is dominated by the Fermi resonance with the overtone of the ν_2 ,²⁴³ furthermore, it is a dark mode for IR.

Here, we demonstrate that the CO₂ ν_3 mode reports on its local solvent environment by showing the sensitivity of the ν_3 frequency and dynamics to variation in solvent anion in a series of imidazolium ionic liquids; furthermore, we show that ν_3 reports a broad range of solvation timescales in these ionic liquids. We employ electronic structure calculations to investigate the mapping of vibrational frequencies onto structures of CO₂-anion-cation clusters. We show that, despite apparent complexity, the CO₂ linear and 2D-IR lineshapes can be interpreted using simple and accurate physical models. Finally, we establish correlations between the measured dynamics of CO₂ and the macroscopic properties of its ionic liquid solvent.

The paper is organized as follows. Initially, we present the analysis and interpretation of the linear CO₂ spectrum (Section 4.4.1), including a discussion of its temperature dependence. Next, we describe our results from electronic structure calculations on CO₂-anion-cation clusters and its relationship to our experimental data (Section 4.4.2), followed by a simple model of CO₂ that is able to reproduce the observed trends (Section 4.4.3). We then present an overview of the 2D-IR spectra (Section 4.4.4), including a kinetic analysis of the observed shoulders and cross-peaks (Section 4.4.5), assignments of the spectral features (Section 4.4.6), and modelling of the main ν_3 peak (Section 4.4.7) and shoulders and cross-peaks (Section 4.4.8). Finally, we present a discussion of the physical interpretation of our results (Section 4.5), conclusions (Section 4.6) and methods (Section 4.3).

4.3 METHODS

4.3.1 Materials

Ionic liquids were obtained from Ionic Liquids Technologies, Inc (IoLiTec), and used without further purification (except for [Im_{4,1}][BF₄], which was purified prior to experiments using the procedure described by Giernoth and Bankmann.²⁵²) Ionic liquid samples were stored in ambient conditions; however, prior to experiments, samples dried under vacuum at 50 mTorr.

4.3.2 FTIR

FTIR spectra were measured using a $N_{2(g)}$ -purged Nicolet 6700 FTIR instrument (ThermoFisher Scientific). Ionic liquid samples were loaded with CO_2 (99.8% purity, Matheson TRIGAS) in an airtight custom glass vial, with a septum that allows access to the CO_2 -loaded ionic liquid. An aliquot of the liquid sample was sandwiched between two 2 mm-thick CaF_2 optical windows (Crystran Ltd, UK) separated by a 25 μm Teflon spacer, which were held in a brass sample cell. The cell was assembled in a glove bag to limit adsorption of atmospheric water. Spectra were obtained for both the neat ionic liquid and for the ionic liquid loaded with CO_2 .

For temperature-dependent measurements, the sample was temperature-controlled by using a cooling/heating recirculating chiller (Fisher Isotemp) to control the temperature of the sample cell holder. The sample temperature was monitored by measuring the temperature at the optical window using a thermocouple (National Instruments USB-TC01 J-type).

4.3.3 2D-IR

4.3.3.1 Generation of femtosecond mid-IR pulses The experiments utilize a commercial Ti:Sapphire chirped pulse amplifier laser system ($\lambda = 805$ nm, 5 kHz repetition rate, 120 fs pulse duration) (Coherent Vitesse / Coherent Legend Elite).

A home-built optical parametric amplifier (OPA) generates the mid-IR pulses ($\lambda = 12$ to 2 μm), corresponding to around 830 cm^{-1} to 5000 cm^{-1} . The OPA design leads to noise suppression in the resulting mid-IR pulses.²⁰⁴ The spectral bandwidth after the OPA is about 200 cm^{-1} . For these experiments, we tune the OPA wavelength to 4.3 μm . Mid-IR pulse energy entering the 2D spectrometer is approximately 2.2 μJ per pulse.

4.3.3.2 2D Spectrometer The 2D-IR spectrometer uses a pump-probe geometry,²⁵³ in which the first two mid-IR pulses travel collinearly to the sample. A Mach-Zehnder interferometer controls the coherence time t_1 between these pulses. A delay stage after the interferometer controls the population time t_2 between the second and third pulses. The signal, which contains both rephasing and non-rephasing components, is emitted in the

direction of the probe pulse (\vec{k}_3), which also serves as a local oscillator to heterodyne the signal.

A 150 line/mm grating in a single monochromator disperses the signal in ω_3 onto a liquid N₂-cooled 2x32 channel mercury cadmium telluride (MCT) detector. The signal in ω_1 is indirectly acquired by scanning along t_1 using the Mach-Zehnder interferometer, and then applying a numerical Fourier transform to the resulting t_1 -dependent signal at each data point in ω_3 (which also removes the transient absorption signal). The delay changes as the interferometer scans along t_1 are acquired by comparing the interference pattern generated by a He:Ne beam which travels a parallel path through the interferometer.

A series of spectra in t_2 are then acquired by varying the population time between the second and third laser pulses, and then obtaining a spectrum in ω_1 and ω_3 at each population time.

4.3.4 Global Fitting and Bootstrapping

Global fitting of spectra utilizes a third-order response function formalism in the semi-impulsive limit, including the Condon approximation and also the approximation of the cumulant expansion truncated after second order. A constrained nonlinear optimization algorithm (`fmincon` MATLAB) is used to minimize the magnitude of the sum of squared error between each data point in the set of spectra and a corresponding data point in a calculated spectrum. A bootstrapping algorithm²⁵⁴ establishes the error of the global fitting result. The global fitting algorithm was run using synthetic data sets composed of a random selection of the original data points taken with replacement. The distribution of the fitting parameters after 100 iterations provided the error estimate.

4.3.5 Computational Details

All calculations were performed with a development version of the Q-Chem program package²⁵⁵, employing the B3LYP density functional, the 6-31G(d,p) basis set, and a (100,302) grid for the numerical quadrature. All SCF calculations were tightly converged to below 10⁻⁹ a.u. for the DIIS error. Gas-phase geometry optimizations of free CO₂ and the CO₂-

ionic liquid clusters were converged to changes of 1×10^{-8} a.u. in the energy, 1×10^{-6} a.u. in the nuclear displacement, and 1×10^{-6} a.u. in the gradient. Optimized structures were confirmed as minima via harmonic frequency calculations using analytic Hessians. Frequencies were scaled by a factor of 0.9627 (Table 6 Merrick et al.)²⁵⁶.

For the calculations including the electrostatic and polarization effects of the ionic liquid with charge transfer disabled (“ $+\Delta\omega_{\text{FRZ}} + \Delta\omega_{\text{POL}}$ ” in Figure 12), absolutely localized molecular orbitals (ALMOs)²⁵⁷ were employed, with the ionic liquid constituents as one combined fragment and the CO_2 as another fragment. Solution of the ALMO equations is requested by setting `frgm_method = gia`. Charge transfer between fragments is disabled by setting `frgm_lpcorr = 0`.

For the calculation of complementary occupied-virtual pairs (COVPs), an ALMO-EDA calculation is performed where charge transfer is allowed (`frgm_lpcorr = rs_exact_scf`).

4.4 RESULTS AND DISCUSSION

4.4.1 Linear IR Spectroscopy Results

The linear spectra of CO_2 establish that the ν_3 mode is sensitive to the anion, and set the stage for discussing the spectroscopic features present in the 2D-IR spectra.

The ν_3 vibration absorbs strongly around 2340 cm^{-1} in a spectral region with no strong solvent absorbances (Figure 10A). The lineshape of the ν_3 band (Figure 10B) appears mostly Lorentzian, with a low frequency shoulder.

Changing the anion causes both the full-width at half-maximum (FWHM) and center frequency of ν_3 to change (Figure 10C). We varied the anion, rather than the cation, because the anion dominates CO_2 solubility in ionic liquids.^{15,185,258} Anions studied were hexafluorophosphate (PF_6^-), tetrafluoroborate (BF_4^-), bis-(trifluoromethylsulfonyl)imide (Tf_2N^-), triflate (TfO^-), trifluoroacetate (TFA^-), dicyanamide (DCA^-), and thiocyanate (SCN^-). The cation in all experiments was 1-butyl-3-methylimidazolium ($[\text{Im}_{4,1}]$).

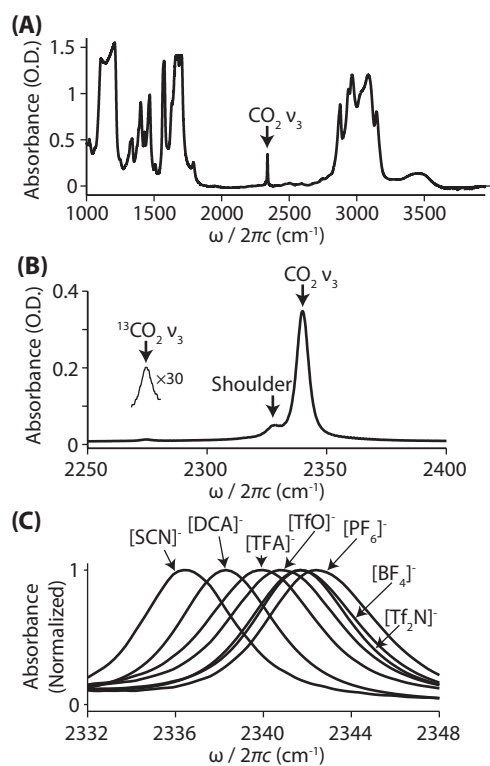


Figure 10: a) Absorption spectrum of CO_2 in $[\text{Im}_{4,1}][\text{TFA}]$ shows the intense antisymmetric stretch absorption at 2340 cm^{-1} ; b) the background subtracted spectrum is Lorentzian with a shoulder at 2328 cm^{-1} , the ν_3 band of the ^{13}C isotopomer is located at 2280 cm^{-1} ; c) The average vibrational frequency of the ν_3 absorption of CO_2 shifts for different anions and the same $[\text{Im}_{4,1}^+]$ cation (background subtracted).

The ν_3 center frequency progressively redshifts from a maximum of 2342.5 cm^{-1} ($[\text{PF}_6^-]$) to a minimum of 2336 cm^{-1} ($[\text{SCN}^-]$). The shoulder moves with the main absorption band and stays $\sim 12\text{ cm}^{-1}$ lower in frequency. Qualitatively, smaller, harder anions like $[\text{SCN}^-]$ and $[\text{DCA}]^-$ create a larger redshift than bulkier, softer anions like $[\text{Tf}_2\text{N}]^-$ and $[\text{TfO}]^-$, which is most likely a function of increased anionic charge density. The increased charge density could red-shift the CO_2 center frequency through an increased local electric field (Stark effect), through charge transfer, or through inductive effects. Quantum chemistry calculations (Section 4.4.2) help to disentangle the driving forces behind this qualitative trend.

The shoulder on the low frequency side of the main ν_3 transition could arise from several possible mechanisms, a “hot-band”, a multiple-quantum transition, or different chemical environments. The temperature dependence of this feature is important in discriminating among these possibilities.

Temperature-dependent FTIR demonstrates that the shoulder on the low frequency side of the main ν_3 transition is a hot band of the ν_3 mode (Figure 11A). Increasing temperature causes a decrease in intensity of the main peak and an increase in intensity of the shoulder, while conserving oscillator strength. The relative magnitude of the shoulder ($\sim 10\%$ of the main band at room temperature) is similar to the expected relative excited state bending mode (ν_2) population predicted by a Boltzmann distribution. We fit the spectra in Figure 11A to two Voigt profiles (one for the main peak, and one for the first shoulder seen on the 2D-IR).

A van’t Hoff analysis of the logarithm of the relative peak heights against $1/T$ gives an activation energy of $810 \pm 30\text{ cm}^{-1}$. This value is near the energy of the ν_2 bending vibration (667 cm^{-1}). Residual gas lines and nonlinearity of the detector contribute to the systematic error of this measurement. Nevertheless, the temperature dependence strongly suggests that the first shoulder is due to one quantum of the bending mode which is excited thermally and is anharmonically coupled to the ν_3 mode.

The temperature dependence and hot-band assignment are important components of our interpretation of the shape of the 2D-IR spectra (Section 4.4.5) and their time-dependence (Section 4.4.8).

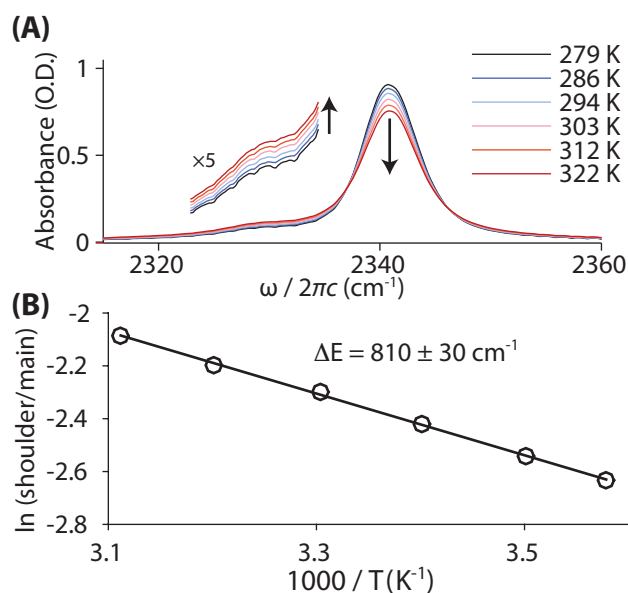


Figure 11: (A) Temperature dependence of the ν_3 spectrum in $[\text{Im}_{4,1}][\text{TfO}]$ shows transition of intensity from the main peak to the shoulder with increasing temperature, indicating a temperature-dependent two-state transition. (B) Relative intensity of shoulder to the main band (based on fitting to Voigt profiles) follows a van't Hoff temperature dependence, indicating an energy barrier of around 800 cm^{-1} , which closely follows the prediction from the temperature dependence of bending mode population.

4.4.2 Vibrational Frequency Calculations

Electronic structure calculations provide a rationale for the observed trend in vibrational frequencies.

Harmonic frequency calculations reproduce the general trend that ν_3 progressively redshifts with decreasing anion size (Table 2). We simplify the solvated CO₂ structure to a gas-phase cluster consisting of one CO₂ with one cation-anion pair, with 1,3-dimethylimidazolium (Im_{1,1}) as the cation. When scaled with the appropriate factor²⁵⁶, the simulations calculate vibrational frequencies within a few wavenumbers of the experimental value. The ordering of anions mostly agrees with experiment as well, the only outliers being [TFA]⁻ and [SCN]⁻, which are located only 2.3 cm⁻¹ apart.

The level of agreement between experiment and theory is good, given that the condensed phase environment is neglected. That such a simple representation reproduces the general trends so well suggests that the interactions of CO₂ are dominated by local effects in its immediate surroundings. Future work will address the condensed phase effects by sampling representative structures from molecular dynamics simulations and repeating the analysis in the context of larger solvation shells.

Encouraged by the fact that the electronic structure calculations reproduce the experimental trends in ν_3 frequencies, we decompose the calculated vibrational frequencies into different components using absolutely localized molecular orbitals (ALMO), in analogy to ALMO energy decomposition analysis (ALMO-EDA).^{257,259,260}

Unlike standard quantum chemical calculations, where individual molecular orbitals may delocalize over more than a single fragment, each ALMO is composed of atomic orbitals from a single fragment. This constraint allows us to control charge transfer between fragments and to quantify the interaction between fragments in physically intuitive terms.

The total vibrational frequencies ω_{tot} and vibrational shifts $\Delta\omega_{\text{int}}$ from gas phase (“free”) CO₂ for each mode ν may be written as:

$$\omega_{\text{tot}} = \omega_{\text{free}} + \Delta\omega_{\text{int}} \tag{4.3}$$

where

$$\Delta\omega_{\text{int}} = \Delta\omega_{\text{GEOM}} + \Delta\omega_{\text{FRZ}} + \Delta\omega_{\text{POL}} + \Delta\omega_{\text{CT}} \tag{4.4}$$

where $\Delta\omega_{\text{GEOM}}$ (geometric distortion) corresponds to the change in frequency caused by distortion of fragments from their free geometries to their cluster geometries, $\Delta\omega_{\text{FRZ}}$ (the frozen orbital interaction) results from the combined electrostatic interaction and Pauli repulsion between the filled, unrelaxed orbitals of each fragment, $\Delta\omega_{\text{POL}}$ (polarization) is due to the relaxation of a fragment’s orbitals in the field of the other fragments, and $\Delta\omega_{\text{CT}}$ (charge transfer) is from occupied-virtual orbital donation between orbitals of different fragments.²⁶¹

The cluster environment can affect the vibrational frequency of CO_2 in two different ways. The first depends on the anharmonic potential surface of a free CO_2 molecule. In a harmonic system, the spring constant, k , uniquely determines the vibrational frequency for all nuclear positions (i.e., the curvature of a quadratic potential is constant). CO_2 ’s potential energy surface, however, is inherently anharmonic. Any change in geometry will thus cause a change in the ν_3 vibrational frequency. In other words, the cluster can change the ν_3 frequency just by shifting the location of minimum of the CO_2 potential ($\Delta\omega_{\text{GEOM}}$). The second results from changes in the local curvature of CO_2 ’s potential energy surface due to interactions with the surrounding cluster ($\Delta\omega_{\text{FRZ}} + \Delta\omega_{\text{POL}} + \Delta\omega_{\text{CT}}$).

We focus on the following grouping of terms: (1) distortion of isolated CO_2 to its cluster geometry ($\Delta\omega_{\text{GEOM}}$), (2) the combined frozen orbital and polarization contributions through use of ALMOs ($\Delta\omega_{\text{FRZ}} + \Delta\omega_{\text{POL}}$), and (3) charge transfer between the fragments in the cluster ($\Delta\omega_{\text{CT}}$).

The final frequency, ω_{tot} , correlates most strongly with $\Delta\omega_{\text{GEOM}}$ ($R^2 = 0.96$), indicating that geometrical distortion of CO_2 dominates the frequency shift. Depending on the particular geometry that CO_2 adopts in the cluster, $\Delta\omega_{\text{GEOM}}$ can vary by $\pm 6 \text{ cm}^{-1}$ (Figure 12).ⁱ Electrostatics and charge transfer both change the local curvature of the potential energy surface; however, their effects are mostly uniform across the ionic liquids studied. When we turn off charge transfer between fragments, ν_3 blue-shifts on average by $\langle \Delta\omega_{\text{FRZ}} + \Delta\omega_{\text{POL}} \rangle = +2.8 \pm 0.6 \text{ cm}^{-1}$. Modelling the cluster geometry as a field of point charges increases this blue shift to $+4.4 \pm 0.6 \text{ cm}^{-1}$ (Supplementary Information), which may indicate that a point-charge representation of the cluster over-polarizes the QM region^{262,263} Allowing charge trans-

ⁱSince ω normally refers to an angular frequency, this quantity might more rigorously be called $\Delta\omega_{\text{GEOM}}/2\pi c$; however, for convenience of notation, we chose to use spectroscopic units uniformly in this section. That is, all frequencies are given in wavenumbers, rather than rads^{-1} .

fer red-shifts the frequencies by $\langle \Delta\omega_{\text{CT}} \rangle = -3.5 \pm 0.8 \text{ cm}^{-1}$. Thus, both electrostatics and charge transfer change the local curvature of the ν_3 potential energy surface. The effects, however, are uniform and nearly cancel. The net result is that the inherent anharmonicity of the CO_2 potential energy surface ultimately dominates the ν_3 frequency.

The geometrical distortion of the CO_2 is driven by charge transfer. Using ALMOs and forbidding charge transfer during relaxation of the cluster removes the variance in $\Delta\omega_{\text{GEOM}}$ (Figure 12B). Once again, both electrostatic and charge transfer interactions act uniformly on the frequency, leading to a negligible variance in ω_{tot} . Without the geometrical distortion due to charge transfer, the vibrational frequencies for all clusters remain within $\pm 2 \text{ cm}^{-1}$ and no longer follow the experimental trend.

The essential point is that charge transfer and electrostatics only affect the vibrational frequency indirectly, through their coupling into the equilibrium CO_2 nuclear geometry. The direct effects of electrostatics and charge transfer on the potential energy surface (and thus the effective spring constant) of ν_3 are uniform across ionic liquids studied and counteract each other.

This DFT-based analysis may over-emphasize charge transfer to some extent. It is well known that DFT over-delocalizes electrons due to self-interaction error, which might exaggerate the amount of charge transfer. In the context of gas-phase anion clusters, both DFT²⁶⁴ and post-Hartree-Fock methods²⁶⁵ have also identified charge transfer as a driver of geometrical distortion of CO_2 , so we expect that our qualitative picture will be robust with respect to the theoretical method. Future work will explore the quantitative differences between the different methods. Furthermore, although our cluster results agree well with experiment, we expect that the extended solvation environment neglected here may introduce screening effects not captured at the cluster level.²⁶⁶ A more sophisticated study of solvation effects could determine whether our finding, that charge transfer dominates the geometric effects which differentiate CO_2 vibrational frequency shifts, is transferable to bulk ionic liquids.

These calculations demonstrate that the ν_3 frequency shift reflects a complex interplay between geometry, electrostatics, and charge transfer. The geometrical distortion is the most important factor in determining the final variation in vibrational frequency with anion identity; however, the equilibrium geometry of the CO_2 itself ultimately depends on inductive

effects, such as charge transfer.

4.4.3 Frequency, Geometry, and Charge Transfer Discussion

To gain chemical insight into the charge transfer process, one can analyze the donor and acceptor orbitals of CO₂ and the ionic liquid. This analysis sheds light on the nature of the geometrical distortion, which, in turn, leads to a simple model for the vibrational frequencies in terms of a few geometrical parameters.

We employ a complementary occupied-virtual orbital pair (COVP) analysis²⁶⁰ to gain insight into the electronic structure effects underlying the charge transfer between CO₂ and the solvent. COVPs provide a way to visualize charge transfer effects, where “each COVP corresponds to an occupied orbital on one molecule donating charge to one specific (complementary) virtual orbital on the other molecule.”²⁶⁷ These orbital pairs are constructed from a singular value decomposition of the occupied-virtual mixing matrix \mathbf{X} that describes charge transfer between the (polarized) fragments upon removing the ALMO fragment localization constraint. While \mathbf{X} contains, in general, excitations between all possible occupied-virtual pairs, the COVP representation of \mathbf{X} is diagonal and thus provides the most compact possible basis for describing charge transfer. The associated singular values allow one to assess the contribution of a particular COVP to charge transfer, and typically one finds that only one or a few orbital pairs dominate the effect (as shown below in this study). The COVP analysis thus allows to conveniently identify and visualize the electron donor/acceptor orbitals pair(s) that significantly contribute to charge transfer.

Charge transfer to the CO₂ originates from occupied orbitals on the anions. The charge is accepted by virtual orbitals on the CO₂. The virtual orbitals are a linear combination of the LUMO and LUMO+1 orbitals, which have σ^* and π^* character, respectively. Charge transfer from the anion has a strong linear correlation to the bend angle ($R^2 = 0.84$). Mechanistically, bending the CO₂ allows σ^* and π^* to mix, lowers the energy of the acceptor orbital, and also maximizes the spatial overlap with the donor orbital. The amount of charge transferred (3–5 me⁻) is small, but the resulting bend angle (3 to 5 Å) can be substantial (Table 3).

CO₂ also donates charge back to the ionic liquid cluster, primarily to the cation. The

Table 2: Experimental and calculated ν_3 vibrational frequencies for CO_2 in various imidazolium (experimental [Im_{4,1}], calculations [Im_{1,1}]) ionic liquids. Calculations are carried out using a gas phase anion-cation- CO_2 cluster at 0 K. The level of agreement between calculations and experimental results indicates that interactions of CO_2 are dominated by local effects in its immediate surroundings.

Anion	Expt. Freq. (cm^{-1})	Calc. Freq. (cm^{-1})	Calc. Freq. (scaled) (cm^{-1})
[PF ₆] ⁻	2342.5	2437.7	2346.8
[Tf ₂ N] ⁻	2341.7	2435.8	2344.9
[BF ₄] ⁻	2341.7	2434.7	2343.9
[TfO] ⁻	2340.9	2431.9	2341.2
[TFA] ⁻	2339.9	2429.3	2338.7
[DCA] ⁻	2338.4	2430.5	2339.8
[SCN] ⁻	2336.5	2430.0	2339.4

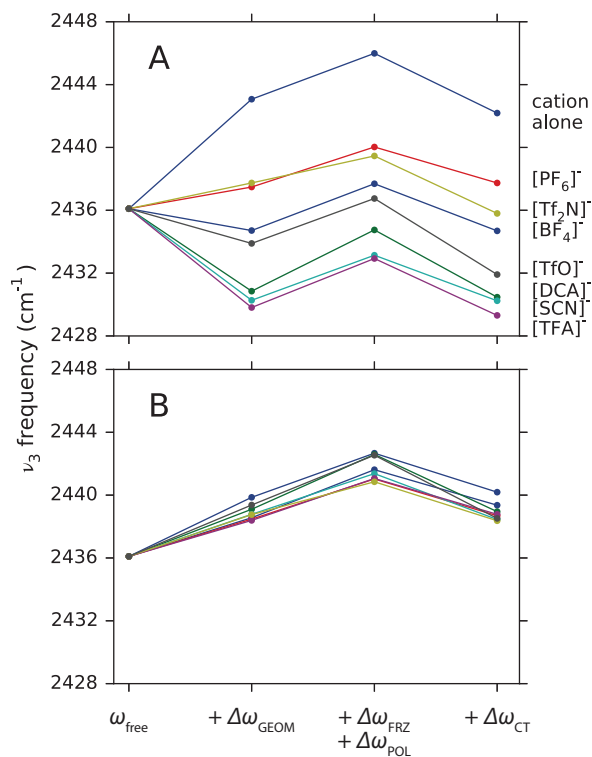


Figure 12: Decomposition of the geometric, electrostatic, and charge transfer contributions to CO_2 ν_3 vibrational frequency shifts. (A) The cluster geometry (including CO_2) was optimized while allowing charge transfer. (B) The cluster geometry was optimized using ALMOs to forbid charge transfer between fragments. The final frequency ($\omega_{\text{tot}} = \omega_{\text{free}} + \Delta\omega_{\text{GEOM}} + \Delta\omega_{\text{FRZ}} + \Delta\omega_{\text{POL}} + \Delta\omega_{\text{CT}}$) correlates most strongly with the change in frequency from geometric distortion ($\Delta\omega_{\text{GEOM}}$).

Table 3: Charge transfer from the anion to CO₂ and from CO₂ to the cation both contribute to the geometrical distortion of the CO₂. The most important geometrical degrees of freedom are the bend angle, θ and the sum of the two carbonyl bond lengths, L .

cluster	CT to CO ₂ (me ⁻)	CT from CO ₂ (me ⁻)	θ (°)	L (Å)
[Im _{1,1}] ⁺	0.079	2.251	0.07	2.3374
[PF ₆] ⁻	3.336	1.012	3.79	2.3379
[Tf ₂ N] ⁻	2.493	1.603	2.64	2.3380
[BF ₄] ⁻	4.558	1.264	4.51	2.3385
[TfO] ⁻	3.009	2.339	4.01	2.3389
[TFA] ⁻	5.131	1.618	5.22	2.3394
[DCA] ⁻	3.376	2.259	4.99	2.3394
[SCN] ⁻	3.317	1.323	4.35	2.3395

amount of charge donated by the CO₂ to the cation (-1 to -2 me) is typically less than the charge donated from the anion, but nevertheless has specific consequences for the resulting geometry. The donor orbital from the CO₂ is a mixture of σ -bonding and π -nonbonding character. The charge donation from the CO₂ is linearly correlated to the carbonyl bond length differences ($R^2 = 0.85$). For the [Im_{1,1}][TfO] cluster, which has the highest charge transfer from CO₂ to the cation (2.32 me⁻), the σ character of the donating orbital causes the carbonyl nearest the cation to lengthen from the gas-phase 1.169 Å to 1.175 Å while the distal carbonyl contracts to 1.163 Å.

The effects of charge transfer to and from the CO₂ can be incorporated into a simple model of the vibrational frequencies. The model is constructed in a vibrational local-mode basis. The effective one exciton vibrational Hamiltonian is

$$H^{(1)} = \begin{pmatrix} \hbar\omega_1 & \beta \\ \beta & \hbar\omega_2 \end{pmatrix} \quad (4.5)$$

where ω_i is the local mode frequency of carbonyl i and β is the coupling between the two local modes. The diagonalized hamiltonian gives symmetric and antisymmetric linear com-

binations of the local modes as the vibrational eigenstates with energies $\hbar\omega_s$ and $\hbar\omega_a$. The splitting between symmetric and antisymmetric vibrations is twice the coupling constant, $\hbar(\omega_s - \omega_a) = 2\beta$, and the average frequencies in local and normal modes are also equal $\hbar(\omega_a + \omega_s)/2 = \hbar(\omega_1 + \omega_2)/2 = \alpha$.

The bend in the CO₂ determines the change in the coupling constant between the local modes, β ($R^2 = 0.94$). The motion of the central carbon atom is the primary motion that couples the two carbonyls. When they are collinear, the motion of one carbonyl directly influences the other. Bending the CO₂ means the carbonyls are no longer collinear, which means that the projection of one local vibration on the other decreases. This decrease, in turn, decreases the effective coupling constant.

The sum of the CO₂ bond lengths L , is correlated to the α ($R^2 = 0.998$). The dependence of α on the geometry of the molecule is not as straightforward than that of β . In the strong coupling limit, $\beta \gg |\hbar\omega_2 - \hbar\omega_1|$, the symmetric and antisymmetric stretching frequencies only depend on the average frequencies, $(\hbar\omega_1 + \hbar\omega_2)/2$. As such, the geometrical asymmetry induced by charge transfer from the CO₂, which weakens one bond and strengthens the other, is largely averaged out. Only a weak correlation between the charge donated from the CO₂ and the α remains. The sum of the bond lengths, L , however, reports exactly this difference in total bonding strength. Though the changes in L are minute ($\sim 0.001 \text{ \AA}$), the effect on the vibrational frequencies is not.

Because of the strong linear correlation with these two geometrical variables, we propose that the simplest model of the scaled vibrational frequencies is $\alpha(L)$ and $\beta(\theta)$, where

$$\alpha(L) = 9523.8 \text{ cm}^{-1} - (3415.3 \text{ cm}^{-1} \text{ \AA}^{-1}) L \quad (4.6)$$

and

$$\beta(\theta) = -515.7 \text{ cm}^{-1} + (1.12 \text{ cm}^{-1} \text{ deg}^{-1}) \theta \quad (4.7)$$

where α and β are in units of cm^{-1} , L is in \AA , and θ is in degrees. The one exciton Hamiltonian

$$H^{(1)} = \begin{pmatrix} \alpha(L) & \beta(\theta) \\ \beta(\theta) & \alpha(L) \end{pmatrix}, \quad (4.8)$$

reproduces the scaled harmonic frequencies with an RMS error of 1.2 cm^{-1} and the experimental frequencies with an RMS error of 4 cm^{-1} .ⁱⁱ

Following a detailed investigation of the charge transfer, the participating orbitals, and the effects of charge transfer on the CO_2 geometry, we have put forward a simple model that successfully reproduces the calculated vibrational frequencies and, to a reasonable extent, the experimental frequencies, with no free parameters.

4.4.4 2D-IR Spectroscopy Overview

While linear spectroscopy shows the sensitivity of CO_2 to its local environment, it cannot address the ultrafast dynamics of the chromophore. 2D-IR, however, directly reports on the dynamic structural relaxation around CO_2 . 2D-IR of CO_2 in $[\text{Im}_{4,1}][\text{TFA}]$ introduces many of the features that are general across all of the ionic liquids studied.

The 2D spectra of the ν_3 mode of CO_2 in $[\text{Im}_{4,1}][\text{TFA}]$ (Figure 13A and B) show the main ν_3 band, two diagonal shoulders, and cross-peaks between them. The observed peaks cannot be explained without also keeping track of the states of the CO_2 symmetric stretch and bending modes in the vibrational state. The total vibrational wavefunction is specified by $|\nu_1\nu_2^l\nu_3\rangle$, where ν_1 is the number of quanta in the symmetric stretch, ν_2 is the number of quanta in the bending mode, l is the vibrational angular momentum quantum number of the bending mode, and ν_3 is the number of quanta in the antisymmetric stretch.

The main band consists of a pair of intense peaks corresponding to the $|00^00\rangle \rightarrow |00^01\rangle$ and $|00^01\rangle \rightarrow |00^02\rangle$ (1a and 1b) transitions, separated by the anharmonicity of $\nu_3 \sim 24 \text{ cm}^{-1}$. Due to ground state bleach, 1a appears as a negative (blue) feature, while 1b, from excited state absorption, is a positive (red) feature. The ν_3 shoulder appears as a pair of small peaks (2a and b), shifted along the diagonal by -12 cm^{-1} in ω_1 and ω_3 . A second apparent shoulder, not seen on FTIR, presents as a pair of smaller peaks (1e and 1f), shifted along the diagonal from the main band by -24 cm^{-1} in ω_1 and ω_3 . At early population times, there is an apparent cross-peak between the main peak and second shoulder (1c). Cross-peaks

ⁱⁱSee Appendix A.1.2 for 2D-IR spectra of CO_2 in each ionic liquid, as well as a comparison of center line slope and global fitting results for correlation times, and more detailed computational results. Additionally, there is information on fitting of the one exciton Hamiltonian model for unscaled frequencies, and vibrational frequency calculations of CO_2 in a field of point-charges that approximates the cluster geometry.

grow in between the first shoulder and main peak (2-1a and b, 1-2b) over t_2 . The expected cross-peak 1-2a cannot be seen due to cancellation with the overwhelming opposite signal from the 1b.

The combination of CO₂'s high molar absorptivity ($\sim 1000 \text{ M}^{-1} \text{ cm}^{-1}$) and the ε^2 dependence of the third-order signal causes the 2D signal from CO₂ to dominate the spectrum in intensity. Contributions from solvent overtones in the background are smaller than the level of noise in the spectrum. Thus, the 2D signal reflects the vibrational modes of CO₂, rather than solvent background, and the solvent can only affect the 2D spectrum through intermolecular couplings with CO₂ vibrational modes.

The unambiguous spectral diffusion of 1a and 1b over the 50 ps population time demonstrates that the line is not entirely in the motional narrowing (homogeneous) limit. That is, ν_3 will allow us to resolve the dynamics of structural relaxation around CO₂.

The observations of a complex pattern of peaks and of spectral diffusion on a tens of picoseconds timescale for CO₂ in [Im_{4,1}][TFA] are general features of the spectra in all of the tested ionic liquids and are described in detail in the next two sections.

4.4.5 2D-IR Shoulders and Cross-Peaks

Careful analysis of the relative kinetics of the diagonal peaks and cross-peaks (Figure 14) provides insight into how the coupling of CO₂ vibrational modes and their stochastic dynamics create the observed spectrum.

Orientalional and vibrational relaxation of CO₂ cause a decrease in spectral intensity over t_2 . The main peak (1b) shows an initial rapid decrease in intensity from orientation relaxation, followed by a slower decay over ~ 100 ps, from vibrational relaxation processes. Polarization-controlled studies can remove the contribution from orientational relaxation, and provide an explicit assessment of vibrational relaxation rate.^{197,268}

The shoulders and cross-peaks are significantly weaker than the main peak, and also relax over t_2 ; however, analysis of their kinetics relative to the main band reveals the underlying stochastic dynamics of CO₂ vibrational modes.

The first diagonal shoulder (2b) decays more quickly than the main band, decreasing to

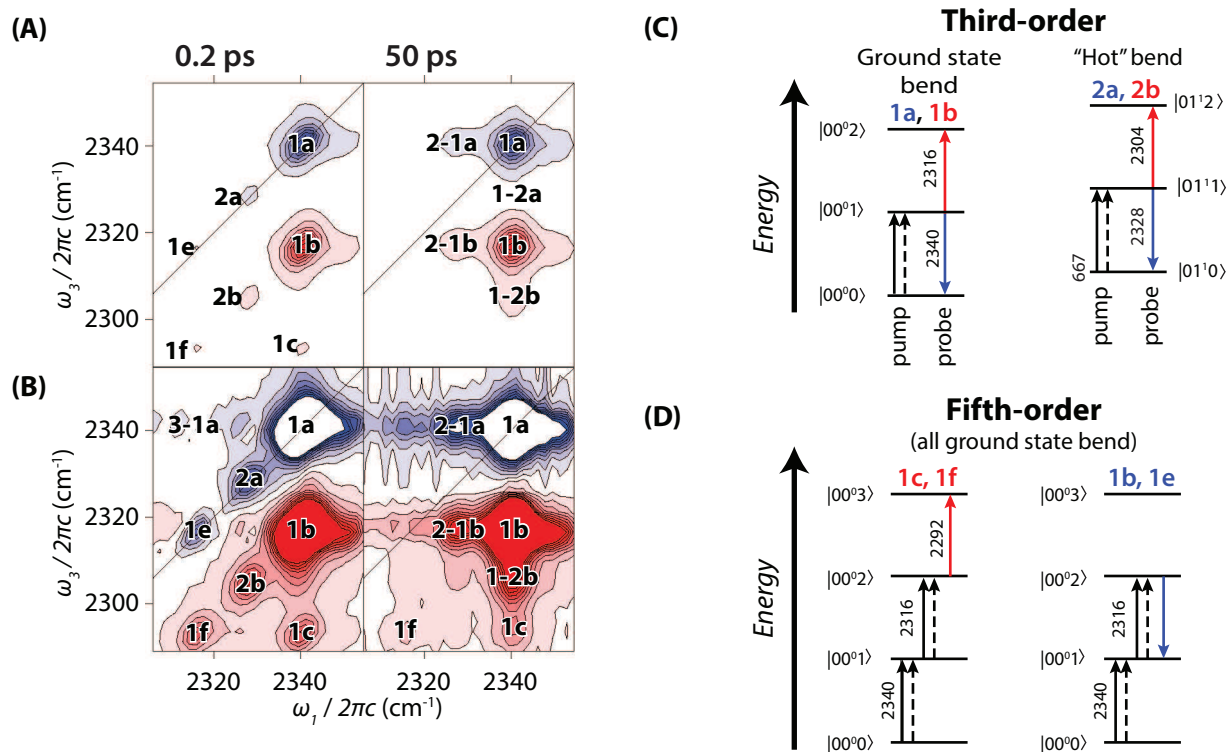


Figure 13: **(A)** 2D-IR spectrum of CO₂ in [Im_{4,1}][TFA] at $t_2 = 0.2$ and 50 ps. The peak labels correspond to transitions in **(C)** and **(D)**. **(B)** The same spectrum as **(A)** with contours limited to 10% of the maximum in the z -direction. Structure of the diagonal shoulders and cross-peaks can be seen much more readily. **(C)** and **(D)** Vibrational energy level diagrams for observed third-order **(C)** and fifth-order **(D)** bands of CO₂ in [Im_{4,1}][TFA]. Quantum numbers correspond to $|\nu_1 \nu_2^l \nu_3\rangle$. Transition frequencies are labeled in wavenumbers (cm⁻¹), and a label corresponding to the peaks in **A** and **B**. The color of the label indicates whether the expected peak is negative (blue) or positive (red).

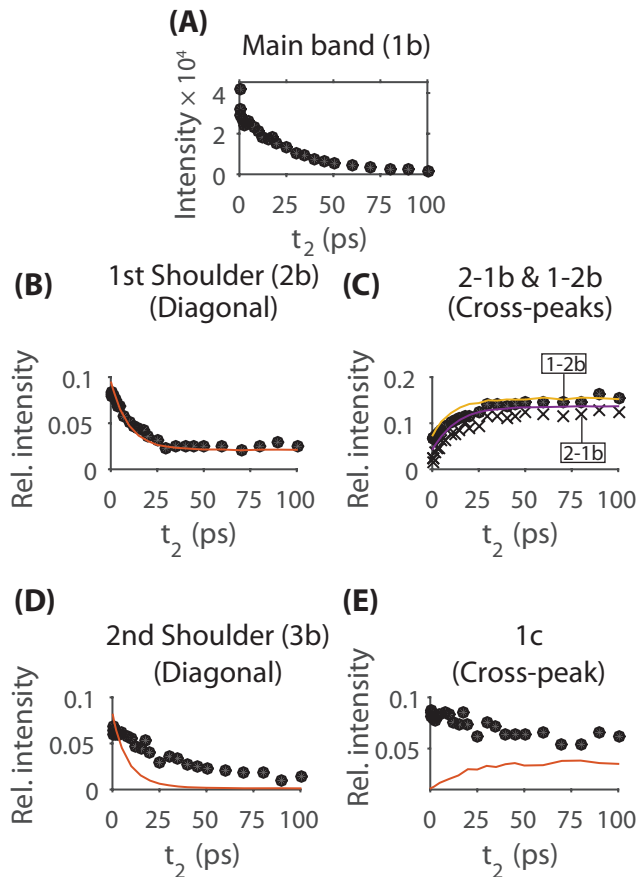


Figure 14: Kinetic analysis of $[\text{Im}_{4,1}][\text{TFA}]$. (A) Absolute intensity of the main peak (1b) with increasing t_2 . Decreased intensity results from both orientational and population relaxation. (B)-(E) show intensities relative to A. Discrete data points represent experimental data, while lines show data from stochastic simulations (Section 4.4.8). (B) and (C), which result from the first diagonal shoulder (2b) and its cross-peaks with the main band (1-2b / 2-1b) show good agreement between experimental and simulated kinetics. (D) and (E), which result from the second diagonal shoulder (3b) and the apparent cross-peak (1c) show distinct kinetics, which cannot result from the same stochastic bending mode fluctuations, and point to a direct transition.

a minimum intensity at ~ 25 ps followed by a (relative) steady state (Figure 14). Cross-peaks between the first shoulder and the main band (2-1b and 1-2b) start at a minimum intensity, and then increase, before reaching a relative steady state by 25 ps. This behavior points to dynamic exchange between $|00^01\rangle$ and $|01^11\rangle$, which give rise to the diagonal peaks (Section 4.4.8).

The second diagonal shoulder (3b) decreases in intensity relative to the main band, but more slowly than the first shoulder. The apparent cross-peak 1c decreases in relative intensity over t_2 with slower kinetics than the second shoulder. This behavior contrasts with that of the cross-peaks 1-2b and 2-1b, and indicates that 1c arises from a direct vibrational transition, rather than dynamic exchange.

4.4.6 Peak Assignment

The Dunham expansion for anharmonically coupled vibrational modes provides a theoretical framework for building an analysis of coupled vibrational modes:

$$E = \sum_i \hbar\omega_i \left(n_i + \frac{1}{2} \right) + \sum_{ij} x_{ij} \left(n_i + \frac{1}{2} \right) \left(n_j + \frac{1}{2} \right) \quad (4.9)$$

where ω_i is the frequency of the mode, n_i is the number of quanta in the mode, and x_{ij} are anharmonic coupling constants. It directly follows that the energy of a particular mode is given by:

$$\nu_{n_k \rightarrow n_k+1} = \nu_k + 2n_k x_{kk} + \sum_{i \neq k} x_{ij} n_i, \quad (4.10)$$

which implies that transition energy will decrease by x_{ij} for every quantum of energy in an anharmonically coupled mode.²⁶⁹ Gas phase vibrational calculations predict $x_{23} \approx -12 \text{ cm}^{-1}$ per quantum in ν_2 .^{270,271}

The first shoulder can then be explained by anharmonic coupling of excited state bending modes with the asymmetric stretching mode. This coupling causes a frequency shift of -12 cm^{-1} , and creates a shoulder on the linear and the 2D spectra (peaks 2a/2b on 2D-IR). Stochastic fluctuations in thermally populated bending modes cause dynamic 2D-IR cross-peaks.

This mechanism for dynamic cross-peaks is not unique to CO₂ in ionic liquids; however, it is a nearly ideal system in which to observe and analyze it. The narrow total linewidth ($\sim 6 \text{ cm}^{-1}$), combined with a large anharmonic coupling constant ($x_{23} = -12 \text{ cm}^{-1}$), leads to clear segregation of the resulting frequencies into distinct peaks. The difference in energy between the ground and first excited state ν_2 modes is only around $3k_{\text{B}}T$, which is low enough to be thermally accessible, but high enough to be quantized. Finally, the rate of stochastic fluctuations in bending mode states is slow enough to preserve distinct diagonal bands at short population times, but fast enough to allow dynamic cross-peaks over the timescale of the experiment ($\sim 100 \text{ ps}$).

Alternative hypotheses can be ruled out. There are two possibilities that need to be addressed. First, the shoulder is often assigned to a multiquantum transition. Second, the shoulder and cross-peaks could be due to chemical exchange.

The first ν_3 shoulder in our spectra is also present in the FTIR of CO₂ dissolved in organic liquids and many polymers, and is often attributed to a multiquantum transition $\nu_3 + \nu_2 - \nu_2$,^{112,114,272-274} where the difference in energy is attributed to splitting of normally degenerate CO₂ ν_2 and $\bar{\nu}_2$ bending modes. (This combination should perhaps be written as $\nu_3 + \nu_2 - \bar{\nu}_2$ or $\nu_3 + \bar{\nu}_2 - \nu_2$, but is typically presented without distinguishing between the two bending modes.) This hypothesis fails on several accounts. First, such a multiquantum transition is harmonically forbidden, so the transition dipole moment should be significantly lower than for the one quantum ν_3 transition. The intensity of the shoulder, however, directly follows a Boltzmann distribution for the ν_2 bending modes, which implies that the magnitude of the transition dipole moment is roughly equal for both the fundamental and this multiquantum transition.

Second, with this mechanism, a shoulder on the high frequency side of the fundamental should accompany the observed shoulder on the low frequency side. That is, there is no clear reason why the transition $\nu_3 + \nu_2 - \bar{\nu}_2$, would be strongly allowed, but $\nu_3 + \bar{\nu}_2 - \nu_2$ would not. Third, this hypothesis assumes that the splitting of the bending modes is an identical 12 cm^{-1} , but this is not the case.¹¹³ Finally, in the 2D spectrum, this combination band would give rise to cross-peaks between the first shoulder and the main band (since each a CO₂ molecule could undergo either transition with excitation), which would be present at the

earliest population times, and would only relatively decay (rather than relatively increase) with t_2 . This behavior contradicts the observed spectral kinetics.

The temperature dependence of the shoulder (Figure 11) also excludes different chemical environments (such as multiple equilibrium geometries of a CO₂-anion interaction) undergoing chemical exchange. In this hypothesis, the most intense feature would be due to free CO₂ and the shoulder to CO₂ with a stronger chemical interaction. The growth of the cross-peaks would correspond to the exchange of these populations. However, the free CO₂ band should be entropically favored and increase with increasing temperature while the shoulder should be enthalpically favored and decrease with increasing temperature. The opposite is observed, so this hypothesis can be ruled out. Additionally, the equal relative energy spacing of the diagonal shoulders from the main band for CO₂ in every ionic liquid studied strongly suggests that the additional peaks arise from the CO₂ itself, rather than from distinct chemical environments.

In contrast, the explanation of anharmonic coupling between ν_2 and ν_3 fits the temperature dependence, the transition dipole scaling, and accounts for the cross-peak kinetics. In our picture, each step requires only a one quantum transition for each peak, explains the presence of a shoulder on only one side of the fundamental, and correctly reproduces the cross-peak kinetics (over t_2) between the first shoulder and main band due to thermal excitation and de-excitation of the bend.

The apparent cross-peak 1c, as well as the second apparent shoulder (1e and 1f) are fifth-order signals, as can be shown by pump power-dependence, frequencies, and sign show that it is a fifth-order signal, as are several other features. Assignments of the ν_3 2D-IR spectrum of carbon dioxide in 1-butyl-3-methylimidazolium trifluoroacetate [Im_{4,1}][TFA], are given in Figure 13 and Table 4).

The magnitude of third-order signal is linear in pump light intensity, since there are two pump electric field interactions, while that of fifth-order signal (with four electric field interactions) is quadratic. We assessed the magnitude of each peak when the pump power was changed by a factor of two (Table 4). There is a clear distinction between the pump power dependence of the third order signals (1a, 1b, 2a, 2b, and their population exchange cross-peaks) and the fifth order signal (1c, 1e, 1f, and 31a). The reported intensity ratio is

the ratio of volumes of a single peak when the pump power doubles. Thus, for the main ‘red’ peak (1b: ν_3 excited state absorption with ground state ν_2), peak volume goes up by a factor of 2.2 ± 0.1 when pump power doubles. Peak 1c’s volume, however, increases by a factor of 3.3 ± 0.2 .

The fifth-order perturbative pathways have previously been described by Garrett-Roe and Hamm for 3D-IR (five IR pulse) spectroscopy.⁷¹ The assignment of a “name” for each fifth-order pathway (Table 2 & Figure 15) follows the scheme used by Garrett-Roe and Hamm, where pathways are described by listing the vibrational quantum numbers of the three coherent states that contribute to them. Non-rephasing diagrams are shown for all pathways.

Since a 2D-IR experiment only has two coherence times (which give two frequency axes), we can only resolve two of the three coherences in the fifth-order pathway. When up-pumping occurs during the first two (“pump”) pulses, either t_1 or t_3 will be unresolved. Thus, each pathway can give two spectral peaks on a 2D-IR spectrum, if the coherent frequencies in t_1 and t_3 differ. For fifth-order pathways in Table 2, the coherence noted in parenthesis does not contribute to the observed peak, since oscillation of the first coherence will not be observed when there are multiple electric field interactions during a single 100 fs pulse. That is, the pathway 10|21|32 contributes to peaks 1c and 1f. Peak 1f results from up-pumping during the first pump pulse, (10) |21|32, and thus only the $|2\rangle\langle 1|$ and $|3\rangle\langle 2|$ coherences are observed. Peak 1c results from up-pumping during the second pulse, 10| (21) |32, and thus only the $|1\rangle\langle 0|$ and $|3\rangle\langle 2|$ coherences are observed. The center frequency and sign of the peak amplitude for each observed fifth order peak matches that predicted by the corresponding fifth-order pathway (Table 2).

The peaks 1c, 1e, 1f, and 3-1a are fifth-order signals, not cascading third-order signals. Two of the peaks, 1c and 1f, cannot be generated by a cascade, because they involve walking up the vibrational ladder to a $|3\rangle\langle 2|$ coherence. Given the presence of these unambiguously direct fifth-order signals, we would expect to find spectra contributions from other fifth-order pathways. Peaks 1e and 3-1a are located where we would predict additional fifth-order signal. The correspondence of the sign of the signal to those predicted by a direct fifth-order pathway is also important, because the relative signs of cascading third-order signals and

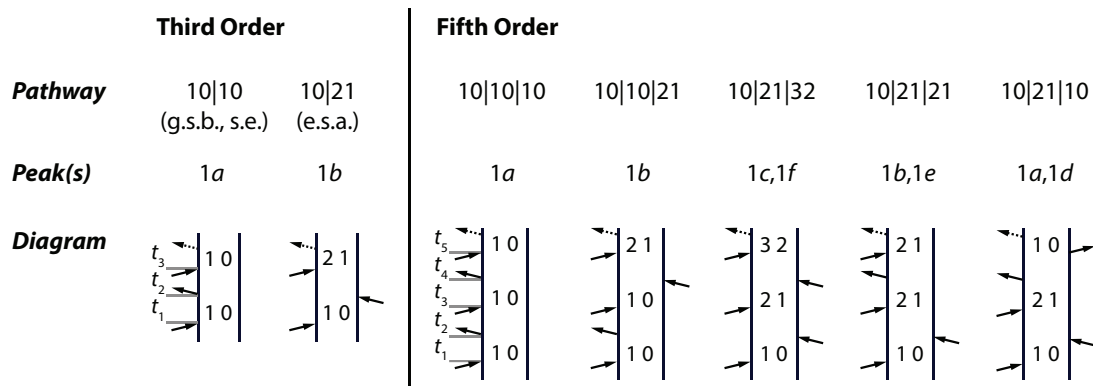


Figure 15: Double-sided Feynman diagrams, pathway labels, and peaks for third- and fifth-order peaks in the CO₂ 2D-IR spectrum (non-rephasing pathways shown). Labels for pathways correspond to those used by Garrett-Roe and Hamm in their description of purely absorptive 3D-IR spectra.⁷¹ In a three optical pulse experiment (like 2D-IR), only two of the three coherences of a fifth-order signal can be resolved. Thus, depending on whether up-pumping occurs during the first or second pump pulse, either t_1 or t_3 will be unresolved in the fifth-order pathways. This effect can lead to multiple peaks on the 2D-IR spectrum from a single fifth-order pathway.

fifth-order signals are opposite (due to the difference of i^2 in the pre-factor in the infrared). Furthermore, the relative magnitudes follow the predictions based on the various pathways through population states and harmonic transition dipole moment scaling.⁷¹ Finally, the relative peak intensities, including those of direct third-order signals, do not substantially vary with the concentration of the chromophore. Cascaded signals scale proportionally to c^2 , and thus would not scale with the other peaks on the spectrum.

4.4.7 Modelling of Main Band

The 2D peak of a specific vibrational mode encodes the frequency-fluctuation correlation function (Equation 4.1) in its lineshape. Lineshape analysis can extract the timescale of structure relaxation around that mode, by quantifying spectral diffusion, or change in diagonal character (or ellipticity), of a peak over t_2 .

The intense ν_3 peak clearly exhibits spectral diffusion in each ionic liquid studied (Figure 47). Qualitatively, at early population times, the main ν_3 peaks have diagonal character. As a function of the population time, t_2 , the peaks become rounder. The rate of ν_3 spectral diffusion varies in the ionic liquids tested, indicating a broad range of timescales for structural relaxation in the different solvents. The rate is slowest in $[\text{Im}_{4,1}][\text{PF}_6]$ (Figure 47A) and fastest in $[\text{Im}_{4,1}][\text{DCA}]$ (Figure 47C). The vibrational relaxation time slow enough to allow us to measure over 100 ps of dynamics.

We used a global fitting algorithm to quantify the rate of spectral diffusion for ν_3 in each ionic liquid (Figure 47). The main peak in the 2D spectrum is sufficiently separated from the shoulders that it can be treated independently. Simulated spectra were calculated using a third-order response function formalism in the semi-impulsive limit. The frequency-fluctuation correlation function

$$c_2(t) = \frac{\delta(t)}{T_2} + \Delta^2 \exp\left(-\frac{t}{\tau_c}\right), \quad (4.11)$$

corresponds to a physical system in which CO_2 senses two distinct timescales of motion. Fast motions, in the homogeneous limit, are modeled by first term, which describes a loss of correlation that is too fast to be quantified. In the time domain lineshape function, this

Table 4: Peak parameters related to the assignment of peaks in the 2D-IR spectrum of CO₂ in [Im_{4,1}][TFA] to third-order or fifth-order signal. Pathways are labeled with the non-rephasing coherences they exhibit. Parenthetical coherences are not observed due to the timing of up-pumping (thus, 10—(21)—32 indicates a pathway with observed 2D-IR frequencies of ($\omega_1, \omega_3 = \omega_{01}, \omega_{23}$).

Peak Label	Center (ω_1, ω_3)	Peak Vol. Ratio ⁱⁱⁱ	Sign	Order	Pathway ^{iv}
1a	(2341.5, 2341.5)	2.2 ± 0.01	—	3	10 10 (g.s.b./s.e.)
1b	(2341.5, 2317.5)	2.2 ± 0.02	+	3	10 21 (e.s.a.)
2a	(2329.5, 2329.5)	1.9 ± 0.03	—	3	‘hot’ g.s.b./s.e.
2b	(2329.5, 2305.5)	2.5 ± 0.1	+	3	‘hot’ e.s.a.
21a	(2329.5, 2341.5)	1.7 ± 0.2	—	3	pop. exch.
21b	(2329.5, 2317.5)	2.4 ± 0.04	+	3	pop. exch.
1e	(2317.5, 2317.5)	3.8 ± 0.2	—	5	(10) 21 21
1f	(2317.5, 2293.5)	3.5 ± 0.1	+	5	(10) 21 32
1c	(2341.5, 2293.5)	3.3 ± 0.2	+	5	10 (21) 32
31a	(2317.5, 2341.5)	3.4 ± 0.4	+	5	(10) 21 10

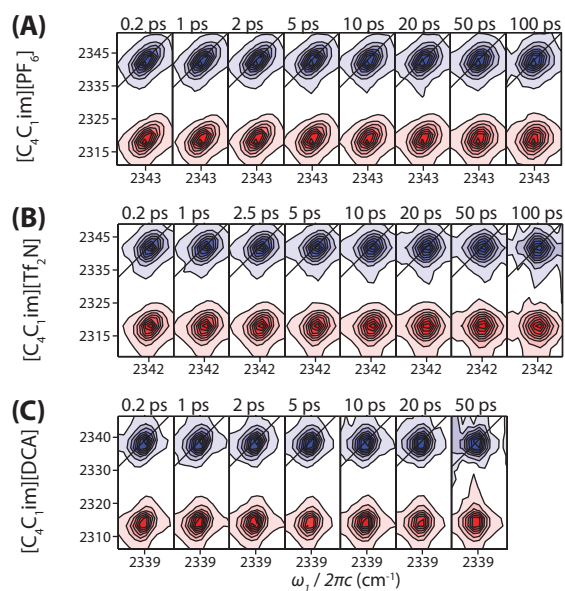


Figure 16: Experimental 2D-IR spectra of CO₂ in [Im_{4,1}] (A) [PF₆], (B) [Tf₂N], and (C) [DCA] show the range of timescales for spectral diffusion in ν_3 . Spectral diffusion results from local structural relaxation around CO₂. Spectral modelling quantifies the timescale of this structural relaxation, and indicates that the timescale varies by up to an order of magnitude between ionic liquid solvents, and that CO₂ dynamics are likely gated by anion dynamics in these ionic liquids. Spectra for CO₂ in other ionic liquids tested can be found in Supplementary Information.

leading term describes exponential decay in the ensemble response from dephasing, (with time constant T_2); the resulting lineshape in frequency space is a Lorentzian with FWHM of $(\pi T_2)^{-1}$.

The second term corresponds to processes in the spectral diffusion regime, which create a Kubo lineshape. In the slow modulation limit (where $\tau_c \Delta \gg 1$), correlations do not change over the timescale of the molecular response. The resulting lineshape function describes a time-domain Gaussian with a variance of Δ^{-2} ; the corresponding lineshape in frequency space is a Gaussian with FWHM of 2.355Δ .

The analytical lineshape function:

$$g(t) = \frac{t}{T_2} + \Delta^2 \tau_c^2 \left[\exp\left(-\frac{t}{\tau_c}\right) + \frac{t}{\tau_c} - 1 \right], \quad (4.12)$$

can be used to calculate 2D spectra. Normalization of spectra before fitting removes any contribution from vibrational or orientational relaxation, which we do not model. A constrained nonlinear optimization algorithm globally fits the calculated spectra to experimental spectra by minimizing the sum of squares difference between the data and calculation. The algorithm optimizes T_2 , τ_c , and Δ , in addition to the central frequency, anharmonicity, the $|00^01\rangle \rightarrow |00^02\rangle$ transition dipole moment, and the phase. The resulting spectral diffusion time, τ_c , shows good agreement with that obtained by center line slope (CLS) analysis (Supporting Information).

Experimental and optimized calculated spectra agree in terms of overall lineshape and rate of spectral diffusion (Figure 17). The resulting lineshape parameters can then be used as input for spectral modelling that treats the shoulders and cross-peaks of the spectrum (Section 4.4.8).

The lineshape parameters (Table 5) for ν_3 , combined with insights from computational modeling of CO_2 -anion-cation clusters, help to refine a physical picture of the solvation environment of CO_2 in ionic liquids. The timescale of frequency fluctuation correlations (τ_c) for CO_2 varies by up to an order of magnitude between the solvents, from 13 ± 3 ps in $[\text{Im}_{4,1}][\text{DCA}]$ to 104 ± 10 ps in $[\text{Im}_{4,1}][\text{PF}_6]$. The inhomogeneous width (Δ) which is largest in PF_6^- and smallest in DCA^- reflects the diversity of local environments reported by CO_2

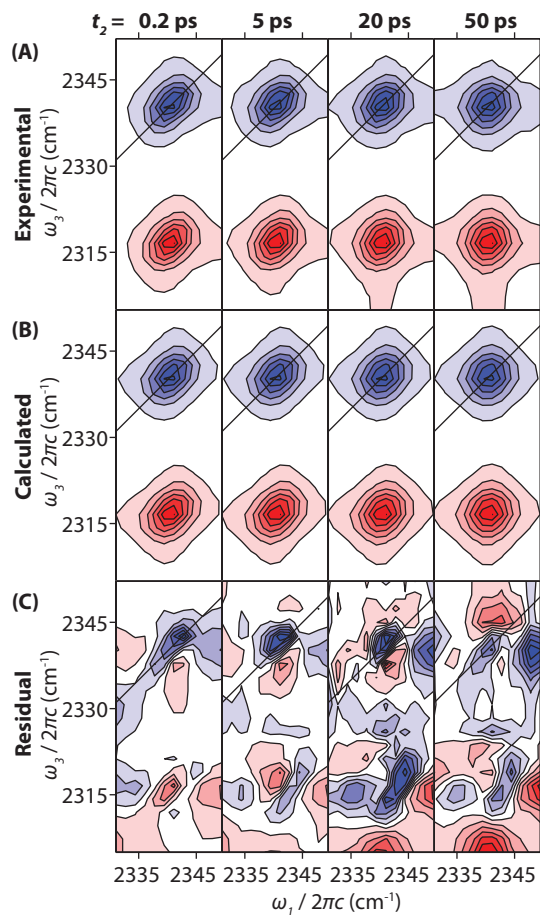


Figure 17: Example of global fitting of spectra. (A) Experimental 2D-IR spectra of CO_2 in $[\text{Im}_{4,1}][\text{TFA}]$. (B) Calculated 2D-IR for ν_3 based on a third-order response function, which is fitted to A by optimizing the correlation time τ_c , frequency range Δ , and dephasing time T_2 , in addition to several other parameters (see text). (C) Residual between the experimental and calculated spectra.

Table 5: Best fit correlation function parameters, by ionic liquid. τ_c indicates the timescale of structural relaxation around CO₂, the inhomogeneous linewidth Δ reflects the range of frequencies experienced by CO₂ in different local environments of each ionic liquid, and the homogeneous dephasing time T_2 arises from fast motions, such as librations, of CO₂.

Anion	Δ (cm ⁻¹)	τ_c (ps)	T_2 (ps)
[PF ₆] ⁻	2.0 ± 0.1	104 ± 10	3.3 ± 0.1
[Tf ₂ N] ⁻	1.6 ± 0.1	26 ± 5	2.8 ± 0.1
[TfO] ⁻	1.7 ± 0.1	25 ± 5	2.7 ± 0.1
[TFA] ⁻	1.8 ± 0.1	40 ± 5	2.6 ± 0.1
[DCA] ⁻	1.6 ± 0.1	13 ± 3	3.2 ± 0.2
[SCN] ⁻	1.8 ± 0.1	16 ± 3	3.4 ± 0.1

in an ionic liquid. The dephasing time (T_2), which varies from 2.6 to 3.4 ps, is longer than typical dephasing times in molecular solvents.

A quantitative analysis based on lineshape theory has allowed us to determine the dynamical timescales, dephasing times, and inhomogeneous linewidths for ν_3 in the six ionic liquids studied.

4.4.8 Modelling of Shoulders and Cross-Peaks

Having quantified the change in shape of the main 2D ν_3 band, we now turn to modelling of the dynamics encoded in the diagonal shoulders and cross-peaks.

Fluctuations in the CO₂ ν_2 population can be described by a thermal equilibrium between n bending modes:

$$|00^00\rangle \xrightleftharpoons[k_r]{k_f} |01^10\rangle \cdots \xrightleftharpoons[k_r'']{k_f''} |0n^l0\rangle \quad (4.13)$$

The rate of transition between the ground and first excited state, k_f , combined with the Boltzmann distribution of states, determines the remaining rates. k_f is ultimately determined by the probability of stochastically gain a quantum of energy in a CO₂ bending mode,

most likely through collisions in the local environment. The first backwards rate, k_r , is directly analogous to the off-equilibrium vibrational energy relaxation rate.

A model that combines probabilistic fluctuations in bending mode population based on Equation 4.13 with standard response function treatment is able to capture the essential physics required for such stochastic hot bands and their cross-peaks. The frequency of the ν_3 mode has two sources of variation: (1) the classical bath of intermolecular modes usually encountered in solvation dynamics and (2) the quantum bath of intramolecular vibrations to which the ν_3 band is coupled. The frequency of the ν_3 mode, $\omega(t)$ fluctuates as

$$\omega(t) = \langle \omega \rangle + \delta\omega_{\text{inter}}(t) + \delta\omega_{\text{intra}}(t). \quad (4.14)$$

This stochastic frequency can be used as an input to standard nonlinear response function formalism. For example, the first order response function

$$R^{(1)}(t) \propto \exp(-i\langle \omega \rangle t) \times \left\langle \exp \left(-i \int_0^t dt' \delta\omega_{\text{inter}}(t') + \delta\omega_{\text{intra}}(t') \right) \right\rangle, \quad (4.15)$$

can be separated into the two parts, assuming the intra- and inter-molecular modes are uncorrelated,

$$R^{(1)}(t) \propto \exp(-i\langle \omega \rangle t) \times \left\langle \exp \left(-i \int_0^t dt' \delta\omega_{\text{inter}}(t') \right) \right\rangle \times \left\langle \exp \left(-i \int_0^t dt'' \delta\omega_{\text{intra}}(t'') \right) \right\rangle. \quad (4.16)$$

The intermolecular component can be treated with the cumulant expansion truncated at second order

$$R^{(1)}(t) \propto \exp(-i\langle \omega \rangle t - g(t)) \times \left\langle \exp \left(-i \int_0^t dt'' \delta\omega_{\text{intra}}(t'') \right) \right\rangle. \quad (4.17)$$

where $g(t)$ is the lineshape function. The extension to third-order response functions is straightforward.

We performed a stochastic simulation in which an ensemble of trajectories was generated by allowing probabilistic instantaneous transitions between the ground and excited states of the ν_2 , with upward and downward rates consistent with the equilibrium populations. These transitions were allowed to happen at any point in the simulation, including during the coherence times.

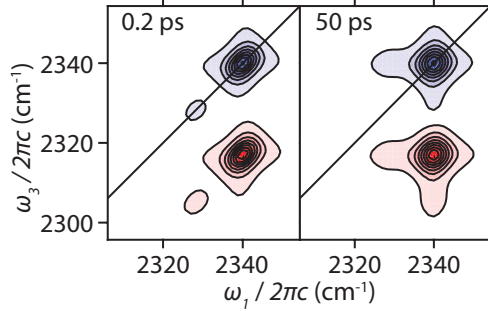


Figure 18: Calculated spectrum of CO₂ in [Im_{4,1}][TFA] at $t_2 = 0.2$ and 50 ps. Spectra are based on a stochastic simulation that allows the bending mode of a particular oscillator to fluctuate over the course of the experiment (while preserving a Boltzmann distribution). The lineshape as a function of t_2 closely approximates the lineshape of the main peak (1a and 2a), first diagonal shoulder (1b and 2b), and cross-peaks (1b,a; 2a,b and 2b,a) in the experimental spectra (Figure 13).

The simulated lineshape is sensitive to the rate of thermal fluctuations in ν_2 . By tuning the rate constant k_f of stochastic fluctuation from the ground state into the first excited state and enforcing detailed balance to preserve equilibrium, we can control (1) whether or not diagonal shoulders will appear, and (2) the kinetics of cross-peak formation. In the limit of fast fluctuations, there are no clearly observed shoulders or cross-peaks, as all three peaks coalesce into a single band. In the limit of slow fluctuations, there are clearly defined shoulders, which persist throughout the experimental timescale, and cross-peaks do not grow into the spectrum. In an intermediate regime, we are able to reproduce both the lineshape and kinetics (Figures 18 and 14) seen in the relative intensities of the first shoulder and the cross-peaks between it and the main peak as functions of population time.

The microscopic rate constant (k_{up}) for CO₂ bending mode fluctuations in [Im_{4,1}][TfO], from the Monte Carlo simulations is estimated to be $k_{\text{up}} = 2.5 \pm 0.1 \text{ ns}^{-1}$. The corresponding down rate, which is analogous to the vibrational relaxation rate in off-equilibrium pump-probe experiments, is estimated to be $k_{\text{down}} = 30 \pm 12 \text{ ns}^{-1}$. The kinetic Monte Carlo simulations include the non-equilibrium pumping that was explained by Fayer et al.²⁷⁵. Their

pump-probe measurements showed an increase in the ground state bleach band due to differences in transition dipole moment between the ground state $|000\rangle$ and the ‘hot’ band $|01^10\rangle$ transition dipole moments. The 2D measurement resolves the excitation frequency, so those dynamics are visible as a separate cross-peaks, where the pump-probe measurement observes the sum of the two peaks (the projection of the spectrum onto the ω_3 -axis). The main ground state bleach decays with bending mode exchange and the cross-peak grows. If the dipoles of the two states are the same these two terms cancel in the pump-probe measurement; however, the differences in dipole lead to effective rises in the pump-probe ground state bleach signal.

4.5 MOLECULAR INTERPRETATION

The resulting molecular picture is that the slower dynamics of the ionic liquid solvent *gate* CO_2 ’s dynamics in solution. The slow timescale (τ_c) arises from structural relaxation of the solvent around CO_2 , and corresponds to the breakup of local ion shells. Until this liberating event, CO_2 is caged in a relatively well-ordered local environment. Librational and other fast motions only sample a narrow range of instantaneous frequencies, but the variation in instantaneous frequency between different local environments gives rise to the inhomogeneous linewidth.

We assign the inhomogeneous width, Δ , to the interactions of the CO_2 with its local ion cage. Because charge transfer drives the distortion of the CO_2 geometry, and the geometry determines the ν_3 frequency, Δ reports the range of local structural motifs that the CO_2 can sample. This range varies from 2 cm^{-1} in $[\text{PF}_6]$ to 1.6 cm^{-1} in $[\text{DCA}]$ (a 20% decrease). Δ is also not strongly correlated to the average frequency shift or other structural parameters, and so we attribute it to the range of structures in the condensed phase.

The inhomogeneous linewidth of CO_2 is the narrowest of the IR probes in recent 2D-IR experiments. Thiocyanate, SCN^- , has a total inhomogeneous linewidth $\Delta_{\text{total}} \sim 8\text{ cm}^{-1}$,⁸¹ heavy water, HOD , $\Delta_{\text{total}} \sim 5\text{ cm}^{-1}$,²⁴¹ and CO_2 $\Delta_{\text{total}} \sim 2\text{ cm}^{-1}$. This trend reflects the strength of the coupling of the vibrational chromophore to its environment. The SCN^-

anion is directly integrated into the ion network and hydrogen-bonded to the imidazolium cation through the 2-position. HOD interacts more weakly with the ionic liquid. It associates primarily with the anion, but it is sensitive to the electric field projected on the OH (or OD) bond axis. Because HOD is dipolar, it still experiences relatively large frequency fluctuations. CO₂ is even more weakly still coupled to its environment. CO₂, which has a quadrupole moment and no dipole moment, is even less influenced by the local electric fields and is sensitive to the more chemical nature of the CO₂-anion-cation interaction.

Similarly, we assign the spectral diffusion time, τ_c , to a local ion cage’s lifetime around CO₂. The observed timescale reflects the time for the ion cage around CO₂ to break up and permit CO₂ to move to a novel local environment. This interpretation is consistent with previous computational work which indicate that the ionic liquid solvent reorients spontaneously to accommodate CO₂ in well-defined locations in the ionic liquid,¹⁷² and with NMR studies showing a well-defined angular distribution of CO₂ around the cation.¹⁸

The bulk viscosity, η , serves as a proxy for this rate of diffusion which we can compare across the anions. Of course, small, neutral molecules like CO₂ experience less friction from the solvent than the viscosity implies.^{174,276} Nevertheless, the linear correlation of bulk viscosity and τ_c ($R^2 = 0.82$) supports our assignment (Figure 19). This correlation further suggests that the motion of the smaller, more mobile CO₂ through the ionic liquid is gated by the motion of the solvent ions.

CO₂ has a Lewis acid-base interaction with the anion of the ionic liquid. Isolated water has possible hydrogen bonds with both the anion and the cation. SCN⁻ has a strong electrostatic attraction to the cation. Thus, all three chromophores have different specific interactions with their ionic liquid solvent. Nevertheless, the correlation times seen in 2D-IR studies of [SCN]⁻ in [Im_{4,1}][Tf₂N]⁸¹ and D₂O/HOD in [Im_{4,1}][PF₆]²⁴¹ follow the same viscosity trend, when you account for the expected $\sim 25\%$ decrease in the viscosity of [Im_{4,1}][PF₆] with $\chi_{\text{H}_2\text{O}} \approx 0.04$.²⁷⁷ This fact suggests that each of these chromophores is reporting on the local diffusive motion of the surrounding solvent, despite the fact that SCN⁻, water, and CO₂ have different specific interactions with the ions in their solvation shells.

Furthermore, recent MD simulations suggest a direct relationship between ion cage lifetime and bulk transport properties such as self-diffusivity and conductivity.³ While diffusivity

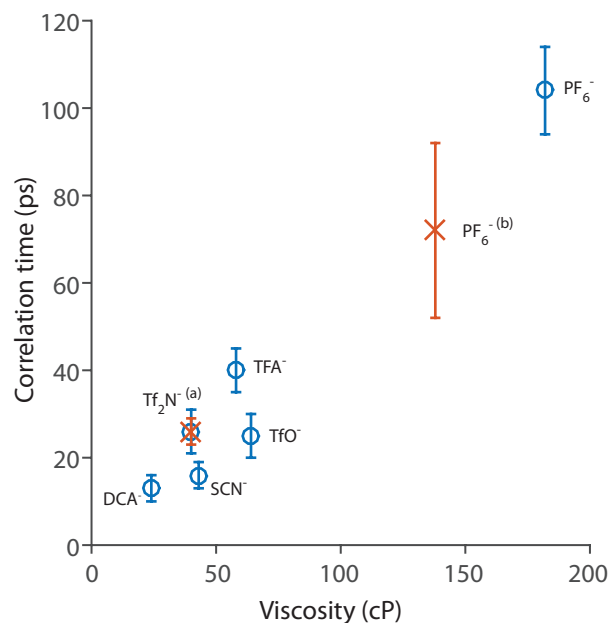


Figure 19: Correlation time, τ_c , compared with viscosity for the 1-butyl-3-methylimidazolium ionic liquid solvent. Data points marked with an ‘O’ are from CO₂ in this work, while those marked ‘X’ are correlation times from other works (a) SCN⁻ in [Im_{4,1}][Tf₂N],⁸¹ (b) HOD in [Im_{4,1}][PF₆],²⁴¹ with ionic liquid viscosity scaled to account for water content.²⁷⁷ Literature values for viscosity were used for all ionic liquids.^{278–280}

of CO₂ and self-diffusivity of an ionic liquid are not identical parameters, the dynamics reported by CO₂ and [SCN]⁻⁸¹ in [Im_{4,1}][Tf₂N] are nearly identical, and both have been related to ion cage lifetime. Thus, it is reasonable to speculate that CO₂ mass transport in these ionic liquids may depend also depend on ion cage lifetime. In this case, the correlation times reported could provide an avenue to directly address the molecular mechanism of CO₂ mass transport in ionic liquids, and might even give insight into other transport properties such as self-diffusivity and conductivity.

The homogeneous dephasing time, T_2 , depends on both the timescale of fast motions for CO₂, τ_H , and on the frequency range experienced during those motions, Δ_H ($T_2 = (\Delta_H^2 \tau_H)^{-1}$). Experimentally, it is impossible to disentangle these two contributions, but the dephasing time (~ 3 ps) is significantly longer than that seen for either HOD (~ 1 ps) or SCN⁻ (~ 1.4 ps) in ionic liquids. Thus, either CO₂ samples a relatively narrow frequency range during its homogeneous motions, or the those motions are particularly fast. Based on the small inhomogeneous linewidth, Δ , and the fact that CO₂ is a small molecule whose moment of inertia (and consequently, the timescale for fast motions such as librations) is unchanged between ionic liquids and molecular solvents, it seems reasonable that the long dephasing time results from a narrow frequency range in a well-defined local environment, rather than a decrease in solvent interactions that slow the molecule.

Furthermore, the computational results show that, in gas phase clusters, CO₂ bends and adopts a distorted equilibrium geometry. In condensed phase dynamics, transitioning from a linear to a bent geometry could be one method of populating an excited state bending mode, and could have a direct impact on k_f , the rate of bending mode transitions. In principle, the spectral diffusion rate should influence the rate of transition between equilibrium geometries, and thus drive excitation and de-excitation of bending modes. Since we are able to model k_f based on equilibrium measurements, a systematic study of ionic liquids with different spectral diffusion rates could experimentally elucidate to how the motions of the solvent around a small molecule influence stochastic fluctuations in bending mode population.

These molecular mechanisms can be both tested and clarified by the comparison of these results to simulation. Frequency mapping techniques, combined with classical molecular dynamics simulations can be used to calculate the IR absorption spectrum and the spectral

diffusion of modes of interest for small molecules such as water,^{68,281,282} nitriles and thiocyanate,^{102,103} and azides^{283,284} in molecular solvents. More recently these methods have been expanded to explore isolated water in imidazolium ionic liquid solvents²⁸⁵, with good agreement with experiment.²⁴¹ Similar approaches for CO₂ could verify the molecular mechanism of CO₂ solvation in ionic liquids. It is likely, given the calculated dependence of ν_3 on CO₂ geometry, that any molecular dynamics simulation would need to account for the geometrical distortion of the CO₂ due to charge transfer, either directly via on-the-fly QM calculations, or with a classical proxy that indirectly accounts for these effects.

These initial studies utilized imidazolium-based ionic liquids because they are commercially available, are “archetypal,” and are relatively well-characterized; thus, they provide a good initial platform on which to develop spectroscopic methods. Many ionic liquids of interest, however, involve either novel classes of anions and cations or chemical modification of existing ionic liquids. The changes in solvent structure and dynamics that result from such modifications are generally *not* well-understood. This type of spectroscopy can provide valuable molecular insights into how and why chemical modification of ionic liquids determines bulk properties of interest, especially CO₂ uptake and local ion mobility (which is related to viscosity and conductivity). Chemisorbing ionic liquids are also of interest, especially for carbon capture applications, and many (1) have an initial physisorption step, and (2) have an equilibrium between physisorbed and chemisorbed (reacted) CO₂. These types of studies could help to elucidate the molecular mechanisms of the equilibrium between CO₂ in its free and bound forms.

4.6 CONCLUSIONS

We have demonstrated that the CO₂ ν_3 mode can act as a probe of local structure and dynamics in imidazolium ionic liquids. This method has potential application to the analysis of structure and dynamics in ionic liquids being developed for CO₂ capture.

The ν_3 frequency is sensitive to the timescale of local structural relaxation in ionic liquids. The timescale of this relaxation, τ_c is determined by spectral modelling using a third-order

response function formalism, with a Bloch-Kubo lineshape. For the imidazolium ionic liquids studied, τ_c varies by as much as an order of magnitude between solvents, and correlates with the viscosity of the ionic liquids. The molecular mechanism posited for this timescale is the breakup of local ion cages around the CO_2 .

Computational studies aid understanding the origin of the ν_3 center frequency shifts in different imidazolium ionic liquids and suggest that geometrical distortion of the CO_2 , driven by charge transfer from the anion into virtual orbitals of CO_2 and from occupied orbitals of CO_2 into virtual orbitals of the cation. A simple one exciton Hamiltonian is able to reproduce the scaled harmonic frequencies with an RMS error of 1.2 cm^{-1} by accounting for dependence of average frequency, α , on total bond length, L , and the coupling constant, β , on magnitude of the angular distortion of CO_2 , θ .

Anharmonic coupling of ν_2 and ν_3 allows thermal fluctuations of ν_2 population to stochastically shift the CO_2 ν_3 by units of -12 cm^{-1} (the coupling constant), and cause the appearance of a shoulder and dynamic cross-peaks on the 2D spectrum. Modelling of the stochastic bending mode population over the timescale of the experiment gives an estimate of the rate of excitation and de-excitation of bending mode population in the condensed phase at thermal equilibrium, estimated to be $k_f = 2.5 \pm 1 \text{ ns}^{-1}$ and $k_r = 30 \pm 12 \text{ ns}^{-1}$. Additional spectral features (the “second shoulder” and apparent “cross-peak” 1c) arise from fifth-order signal.

The molecular picture that arises from this work is one in which imidazolium ionic liquids solvate CO_2 in well-defined local environments. The interactions of CO_2 with its solvent are dominated by local interactions with its nearest neighbor anion and cation. The picosecond dynamics of CO_2 are gated by the slower local diffusive motions of the anion and cation, whose translations and rotations are hindered due to electrostatic friction from surrounding ions, and potentially due to dispersive interactions between nanosegregated alkyl chains.

The methods and analysis developed in this work describe CO_2 in imidazolium ionic liquids. We expect that they will be transferable, however, to broad classes of materials, such as polymers or metal-organic frameworks, as well as to other ionic liquids.

5.0 EUTECTIC IONIC LIQUID MIXTURES AND THEIR EFFECT ON CARBON DIOXIDE

The text in this chapter has been adapted from Ivanova A. S.; Brinzer, T.; Roth E. A.; Kusuma V. A.; Watkins, J. D.; Zhou, X.; Luebke D.; Hopkinson, D.; Washburn, N. R.; Garrett-Roe, S.; and Nulwala, H. B. *RSC Adv.* **2015** *5*, 51407-51412.¹ The author's contribution includes the collecting and analyzing the 2D-IR spectra of CO₂, initially noting the link between changes in CO₂ dynamics and changes in conductivity, and positing a potential molecular mechanism thereof. The author also edited and in some cases re-wrote significant sections of the manuscript.

5.1 CHAPTER SUMMARY

A simple binary system of compounds resembling short-chain versions of popular ionic liquids has been shown to have surprisingly complex properties. Combining methylated versions of pyridinium and pyrrolidinium bis(trifluoromethylsulfonyl)imide gave desirable properties such as low viscosity and high conductivity solubility per unit volume. The binary combinations studied in this study showed that these materials were stable liquids at 50 °C and had a threefold improvement in conductivity over [Im_{6,1}][Tf₂N]. Despite the high densities of these materials, 2D-IR studies indicate increased ion mobility, likely due to the lack of hindering alkyl chains.

¹DOI: 10.1039/c5ra06561e

5.2 INTRODUCTION

Ionic liquids (ILs) have a potential advantage over existing solvents as a green medium due to their wide liquid range, outstanding solvation potential, negligible vapour pressure, thermal stability, and recyclability.^{121,286,287} These properties have prompted their use as lubricants, electrolytes for energy storage, CO₂ capture media, coatings, and fuel cells.^{129,221,288,289} However, the optimization of IL properties for a given application is a challenge. Through skilful manipulation of the IL structures, one can target specific properties such as viscosity, solubility, conductivity, melting point, density, and refractive index.^{121,124,221,290–292} In principle, one can design novel ILs with the exact properties needed, but in practice, this is a daunting goal to achieve.

ILs are complex solvents, whose properties ultimately depend on multiple intermolecular forces, including hydrogen bonding, ionic/charge-charge, dipolar, π - π , n- π , and van der Waals interactions. These interactions are quite complex when compared to simple solvents. Thus, it is difficult to tune the properties of ILs without extensive synthetic manipulation and careful characterization. One simple, alternative route to access specific properties is by creating mixtures of ILs.^{293,294} The properties of IL mixtures have been shown to be distinct from those of the parent compounds and researchers have started to evaluate binary and ternary mixtures.^{191,226,295–298,227,299–301} The mixing of ILs can improve liquid range and compound various properties of the ILs. Ionic materials having melting points over 100 °C have not been extensively studied and there remains an opportunity to further extend their useful properties.²²⁷ The exception is the work of Maximo et al.²²⁷ who have studied the melting behaviour of ionic solids mixtures.

Ionic solids are crystalline materials with high density. Similar to normal salts, these organic solids show eutectic behaviour upon mixing. In our work, various compositions of mixtures combining 1,1-dimethylpyrrolidinium, 1-methylpyridinium and bis-(trifluoromethylsulfonyl)imide ($[\text{C}_1\text{C}_1\text{pyrr}]_x[\text{C}_1\text{pyr}]_{(1-x)}[\text{Tf}_2\text{N}]$ - subscripts indicate the mole fraction), which are crystalline solids at room temperature were studied (Fig. 20). This combination is unusual because it lacks the bulky alkyl chains normally used to disrupt the crystal lattice packing and lower the melting points of traditional ILs. In contrast to Maximo's work, the

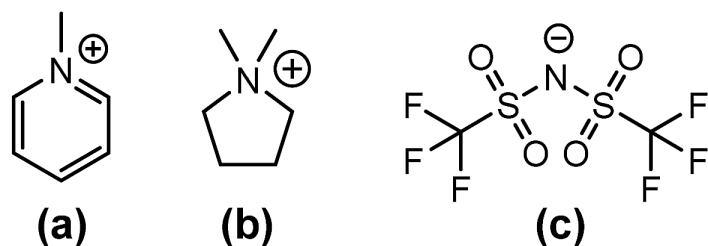


Figure 20: Components of the synthesized novel ionic liquids: (a) 1-methylpyridinium cation $[C_1\text{pyr}]$; (b) 1,1-dimethylpyrrolidinium cation $[C_1C_1\text{pyrr}]$; and (c) bis-(trifluoromethyl-sulfonyl)imide anion $[\text{Tf}_2\text{N}]$.

anion used in this study is elongated.

Typically, ILs rely on molecular asymmetry to disrupt the crystalline ordering of the ions and widen the liquid range.³⁰² With symmetric cations, this effect must be achieved by other means. By combining two cations with different electronic structures or crystal phases, we aimed to introduce defects into the molecular ordering and induce a eutectic effect, resulting in a lower melting point.²⁹⁴ In addition, the shortened alkyl chains should eliminate the problem of tail group domains causing spatial heterogeneity,¹⁶³ potentially increasing the rate of diffusion through the IL and thus improving the kinetics of gas adsorption.¹²⁶ Though gas solubility is known to generally increase with the size and flexibility of ionic structures, for CO_2 the dominant effect is the gas-anion interaction.³⁰³ Finally, the decreased cation size should increase the charge density of the mixture, possibly improving the conductivity. Thus, the combination $[C_1C_1\text{pyrr}]_x[C_1\text{pyr}]_{(1-x)}[\text{Tf}_2\text{N}]$ should result in a low-melting, conductive mixture with good gas solubility, making it widely applicable.

5.3 EXPERIMENTAL

5.3.1 Synthetic Details

[C₁C₁pyrr][I]. Pyridine (8.2 mL, 101 mmol) was stirred into acetonitrile (50 mL) at room temperature in air. The solution was cooled in an ice/water bath while slowly adding methyl iodide (7.6 mL, 121 mmol). The resulting clear yellow solution was allowed to warm to room temperature and stirred for 7.5 hours. Diethyl ether (~40 mL) was added and resulted in the precipitation of a white powder. This product was collected on a fine sintered glass frit and rinsed three times with diethyl ether. A second batch of precipitate was collected from the filtrate and combined with the first. This solid was then dried in vacuo, yielding a white powder with a faint yellow tinge as a crude product (22.16 g, 100 mmol, 99.3%). ¹H NMR (300 MHz, (CD₃)₂SO): δ 9.00 (d, 2H), 8.59 (t, 1H), 8.14 (t, 2H), 4.36 (s, 3H).

[C₁C₁pyrr][Tf₂N]. Lithium bis-(trifluoromethylsulfonyl)imide (31.79 g, 111 mmol) in water (50 mL) was added to a solution of 1-methylpyridinium iodide (22.16 g, 100 mmol) in water (35 mL) at room temperature in air. The resulting mixture of colorless liquid and white precipitate was stirred for 2 hours. Then, the solid product was collected on a fine sintered glass frit and rinsed three times with water. This white powder was then dissolved in ethyl acetate (~50 mL) and washed with an equivalent amount of water, shaking gently to avoid an emulsion. The organic layer was collected and dried with MgSO₄, and then the solvent was removed by rotary evaporation, yielding a white powder (24.41 g, 65.2 mmol, 65.0%). ¹H NMR (300 MHz, (CD₃)₂SO): δ 8.98 (d, 2H), 8.57 (t, 1H), 8.13 (t, 2H), 4.35 (s, 3H). ¹³C NMR (300 MHz, (CD₃)₂SO): δ 146.0, 145.5, 128.1, 119.9 (q), 48.4. ¹⁹F NMR (300 MHz, (CD₃)₂SO): δ 78.7.

[C₁pyr][I]. 1-Methylpyrrolidine (10.4 mL, 99.8 mmol) was added into acetonitrile (50 mL) and stirred at room temperature in air. The solution was cooled in an ice/water bath while slowly adding methyl iodide (7.5 mL, 120 mmol). The resulting cloudy white mixture was allowed to warm to room temperature and stirred for 7.5 hours. Diethyl ether (~50 mL) was added to complete the precipitation. This product was collected on a fine sintered glass frit and rinsed three times with diethyl ether. A second batch of precipitate was collected from

the filtrate and combined with the first. This solid was then dried in vacuo, yielding a white powder with a yellow tinge (20.73 g, 91.3 mmol, 91.5%). ^1H NMR (300 MHz, $(\text{CD}_3)_2\text{SO}$): δ 3.47 (m, 4H), 3.10 (s, 6H), 2.10 (m, 4H).

[C₁pyr][Tf₂N]. Lithium bis[(trifluoromethyl)sulfonyl]imide (31.06 g, 108 mmol) in water (70 mL) was added to a solution of 1,1-methylpyrrolidinium iodide (22.33 g, 98.3 mmol) in water (20 mL) at room temperature in air. The resulting mixture of colorless liquid and white precipitate was stirred for 2 hours. Then, the solid product was collected on a fine sintered glass frit and rinsed three times with water. This white powder was then dissolved in dichloromethane and washed with an equivalent amount of water, shaking gently to avoid an emulsion. The organic layer was collected and dried with MgSO_4 , and then the solvent was removed by rotary evaporation, yielding a white powder (24.85 g, 65.3 mmol, 66.5%).

Note: all compounds were tested with aq. silver nitrate (1 M) solution. No visible silver halide formation was observed.

Further experimental details are provided in Appendix [A.2](#).

5.4 RESULTS AND DISCUSSION

5.4.1 Melting behavior

The melting point and thermal stability of the mixtures were used as an initial screening methodology. The thermal stability was determined using thermogravimetric analysis (TGA) to identify the onset temperature of decomposition for each sample. In all cases, the onset point was above 415 °C with a ramp rate of 10 °C min⁻¹, representing a ~65 °C improvement over typical IL decomposition temperatures. This improvement was due to the removal of alkyl chains, which would normally decompose before the rest of the molecule, mainly due to the presence of alpha and beta protons. The absence of the alkyl chain lengths would also result in higher ionicity and conductivity. The melting points were obtained by differential scanning calorimetry (DSC) using a 10 °C min⁻¹ ramp rate and were plotted to observe the effect of the sample composition on the melting temperature (Fig. [21](#)). We also performed

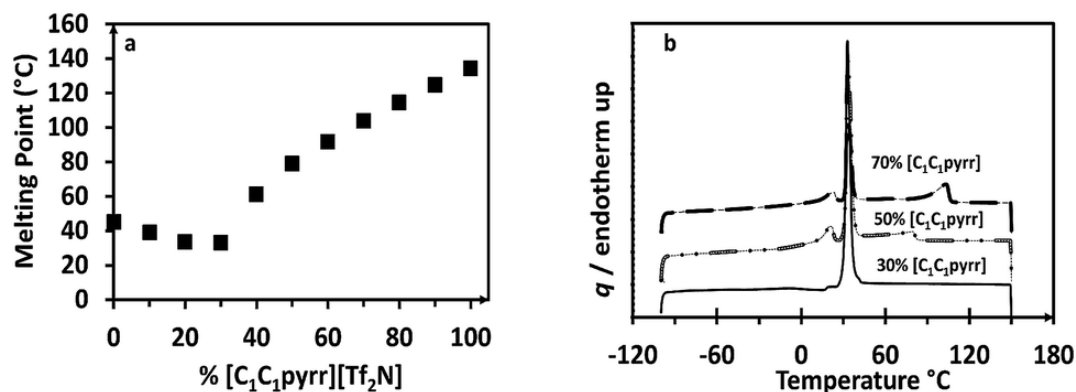


Figure 21: (a) DSC heating curves for $[\text{C}_1\text{C}_1\text{pyrr}]_{0.3}[\text{C}_1\text{pyr}]_{0.7}[\text{Tf}_2\text{N}]$ (solid), $[\text{C}_1\text{C}_1\text{pyrr}]_{0.5}[\text{C}_1\text{pyr}]_{0.5}[\text{Tf}_2\text{N}]$ (short dashes), and $[\text{C}_1\text{C}_1\text{pyrr}]_{0.7}[\text{C}_1\text{pyr}]_{0.3}[\text{Tf}_2\text{N}]$ (long dashes). (b) Melting points for the binary combinations of ILs measured using DSC with a heating rate of $10\text{ }^\circ\text{C min}^{-1}$.

modulated DSC experiments on 3 samples and found no deviation from normal DSC in this case. In cases where multiple peaks were observed, the highest-temperature peak was assumed to be the melting point, ensuring a fully liquid sample. Nevertheless, the multi-phasic behaviour of such samples indicates the potential plastic³⁰⁴ or liquid crystal³⁰⁵ properties and is worth further exploration for electrolytic applications. The lowest melting point of the combinations was observed for $[\text{C}_1\text{C}_1\text{pyrr}]_{0.3}[\text{C}_1\text{pyr}]_{0.7}[\text{Tf}_2\text{N}]$, which exhibits a shallow eutectic point of $33.0\text{ }^\circ\text{C}$. In total, four samples ranging from 0%-30% $[\text{C}_1\text{C}_1\text{pyrr}][\text{Tf}_2\text{N}]$ were completely liquid below $50\text{ }^\circ\text{C}$. We focused on analysing the CO_2 capture properties of these low-melting candidates.

Interestingly, the pyridinium parent compound and several of the binary combinations exhibit a strong supercooling effect, with crystallization occurring at as much as $60\text{ }^\circ\text{C}$ below the melting temperature. These samples were meta-stable liquids at room temperature unless crystallization was seeded or initiated through mechanical forces, at which point rapid crystallization was observed. Such behaviour suggests a kinetically hindered nucleation step in the pyridinium compound, possibly exacerbated in the mixtures due to the complex stacking interactions of multiple cations.

Table 6: Data summary for eutectic IL samples compared to [Im_{6,1}][Tf₂N].

	[Im _{6,1}][Tf ₂ N]	[C ₁ pyr][Tf ₂ N]	% [C ₁ C ₁ pyrr][Tf ₂ N]		
			10	20	30
T_m , °C	-7 (ref. 9)	45	39	34	33
η^{ii} , mPa s	25 (ref. 9)	23.9	24.7	25.1	26.2
ρ^{iii} , g ³ cm ⁻¹	1.35 (ref. 9)	1.58	1.57	1.55	1.54
k_{H}^{iv} (atm)	46.8	66.5	52.3	47.6	51.7
κ^{v} (mSv cm ⁻¹)	4.07	—	11.2	12.2	11.9
C_p^{vi} (J mol ⁻¹ K ⁻¹)	604 (ref. 18)	434	454	462	463

5.4.2 Viscosity

Low viscosity of the IL is responsible for enhancing the kinetics in gas capture and reaction media. Viscosities were measured at 50 °C for the low-melting samples (Table 6). 1-Hexyl-3-methylimidazolium bis(trifluoromethylsulfonyl)imide or [Im_{6,1}][Tf₂N] was used as a baseline standard for the efficacy of other ILs^{191,306,307} and has been selected as a reference ionic liquid for an IUPAC experimental validation project. It has a melting point of -7 °C.²⁹⁷ At 50 °C, the viscosity of [Im_{6,1}][Tf₂N] is 26 mPa s, which is higher than most of our low-melting candidates at 50 °C. Though the melting temperature steadily decreases from 0%-30% [C₁C₁pyrr][Tf₂N], the viscosity increases along the series. This unexpected trend suggests that the individual components are more important in determining the viscosity than the proximity of measuring temperature to the melting point.

5.4.3 CO₂ Uptake and Density

The densities of the samples at 50 °C are all significantly above those of [Im_{6,1}][Tf₂N], as expected for a system involving small, symmetrical cations and lacking alkyl chains (Table 6). A slight decrease in density as the fraction of [C₁C₁pyrr][Tf₂N] increases was noted, which can be explained by the increased proportion of pyrrolidinium cations interfering with

the orderly stacking.

Intuitively, a high density should lower free volume and reduce CO₂ uptake.³⁰⁸ We find, however, that increase in ionic concentration improves the CO₂ solubility of the overall system per unit volume. The CO₂ solubility of the IL mixtures was evaluated by equilibrating each liquid under varying pressures of CO₂ gas at 50 °C and measuring the amount absorbed. These results were then fitted to a polynomial curve and interpolated to account for the variance in pressure during the measurements. The results indicate that on the practical basis of moles of CO₂ per volume of IL mixture, the [C₁C₁pyrr]_{0.2}[C₁pyr]_{0.8}[Tf₂N] showed comparable absorbance of CO₂ to [Im_{6,1}][Tf₂N] at low pressures and up to 8% higher at elevated pressures (Fig. 22), which makes it more applicable for warm gas purification. It is suspected short alkyl chains increase the overall ionic nature of the system, improving the CO₂ solubility per unit volume. Such increased CO₂ solubility is promising for future trials with mixed systems of truncated cations.

5.4.4 Heat Capacity

For applications that involve heating the ionic liquid, the heat capacity at constant pressure (C_p) determines how much energy will be required. The samples' heat capacities were measured using DSC at three different temperatures (Fig. 23). The heat capacities range from 430 to 620 J mol⁻¹ K⁻¹, with some fluctuation in the general upwards trend with increasing [C₁C₁pyrr][Tf₂N] content. Overall, the heat capacities are lower than that of [Im_{6,1}][Tf₂N] most likely due to the fewer intramolecular degrees of freedom in the smaller ionic mixtures.

5.4.5 Conductivity

The electrical conductivity of IL compounds determines their usefulness in electrochemical applications. The three binary combinations (10%-30% [C₁C₁pyrr][Tf₂N]) that were stable liquids at 50 °C were measured for conductivity at this temperature. The results ranged from 11.2 to 12.2 mSv cm⁻¹, which is a three-fold improvement over [Im_{6,1}][Tf₂N]'s conductivity of 4.1 mSv cm⁻¹ (Table 6). This could be partially due to the increased charge per unit volume that results from smaller cations, but the significant boost suggests other mechanisms are

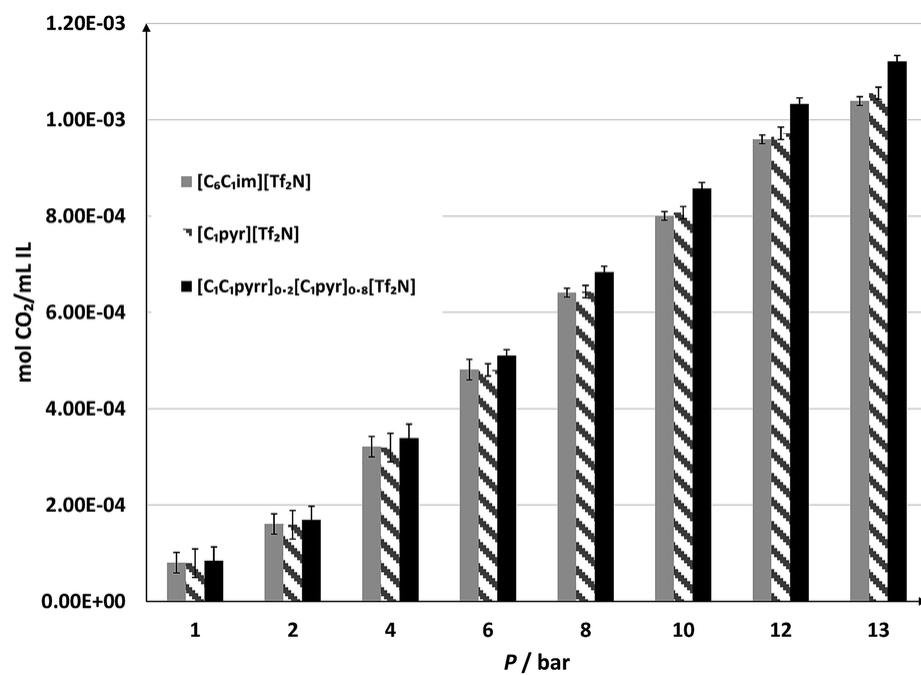


Figure 22: CO₂ sorption of [Im_{6,1}][Tf₂N],³⁰⁹ [C₁pyr][Tf₂N] and the best-absorbing binary mixture measured at 50 °C and various pressures, interpolated from the experimental data. Sorption is shown as moles CO₂ absorbed by a given starting volume of ionic liquid.

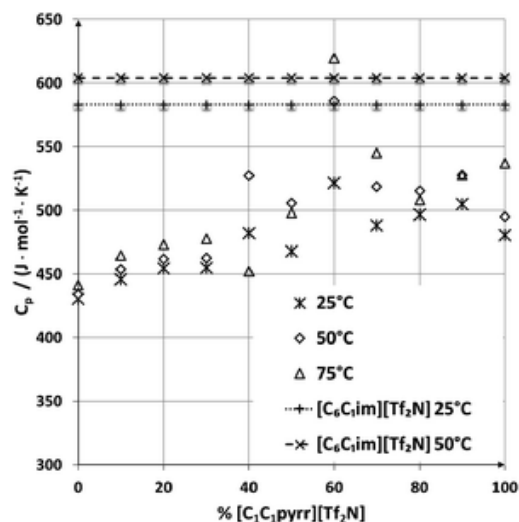


Figure 23: The heat capacities for all samples measured at 25, 50 and 75 °C. Data for $[\text{Im}_{6,1}][\text{Tf}_2\text{N}]$ at 25 and 50 °C is shown for comparison.²⁹⁷ Error bars are omitted for clarity (error = 1%).

at work as well. An alternate explanation for the increase in conductivity may be the inability of this system to form any ionic liquid aggregates and nano-domains^{302,310} due to the lack of hydrocarbon chains. Their high conductivity makes these binary mixtures potential candidates for electrochemical applications.

Two properties of these novel ionic liquid mixtures are particularly interesting. First, the conductivity is nearly three times that of $[\text{Im}_{6,1}][\text{Tf}_2\text{N}]$ even though the dynamic viscosity is the same within 5%. Second, the solubility of CO_2 is comparable between the mixtures and $[\text{Im}_{6,1}][\text{Tf}_2\text{N}]$, despite a 15% increase in density.

5.4.6 Molecular insights via 2D-IR spectroscopy

To gain a better understanding of the microscopic causes of these macroscopic observations, we used 2D-IR spectroscopy to probe the picosecond dynamics of the mixtures compared with $[\text{Im}_{6,1}][\text{Tf}_2\text{N}]$. 2D-IR spectroscopy is a coherent vibrational spectroscopy, which is analogous to 2D NMR spectroscopy. Where 2D NMR correlates nuclear spins, 2D-IR correlates

molecular vibrational frequencies. The 2D-IR line shape encodes the rate at which the local environment changes around a molecule.

Not all molecular vibrations are sufficiently intense to observe in a 2D-IR spectrum; CO₂, however, is an ideal vibrational chromophore for 2D-IR in ionic liquids.³¹¹ The vibrational spectrum of the CO₂ asymmetric stretch depends on local intermolecular interactions such as electrostatic, charge transfer, and hydrogen bonding.

We used the CO₂ asymmetric stretch as a probe for 2D-IR spectroscopy to investigate the differences in the local environment experienced by CO₂ in both [C₁C₁pyrr]_{0.3}[C₁pyr]_{0.7}[Tf₂N] and [Im_{6,1}][Tf₂N] (Fig. 24). While this experiment has direct motivation from the potential use of these novel ionic liquids for carbon capture, this molecular probe also allowed us to investigate the local motions of the cation and anion, which are important for understanding the differences in conductivity between the ILs, and which CO₂ does not greatly disrupt. The microscopic dynamics in the two ILs are markedly different. Spectra of the CO₂ asymmetric stretch in both ILs start to elongate in the diagonal direction (Fig. 24A and D), which indicates a distribution of local environments. At 5 ps, the 2D-IR spectrum of [C₁C₁pyrr]_{0.3}[C₁pyr]_{0.7}[Tf₂N] becomes round, indicating that the environment around the CO₂ molecule was randomized (Fig. 24B), whereas the 2D-IR spectrum of [Im_{6,1}][Tf₂N] retains some diagonal character (Fig. 24E), indicating that the environment around the CO₂ molecules remains similar. In [Im_{6,1}][Tf₂N], the spectrum becomes round at a 50 ps time scale (Fig. 24F).

This qualitative picture can be quantified by non-linear least squares fitting of the spectra to third-order response functions.³¹¹ The three important parameters from the analysis are the dephasing time (T_2), which controls the anti-diagonal width of the spectra; the inhomogeneous width (Δ), which controls the diagonal width of the spectra; and the spectral diffusion time (τ_c), which controls the rate of change of shape of the spectra. T_2 is related to fast local motions such as hindered rotations (librations), Δ is related to the distribution of different environments, and τ_c is the time scale for relaxation of those initial environments. In [C₁C₁pyrr]_{0.3}[C₁pyr]_{0.7}[Tf₂N], CO₂ shows a marked decrease in τ_c and an increase in T_2 compared with that seen in [Im_{6,1}][Tf₂N]. The difference in τ_c we attributed to differences in the rotational ease of the ions of CO₂'s first solvent shell. The increased dephasing time,

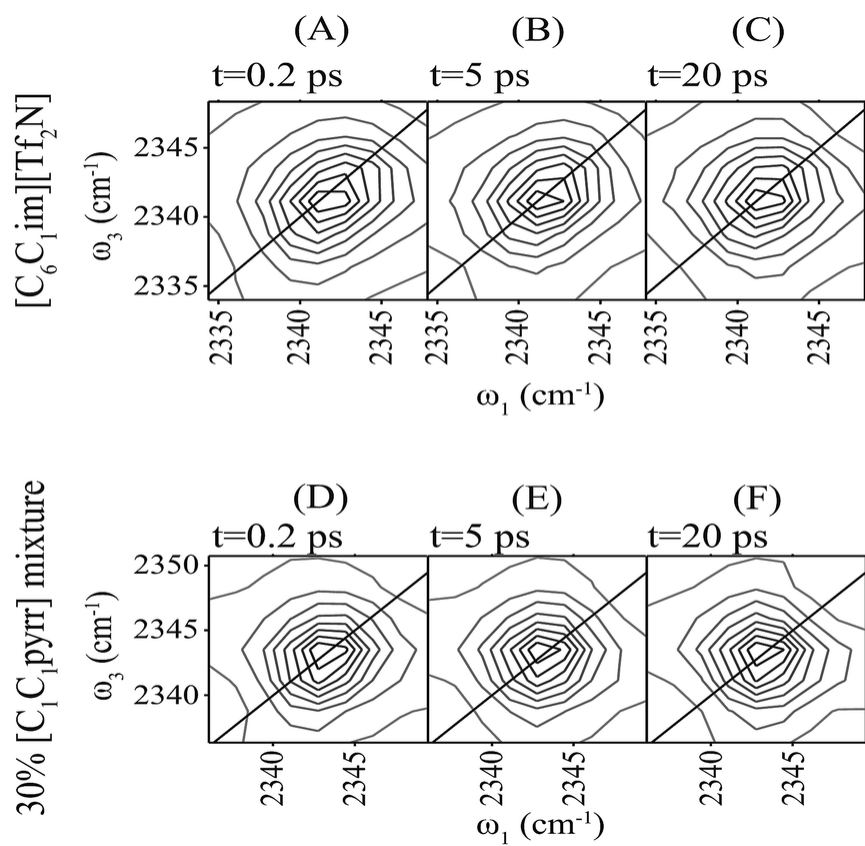


Figure 24: 2D-IR spectra of the CO₂ anti-symmetric stretch in [Im_{6,1}][Tf₂N] and in [C₁C₁pyrr]_{0.3}[C₁pyr]_{0.7}[Tf₂N].

Table 7: A comparison of the best fit parameters for solvation dynamics of CO₂ in [Im_{6,1}][Tf₂N] and [C₁C₁pyrr]_{0.3}[C₁pyr]_{0.7}[Tf₂N] from 2D-IR spectral fitting

Sample	Δ (cm ⁻¹)	τ_c (ps)	T_2 (ps)
[Im _{6,1}][Tf ₂ N]	1.4 ± 0.1	47 ± 9	2.4 ± 0.03
[C ₁ C ₁ pyrr] _{0.3} [C ₁ pyr] _{0.7} [Tf ₂ N]	1.5 ± 0.1	6 ± 2	3.0 ± 0.2

T_2 , likely results from a narrower distribution of CO₂ frequencies during homogeneous motions, perhaps due to the loss of largely uncharged hexyl chains in the first solvation shell of [C₁C₁pyrr]_{0.3}[C₁pyr]_{0.7}[Tf₂N]. Δ is similar for the two ILs (Table 7).

The most striking spectroscopic difference is the eight-fold decrease in τ_c between CO₂ in [Im_{6,1}][Tf₂N] and [C₁pyr]_{0.7}[C₁C₁pyrr]_{0.3}[Tf₂N]. Previous work has identified that, in a range of imidazolium ionic liquids, τ_c for CO₂ is correlated to the solvent viscosity.³¹¹ CO₂ in [Im_{6,1}][Tf₂N], as expected, falls on this trend line. The IL mixture, however, despite a similar viscosity, shows considerably faster relaxation of the local structure around CO₂, as evidenced by τ_c . We hypothesize that the removal of hexyl chains in the novel mixtures removes the steric hindrance to rotational motions of the cation. Therefore, CO₂ can move relatively quickly between different local environments.

This spectroscopic finding also provides insight into a possible molecular mechanism for the increased conductivity seen in [C₁pyr]_{0.7}[C₁C₁pyrr]_{0.3}[Tf₂N] compared to [Im_{6,1}][Tf₂N]. Under an external potential, the decreased energy barrier to solvent reorientation, as described above, should allow easier molecular reorientation to permit ion transport and thus conduction. This effect, combined with decreased intermolecular friction due to the lack of bulky alkyl chains, and increased charge density (due to decreased IL molar volume), provide a plausible explanation for the increased conductivity. It may be possible to exploit combinations of these mechanisms to guide the design of ionic liquids with high conductivity for electrochemical applications.

5.5 CONCLUSIONS

By mixing two dissimilar cations with shortened alkyl chains, useful properties can be accessed and tuned. Mixing the two compounds increases the mobility of the cation, which leads to greatly increased conductivity that is promising for electrochemical applications. The removal of the hexyl chain also decreases the heat capacity of the IL, which can be important for variety of thermal applications. Despite an increase in density, the CO₂ solubility of the novel compounds and mixtures remains comparable to that of [Im_{6,1}][Tf₂N] and the best mixture depresses the melting point below 35 °C. The melting point and CO₂ solubility can likely be improved with further experimentation. This approach shows promise as a general strategy to inexpensively optimize the properties of ionic liquids by mixing simple salts, rather than the complicated synthesis of new ILs.

5.6 ACKNOWLEDGMENTS

This research was supported by the U.S. Department of Energy's National Energy Technology Laboratory under the contract DE-FE0004000. Part of this work was also supported by ACS PRF Award # 53936-DNI6.

6.0 FREQUENCY AND ROTATIONAL DYNAMICS OF CO₂ IN 1-BUTYL-3-METHYLIMIDAZOLIUM BIS-(TRIFLUOROMETHYLSULFONYL)IMIDE

The text in this chapter has been adapted from a manuscript in preparation. The author's contributions include writing much of the manuscript, performing all experimental work, and interpreting frequency and orientational correlation function results.

6.1 INTRODUCTION

The rising concentration of CO₂ in the atmosphere due to human activities is predicted to have long lasting negative effects on the environment. Post-combustion carbon capture and sequestration is one technique for controlling carbon emissions from fossil fuel energy sources that has received a great deal of attention. In this method, a CO₂ sorbent is used to absorb, transport, and then desorb CO₂, effectively recycling the sorbent. Due to the combination of chemical tunability and relatively high CO₂ sorption capacity, ionic liquids are potential next-generation sorbents for carbon capture. They may also have use, for the same reasons, in the "sweetening" of natural gas.^{17,122,312,313} The combination of high CO₂ solubility with negligible volatility also points to the potential use of ionic liquids in extractions with supercritical CO₂,^{180,187,314} or in CO₂/IL multiphase catalysis.^{286,315,316}

In each of these systems, the interactions of carbon dioxide with the anion and cation in the ionic liquid ultimately determines many of the static and dynamical properties of the system, and the viability of the specific ionic liquid for each purpose. In physisorbing ionic liquids, the CO₂-IL interaction depends most strongly on the anion, due to a Lewis acid-

base interaction between the electronic deficient central carbon of CO₂ and the electron rich anion.¹¹³ There are additional, weaker interactions with the cation, in particular a moderate interaction with the cation tail, as well as potential interactions between the π -system of aromatic cations and CO₂.¹² Many insightful thermodynamic,^{173,188,191,317,318} spectroscopic,^{18,186,187,243,275,311,319–322} and computational studies^{12,15,172,175,176,323–325} have helped to elucidate the physics and chemistry of CO₂ sorption and solvation in ionic liquids, although sometimes with apparently conflicting results. Experimental studies have provided valuable insights; however, connecting them directly to molecular interactions can at times be challenging. Computational studies offer unparalleled insights into molecular mechanisms; however, they must often be compared with bulk experimental properties. Direct comparison with experiment can be challenging. An ideal situation would enable the comparison of experimental data that reported on molecular length scales and femtosecond time scales (the length and time scales of computation) directly with results from computational simulations of CO₂ and ionic liquids.

Ultrafast vibrational spectroscopy provides dynamical data on the requisite femtosecond to picosecond timescale,^{72,197,239} and can depend on the local solvation environment of small molecular probes. For CO₂ in an ionic liquid, the resultant spectral dynamics depend intimately on the transient interactions of the CO₂ molecule with the ions in its local environment at equilibrium. These dynamics are in principle directly comparable to those extracted from computational simulations.

Several simulation methods, including *ab initio* molecular dynamics (AIMD) simulations, can be used to calculate the vibrational spectra of soft condensed phase systems, such as ionic liquids. AIMD has several advantages, especially for systems that might be expected to undergo a chemical reaction;¹² however, the cost of performing a QM calculation at each step precludes the facile investigation of long time dynamics in ionic liquid systems, which relax very slowly.

A purely classical simulation enables the calculation of long time trajectories in ionic liquids (1 μ s in the current study), which are necessary to fully resolve the slow dynamics in ionic liquids, which take place on a timescale of several nanoseconds in room temperature ionic liquids.^{249,326} Such a simulation contains information on the low frequency spectral

density that modulates the time-dependent transition energy of CO₂ through its solvent-perturbed potential energy surface, but does not directly report on high frequency vibrational modes.

Development of a spectroscopic map for a vibrational probe molecule, like CO₂, allows for the calculation of its vibrational frequency at every time step of a classical simulation through parameterization of the quantum mechanical frequency to classical observables. Such maps thus allow the simulation of long time trajectories of high frequency solute vibrational modes in ionic liquids, which can then fully resolve the vibrational frequency dynamics, and can be directly compared with the frequency dynamics extracted from ultrafast experimental studies.^{103,327–330}

Motivated by the desire to more deeply understand the physical mechanism of CO₂ solvation and dynamics, we have set out to develop, validate, and apply a spectroscopic map that linked the frequency fluctuation dynamics of CO₂'s antisymmetric stretching mode (ν_3) with its local environment in an ionic liquid. Part I of this study¹⁰ developed quantum mechanical and molecular mechanical (QM/MM) protocols to calculate accurate anharmonic vibrational frequencies of the CO₂ antisymmetric stretching mode (ν_3) in the physically absorbing (i.e. non-reactive) ionic liquid 1-butyl-3-methylimidazolium hexafluorophosphate ([Im_{4,1}][PF₆]). Part II¹⁰⁷ used these protocols to develop and validate a semi-empirical spectroscopic map for the CO₂ ν_3 frequency in the same ionic liquid. This spectroscopic map provides an approximation for the CO₂ ν_3 frequency, which normally must be calculated quantum mechanically, at each time step of a purely classical simulation using knowledge of the forces between the ionic liquid and the solute.

This study (part III) focuses on comparison of the results from using the newly developed spectroscopic map with classical MD simulations to experimental results from polarization controlled pump-probe and 2D-IR spectroscopies. We first compare the experimental linear FTIR spectrum with the spectrum from simulation (calculated directly using the fluctuating frequency approximation). We then compare both the reorientational and frequency dynamics of carbon dioxide from ultrafast infrared spectroscopy experiments and MD simulation. Finally, we decompose³³¹ the simulated spectral diffusion into components arising from important moieties in the ionic liquid (cation ring, cation tail, and anion components),

and relate this to the structure and dynamics of the liquid.

6.2 METHODS

6.2.1 Experimental Methods

The ionic liquid 1-butyl-3-methylimidazolium hexafluorophosphate ($[\text{Im}_{4,1}][\text{PF}_6]$) (IoLiTec, 99% purity) was used without further purification. It was kept in a glove box prior to use, and was further dried at 50 °C using a rotary vane vacuum pump (<10 mTorr) for approximately 3 hours prior to experiments. Carbon dioxide (99.8% purity, Matheson TriGas) was loaded using an airtight glass vial into the ionic liquid samples prior to experiments.

FTIR spectra were obtained using a Nicolet 6700 FTIR spectrometer (ThermoFisher Scientific). FTIR sample cells consisted of an aliquot of the CO₂-loaded ionic liquid sample sandwiched between two 2 mm thick CaF₂ windows. The windows were separated by a 25 μm PTFE spacer and housed in a brass cell. The sample cells were assembled in a nitrogen-purged glove bag to limit contamination with atmospheric water.

The optical parametric amplifier²⁰⁴ and 2D-IR spectrometer²⁰⁵ setup have previously been described in detail. The OPA was used to convert the output of a commercial chirped-pulse amplification Ti:Sapphire laser (Coherent Legend Elite) into the ~100 fs pulses of 4.3 μm light used for ultrafast IR experiments. Polarization control of the mid-infrared pump pulses was accomplished using a $\lambda/2$ mid-IR waveplate and wire grid polarizer combination. 2D-IR spectra were obtained at the magic angle condition for pump light (54.74°) IR pump-IR probe spectra were obtained in parallel and perpendicular polarizations by setting the waveplate to rotate the optical polarization by 45°, and collecting each spectrum with the polarizer at 0° (parallel) and 90° (perpendicular) positions.

6.2.2 Simulation Methods

6.2.2.1 MD Simulations Simulations were performed using the same methods and force fields as in the previous report,¹⁰⁷ excepting that CO₂ was held rigid throughout using the Large-scale Atomic/Molecular Massively Parallel Simulator (LAMMPS) rigid fix.^{107,332} Initial positions and velocities for 256 ions pairs of [Im_{4,1}[PF₆]] and a single CO₂ molecule were taken from a prior simulation that had been used to create a spectroscopic map.^{10,107} Prior to performing the MD simulations that were analyzed for frequency trajectories, the system was subjected to the following equilibration procedure: 1 ns in the NVT ensemble at 300 K, 1 ns raising the temperature to 600 K, 1 ns lowering the temperature to 300 K, 1 ns in the canonical (NVT) ensemble at 300 K, and 1 ns in the microcanonical (NVE) ensemble. This procedure breaks up long-lived ion cages and results in decorrelation of atomic positions and velocities from the starting sample. The simulation was then run in NVE for 10 ns, generating one set of initial conditions for production simulations each 1 ns. Each set of initial conditions was again subjected to the same equilibration procedure as above. This ensures that each final NVE trajectory is distinct from the generation simulation trajectory. Each of these ten simulations was run in the NVE ensemble for 100 ns, for a total of 1 μs of simulation data.

6.2.2.2 Vibrational Frequency Calculations The CO₂ asymmetric stretching mode (ν_3) vibrational frequency was calculated every 4 fs, using the previously developed empirical spectroscopic map¹⁰⁷ of the form:

$$\omega_a = \omega_g + \langle \Delta\omega_\theta \rangle + b_1 E_O^{\text{cation}} + b_2 E_O^{\text{anion}} + c_1 U_O + c_2 U_C \quad (6.1)$$

where ω_g is the experimental gas phase frequency, and E and U are the weighted electric field and Lennard-Jones interactions with the solvent. The average angular contribution ($\langle \Delta\omega_\theta \rangle$) red-shifts the frequency distribution from that of a rigid CO₂ molecule by 2.7 cm⁻¹.¹⁰⁷ This value was used as a fixed parameter in the spectroscopic map for this work, as the MD simulations were run with rigid CO₂.

FTIR spectra were calculated using the fluctuating frequency approximation (FFA).³³³

$$I(\omega) = \int_0^\infty dt \exp(i\omega t) \langle \vec{\mu}_{01}(t) \cdot \vec{\mu}_{01}(0) \exp\left(-i \int_0^t d\tau \delta\omega(\tau)\right) \rangle \exp(-t(2T_1)^{-1}) \quad (6.2)$$

The FFA includes dynamical effects such as inhomogeneous broadening and motional narrowing ($\exp\left(-i \int_0^t d\tau \delta\omega(\tau)\right)$). It also includes rotational broadening and non-Condon effects through the transition dipole terms ($\vec{\mu}_{01}(t)$), and lifetime broadening through the exponential decay in T_1 . T_1 , the vibrational population lifetime, is taken from experiment. Because the transition dipole moment of CO₂ is independent of frequency, $\vec{\mu}_{01}(t)$ was taken to be a normalized CO bond vector.

The two-point frequency fluctuation correlation function (FFCF) has the form of the vibrational frequency autocorrelation function

$$C_\omega(t) = \frac{\langle \delta\omega(t)\delta\omega(0) \rangle}{\langle \delta\omega(0)\delta\omega(0) \rangle} \quad (6.3)$$

where $\delta\omega(t) \equiv \omega(t) - \langle \omega \rangle$ is the instantaneous difference between the vibrational frequency and its ensemble average. The correlation function was calculated as the average of the correlation function from each of the 100 ns production runs, in order to decrease the total time of simulation by running in parallel. The instantaneous standard error for all final average FFCFs was less than 2% at all times.

6.3 RESULTS AND DISCUSSION

6.3.1 Linear Spectrum

The experimental FTIR spectrum of the CO₂ asymmetric stretching mode in [Im_{4,1}][PF₆] (Figure 25) shows a main peak near 2342.5 cm⁻¹, in a spectrally clear region, with a full width at half maximum of 6.2 cm⁻¹. The main line appears nearly Lorentzian; however, it is not completely motionally narrowed. There is a low frequency shoulder (ν'_3) that arises from anharmonic coupling of the stretching (ν_3) and degenerate bending (ν_2) modes. This coupling causes a 12 cm⁻¹ decrease in the stretching mode transition frequency when the bending

Table 8: Central frequency (ω_0) and FWHM for the CO₂ asymmetric stretch in [Im_{4,1}][PF₆]. Here, ν_3 refers to transitions arising from the ground vibrational state $|00^00\rangle$, while ν_3' refers to transitions with starting from the ground state stretching mode with a thermally populated bending mode $|01^10\rangle$.

	FWHM (cm ⁻¹)	ω_0 (cm ⁻¹)
ν_3	6.2	2342.5
ν_3^i	6.2	2330
ν_3 (computation)	2.9	2345.7
ν_3' (computation)	N/A	N/A

mode is in its thermally populated first excited state.³¹¹ The linewidth of the shoulder is comparable to that of the main band (6.2 cm⁻¹), based on fitting with a Voigt profile (Table 8). Compared with other 1-butyl-3-methylimidazolium ionic liquids previously tested,³¹¹ CO₂'s asymmetric stretching mode is relatively blue shifted in [Im_{4,1}][PF₆].

The linear infrared CO₂ asymmetric stretching mode spectrum was also calculated from the MD simulation using the fluctuating frequency approximation (Equation 6.2).³³³ Since the molecular dynamics simulation uses “rigid” CO₂, it does not reproduce the shoulder (ν_3'), as this requires a thermally populated bending mode that can stochastically transition during the experiment.³¹¹ Using a flexible CO₂ also does not reproduce the low frequency shoulder, and leads to unphysical oscillations in the calculated FFCF and distortions of the peak shape;¹⁰⁷ therefore, calculation focused on comparison with the main ν_3 band.

The simulated spectrum's center frequency of 2345.73 cm⁻¹ agrees well with that of the experiment. The line is, however, narrower than the experimental line, with a FWHM of only 2.9 cm⁻¹ (Table 8). The calculated peak is symmetric, as is the experimental lineshape (Figure 25B).

The FFA correctly includes dynamical effects such as motional narrowing, inhomogeneous broadening, and rotational broadening. The vibrational population lifetime (T_1) was assumed to be 58 ps, based on experimental results. Due to the large T_1 time, there is not

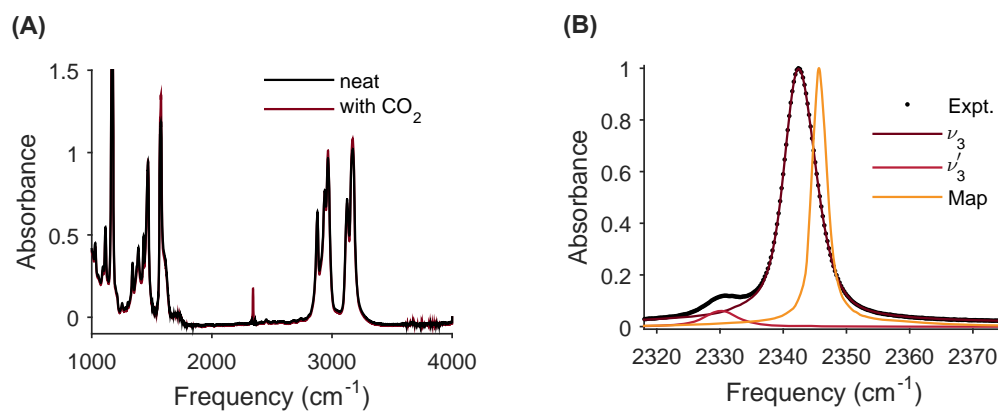


Figure 25: The CO₂ antisymmetric stretch comprises a main peak from the ground vibrational state (ν_3) and a low frequency shoulder from anharmonic stretch-bend coupling (ν'_3). **(A)** The FTIR spectrum of [Im_{4,1}][PF₆] with and without CO₂. The sharp CO₂ antisymmetric stretching mode lies in a spectrally clear region. **(B)** The solvent-subtracted spectrum shows the CO₂ antisymmetric stretch, including both the main band and the “hot” ν'_3 shoulder. The computed “rigid” CO₂ spectrum captures the overall shape and central frequency of the ν_3 mode, but underestimates the linewidth.

a significant effect on the lineshape from lifetime broadening. The narrowness of the band compared with the experimental spectrum most likely results from the underestimate of width of the instantaneous frequency distribution compared with experiment;¹⁰⁷ however, we expect that the frequency dynamics will correctly qualitatively model those experienced by CO₂ experimentally.

6.3.2 Orientational and Population Dynamics

The ultrafast orientational dynamics of carbon dioxide can be assessed both experimentally and computationally. Experimentally, the orientational correlation function, as well as the population relaxation, can be determined from polarization-controlled pump-probe measurements. Computationally, the orientational correlation function for CO₂ can be computed directly from MD trajectories.

The ultrafast IR pump-probe spectrum shows the change in absorbance (ΔA) of a vibrational band when it is perturbed by an initial pump pulse. The transient absorption signal decays with orientational relaxation of the initial anisotropic distribution of vibrators excited by the laser pulse back to the overall orientational distribution in the liquid (normally an isotropic distribution). The signal also decays with population relaxation back to the ground state.

The all-parallel polarization (ZZZZ) pump-probe signal of CO₂ in [Im_{4,1}][PF₆] decays on a several-hundred picosecond time scale (Figure 26). The pump-probe spectrum has a negative peak from transient depletion of the ground state (g.s.b.) and a positive peak from absorption out of the excited state (e.s.a.) (Figure 26A). Both peaks are narrow, as might be expected from the narrow overall linewidth of ν_3 (6.2 cm⁻¹). There is a low-frequency shoulder on both the g.s.b. and e.s.a. peaks, from the previously assigned hot ν'_3 mode, however, the narrowness of the bands (~ 6 cm⁻¹) causes them to not significantly affect the amplitudes of the main bands.

Control of the relative optical polarizations of the pump and probe pulses enables separating the anisotropic component of the transient absorption (containing information on orientational dynamics) from the isotropic component (containing information on population

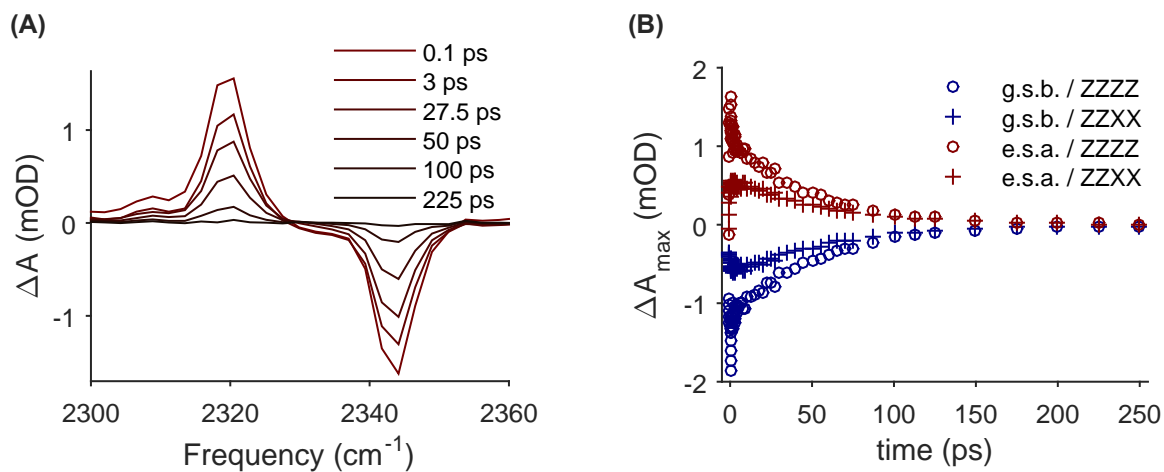


Figure 26: (A) The IR pump-probe spectrum of CO₂ in [Im_{4,1}][PF₆] comprises a narrow negative peak from transient bleaching of the ground state (g.s.b.) and a narrow positive peak from excited state absorption (e.s.a.), as well as low frequency shoulders from the hot ν'_3 band. (B) The magnitudes of the signals from both the all parallel (ZZZZ) and crossed (ZZXX) polarizations decay on approximately a 250 ps time scale.

relaxation).

$$I_{\parallel}(t) = I_{\text{iso}}(t) (1 + 0.8C_2(t)) \tag{6.4a}$$

$$I_{\perp}(t) = I_{\text{iso}}(t) (1 - 0.4C_2(t)) \tag{6.4b}$$

where I_{\parallel} and I_{\perp} are the signals from the parallel and perpendicular optical polarization configurations of the pump and probe pulses. I_{iso} is magnitude of the isotropic signal, and $C_2(t)$ is the second Legendre polynomial correlation function (the orientational correlation function for the transition dipole moment of the $\text{CO}_2 \nu_3$ mode)

$$C_2(t) = \langle P_2 [\vec{r}(t) \cdot \vec{r}(0)] \rangle \tag{6.5}$$

Taking the appropriate linear combinations of I_{\parallel} and I_{\perp} allows the recovery of the time-dependent isotropic signal and anisotropy (α) in the signal.

$$I_{\text{iso}}(t) = \frac{I_{\parallel}(t) + 2I_{\perp}(t)}{3} \tag{6.6a}$$

$$\alpha(t) = \frac{I_{\parallel}(t) - I_{\perp}(t)}{3I_{\text{iso}}(t)} = 0.4C_2(t) \tag{6.6b}$$

The amplitude of the fully isotropic signal decays by population relaxation ($\tau_{\text{decay}} = T_1$). Thus, the rate of relaxation out of the excited state can be determined by fitting the decay time. Fitting the decay of the isotropic signal (Figure 27) reveals a T_1 time of 55 ± 5 ps, which fits the observed long time dynamics excellently. The optical up-pumping effect of the ν'_3 shoulder, arising from its larger transition dipole moment compared with the main band,^{275,334} does not appear to disturb the observed population relaxation which remains monoexponential, most likely due to the low magnitude of the relative effect.

The anisotropy (Equation 6.6) gives the second Legendre polynomial correlation function, which can also be calculated directly from molecular dynamics trajectories. For this work, the $\vec{r}(t)$ chosen was the CO bond vector, as in the implementation of the FFA. The correlation function was averaged over all independent simulations to provide sufficient statistical weight.

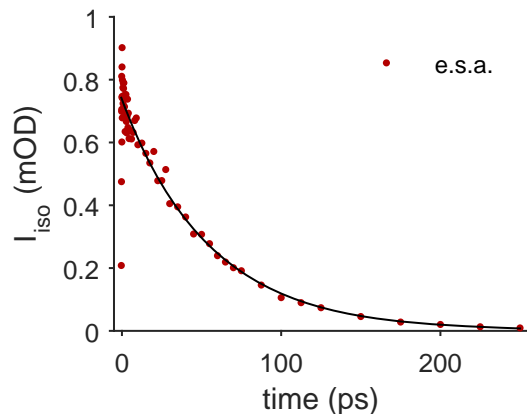


Figure 27: The amplitude of the the isotropic signal (I_{iso}) of CO_2 in $[\text{Im}_{4,1}][\text{PF}_6]$ decays exponentially, yielding a population time of 55 ± 5 ps.

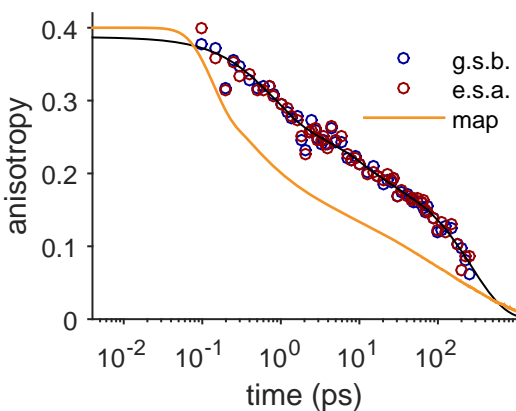


Figure 28: The orientational relaxation of CO_2 shows a multiexponential character, which could be indicative of complicated dynamics in a homogeneous environment (wobbling-in-a-cone) or of heterogeneous microenvironments leading to an average of heterogeneous dynamics. Anisotropy from g.s.b. and e.s.a. overlap, showing that the orientational dynamics of CO_2 are not affected by excitation of ν_3 . The anisotropy from MD simulation correctly captures the multiexponential character of CO_2 's reorientational dynamics, with good agreement with the experimental OCF. The MD simulation overestimates the rate of orientational relaxation in the first picosecond compared with experiment.

Table 9: Anisotropy ($\alpha = 0.4C_2$) fitting results (experiment).

	Amplitude		Time constant (ps)
a_1	0.12 ± 0.01	τ_1	0.7 ± 0.2
a_2	0.07 ± 0.01	τ_2	10 ± 4
a_3	0.20 ± 0.01	τ_3	270 ± 30

At $t=0$, the anisotropy should be equal to 0.4, since the initial and final positions of the transition dipole moment are perfectly correlated. In experimental data, fast inertial motions during optical pulse overlap often result in a decrease of this initial value in fittings of experimental results. The experimentally observed orientational dynamics of CO_2 (Figure 28) fit well to a triexponential decay model

$$\alpha(t_2) = \sum_{i=1}^3 a_i \exp(-t\tau_i^{-1}) \quad (6.7)$$

There is a fast component of around 0.7 ± 0.2 ps, an intermediate component of around 10 ± 4 ps, and a long timescale of around 270 ± 30 ps (Table 2). The experimentally accessible time window of 250 ps (due to the length of the translation stage in the pump-probe setup) prevents a complete determination of the long time dynamics, and it is possible that there are some unresolved very long time components of CO_2 's orientational relaxation.

The sum of pre-exponential factors is 0.39, almost equal to the theoretical maximum of 0.4, likely indicating that fast inertial motions are hindered by the ionic liquid, which gates the orientational relaxation of CO_2 . The anisotropy from both the ground state bleach and excited state absorption peaks follow the same trend line (Figure 28)), indicating that the rotational dynamics of CO_2 are not affected by excitation of the asymmetric stretching mode in this ionic liquid.

Comparison of the experimental anisotropy with the rotational correlation function (scaled by 0.4 to match the anisotropy) from simulation overall show good agreement (Figure 28). The simulation correctly captures the multiexponential character of orientational de-correlation. Furthermore, the timescale of global orientational relaxation is very similar.

Table 10: Orientational correlation function (C_2) fitting results (simulation).

i	a_i	τ_i (ps)
1	0.35	$0.18 \pm 2 \times 10^{-4}$
2	0.25	$1.3 \pm 2 \times 10^{-3}$
3	0.12	16.8 ± 0.02
4	0.13	$107.7p \pm 0.08$
5	0.15	596.4 ± 0.2

The simulation does seem to incorrectly predict partial orientational relaxation over the first picosecond that the experiment does not show; however, the remainder of the correlation function closely tracks the experimental reorientational dynamics.

Longer time scales (up to 1 ns) are also available to simulation. Thus, the simulated trajectories can potential observe long time dynamics that are inaccessible to the current experiment.

The orientational correlation function from simulation is best fit by the sum of five exponentials, rather than the triexponential model of experiment (Table 3).

$$C_2(t) = a_1 \exp(-t^2\tau_1^{-2}) + \sum_{i=2}^5 a_i \exp(-t\tau_i^{-1}) \quad (6.8)$$

There are early large amplitude components with time constants of 180 fs and 1.3 ps respectively, followed by approximately evenly weighted components with time constants of 16.9 ps, 107.9 ps, and 567 ps (Table 10). It is likely that the long experimental time constant of 270 ± 30 ps is reporting on a combination of the 107.9 and 567 ps timescales, since we do not have a large enough experimental time window to fully resolve these dynamics.

There is good agreement overall between the experimental and computational orientational correlation functions. There are minor disagreements over the amplitude of CO_2 's orientational relaxation in the first picosecond, which the simulation overestimates, and the number of time constants required to describe CO_2 orientational relaxation at long times, which the current experiment cannot fully resolve.

The multiexponential character of CO₂'s rotational dynamics could arise either from distinct subensembles of CO₂ in heterogeneous microenvironments, or from hindered rotations in a more homogeneous local environment that relaxes with multiexponential character (“wobbling-in-a-cone”). These third-order experiments do not provide a direct way to determine which of these hypotheses best explain the observed dynamics, though it may be possible to experimentally determine using higher order nonlinear spectroscopies.

6.3.3 Frequency Fluctuation Dynamics

The CO₂ ν_3 spectrum is sensitive to changes in the local environment of ionic liquids,^{10,107,311} and can be used as a probe to sense local dynamics around the CO₂ molecule, through the frequency fluctuation correlation function (Equation 6.3). The FTIR spectrum is relatively insensitive to subtle differences in dynamics; however, the two-dimensional infrared (2D-IR) spectrum contains sufficient information to recover the FFCF.

The 2D-IR spectra of the CO₂ ν_3 mode in room temperature [Im_{4,1}][PF₆] were obtained at the magic angle polarization condition between the first two (“pump”) pulses and the third (“probe”) pulse. This polarization condition weights all rotations of the CO₂ equally, resulting in an isotropic spectrum that can be directly compared with the frequency dynamics from MD simulations, which are assumed to be isotropic for a bulk liquid sample.

A 2D-IR spectrum depends on the amplitude of the third-order polarization as a function of initial and final frequencies (ω_1 and ω_3) at a specific population time (t_2). Each 2D-IR peak comprises a negative (blue) portion, along the $\omega_1 = \omega_3$ diagonal, from transient bleaching of the ground state (g.s.b.) and from stimulated emission (s.e.), and a positive (red) peak from excited state absorption (e.s.a.). The g.s.b./s.e. peak is centered at the ground state transition frequency, while the e.s.a. peak is centered at the first excited state transition frequency; they are separated in ω_3 by the anharmonicity of the vibrational mode (since to the first-order approximation, excited state absorption, which requires three electric field interactions, occurs only after the third optical pulse).

In the limit of inhomogeneous broadening, each spectrum may be considered as the conditional probability of a CO₂ molecule to have the final frequency ω_3 , given its initial

frequency ω_1 . At early t_2 times, the peak is stretched along the diagonal (Figure 29) from correlation in the initial and final frequencies, indicating that the local environment around CO_2 has not yet completely randomized. With increasing population time, local translations and rotations cause the local structure to relax, and the “memory” of the initial frequency is lost, causing the peak to become more rounded. The time scale of this local relaxation depends deeply on the system being studied; however, in ionic liquids, it tends to take from tens to hundreds of picoseconds.

Visually, one can see that the timescale of local relaxation near CO_2 in $[\text{Im}_{4,1}][\text{PF}_6]$ is quite long, as the spectrum is still quite stretched along the diagonal at 25 ps, and some small amount of “tilt” of the spectrum persists even to 200 ps (Figure 29). The timescale of this local relaxation can be quantified using a frequency fluctuation correlation function (FFCF). Methods to quantify the FFCF from the shape of the 2D-IR spectrum are diverse, and have been widely studied. The most common are graphic fitting methods, such as ellipticity, nodal slope, phase-slope, or centerline slope, though significant work has also been done using global fitting to spectra calculated from third-order response functions.

In this work, we used centerline slope (CLS) to approximate the value of the FFCF at each t_2 time of each spectrum. The FFCF was fitted to a modified Kubo lineshape

$$c_2(t) \approx \sum_i \frac{\Delta_i^2 \exp(-t\tau_i^{-1})}{\Delta_{\text{tot}}^2} = \sum_i a_i \exp(-t\tau_i^{-1}) \quad (6.9)$$

where Δ_i^2 is the variance in frequency associated with each correlation time τ_i , and Δ_{tot}^2 is the variance of the total frequency distribution. CLS fits for the normalized correlation function directly, and thus determines normalized coefficients (a_i). In the limit of inhomogeneous broadening, $a_i \approx \Delta_i^2 \Delta_{\text{tot}}^{-2}$. The initial time point for a CLS fit will usually start at a value less than 1, due to the inability to resolve dynamics in the fast (motional narrowing) limit.

The resulting FFCF shows a triexponential decay with increasing population time. A biexponential fit with a constant offset reproduces the experimental observed dynamics faithfully (Figure 30 and Table 11). There is a short time constant of 4.4 ± 0.9 ps, and a long time constant of 92 ± 12 ps. The constant offset of 0.15 indicates dynamics that are too slow to be resolved in the experimentally accessible time window. A biexponential underestimates correlation at long times ($t_2 > 125$ ps), while a triexponential faithfully reproduces the

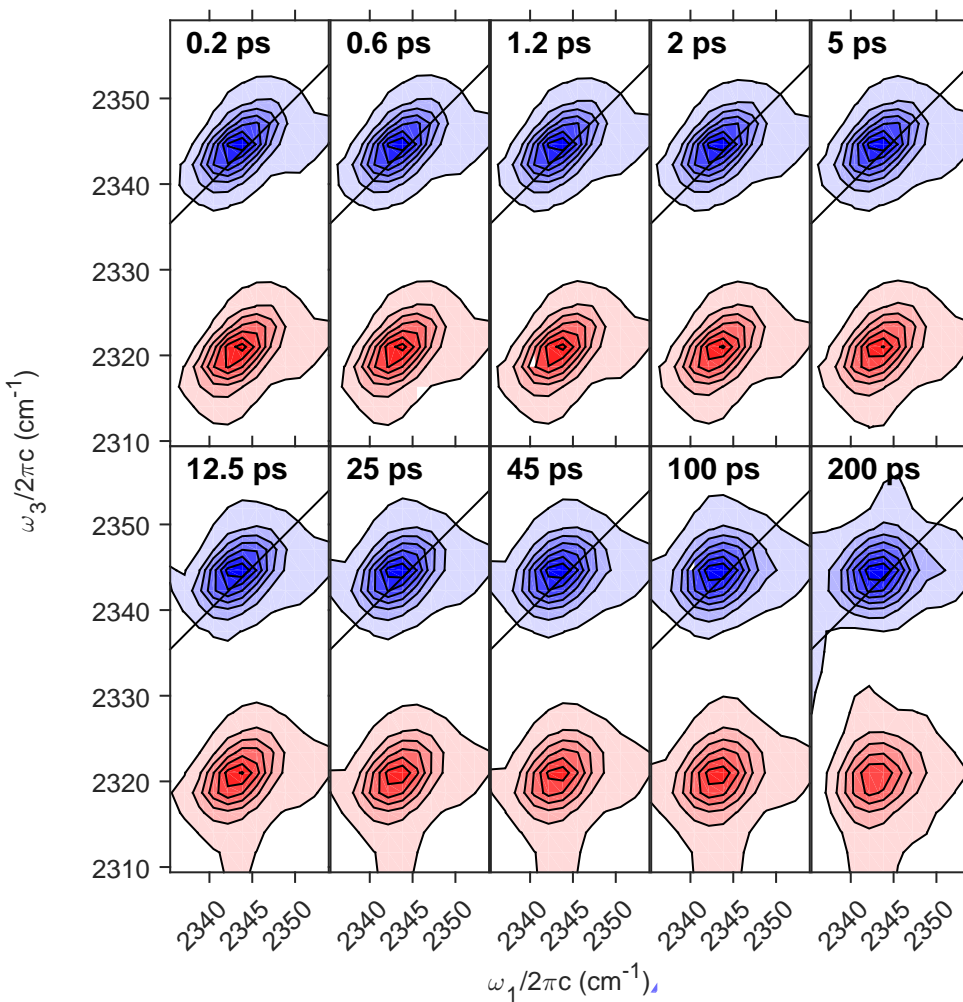


Figure 29: The isotropic (magic angle) 2D-IR spectra of CO_2 in $[\text{Im}_{4,1}][\text{PF}_6]$ show slow final relaxation of the initial frequency of CO_2 . The spectra, initially stretched along the $\omega_1 = \omega_3$ diagonal, become more rounded as the population time is increased, due to spectral diffusion. Even at 200 ps, however, there is some residual “tilt” to the spectra, indicating that local relaxation of CO_2 in its environment is not yet complete.

Table 11: Coefficients with 95% confidence intervals from fitting the experimental FFCF (from CLS) to a biexponential with a constant offset. The constant offset indicates slow dynamics that cannot be fully resolved within the experimental window.

Parameter	value with 95% confidence interval
a_1	0.115 ± 0.009
a_2	0.29 ± 0.01
τ_1	4.5 ± 0.9 ps
τ_2	90 ± 10 ps
c	0.15 ± 0.02

dynamics well but has high uncertainties for the intermediate and long time constants due to cross correlation between their values. The total amplitude of the calculated correlation function (0.55) agrees well with the CLS fits, but is significantly higher than the value of around 0.13 we would have predicted given our previous estimate of the total linewidth and the amplitudes of Δ_i^2 from global fitting.¹⁰⁷

The computational correlation function, as stated above, results from calculating the frequency-frequency correlation function, using the time evolution of the difference between the initial frequency and its time-independent average value ($\delta\omega(t) = \omega(t) - \langle\omega\rangle$). Frequency trajectories from the previously developed empirical spectroscopic map.¹⁰⁷ Since the correlation can be calculated at every time step, it captures short time dynamics that would be lost in the homogeneous linewidth for experimental data.

Fitting the computational correlation function to a sum of exponential decays shows complicated and multiexponential dynamics, also fitting well to the sum of a Gaussian and four exponentials (similar to Equation 6.8 for the orientational correlation function). The fastest inertial motions, which also contribute the largest component to the FFCF's amplitude, are captured with a Gaussian with a time constant of 70 fs. The fastest exponential component has a time constant of 650 fs. There are two intermediate time constants of 16.8 and 177.2 ps, and a final small amplitude long time constant of 1035 ps that corresponds to

Table 12: Frequency fluctuation correlation function (c_2)fitting results (simulation).

i	a_i	τ_i (ps)
1	0.62	$0.07 \pm 5 \times 10^{-5}$
2	0.19	$0.65 \pm 1 \times 10^{-3}$
3	0.06	16.8 ± 0.02
4	0.07	177.2 ± 0.2
5	0.02	1035 ± 4

complete relaxation of the initial CO₂ frequency to its ensemble average (Table 12).

Unlike the orientational correlation function, the computational correlation function disagrees with the experimental correlation function. Disagreement in the early time is expected, as simulation is able to fully resolve the early time frequency dynamics that are inaccessible to experiment; however, the magnitude of the correlation from about 1 ps onwards differs by a factor of approximately 4.5 between experiment and simulation (Figure 30A and B).

One possible cause of this discrepancy is from systematic errors in the estimation of the FFCF values from the experimental 2D-IR spectra by graphical fitting. The centerline slope (CLS) applied here handles narrow lines better than many other fitting methods; however, it still implicitly assumes the inhomogeneous broadening limit, which is clearly inaccurate for a narrow line such as CO₂.

To test this explanation of the discrepancy between the computed and experimental results, we decided to apply CLS fitting to spectra calculated from the MD simulation. We calculated spectra from the computational correlation function using analytical response functions (Section 3). The previous lower estimate of the instantaneous frequency width ($\Delta_{\text{tot}} = 6 \text{ cm}^{-1}$)¹⁰⁷ served as an estimate for the total linewidth of the peak. The experimental frequency range was used rather than the computed frequency range to try to remove the effects of the underestimation of the linewidth by the spectroscopic map (Section 6.3.1) The calculated 2D-IR spectra were then fitted using the CLS method to extract values for the

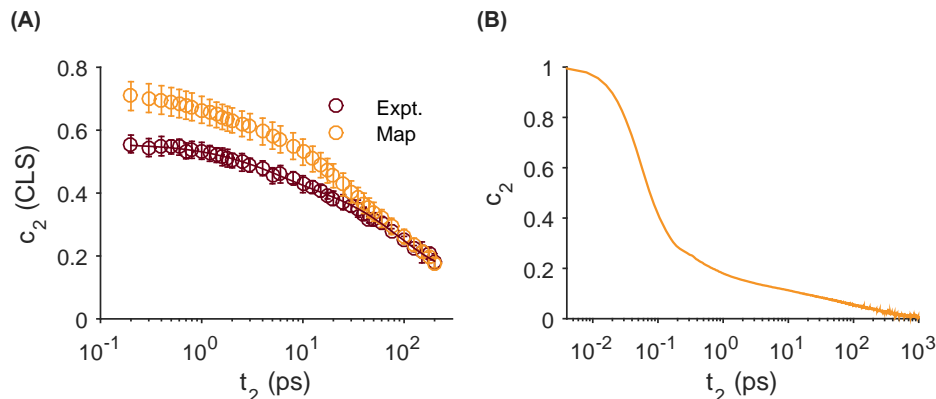


Figure 30: Experimental and computed FFCF of CO_2 in $[\text{Im}_{4,1}][\text{PF}_6]$. (A) Correlation values from CLS fitting of experimental spectra and spectra calculated from the computational correlation function using a response function formalism show good qualitative agreement, with the computational data slightly overestimating the initial correlation. (B) The underlying FFCF computed from MD trajectories using the spectroscopic map.

correlation at each time point (which were chosen to match experimental time points). The resulting correlation values agree extremely well with those from experiment, mainly varying in the amplitudes of the early time components (Figure 30A).

This result suggests that the frequency dynamics extracted from simulation correctly capture the timescales and even the relative amplitudes of the processes governing spectral diffusion of CO_2 in $[\text{Im}_{4,1}][\text{PF}_6]$. The largest source of disagreement in experimental and computed values of c_2 arises from the impact of the motional narrowing of the CO_2 ν_3 mode on the accuracy of the amplitude reported by CLS. This finding corresponds with the finding that the amplitudes from CLS differ from those obtained from a normalized correlation function from global fitting of data (which naturally handles motional narrowing well, but cannot provide a discrete value of the correlation for every point in t_2).

6.3.4 FFCF Decomposition

The strong qualitative agreement between the correlation functions from simulation and experiment suggests that more detailed investigation of the computational correlation function will yield physical insights into the solvation of CO₂. The most straightforward analysis is to decompose the computed frequency fluctuation correlation function into contributions from the anion and the cation (Figure 31). Since all cations and anions comprise the entire solvent environment, the total frequency fluctuation is the sum of contributions from the cation and anion. Both the anion and the cation contribute significantly to the vibrational frequency of CO₂'s ν_3 mode, through electrostatics and Pauli repulsion¹⁰ (implicitly captured here through the Lennard Jones forces).

Initially, the anion and cation contribute almost equally to the frequency environment, with the cation contributing around 14% more. By 50 fs, however, inertial motions have washed out nearly 40% of the cation's contribution to the initial frequency state, and only around 25% of the anion's contribution. By 400 fs, the dominant contribution to the continued frequency correlation comes from the anion, which contributes nearly 40% more than the cation. The proportion of the ongoing frequency correlation due to the anion continues to increase with time. By the end of the simulation (1 ns), the anion contributes nearly 75% to the ongoing correlation (approximately 2.5 \times as much as the cation).

The contributions of the cation to spectral diffusion can themselves be decomposed into components from the polar imidazolium head group ("ring") and the mostly nonpolar alkyl chains ("tail") (Figure 31). Of the two, the aromatic imidazolium ring contributes the most to CO₂'s frequency shift at all times. There is a non-trivial (\sim 13%) contribution from the alkyl tails; however, much of this contribution is lost in the inertial sub-50 fs timeframe. By 100 fs, the alkyl chains only contribute around 4% to the ongoing frequency correlation. The frequency correlation from the cation itself shows a single small amplitude oscillation between 200 and 400 fs, which results from motions of the polar head group. This oscillation suggests a slightly underdamped character to the oscillation, likely resulting from rattling of the cation in its solvent cage.

Several physical insights arise from this treatment. Nearly all of the contributions to the

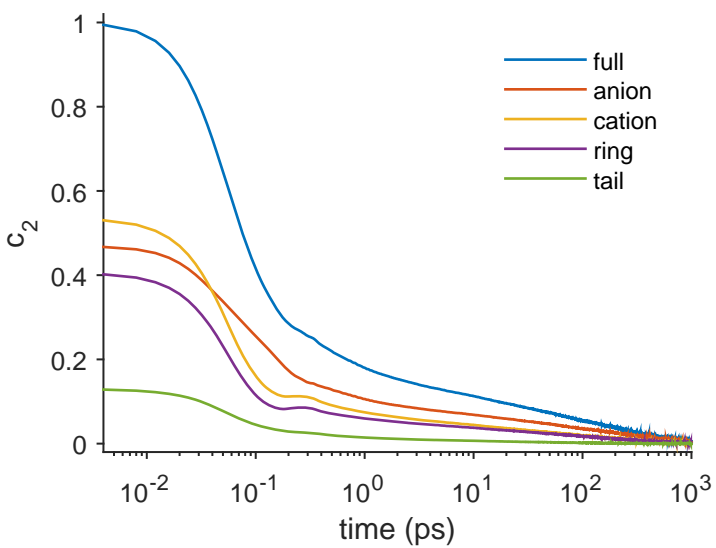


Figure 31: Decomposition of frequency fluctuation correlation function for CO_2 into components from the anion and cation. The cation, especially the ring, is most important in determining the initial frequency of CO_2 , but most of this memory is lost in the first 100 fs. Dynamics of the anion dominate the observed long time FFCF of CO_2 .

CO_2 ν_3 frequency arise from the polar regions of the ionic liquid, strongly suggesting that, at least in this liquid, CO_2 is not strongly associated with the nascent non-polar domains.

The rapid loss, in under 100 fs, of over half of CO_2 's frequency correlation, in concert with the narrow total linewidth of only around 6 to 10 cm^{-1} ¹⁰⁷ contributes to the significant motional narrowing of CO_2 's ν_3 lineshape.

The rapid rate of initial frequency correlation decay, combined with the extremely slow overall loss of frequency correlation, suggests that the initial frequency loss may be due to Lennard-Jones interactions. These interactions depend strongly on short range interactions, especially for repulsive type interactions. We have previously seen that CO_2 dynamics are gated by slow motions of the ionic liquid³¹¹. This finding, combined with quantum calculations indicating the importance of Pauli repulsion in determining the frequency of CO_2 , indicate that CO_2 is likely in a somewhat crowded ionic environment. In such an environment, even low amplitude motions of CO_2 or the surrounding liquid would cause significant changes in the Lennard-Jones force experienced by CO_2 (due to the r^{-12} dependence of the repulsive interaction), which would cause frequency shifts.

The long time frequency dynamics of CO_2 are dominated by the anion, suggesting a longer-lived association of CO_2 and the anion compared with the cation (since the anion continues to affect CO_2 's frequency for a longer period of time). Indeed, the time scale of the longest component of the frequency fluctuation correlation matches the lifetime of ion pairs calculated by Zhang and Maginn nearly exactly.³ Intuitively, this effect might be explained by a Lewis acid-base interaction between the CO_2 and anion; however, such an effect cannot occur in a simulation with no charge transfer. It is plausible that the association results from an electrostatic interaction between the quadrupole of carbon dioxide with the electric field generated by the anion. Further computational analysis (in development) strongly suggests this to be the case.

6.4 CONCLUSIONS

Here, we have utilized a spectroscopic map to refine the molecular interpretation of the ultrafast vibrational spectra of CO₂ in 1-butyl-3-methylimidazolium hexafluorophosphate ([Im_{4,1}][PF₆]).

There is qualitative agreement between the spectral lineshape from FTIR and that calculated from MD simulation using our newly developed spectroscopic map.¹⁰⁷ While the computational spectrum does not capture the low frequency shoulder (due to the use of rigid CO₂), the overall shape and frequency of the spectrum agree well. The computational spectrum underestimates the experimental linewidth.

The vibrational lifetime and orientational dynamics of CO₂ were determined from polarization controlled IR pump-probe measurements of CO₂. Over the experimentally accessible timescale, there is good agreement between the experimental anisotropy and the computational second Legendre polynomial correlation function. Simulation overestimates the orientational relaxation of CO₂ at early times, but otherwise shows excellent agreement with experiment. In addition to the triexponential reorientational dynamics indicated by the experimental anisotropy, the simulation is able to separate longer time dynamics ($\tau_c \approx 600$ ps) which cannot be resolved experimentally.

In order to compare the experimental and simulation FFCF results, 2D-IR spectra were calculated using the simulated FFCF, and then analyzed using the centerline slope method (the same method of analysis as the experimental spectra, see Section 3.2.2). The c_2 values from CLS show excellent agreement between experiment and simulation. The discrepancy between the CLS values from the experimental spectrum and the FFCF calculated directly using the spectroscopic map are attributed to artifacts in the amplitudes reported by CLS when dealing with a very narrow line, as CO₂.

Decomposition of the simulated FFCF into components arising from the anion and cation helps to refine the physical picture of the local environment of CO₂ in [Im_{4,1}][PF₆]. CO₂ interacts more strongly with the polar regions than the apolar alkyl tails. The dynamical picture that arises is complicated, as might be expected from the multiexponential character of the FFCF. The early time dynamics of CO₂ are dominated by local non-electrostatic

(Lennard-Jones and Pauli repulsion¹⁰) interactions that cause frequency fluctuations on the timescale of inertial motions (sub-100 fs, with the largest contributions from the cation head group. The substantial frequency correlation loss during these inertial motions help contribute to the motional narrowing of the CO₂ line. The longer time dynamics, out to 1 ns, are dominated by the anion, consistent with the “gating” effect previously described.³¹¹ The longest timescale of the FFCF matches the timescale of ion pairing in [Im_{4,1}][PF₆] that was previously identified in MD studies,³ and suggests a long-lived interaction with the anion. Given the lack of charge transfer in these MD simulations, the mechanism of this interaction is posited to be a charge-multipole interaction between the anion and CO₂’s quadrupole.

Extension of this project, through alkyl chain length and temperature variation, could help to further unravel the effects of mesoscopic domain structure on CO₂ dynamics, and could give further insight into the energetics that govern of spectral diffusion (Chapters 7 and 8).

Fifth-order spectroscopies could help to determine whether the multiexponential character of the orientational and frequency dynamics results from complicated dynamics in a homogeneous local environment, or from dynamics in heterogeneous subensembles.

6.5 ACKNOWLEDGEMENTS

SAC is grateful for financial support from the National Science Foundation (CHE-1565471), the American Chemical Society Petroleum Research Fund (52648-ND6), and the Sustainable Energy Initiative at the University of Notre Dame. SAC and CAD are also thankful for high performance computing resources and support from the Center for Research Computing at the University of Notre Dame.

7.0 TEMPERATURE AND CHAIN LENGTH DEPENDENCE OF ULTRAFAST VIBRATIONAL DYNAMICS OF THIOCYANATE IN ALKYLIMIDAZOLIUM IONIC LIQUIDS: A RANDOM WALK ON A RUGGED ENERGY LANDSCAPE.

The text in this chapter has been adapted from Brinzer, T.; and Garrett-Roe, S. *J. Chem. Phys.* **2017** *147*, 194501. The author’s contributions include design and implementation of the temperature-control FTIR and 2D-IR setup (but not the sample cell holder), the experimental work, theoretical modeling, and composing the manuscript.

7.1 CHAPTER SUMMARY

Ultrafast two-dimensional infrared spectroscopy (2D-IR) of a thiocyanate vibrational probe (SCN^-) was used to investigate local dynamics in alkyylimidazolium bis-(trifluoromethyl-sulfonyl)imide ionic liquids ($[\text{Im}_{n,1}][\text{Tf}_2\text{N}]$, $n = 2, 4, 6$) at temperatures from 5 to 80 °C. The rate of frequency fluctuations reported by SCN^- increases with increasing temperature and decreasing alkyl chain length. Temperature-dependent correlation times scale proportionally to temperature-dependent bulk viscosities of each ionic liquid studied. A multimode Brownian oscillator model demonstrates that very low frequency ($< 10\text{cm}^{-1}$) modes primarily drive the observed spectral diffusion, and that these modes broaden and blue shift on average with increasing temperature. An Arrhenius analysis shows activation barriers for local motions around the probe between 5.5 to 6.5 kcal mol $^{-1}$ that are very similar to those for translational diffusion of ions. $[\text{Im}_{6,1}][\text{Tf}_2\text{N}]$ shows an unexpected decrease in activation energy compared to $[\text{Im}_{4,1}][\text{Tf}_2\text{N}]$ that may be related to mesoscopically ordered polar and

nonpolar domains. A model of dynamics on a rugged potential energy landscape provides a unifying description of the observed Arrhenius behavior and the Brownian oscillator model of the low frequency modes.

7.2 INTRODUCTION

The properties of ionic liquids arise from the combination of liquid structure and dynamics. Dynamic intermolecular processes, such as self-diffusion and transient ion pairing, help to determine mass transport, conductivity, and viscosity in these complex fluids. Indeed, seemingly small changes in ionic liquid structure, such as methylating at the 2-position of an imidazolium cation, can nearly double an ionic liquid’s viscosity.¹⁴⁵ Computational studies strongly suggest that many of the transport properties ionic liquids, regardless of mesoscopic polar/apolar domain formation, are due to formation of transient charge-enhanced (“stiff”) and charge-depleted (“soft”) regions from local ion density fluctuations.¹⁷⁶

The timescale of local relaxation of the solvent environment correlates with bulk viscosity in ionic liquids,^{81,311} which is not surprising, as a molecule changing its local solvent environment is a necessary condition for translational diffusion. Indeed, recent computational work suggests that ion pair and ion cage lifetimes in ionic liquids *universally* govern the transport properties that are responsible for properties such as bulk viscosity.³ These properties are important for nearly all applications of ionic liquids. An intimate and extensive understanding of local structure and dynamics in ionic liquids could thus catalyze the development of ionic liquid applications.

Deeply understanding the ultrafast dynamics and structure, especially around solvated small molecules and ions, in ionic liquids requires techniques with high spatial and temporal resolution. Computational methods, of course, can access the necessary femtosecond time scales and atomic length scales. Few experimental methods, however, can provide the requisite time and spatial resolution to deeply investigate these solvent environments. Time-resolved vibrational spectroscopy, using small vibrational probes, can access both the ultrafast time scales and local length scales. It is sensitive to local solvation structure through

the vibrational solvatochromism of the probed vibrational modes.

Coherent multidimensional vibrational spectroscopies have elucidated structural and rotational dynamics in ionic liquids, using diverse reporters such as cyanates and nitriles, azides and azido compounds, dissolved gases, and aqueous and organic co-solvents.^{84,241,311,335–338} Tamimi *et al.*³³⁷ measured polarization-resolved pump-probe and 2D-IR spectroscopy of SeCN⁻ in alkyimidazolium ionic liquids of varying chain length at room temperature. They observed hydrodynamic scaling of slower rotational motions. Analysis of frequency fluctuations from 2D-IR showed a fast timescale that did not change with chain length, and a slow timescale that increased nonuniformly and nonhydrodynamically with chain length.³³⁷

Ultrafast two-dimensional vibrational spectroscopy (2D-IR) experiments reveal a set of time constants associated with various solvent and solute motions, through coupling of the probed high frequency vibrational mode to low frequency (intramolecular) modes. Changes in the relative alignment of a probe molecule and in its local environment will cause changes in its instantaneous vibrational frequency, via electrostatic (Stark effect) and non-electrostatic (exchange-repulsion, dispersion, hydrogen bonding) interactions.^{10,106,339,340} As solvent ions and the vibrational probe move relative to each other, the instantaneous frequency of the vibrational probe changes. Thus, translational and rotational diffusion cause a random walk of the probe’s frequency, or “spectral diffusion.”

The time-dependent 2D-IR spectrum can be thought of as a conditional probability, the probability of a probe vibration to have a final frequency ω_3 at time $t = t_2$ given its initial frequency ω_1 at time $t = 0$, weighted by the initial distribution. Oscillators excited at initial frequency ω_1 undergo a random walk in frequency space until they eventually reach the equilibrium distribution. 2D-IR spectroscopy quantifies this process through the change in 2D lineshape, which reflects the time-dependent correlation between initial and final vibrational frequencies. A frequency fluctuation correlation function (FFCF)

$$c_2(t) = \frac{\langle \delta\omega(t)\delta\omega(0) \rangle}{\langle \delta\omega(0)\delta\omega(0) \rangle} \quad (7.1)$$

is the statistical signature of vibrational frequency changes. The characteristic timescales of correlation loss are those of the low frequency (inter)molecular motions that couple to the

vibrational probe. The Fourier transform of the FFCF gives the spectral density

$$\tilde{C}(\omega) = \int_{-\infty}^{\infty} dt \exp(i\omega t)C(t) = 2\Re \int_0^{\infty} dt \exp(i\omega t)C(t) \quad (7.2)$$

of the molecular motions and vibrations that couple into the probed mode.¹⁹⁶ Here \Re means the real component.

The temperature-dependent dynamics contain information on the energetic barriers of molecular motions in the condensed phase, which can be compared with the barriers from MD simulations. In contrast to many other spectroscopic methods, only a relative handful of temperature-dependent 2D-IR spectroscopy experiments have examined these questions.^{63,338,341}

Glasses are a useful starting point for understanding the temperature-dependent dynamical properties of ionic liquids. Ionic liquids show structural^{6,157,158,160,161,342–345} and dynamical^{5,7,20,176,346,347} complexity characteristic of glass forming liquids. Glass forming systems have regimes of “uncooperative” activated dynamics, and “cooperative” super-Arrhenius dynamics, depending on how close the temperature is to the glass transition and the strength or fragility of the glass^{348–351}. Around the glass transition, glass formers can display non-Arrhenius temperature dependence of their structural relaxation rates due to the progressive quenching of structural relaxation pathways (jamming).³⁵² At temperatures sufficiently far above the glass transition, however, the most systems show normal Arrhenius behavior. These experiments are performed in the 5 to 100 °C range (~ 90 °C above the glass transition), which is typically in the normal activated regime.

In this manuscript, we examine the temperature-dependent spectral diffusion of a small charged probe molecule (SCN^-) in a series of imidazolium ionic liquids ($[\text{Im}_{n,1}][\text{Tf}_2\text{N}]$, $n = 2, 4, 6$; Figure 32). The room temperature spectral diffusion of this type of probe molecule has previously been studied in this class of ionic liquids.^{336,337} We first present the temperature-dependent FTIR and 2D-IR spectra, then describe changes in the low frequency spectral density using a multimode Brownian oscillator, and analyze the temperature-dependence of dynamics from 2D-IR with an Arrhenius analysis. Finally, we present a conceptual model that incorporates ideas from both the multimode Brownian oscillator and the Arrhenius analysis in a unified framework.

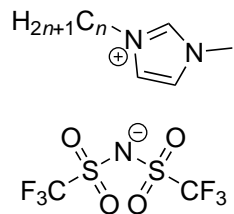


Figure 32: The ionic liquid solvents studied, 1-alkyl-3-methylimidazolium bis-(trifluoromethylsulfonyl)imide ($[\text{Im}_{n,1}][\text{Tf}_2\text{N}]$).

7.3 METHODS

Ionic liquids were obtained from Ionic Liquids Technologies, Inc (IoLiTec), and used without further purification. Prior to experiments, samples were heated to 60 °C and dried under vacuum (10 mTorr) with stirring for two hours.

The sample cell comprised 2-mm thick CaF_2 optical flats (Crystran Ltd, UK) separated by a 100 μm PTFE spacer, and held in a brass cell. The cell was assembled in a nitrogen-purged glove bag to minimize sample water contamination.

FTIR spectra were obtained using a nitrogen-purged Nicolet 6700 spectrometer (ThermoFisher) that had been modified to accept a temperature-controlled sample cell holder. Temperature-dependent experiments employed an Isotemp heating / cooling recirculating chiller (Fisher) to control the sample temperature. The sample temperature was measured using a J-type thermocouple (National Instruments USB-TC01), held in thermal contact with the outer face of one of the CaF_2 optical flats. Samples in both the FTIR and 2D-IR experiments were allowed to equilibrate for 30 minutes after a stable temperature reading was reached.

The optical parametric amplifier²⁰⁴ (OPA) and pump-probe geometry 2D-IR spectrometer²⁰⁵ employed in the ultrafast infrared spectroscopy experiments have been previously described in detail.³¹¹ Briefly, the OPA down-converts the 5 kHz 805 nm pulses from a commercial Ti:Sapphire laser source (Coherent Legend Elite), resulting in a low-noise source of 100 fs

mid-infrared optical pulses with bandwidth of $\sim 200 \text{ cm}^{-1}$ and an energy of $\sim 2.5 \text{ }\mu\text{J/pulse}$. These pulses are then optically split into four pulses. The two collinear pump pulses and a weaker probe pulse are spatially overlapped at the sample. A separate reference pulse follows a parallel path to the probe pulse, but is not overlapped with the pump pulses, which corrects for laser fluctuations and first-order signal. Timing between the pulses are controlled by mechanical delay stages. A single monochromator (Horiba) uses a 50 line/mm grating to disperse the signal and reference onto a 2×32 mercury cadmium telluride (MCT) detector (Infrared Systems). The experimental spectrum is acquired by varying the timing between the two pump pulses (t_1), and then numerically Fourier transforming the resulting t_1 -dependent signal into the frequency domain. Spectra were collected using an all-parallel optical polarization

The 2D-IR lineshape was analyzed using ellipticity

$$\varepsilon = \frac{\sigma_D^2 - \sigma_A^2}{\sigma_D^2 + \sigma_A^2} \tag{7.3}$$

where σ_D and σ_A are the diagonal and antidiagonal FWHM of the lineshape. Ellipticity serves as a measure of the two-point frequency fluctuation correlation for that t_2 value.²⁰⁷

7.4 RESULTS AND DISCUSSION

7.4.1 Linear spectroscopy

The $\text{C}\equiv\text{N}$ stretching mode gives a mostly Gaussian lineshape centered around 2055 cm^{-1} , indicating a substantial inhomogeneous component to the line. The temperature-dependent FTIR spectrum in $[\text{Im}_{4,1}][\text{Tf}_2\text{N}]$ (Figure 33) indicates that increasing temperature affects both the equilibrium solvation environment of SCN^- , and the solvent dynamics around it.

Increasing the temperature from 6.4 to 77.4°C induces a red-shift of approximately 0.6 cm^{-1} and a 1.8 cm^{-1} increase in FWHM from 22.1 to 23.9 cm^{-1} (Table 13). Additionally, the line broadening is slightly more noticeable on the red edge of the peak (Figure 33). These findings suggest dynamical changes with temperature, which would give insights

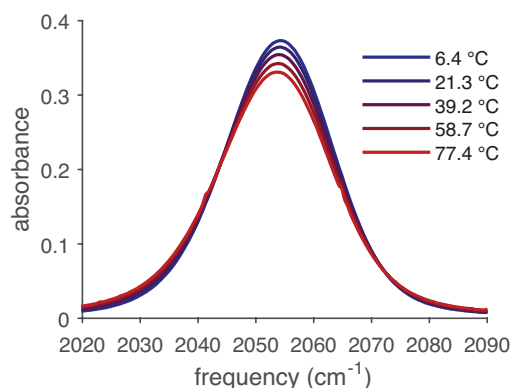


Figure 33: Background-subtracted FTIR absorbance of the SCN^- $\text{C}\equiv\text{N}$ stretch in $[\text{Im}_{4,1}][\text{Tf}_2\text{N}]$ across the temperature range studied. The $\text{C}\equiv\text{N}$ stretch red-shifts and broadens with increasing temperature.

Table 13: Absorption peak parameters, center frequency (ω_c) and full width at half maximum (FWHM), for the $\text{C}\equiv\text{N}$ stretching peak in $[\text{Im}_{4,1}][\text{Tf}_2\text{N}]$, as a function of temperature. Center frequencies were determined by fitting to a Voigt profile, while FWHM were numerically calculated from the background subtracted $\text{C}\equiv\text{N}$ peak.

T (°C)	ω_c (cm^{-1})	FWHM (cm^{-1})
6.4	2054.2	22.1
21.3	2054.2	22.4
39.2	2054.0	22.7
58.7	2053.8	23.2
77.4	2053.6	23.9

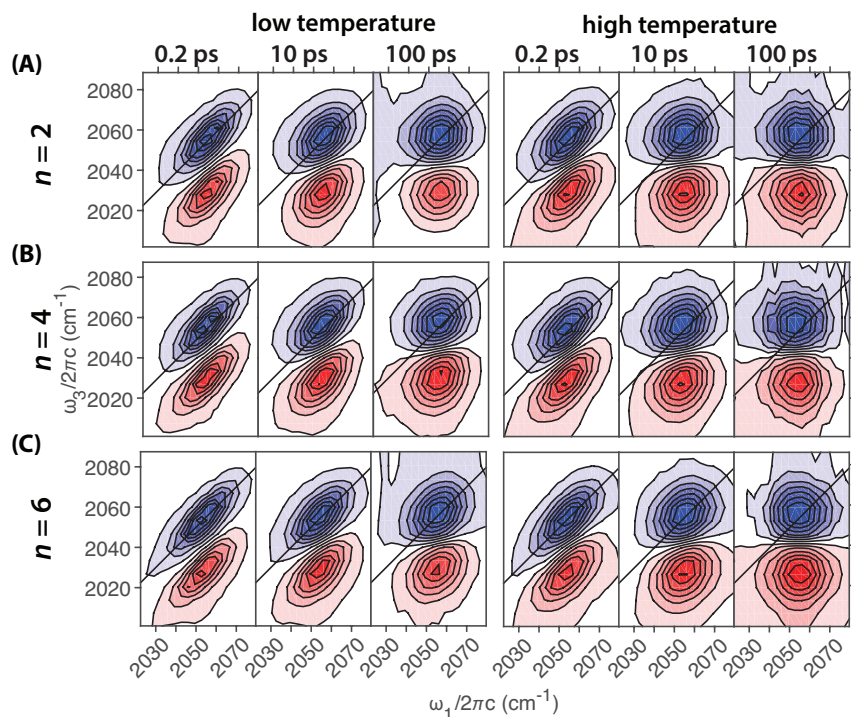


Figure 34: The rate of spectral diffusion increases with temperature and decreases with chain length. Absorptive 2D-IR spectra of the C≡N stretching mode in $[\text{Im}_{n,1}][\text{Tf}_2\text{N}]$ are shown at representative population times and high ($\sim 75^\circ\text{C}$) and low ($\sim 6^\circ\text{C}$) temperatures. At early population times, correlated initial and final frequencies cause the peak to stretch along the diagonal. As time progresses, this correlation decays, and the peak becomes more rounded. C≡N stretch frequencies become decorrelated more quickly at high temperatures, and with shorter chain ionic liquids, due to faster molecular motions changing the local environment.

into the ionic liquid motions and solvation environment. Despite its changes with temperature, it is not possible to invert the FTIR lineshape to obtain the molecular correlation function.²⁹ Though the low frequency modes determine the lineshape, linear spectroscopy does not contain enough information to recover a description of those low frequency modes.

7.4.2 Nonlinear spectroscopy

Two-dimensional infrared spectroscopy contains enough information to describe the low frequency modes. Differences in the local environment of SCN^- across temperatures and ionic liquids cause changes in the homogeneous and inhomogeneous linewidth of the peak on 2D-IR, and in the spectral diffusion rate (Figure 34). Each spectrum comprises a negative (blue) and positive (red) lobe, separated in ω_3 by the anharmonicity of the vibrational mode. The positive lobe reflects excited state absorption during the third optical pulse ($\langle\omega_1\rangle = \langle\omega_{01}\rangle$, $\langle\omega_3\rangle = \langle\omega_{12}\rangle$). The negative lobe reflects stimulated emission and transient bleaching of the ground state ($\langle\omega_1\rangle = \langle\omega_3\rangle = \langle\omega_{01}\rangle$).

The 2D absorptive peak gives the intensity of third-order polarization as a function of initial and final frequency at each t_2 time ($P^{(3)}(\omega_1, \omega_3; t_2)$). At early t_2 times, the antidiagonal and diagonal width of the peaks provide an estimate of the respective contributions of the homogeneous (fast) and inhomogeneous (slow) components of the lineshape. Thus, a peak containing mostly slow dynamics (with a long lifetime) would have a broad diagonal linewidth, and a narrow anti-diagonal linewidth.

The $\text{C}\equiv\text{N}$ stretch peak shows a significant inhomogeneous component and stretches along the diagonal at early t_2 times. The peak becomes more rounded over tens to hundreds of picoseconds (depending on the solvent and temperature) due to molecular motions that randomize the initially well-defined environment experienced by $[\text{SCN}]^-$.

The relative magnitudes of the homogeneous and inhomogeneous components at early t_2 times also vary across ionic liquids studied. Increased alkyl chain length causes the inhomogeneous component to increase and the homogeneous component to decrease. This trend is also consistent with an overall slowing of the solvent dynamics in the longer chain ionic liquid.

Across all temperatures studied, the spectral dynamics slow with increasing $[\text{Im}_{n,1}^+]$ alkyl chain length. At any temperature, the shorter-chain ionic liquid spectrally diffuse more rapidly. Visually comparing spectral shape can qualitatively show this trend, though it is easiest to see when the spectra have partially diffused. Thus the t_2 time where we can most clearly “see” this in the spectral shape varies across the temperatures studied. For example, the difference in shape of the low temperature spectra in $[\text{Im}_{2,1}][\text{Tf}_2\text{N}]$ and $[\text{Im}_{6,1}][\text{Tf}_2\text{N}]$ at long t_2 times (100 ps), arises from faster dynamics in the $[\text{Im}_{2,1}][\text{Tf}_2\text{N}]$ (Figure 34). At high temperatures, where molecular motions are faster, the differences in the timescales of dynamics between ionic liquids are most visually evident in the 10 ps spectra.

Increased temperature speeds up the observed dynamics, as can easily be seen by comparing the $t_2 = 10$ ps spectra in each ionic liquid at high and low temperatures (Figure 34). For any time point studied, the low temperature spectrum shows higher correlation (qualitatively seen in how “stretched along the diagonal” the peak is), indicating slower dynamics.

Comparing the low temperature 100 ps spectrum with the high temperature 10 ps spectrum provides a sense of the magnitude of the dynamical speedup. The similarity shape indicates that the frequency correlation is similar, despite the tenfold difference in population time. That is, increasing the temperature by 70 K speeds up the dynamics coupled to the $\text{C}\equiv\text{N}$ stretch by about an order of magnitude.

The resulting frequency fluctuation correlations were fitted with a trial sum of exponentials to determine the timescales of spectral diffusion. A weighted triexponential model (a normalized triexponential Kubo model) was able to faithfully reproduce the estimated FFCF for SCN^- in each ionic liquid at every temperature

$$c_2(t_2) = \frac{\langle \delta\omega(t_2)\delta\omega(0) \rangle}{\langle \delta\omega(0)\delta\omega(0) \rangle} \approx \sum_{i=1}^3 a_i \exp(-t_2\tau_i^{-1}) \quad (7.4)$$

where a_i and τ_i are the normalized frequency fluctuation amplitude and time constant for the i th component of the FFCF. The term a_i represents the line-broadening due to process i , Δ_i^2 , relative to the total line-broadening, Δ_{tot}^2 , $a_i = \Delta_i^2/\Delta_{\text{tot}}^2$. A biexponential fit also gives a high R^2 value, but systematically underestimated the long time value of each FFCF, a problem that was exacerbated at low temperatures and with longer chain lengths. Nevertheless, the resulting trend is independent of the choice of a bi- or triexponential model.

The fitting results (Table 14 and Figure 35) quantify the strong dependence of dynamics on the temperature. Time constants (τ_1 , τ_2 , and τ_3) for each ionic liquid decrease with increasing temperature. Increased thermal energy provides increased kinetic energy for the translation and rotation of the constituent ions (including SCN^-), which drive spectral diffusion.

The longest time constant (τ_3) increases with alkyl chain length, and decreases with temperature. The short and intermediate time constants (τ_1 and τ_2) are slightly lower in $[\text{Im}_{2,1}][\text{Tf}_2\text{N}]$ than in $[\text{Im}_{\{4,6\},1}][\text{Tf}_2\text{N}]$, indicating faster molecular motions, such as hindered translations and partial relaxation of the solvent cage. These time constants cannot be distinguished between $[\text{Im}_{4,1}][\text{Tf}_2\text{N}]$ and $[\text{Im}_{6,1}][\text{Tf}_2\text{N}]$, indicating similar timescales for these faster molecular motions. The striking difference in spectral diffusion between SCN^- from $n = 2$ to 4 to 6 (Figure 35) depends primarily on the relaxation processes with the slowest timescales. This finding is consistent with those of Tamimi and coworkers in ionic liquids at room temperature,³³⁷ and shows that the observed trend persists across multiple temperatures.

The amplitudes of the Kubo components also depend on temperature. The amplitudes associated with the short and intermediate time constants increase with temperature, while the amplitude of the long time constant decreases, especially in the longer chain ($n = 4$ and $n = 6$) ionic liquids. This finding indicates that the magnitude of frequency fluctuations contributing to the long time constant decreases with increasing temperature. In practice, it means that the molecular motions contributing to individual time constants change with increasing temperature. This trend is broken only for $[\text{Im}_{2,1}][\text{Tf}_2\text{N}]$ at its highest temperature (75.9 °C), which likely results fitting with a triexponential (for consistency), while the magnitudes of the time constants vary by significantly less than an order of magnitude.

Over-interpreting the temperature-dependence of individual time constants from a multiexponential fit of 2D-IR data is dangerous. Even a good empirical fitting function for a specific system (*e.g.* sum of exponentials, stretched exponential, or maximum entropy method) only approximates the dynamics in the molecular ensemble, which are often heterogeneous and have high dimensionality. Since the molecular motions that contribute to individual time constants can change with increasing temperature (amplitude trend above),

Table 14: Triexponential FFCF fitting results. The time constants (τ_i) indicate the timescales of molecular motions that affect the SCN^- frequency, while the amplitudes indicate the relative contribution of those motions to the total inhomogeneous linewidth. Correlation times (τ_{corr}) are the integrated area under the FFCF. Correlation times decreases with increasing temperature and decreasing alkyl chain length, indicating more rapid relaxation around the vibrational chromophore.

$n = 2$							
T ($^{\circ}\text{C}$)	a_1	a_2	a_3	τ_1 (ps)	τ_2 (ps)	τ_3 (ps)	τ_{corr} (ps)
6.8	0.11 ± 0.01	0.31 ± 0.02	0.33 ± 0.03	2.1 ± 0.3	14 ± 2	85 ± 8	32.3 ± 1.3
22.6	0.11 ± 0.01	0.34 ± 0.02	0.28 ± 0.03	1.4 ± 0.2	10 ± 1	52 ± 6	18 ± 1.2
39.6	0.12 ± 0.02	0.35 ± 0.03	0.23 ± 0.04	1.3 ± 0.2	8 ± 1	37 ± 5	11.2 ± 1.0
58.2	0.15 ± 0.02	0.36 ± 0.03	0.16 ± 0.05	1.3 ± 0.2	7 ± 1	26 ± 5	6.9 ± 0.8
75.9	0.12 ± 0.03	0.27 ± 0.05	0.24 ± 0.07	1.0 ± 0.2	4 ± 1	13 ± 2	4.5 ± 0.5
$n = 4$							
6.7	0.11 ± 0.02	0.28 ± 0.03	0.41 ± 0.04	3.0 ± 0.4	22 ± 4	155 ± 20	69.2 ± 5.2
22.6	0.12 ± 0.02	0.31 ± 0.03	0.34 ± 0.04	2.3 ± 0.4	16 ± 3	96 ± 12	37.6 ± 2.7
39.8	0.14 ± 0.02	0.34 ± 0.04	0.27 ± 0.05	1.9 ± 0.4	12 ± 2	59 ± 11	20.2 ± 2.3
58.5	0.12 ± 0.03	0.34 ± 0.05	0.25 ± 0.08	1.2 ± 0.3	8 ± 2	35 ± 9	11.5 ± 1.8
76.2	0.14 ± 0.03	0.41 ± 0.05	0.14 ± 0.08	1.2 ± 0.3	8 ± 2	32 ± 13	7.7 ± 1.6
$n = 6$							
4.9	0.09 ± 0.02	0.24 ± 0.03	0.49 ± 0.05	2.8 ± 0.6	19 ± 5	163 ± 27	84.5 ± 7.8
22.0	0.12 ± 0.02	0.29 ± 0.03	0.39 ± 0.04	2.4 ± 0.4	16 ± 3	113 ± 16	48.4 ± 4.0
39.4	0.12 ± 0.02	0.31 ± 0.03	0.33 ± 0.04	1.7 ± 0.3	11 ± 2	69 ± 10	26.1 ± 2.2
58.7	0.13 ± 0.01	0.34 ± 0.02	0.26 ± 0.03	1.4 ± 0.2	9 ± 1	46 ± 4	15.1 ± 0.8
76.6	0.15 ± 0.02	0.36 ± 0.03	0.18 ± 0.04	1.4 ± 0.2	8 ± 1	33 ± 5	9.1 ± 0.9

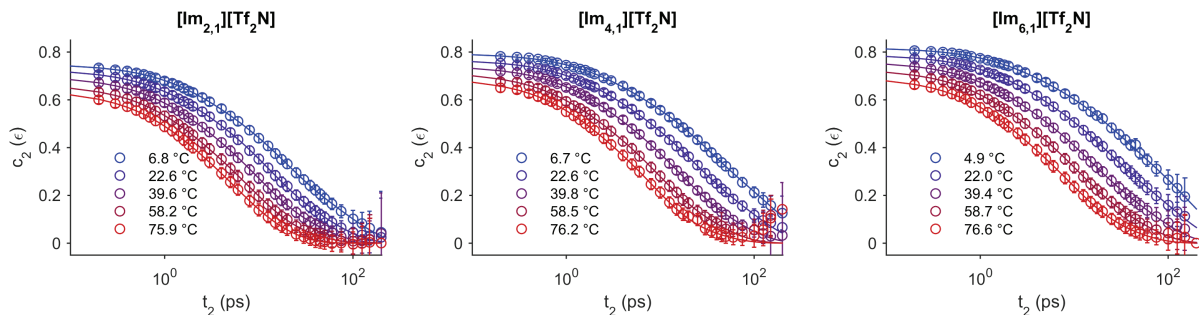


Figure 35: FFCFs for the C \equiv N stretching mode quantify the changes in dynamics in [Im $_n$,1][Tf $_2$ N] with increasing temperature. Colored circles correspond to ellipticities of the 2D-IR spectra, while colored lines represent the corresponding triexponential fit. The frequency fluctuation correlation decays more quickly as temperature increases, and with shorter cation alkyl chain length.

it is not fair to compare individual time constants across temperatures in this system.

An alternative method of analyzing the temperature-dependence of the dynamics expressed in the C \equiv N FFCF is through the correlation time of the sample. The correlation time (Table 14), or integrated area under the normalized FFCF, expresses the dynamics in a single quantity. It depends on all of the inter- and intramolecular modes that couple into the frequency of the vibrational chromophore.

$$\tau_{\text{corr}} = \int_0^{\infty} dt_2 c_2(t_2) \quad (7.5)$$

We used, in this case, the fits to our ellipticity values of the 2D-IR spectra as the normalized correlation function. While this neglects the motionally narrowed component of the ensemble FFCF, that component is negligible given the very long timescale of spectral diffusion in these ionic liquids. Since we expect the coupling of low frequency modes into the chromophore to be relatively temperature-independent, the correlation time (τ_{corr}) should be an unbiased metric for dynamics in each ionic liquid.

We note that the temperature-dependent correlation times for each ionic liquid correlate strongly with that ionic liquid's temperature-dependent viscosity³⁵³ (Figure 36), consistent

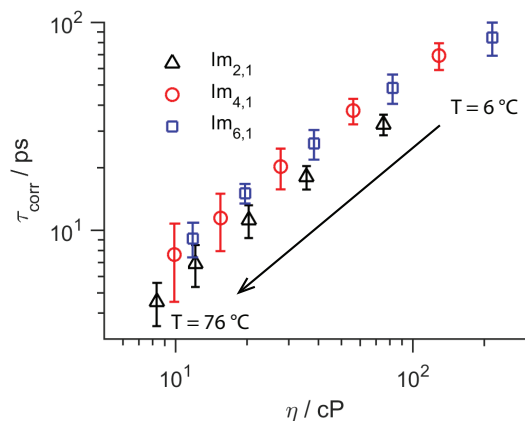


Figure 36: Relationship between correlation time and viscosity³⁵³ for each ionic liquid at each temperature. Viscosities at these specific temperatures interpolated with a piecewise cubic Hermite polynomial method. For each ionic liquid studied, there is a strong correlation between the temperature-dependent viscosity and correlation time; however, at any given temperature, this trend does not hold across ionic liquid chain lengths.

with trends for small molecules,^{174,176} SCN^- ,⁸¹ and CO_2 ,³¹¹ as well as those for anion and cation diffusion. The trend lines in $[\text{Im}_{4,1}^+]$ and $[\text{Im}_{6,1}^+]$ essentially overlap, while $[\text{Im}_{2,1}^+]$ shows a relatively shorter correlation time than would be expected based on the trends of the longer chain ionic liquids. Tamimi *et al.* noticed that the slow rotational diffusion coefficient scaled inversely proportionally to viscosity across alkyl chain lengths. The slow part of frequency fluctuations slowed with increasing chain length, but the timescales were not proportional to bulk viscosity.³³⁷ These results are consistent with the current observed trend (Figure 36), considering any one temperature. Nevertheless, for a single alkyl chain length, the observed temperature-dependent dynamics scale proportionally to viscosity.

7.4.3 Spectral density and multimode Brownian oscillator description

The correlation time depends on the low frequency spectral density (Equation 7.2). The spectral density itself can be modeled as a set of linearly displaced Brownian oscillators

with parameters describing solvent friction (γ_j) and a characteristic frequency (ω_j). For low frequency solvation coordinates, this Brownian oscillator is in an overdamped regime ($\gamma_j \gg 2\omega_j$). In the high-temperature overdamped limit, the real portion of the correlation function, to which 2D-IR spectroscopy is sensitive, is¹⁹⁶

$$C'(t) = \sum_j C'_j(t) = \sum_j \frac{2\lambda_j k_B T}{\hbar} \exp(-\Lambda_j t) \quad (7.6)$$

where $\Lambda_j \equiv \omega_j^2/\gamma_j$, and λ_j is the vibrational Stokes shift due to mode j . The sum of exponential prefactors is equivalent to Δ_{tot}^2 in the Kubo model (Eq. 7.4). This prefactor contains the only explicit temperature-dependence in this expression. It predicts broadening of the spectrum with increased temperature. Temperature does not affect the predicted dynamics.

The observed temperature-dependence of the correlation function requires that the central frequency and solvent friction of the low frequency modes change with temperature. Integrating Equation 7.6 gives the analytical solution that $\tau_{\text{corr}} = \sum_j \Lambda_j^{-1} = \sum_j \gamma_j/\omega_j^2$. The magnitudes of ω_j and γ_j have competing effects on the correlation time. Decreasing ω_j increases τ_{corr} , while decreasing γ_j decreases τ_{corr} .

With only a single metric (correlation time) as a function of temperature, and two parameters in the Brownian oscillator model, it is not possible to unambiguously assign the cause of the increased correlation time with alkyl chain length. It could result either from changes in central frequency or from increased solvent friction; however, modeling (Section 7.4.5) suggests temperature dependence of solvent friction dominates.

In the frequency domain, the odd part of the spectral density is¹⁹⁶

$$\tilde{C}''(\omega) = \sum_j 2\lambda_j \frac{\omega \Lambda_j}{\omega^2 + \Lambda_j^2} \quad (7.7)$$

Using the parameters of the correlation function fits (Table 14), we calculated $\tilde{C}''(\omega)$ (Figure 37). Since the even portion of the spectral density is equal to the odd component times a temperature factor $\coth(\hbar\omega/2k_B T)$, we focus our attention on the odd component. As the correlation time increases, the spectral density shifts to higher frequency and broadens.

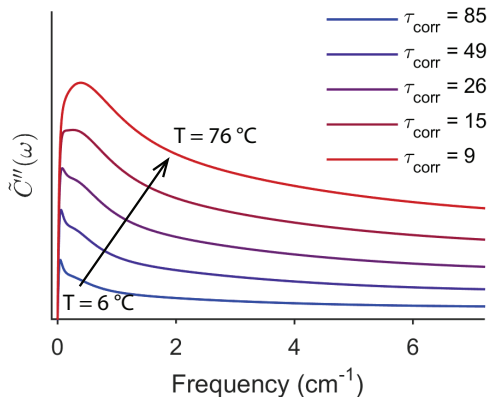


Figure 37: The low frequency spectral density that couples to SCN^- blue shifts and broadens with increasing temperature. This figure shows the odd portion of the spectral density, based on the FFCF of SCN^- in $[\text{Im}_{6,1}][\text{Tf}_2\text{N}]$ and a three mode Brownian oscillator model.

This spectral density is not the raw density of states, but rather the states weighted by their coupling to the high frequency SCN^- mode.

Analysis of spectral diffusion in $[\text{Im}_{6,1}][\text{Tf}_2\text{N}]$ suggests that the low frequency modes responsible for spectral diffusion of SCN^- are in the extremely low in frequency ($<10 \text{ cm}^{-1}$). With increasing temperature (decreasing τ_{corr}), the spectral density blue shifts and broadens (Figure 37)

7.4.4 Arrhenius analysis

We can use the temperature-dependence of the correlation time to assess the energy barriers governing spectral diffusion. Each correlation time serves as an inverse rate for the spectral diffusion process. The rate of spectral diffusion shows an Arrhenius relationship with temperature ($\ln(1/\tau_{\text{corr}}) \propto T^{-1}$) (Figure 38) across the range of temperatures studied. The Arrhenius equation can thus be used to assess the activation barriers governing spectral diffusion

$$\ln k = \ln(1/\tau_{\text{corr}}) = -E_a \left(\frac{1}{k_B T} \right) + \ln A \quad (7.8)$$

The slope of line gives the activation energy (E_a) of the process, and the intercept gives the frequency prefactor (A).

An Arrhenius fit approximates the stochastic diffusion of the frequency on its n -dimensional potential energy surface as a single activation energy, and will likely break down close to the glass transition temperature. We expect, however, that the energetic barriers from this analysis will at a minimum reveal qualitative differences between ionic liquids, and will be a fair approximation of the main barriers that govern spectral diffusion.

The Arrhenius fits to correlation time for SCN^- in each ionic liquid are excellent (Figure 38). The calculated activation barriers in $[\text{Im}_{4,1}][\text{Tf}_2\text{N}]$, while large, are within about $1 k_B T$ of those found by high field diffusion NMR and MD simulations for translational diffusion of anions and cations in $[\text{Im}_{4,1}][\text{Tf}_2\text{N}]$.³⁵⁴ The activation energy found by this analysis is likely lower because of the inclusion of additional small amplitude motions (from fast timescales) with a lower activation barrier in the dynamics reported on by 2D-IR spectroscopy. It is possible to repeat this analysis using the intermediate and long time constants (Appendix); however, as discussed in Section 7.4.2 cross correlation in the amplitudes associated with the time constants (Table 14) precludes assigning a physical significance to the resultant activation barriers. Calculating the correlation times and Arrhenius fits while omitting the fast time component does not substantially change either result (Appendix).

The trend in activation energy across ionic liquids, however, is counterintuitive (Table 15). The activation energy increases by $k_B T$ (at 298 K) from $[\text{Im}_{2,1}][\text{Tf}_2\text{N}]$ to $[\text{Im}_{4,1}][\text{Tf}_2\text{N}]$, and then decreases by $k_B T/3$ for $[\text{Im}_{6,1}][\text{Tf}_2\text{N}]$. This trend differs from the temperature-dependent viscosity and ion self-diffusivity (by NMR) of the $[\text{Tf}_2\text{N}^-]$ anion in $[\text{Im}_{n,1}][\text{Tf}_2\text{N}]$, both of which consistently increase from $n = 2$ to $n = 6$.³⁵³

The low frequency spectral density (Equation 7.2) and multimode Brownian oscillator model provide a potential explanation for this trend. The lower activation energy in $[\text{Im}_{6,1}][\text{Tf}_2\text{N}]$ implies that the spectral diffusion rate is less sensitive to temperature than that in $[\text{Im}_{4,1}][\text{Tf}_2\text{N}]$. We hypothesize that the reason for this trend lies in the evolution of mesoscopically ordered domains in $[\text{Im}_{6,1}][\text{Tf}_2\text{N}]$ that provide additional low frequency solvent modes related to the apolar alkyl tail domains. These modes may have lower solvent drag forces (friction) than modes involving the cation head groups and anions, due to smaller

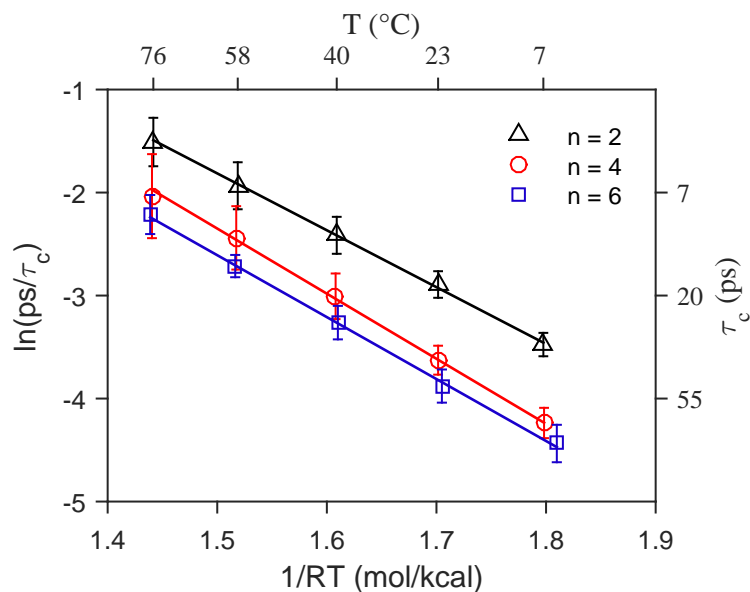


Figure 38: Arrhenius plot of the effect of temperature on correlation time in each $[\text{Im}_{n,1}][\text{Tf}_2\text{N}]$ ionic liquid studied. Symbols with uncertainty indicate the natural logarithm of the correlation time at each temperature, while the lines are the best fit to the Arrhenius equation. The slope of the line gives the coarse-grained activation energy for the motions that cause spectral diffusion.

Table 15: Activation barriers, from an Arrhenius analysis, are relatively large (5.5 to $6.3 \text{ kcal mol}^{-1}$), with the highest barrier found in $[\text{Im}_{4,1}][\text{Tf}_2\text{N}]$.

n	E_a (kcal mol^{-1})	A (fs^{-1})
2	5.5 ± 0.4	0.6 ± 0.4
4	6.3 ± 0.3	1.3 ± 0.7
6	6.0 ± 0.4	0.6 ± 0.4

intermolecular forces (vdW vs. charge-charge interactions). What is then required is that these modes broaden less with increased temperature than those in the polar regions. This hypothesis is reasonable: lower solvent friction should result in a lower energy barrier for exciting molecular motions. Molecular motions drive spectral diffusion. Thus the temperature dependence would be less prominent. Spectral diffusion of SCN^- in $[\text{Im}_{6,1}][\text{Tf}_2\text{N}]$ then has additional (lower friction) solvent motions which contribute to it, which $[\text{Im}_{4,1}][\text{Tf}_2\text{N}]$ lacks. This additional “pathway” for spectral diffusion would then result in the lower energetic barrier.

Finally, some comment is required on the pre-exponential factors recovered from the Arrhenius fits. The frequency prefactors are unphysically high if considered (as in the 1D case) ‘attempt frequencies’ at a barrier-crossing. An attempt frequency of $0.6 < A < 1.3\text{fs}^{-1}$ does not correspond to the physical period for a rate process involving motions of heavy nuclei. Mid-IR-active vibrational modes have periods of around 10 to 30 fs, and the fastest inertial timescales that have been observed are on the order of 50 fs. We are not the first to encounter this result when using an Arrhenius model to treat temperature-dependent spectral diffusion,³⁴¹ though to date a complete explanation has not been provided for it.

7.4.5 Dynamics on a rugged energy landscape

Dynamics on a rough potential energy surface provides a unifying physical picture. The multimode Brownian oscillator picture describes the bath of low frequency modes to which the SCN^- vibrator is coupled. Frequency fluctuations require motion of these collective coordinates, and this motion occurs with a characteristic frequency and a friction coefficient. Assuming the frequencies of the low frequency modes change little over the temperature range of interest, we argue that the dynamics are dominated by the effective friction coefficient. The temperature dependence and Arrhenius analysis show that there is activated behavior. Large barriers ($\sim 6\text{kcal mol}^{-1} \propto 10 k_{\text{B}}T$) are required to fit the trend in the observed dynamics. These two pictures can be unified as motion on a rugged energy landscape (Figure 39a). Progress along the low-frequency coordinate is a thermally activated process. Because the energy surface is rough, and thermal energy is required to move along it, there is friction.

As temperature increases, it is easier to overcome the local barriers and the effective friction decreases, as we observe.

Previous temperature- and solvent-dependent studies of photoisomerizations³⁵⁵ and equilibrium isomerizations⁸⁷ have taken pains to disentangle the effects of activated barrier crossings from dynamical viscosity effects. The rate of such reactions can be influenced both by the activated barrier height, and by solvent viscosity, and it is challenging to disentangle the effects. In this case, however, spectral diffusion of the SCN^- probe molecule is primarily sensitive to intermolecular motions such as translational and rotational diffusion, both of itself and of the surrounding solvent. As such, the energetic barriers we are assessing with our temperature-dependent 2D-IR measurements are (in this case) directly related to the temperature dependence of the solvent viscosity. Specifically, these barriers likely represent the molecular cage-scale activation events that are a principle component of recent theories of viscosity that span wide temperature ranges and account for both activated and glassy dynamics.³⁵¹ Local barriers such as these are relevant in normal activated regime, where Arrhenius dynamics are a good description of the system. At much colder temperatures (approaching the glass transition), collective effects would dominate. Correspondence between our calculated activation barriers and those for translational diffusion of anions and cations in $[\text{Im}_{4,1}][\text{Tf}_2\text{N}]$ (Section 7.4.4) supports this idea.

This qualitative picture can be modeled quantitatively. We construct a one dimensional random walk that reproduces the observed τ_{corr} , E_a , and A . To model spectral diffusion, we used a Markov chain model in which the probability density in frequency space is propagated by a transition matrix, T . The transition matrix allows transitions from one frequency to any other, with probabilities dictated by the Boltzmann distribution, and the rate of these jumps, r , is given as an activated process

$$r = t_{\text{step}} A \exp(-E_a/k_{\text{B}}T) \tag{7.9}$$

where, t_{step} is the simulation step size. The transition matrix then has the form

$$T = \begin{pmatrix} d_1 & rp_1 & rp_1 & \cdots & rp_1 \\ rp_2 & d_2 & rp_2 & \cdots & rp_2 \\ rp_3 & rp_3 & d_3 & \cdots & rp_3 \\ \vdots & & & \ddots & \vdots \\ rp_n & rp_n & \cdots & & d_n \end{pmatrix} \quad (7.10)$$

where p_i is the (normalized) Boltzmann probability of state i

$$p_i = \exp(-V_i/k_B T) / \sum_j \exp(-V_j/k_B T), \quad (7.11)$$

d_i is the diagonal probability of remaining in state i ,

$$d_i = 1 - r + rp_i, \quad (7.12)$$

and V_i is the potential energy of state i . The initial probability, $\rho(t = 0)$ is also the Boltzmann distribution, and the probability distribution is propagated according to

$$\rho(t + t_{\text{step}}) = T\rho(t) \quad (7.13)$$

The two-point frequency fluctuation correlation function is then

$$c_2(t) = \sum_i \sum_f \delta\omega_f p(f, t | i, 0) \delta\omega_i \rho_i(0) \quad (7.14)$$

where $p(f, Nt_{\text{step}} | i, 0) = (T^N)_{if}$ is the conditional probability of reaching microstate f with frequency $\delta\omega_f$ at time $t = Nt_{\text{step}}$ given the initial microstate i with frequency $\delta\omega_i$ at time $t = 0$. The c_2 is normalized and integrated, Eq. 7.5, to give a τ_{corr} just as in the experiment.

The resulting correlation functions and correlation times follow the experimental trends closely (Figure 39b,c). The input activation energy is almost identical to the resulting activation energy (5.5 kcal/mol for $[\text{Im}_{2,1}][\text{Tf}_2\text{N}]$) while the attempt rate is slower by a factor of 3 for this particular model.

The general picture of dynamics on a rough energy landscape can be modeled with many other particular models and transition matrices. For example, dynamics in 1D allowing only nearest neighbor transitions can also fit the observed kinetics when the nearest neighbor spacing is chosen appropriately (data not shown). Other models may also be able to reproduce

the observed trends. We expect that models that contain the essential features of stochastic transitions that are activated diffusion along low frequency modes will likely fit the data. As such, our key conclusion is general to the details of the model. In particular, models based on anomalous diffusion with a distribution of barrier heights may be a promising direction to further explain the multiple timescales that we observe. We note that the observed kinetics can also be fit with a stretch exponential function with the stretching factor, $\alpha \approx 0.6$, which suggests moderate dispersion in the barrier heights.

7.5 CONCLUSIONS

Temperature-dependent 2D-IR has provided insight into the energy landscape around SCN^- in *N*-1-alkyl-3-methylimidazolium bistriflimide ($[\text{Im}_{n,1}][\text{Tf}_2\text{N}]$) ionic liquids of varying alkyl chain lengths ($n = 2, 4, 6$). The observed frequency fluctuation dynamical rates for local motions, which include contributions from hindered translations, rotations (including those of the probe), and complete solvent reorganization, increase with increasing temperature, and decrease with increasing alkyl chain length. The correlation times for these observed frequency dynamics correlate strongly to bulk viscosity of each ionic liquid.

An Arrhenius analysis of the correlation times gives a series of energies on the order of 5.5 to 6.5 kcal mol⁻¹. These values are similar to, but slightly lower than, the calculated energies for anion and cation translational diffusion from high-field diffusion NMR and MD studies. We suspect that this difference results from the inclusion of lower energy motions such as rotations and hindered translations that would not meaningfully contribute to translational diffusion. Combined with the strong correlation between ionic liquid viscosity and correlation time, this finding suggests that these measurements may be sensitive to the lifetime of the transient “stiff” ionic liquid regions described by Araque and co-workers,¹⁷⁶ which are believed to act as a rate-limiting structure for diffusion.

The trend in activation energies across ionic liquids increases from $[\text{Im}_{2,1}^+]$ to $[\text{Im}_{4,1}^+]$ as expected, but unexpectedly decreases for from $[\text{Im}_{4,1}^+]$ to $[\text{Im}_{6,1}^+]$. We suspect that this decrease is explained by the evolution of mesoscopic ordering in $[\text{Im}_{6,1}][\text{Tf}_2\text{N}]$, and its effect

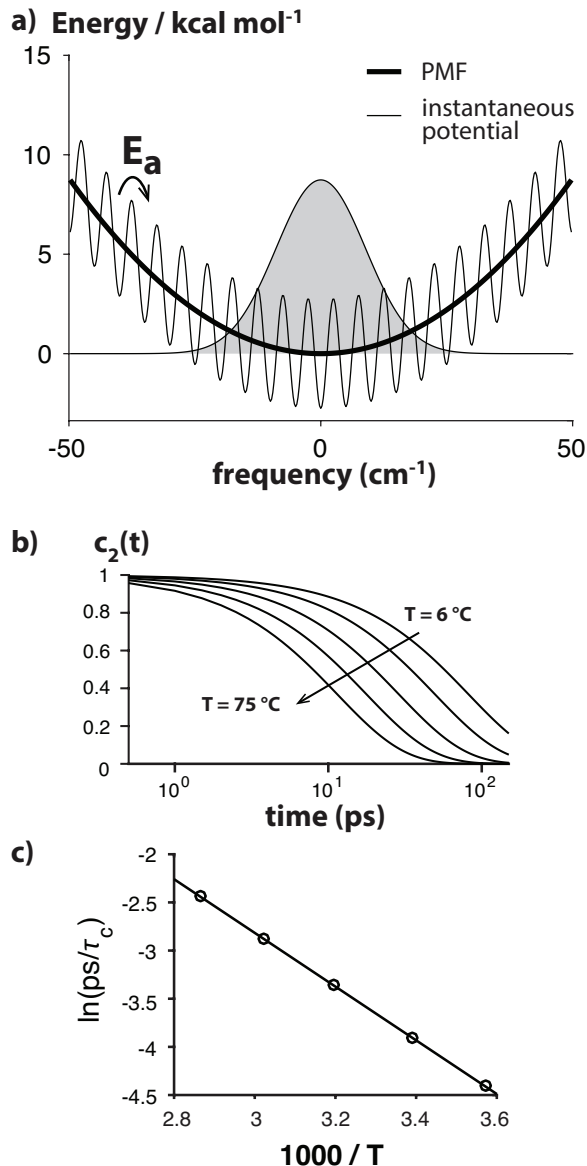


Figure 39: A model of dynamics on a rough energy surface reproduces the experimental trends in τ_{corr} , E_a , and A . a) Motion along a low frequency coordinate requires thermal energy to overcome local activation barriers, E_a . The time averaged potential of mean force (PMF) is smooth and harmonic, but the instantaneous potential has barriers due to local solvent structures. The roughness is the molecular origin of the friction coefficient. b) The time correlation functions from stochastic dynamics on the rugged energy surface match the experimental ones. c) An Arrhenius analysis on the correlation times reproduces the experimentally observed dynamical parameters.

on the low frequency spectral density. It suggests the sensitivity of even an extremely local measurement in the polar region of an ionic liquid to dynamics of the nonpolar domains. Recent theories that coupled local activated motion to long-ranged elastic deformations³⁵¹ may offer a formalism to quantify these effects.

The low frequency modes that couple to the chromophore were modeled as a set of linearly displaced Brownian oscillators. The peak of the odd portion of spectral density lies below $<10\text{ cm}^{-1}$ for $[\text{Im}_{6,1}][\text{Tf}_2\text{N}]$. It broadens and blue shifts with increasing temperature. This trend can be either explained by changes in the central frequencies or the solvent friction in the Brownian oscillator model, rather than from the explicit temperature dependence of the correlation function, which is found in the exponential prefactor that describes the magnitude of frequency fluctuations.

The qualitative picture that spectral diffusion is governed by dynamics on a rugged potential energy landscape provides a unifying model for the observed Arrhenius behavior and the Brownian oscillator model of the low frequency modes. This model describes activated barrier crossing to progress along the rough low-frequency coordinate, resulting in a effective friction decrease with increasing temperature. It suggests that the changes in spectral diffusion with increasing temperature may be more a result of solvent friction than of changing central frequency for the Brownian oscillators. A quantitative version of this model, using a Markov chain model, provides good agreement with experiment.

Further work will be carried out on these systems in the future. Experimental work with both additional chromophores that couple to different solvent motions, and with polarization control that can separate out rotational motions and give a more finely grained measurement of these dynamics is essential. Fifth-order spectroscopies, like three-dimensional infrared (3D-IR)⁷³ and Raman-terahertz spectroscopy,^{74,356} could potentially clarify the origin of the low frequency modes in these ionic liquids, and whether their broadening with temperature is the result of homogeneous or inhomogeneous processes. Finally, the non-physical attempt frequencies, the relation to anomalous diffusion and stretched exponential behavior, and the mapping of real coordinates onto frequency space warrant further study to provide detailed physical insights into the dynamics of these ionic liquids.

7.6 ACKNOWLEDGMENTS

The authors acknowledge financial support from the National Science Foundation (CHE-1454105). T. Brinzer acknowledges funding from the Pittsburgh Quantum Institute (PQI) Graduate Award. T. Brinzer thanks the University of Pittsburgh Dietrich School of Arts & Sciences Machine Shop, especially Mr. Tom Gasmire and Mr. Jeff Sicher. TB also thanks Mr. Zhe Ren for many stimulating conversations, and Profs. Mark Maroncelli and Jindal Shah for insightful questions and discussions.

8.0 CO₂, TEMPERATURE, AND 1-N-ALKYL-3-METHYLIMIDAZOLIUM ALKYL CHAIN LENGTH

8.1 INTRODUCTION

The temperature-dependence of CO₂'s 2D-IR signal in 1-*N*-alkyl-3-methylimidazolium bis-triflimide ([Im_{*n*,1}][Tf₂N]) was studied as a function of alkyl chain length ($n = 2, 4, 6$). As with thiocyanate, the changes in dynamics reported by CO₂ obey those expected for a thermally activated process with large activation barrier (~ 6 to 7 kcal mol⁻¹). Despite the lack of a net charge, and the overall faster dynamics, the *temperature-dependence* of the dynamics corresponds with a larger activation barrier than that reported by [SCN]⁻. The CO₂ dynamics also show a stronger dependence on temperature-dependent viscosity than do thiocyanate's. Taken together with molecular insights from theoretical calculations,^{10,107} these findings suggest that CO₂ in these ionic liquids reports on the dynamics of the anion and cation head groups, which define the solvent cage lifetime and on which self-transport properties in these ionic liquids depend.³

8.2 EXPERIMENTAL METHODS

The FTIR and 2D-IR optical setup, and the temperature control apparatus were identical to those previously described for temperature-dependent 2D-IR measurements of thiocyanate, excepting that a thinner PTFE spacer (Harrick, Inc.) was used to obtain an optical pathlength of 25 μm for the IR sample cell. The OPA was tuned to approximately 4.27 μm (2340 cm⁻¹) to match the center frequency of the primary CO₂ ν_3 absorbance ($|000\rangle-|001\rangle$).

Ionic liquids (1-N-alkyl-3-methylimidazolium bistriflimide ($[\text{Im}_{n,1}][\text{Tf}_2\text{N}]$), $n = 2, 4, 6$) were obtained from IoLiTec, Inc., and used without further purification. Prior to experiments, ionic liquids were dried under vacuum with a sub-10 μTorr rotary vane pump. Ionic liquids were heated to approximately 60 $^\circ\text{C}$ during the drying procedure. Water content of the ionic liquids after drying was less than 100 ppm, by FTIR analysis of the O–H stretching modes. Ionic liquids were loaded with CO_2 (99.8% purity, Matheson TriGas) to obtain a total optical density of approximately 0.3 OD at the ν_3 frequency (approximately 2340 cm^{-1}).

Frequency fluctuation correlation values were estimated using the centerline slope method (Section 3.2.2.2) with a Voigt profile to fit each slice of the spectrum. The spectra were fitted over the FWHM of the peak, to minimize contamination with the more Lorentzian wings of the spectrum (which do not exhibit spectral diffusion).

8.3 RESULTS AND DISCUSSION

8.3.1 Linear Spectroscopy

For each ionic liquid studied, the CO_2 ν_3 band does not change in central frequency with increased temperature. As expected, the main CO_2 peak broadens with increased temperature. Additionally, the overall amplitude of the main peak decreases, while that of the low frequency shoulder (which depends on thermal population in the bending mode ν_2 – Chapter 4) increases. Total oscillator strength (the area under the background subtracted CO_2 spectrum between 2300 and 2400 cm^{-1}) is conserved.

Fits of the main band to a Voigt profile indicate an increasing Lorentzian component (and decreasing Gaussian component) of the peak with increased temperature; however, it is impossible from this to say which portion of this phenomenon results from changes in local dynamics, and which portion results from lifetime and orientational effects. Since lineshape theory predicts broadening of the instantaneous frequency distribution with increasing temperature,¹⁹⁶ it is likely that this change at least partly reflects that the rate of some dynamics previously in the spectrally diffusive regime have shifted to the homogeneous regime (Section

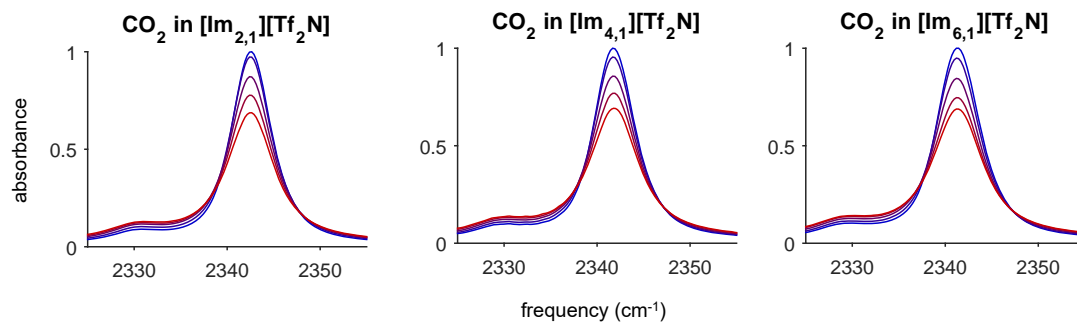


Figure 40: FTIR of CO_2 in $[\text{Im}_{n,1}][\text{Tf}_2\text{N}]$ shows broadening and decreased amplitude of the main band and an increase in the amplitude of the low frequency shoulder of CO_2 (independent of alkyl chain length), consistent with a mechanism of intramolecular anharmonic coupling of the ν_2 and ν_3 modes (Chapter 4). FTIR were taken at 5, 20, 40, 60 and 80 °C.

2.2.2). Ultimately, however, FTIR cannot explicitly resolve this origin of this change.

8.3.2 Nonlinear Spectroscopy

Two-dimensional infrared spectra of CO_2 give additional insight into the changes in the microscopic environment at which the FTIR spectrum hints (Figure 41). Distinct pathways up and down the vibrational ladder give rise to the two peaks seen in each spectrum. Each spectrum comprises a negative blue peak at the 0–1 transition frequency ($R_{1,2,4,5}^{(3)}$) and a positive red peak separated from the negative peak in ω_3 by the anharmonicity of the transition x_{33} ($R_{3,6}^{(3)}$) as discussed in Section 2.1. The expected low frequency shoulder on CO_2 's ν_3 peak from anharmonic coupling of ν_2 and ν_3 and cross-peaks from population exchange of bending modes are present (Chapter 4), but are omitted from this figure as the focus of this chapter is on the dynamics of the main band.

CO_2 in each ionic liquid displays inhomogeneity at early population times, which decreases with increasing temperature (as evidenced by the ratio of the diagonal and antidiagonal peak widths). Since the total linewidth increases with increasing temperature, this indicates that some molecular motions whose dynamics could previously be resolved have increased

in speed, and are now buried in the homogeneous linewidth of the peak. Global fitting of the spectra shows faster dephasing with increased temperature, which is consistent with this finding.

The initial inhomogeneity does not substantially change with increasing alkyl chain length, which is tentatively interpreted as indicating a similar range of frequencies for CO₂; however, due to the substantial portion of the line that is buried in the homogeneous linewidth (Chapter 6),¹⁰⁷ it is possible that this effect only results from overall slowing of the dynamics. Visual inspection of the spectra suggests an order of magnitude increase in the rate of frequency fluctuations from the lowest to the highest temperatures (based on the duration of population time for the spectrum to fully diffuse).

The temperature-dependent dynamics and lineshape of the spectra were quantified using a frequency fluctuation correlation function (FFCF). The shape of the FFCF spectrum is well-approximated by a biexponential decay (Figure 42 and Table 16). The FFCF is generally well-behaved, except for that of CO₂ in [Im_{2,1}][Tf₂N] at 77 °C, which has a slight negative offset. This offset may be due to a local heating effect, since the total absorbance in this sample was around 0.4 OD, which can lead to nonlinear optical processes.

The total inhomogeneity of the spectrum can be quantified by the sum of the amplitudes ($a_1 + a_2$), and confirms that the initial inhomogeneity is similar across alkyl chain lengths, and decreases with increasing temperature. Similar to thiocyanate, the amplitudes of the exponentials are not consistent (within an ionic liquid) across the range of temperatures, indicating that the subset of microscopic dynamics that contribute to each term varies across the temperature range. Because of this effect, the correlation time (Equation 7.5) was again used as a measure of the total rate of dynamics in the system. Despite the narrowness of the line, the contribution of the homogeneous component of the FFCF to the correlation time is negligible in ionic liquid systems.

Correlation times (τ_{corr} , Table 16) decrease approximately an order of magnitude for carbon dioxide in each ionic liquid studied, confirming the change by visual inspection of the spectra. The correlation time increases with increasing alkyl chain length. A vast fraction of the correlation time comes from the longest time relaxation processes ($a_2\tau_2 \geq 0.9\tau_{corr}$ for most temperatures), as does most of the change in correlation time with changing

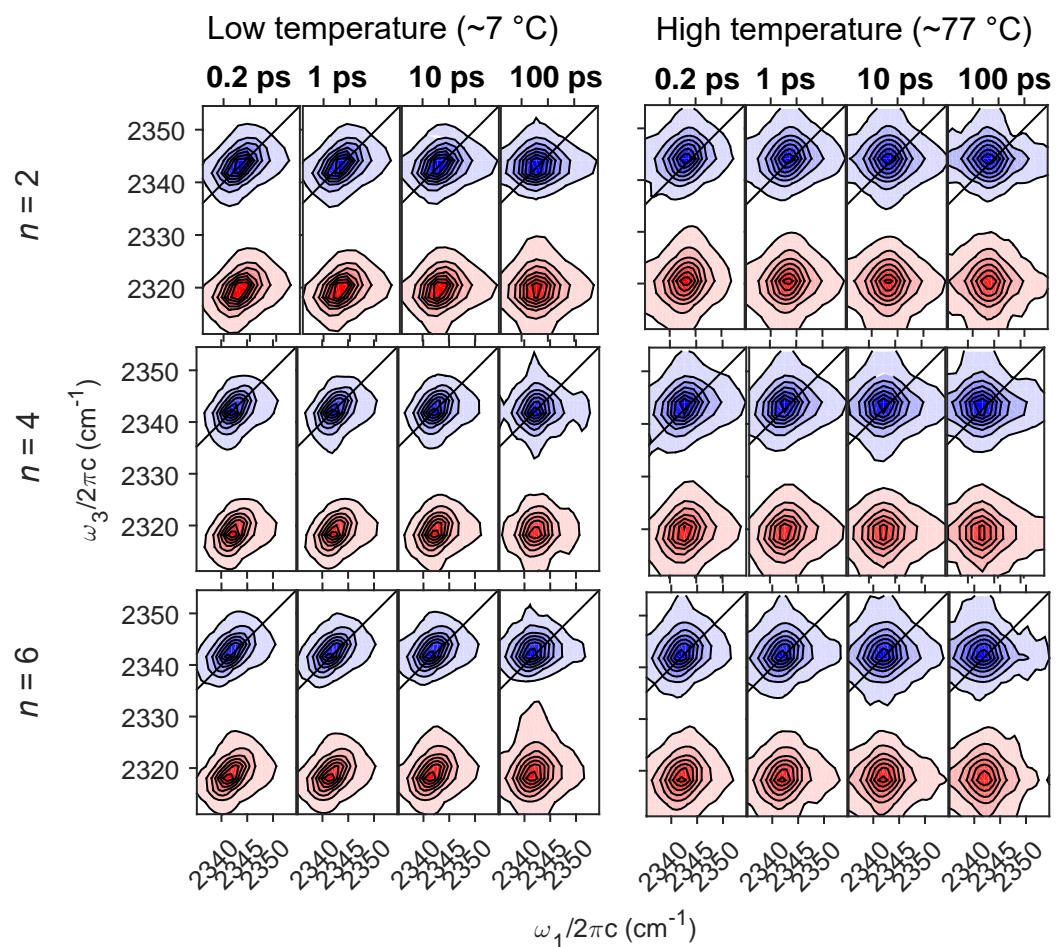


Figure 41: Temperature-dependent 2D-IR of CO₂ in [Im_{*n*,1}][Tf₂N]. The correlation times reported by CO₂ increase with increasing cation alkyl sidechain length, and decrease with increasing temperature.

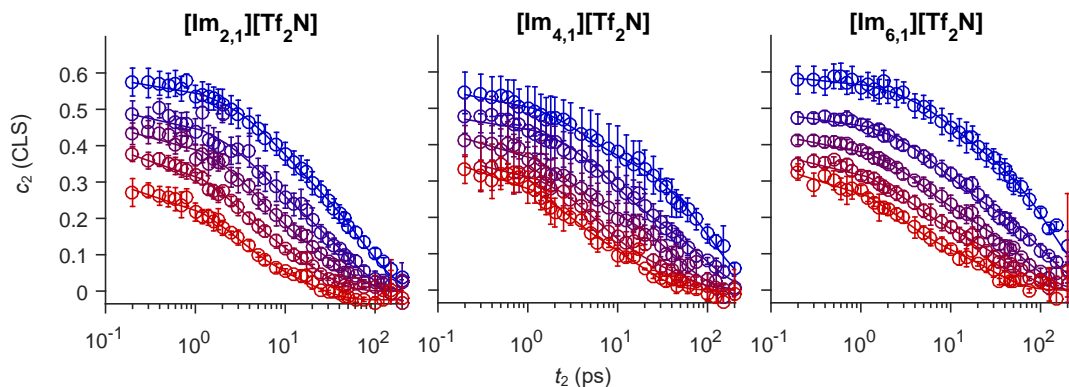


Figure 42: Temperature-dependent FFCF of CO_2 in $[\text{Im}_{n,1}][\text{Tf}_2\text{N}]$. The FFCF quantifies the increased rate of spectral diffusion, indicating that CO_2 's local environment relaxes nearly an order of magnitude faster at the highest temperatures than at the lowest temperatures.

temperature. Assuming that the longest timescales correspond to complete randomization of the solvation environment likely that they reflect the timescale of breakup of a local solvent cages, and thus the correlation time may be sensitive to this effect.

Similar to the case of thiocyanate, the correlation times of CO_2 scale with the viscosity of the ionic liquid solvent (Figure 43). Viscosities from the literature³⁵³ were interpolated using a piecewise cubic Hermite polynomial method. Unlike the case of thiocyanate, these all follow the same trend line (for $[\text{SCN}]^-$, the correlation times in $[\text{Im}_{2,1}][\text{Tf}_2\text{N}]$ are faster than would be predicted by the viscosity/ τ_{corr} relationship in $[\text{Im}_{4,1}][\text{Tf}_2\text{N}]$ and $[\text{Im}_{6,1}][\text{Tf}_2\text{N}]$). The slight curvature of the trend indicates that at low temperature, the correlation time does not scale as quickly as the bulk viscosity, indicating there are likely additional slow processes in the relaxation of the liquid structure (α relaxation), to which the correlation time is not sensitive.

8.3.3 Arrhenius Analysis

An Arrhenius analysis of the temperature-dependent correlation time shows that the correlation times of CO_2 in these liquids can each be modeled as a thermally activated process

Table 16: Best fit coefficients for the FFCF (from CLS) of CO₂ in [Im_{n,1}][Tf₂N]. Correlation times (τ_{corr}) are the integrated area under the FFCF.

T (°C)	a_1	a_2	τ_1 (ps)	τ_2 (ps)	τ_{corr} (ps)
$n = 2$					
6.7	0.19 ± 0.02	0.39 ± 0.02	6 ± 1	68 ± 5	28 ± 2
22.9	0.19 ± 0.04	0.3 ± 0.05	5 ± 2	43 ± 7	14 ± 3
40.6	0.24 ± 0.03	0.21 ± 0.03	4 ± 1	36 ± 4	9 ± 1
59.4	0.2 ± 0.02	0.19 ± 0.02	2.7 ± 0.6	19 ± 1	4.2 ± 0.5
77.0	0.18 ± 0.02	0.14 ± 0.02	2.4 ± 0.4	16 ± 2	2.7 ± 0.4
$n = 4$					
7.3	0.15 ± 0.02	0.4 ± 0.01	4 ± 1	104 ± 5	42 ± 2
22.9	0.22 ± 0.02	0.26 ± 0.02	7 ± 2	83 ± 8	23 ± 3
39.0	0.17 ± 0.03	0.26 ± 0.03	3 ± 1	43 ± 6	12 ± 2
57.0	0.22 ± 0.03	0.14 ± 0.03	5 ± 2	41 ± 9	7 ± 2
75.6	0.16 ± 0.04	0.19 ± 0.04	2 ± 1	17 ± 3	3.6 ± 0.9
$n = 6$					
6.5	0.14 ± 0.02	0.44 ± 0.02	8 ± 3	131 ± 8	59 ± 4
22.5	0.19 ± 0.02	0.29 ± 0.02	7 ± 1	107 ± 9	33 ± 3
39.4	0.17 ± 0.02	0.25 ± 0.02	4.3 ± 0.7	61 ± 5	16 ± 2
58.0	0.16 ± 0.02	0.21 ± 0.02	3.1 ± 0.7	42 ± 4	9 ± 1
76.9	0.17 ± 0.02	0.16 ± 0.02	2.4 ± 0.6	26 ± 4	4.6 ± 0.9

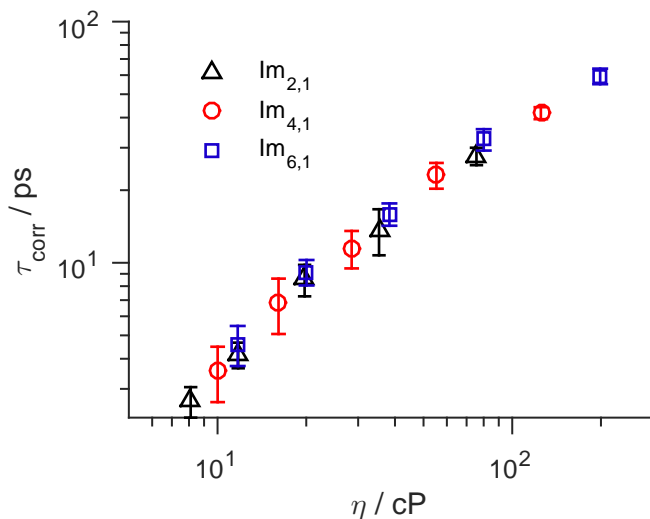


Figure 43: Temperature-dependent correlation times are approximately correlated to the bulk viscosity of each ionic liquid. Viscosities³⁵³ were interpolated using a piecewise cubic Hermite polynomial method.

(Figure 44). Since the observed CO₂ dynamics primarily reflect low frequency intramolecular modes of each solvent (Chapters 4 and 6), and we are relatively far (>90 °C) from the glass transitions for each ionic liquid,³⁵³ this behavior is not surprising.^{348,349} The Arrhenius fit is relatively sensitive to the portion of the 2D-IR peak on which the CLS analysis is performed, and therefore, care was taken to systematically fit the same region of each peak 8.2) Despite the fact that the correlation times of carbon dioxide are faster than those for thiocyanate (Chapter 7, the calculated activation barriers are higher. Additionally, the activation barriers reported by CO₂ do not show a decrease from $n = 4$ to $n = 6$. As in the cases of thiocyanate (Chapter 7) and water,³⁴¹ the pre-exponential factors recovered from the Arrhenius fits are unphysically high for ‘attempt frequencies’ at a barrier-crossing. A similar theoretical treatment of the low frequency modes to that of [SCN]⁻ (Chapter 7), utilizing the low frequency spectral density and the multimode Brownian oscillator, yields a qualitatively similar trend. The overall spectral density blue shifts and broadens with increasing temperature, which could be due to either changes in central frequency of the

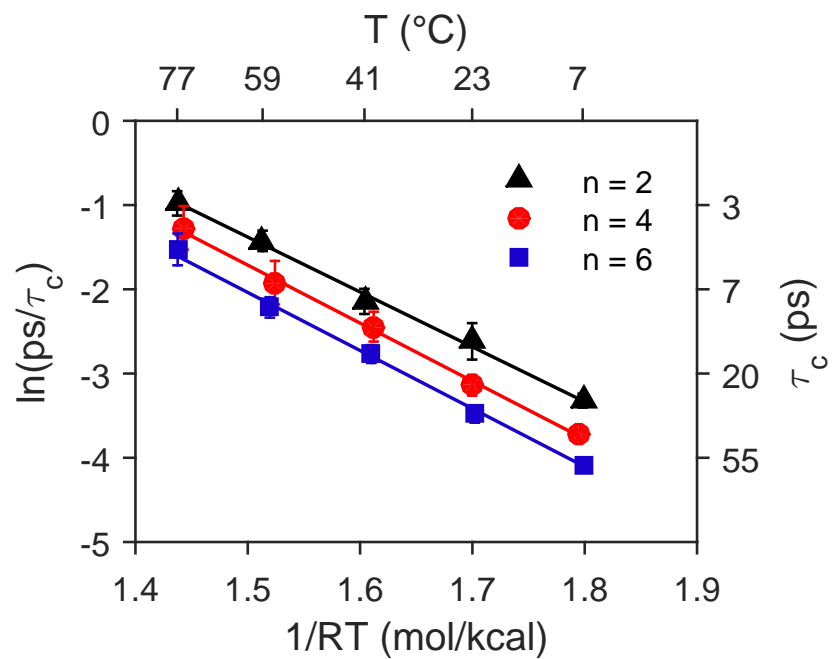


Figure 44: Arrhenius analysis of CO₂ in [Im_{n,1}][Tf₂N].

Table 17: Arrhenius analysis.

n	E_a (kcal mol ⁻¹)	A (fs ⁻¹)
2	6.5 ± 0.5	4 ± 4
4	6.9 ± 0.5	6 ± 5
6	6.9 ± 0.6	4 ± 4

mode, or changes in solvent friction. The change can be modeled using a “rugged energy landscape” model for spectral diffusion, which predicts a decrease in effective solvent friction with increasing temperature, due to thermally activated processes driving spectral diffusion.

Computational modeling of the CO₂ frequency in [Im_{4,1}][PF₆] informs the interpretation of these results (Chapter 6). There, decomposition of the computed FFCE from our recently developed spectroscopic map of CO₂ in [Im_{4,1}][PF₆] into components from the anion, cation ring, and cation alkyl tails indicates that CO₂ ν_3 frequency fluctuations are only very weakly sensitive to motions of the alkyl tails (around 15% of the total frequency fluctuation magnitude), and that the contribution of alkyl tails to the initial frequency state is lost from inertial processes in the first 100 fs. Thus, even in [Im_{6,1}][Tf₂N], which may have explicit nonpolar domains comprised of alkyl tails,¹⁵⁷⁻¹⁶¹ CO₂ is sensitive only to frequency fluctuations in the polar regions.

This model implies that carbon dioxide is reporting on the breakup of the portions of the solvent cavity from the anion and cation head, and that the energy of this solvent cage breakup may be independent of the evolution of alkyl domains (from $n = 4$ to $n = 6$). It is unclear at this time whether the increase in energy from $n = 2$ to $n = 4$ results from differences in rotational motions of CO₂ in [Im_{2,1}][Tf₂N], or if the increasing alkyl chain length results in a restriction of the local motions of the cation head groups or anions in the longer chain ionic liquids, but is not the main contributor to the energetic barriers governing their motions.

The activation barriers are larger than those from calculation or NMR experiment for CO₂ self-diffusion,³⁵⁴ but still qualitatively matches that for anion and cation diffusion. Indeed, the increase in barrier height in the presence of dilute CO₂ matches the prediction from MD simulations, but not from NMR measurements, which show a slight decrease.³⁵⁴ It is unclear if the increased barrier height to (compared with SCN⁻) is due to systematic errors in the method of spectral analysis, or if there is some bias of the measurement towards charge dense regions of the ionic liquid. The higher magnitude of the activation barrier for CO₂ in each ionic liquid (compared to [SCN]⁻) could suggest that CO₂ may be preferentially solvated in regions of the ionic liquid with higher solvent friction due to increased charge density.^{7,175,176} [SCN]⁻, which is part of the ion network, cannot seek out high charge density

(“stiff”) regions of the ionic liquid. It is difficult to think of an experimental method to definitely demonstrate this hypothesis; however, computational modeling could potentially do so.

8.4 CONCLUSIONS

The ultrafast dynamics of carbon dioxide were examined in a series of 1-*N*-alkyl-3-methylimidazolium bistriflimide ionic liquids ($[\text{Im}_{n,1}][\text{Tf}_2\text{N}]$, $n = 2, 4, 6$) at a series of temperatures ranging from 5 to 80 °C. The rate of spectral diffusion of carbon dioxide, which correlates to motions of the cation head group and anion in the ionic liquid, was found to be sensitive to both temperature and alkyl chain, increasing with increased temperature, and decreasing with increased alkyl chain length. The temperature-dependence of the correlation time (which quantifies this rate) is found to correlate strongly with bulk viscosity in each ionic liquid studied. Furthermore, the temperature dependence for the dynamics in each ionic liquid falls in the same trend line (unlike the case of the charged thiocyanate probe). The temperature-dependence of the overall dynamics is consistent with the picture of a stochastic walk on a rough potential energy surface (Chapter 7), with a higher and more consistent barrier than for $[\text{SCN}]^-$. The energetic barrier is tentatively attributed to motions of the anion and cation in charge dense (“stiff”) regions of the ionic liquid^{7,175,176}, to which CO_2 (at equilibrium and at relatively low mole fraction) migrates.

9.0 CONCLUSIONS

Taken together, this work forms the basis of a coherent microscopic picture of the solvation environment of carbon dioxide in alkylimidazolium ionic liquids. The overarching picture is that of multifactorial solvation and dynamics that do not depend purely on a single variable. It is possible, however, to refine the picture within that conceptual framework.

The 2D-IR spectrum of carbon dioxide at first glance appears to be complicated; however, it can be conceptually decomposed into three readily comprehensible sections, (1) the main ν_3 peak, (2) the low frequency shoulder and its dynamic cross-peaks with the main band, and (3) contributions from fifth order signal. The discussion of the main ν_3 peak will begin after discussion of the shoulder and fifth order signal, both because the discussion is significantly longer and because (2) and (3) are generalizable to non-ionic solvents, and potentially to chromophores other than CO_2 . The observation and understanding of both the low frequency shoulder and the fifth-order signal were made significantly easier by the narrowness of the CO_2 ν_3 peak, which allowed them to be cleanly resolved. In a peak with a broader linewidth (like most other IR probes in the condensed phase), these features would probably have been missed, and would have contributed to the spectral evolution of the main peak without being seen or understood.

9.1 CO_2 'S LOW FREQUENCY SHOULDER AND THERMALLY EXCITED BENDING MODE

Anharmonic coupling of the carbon dioxide bending (ν_2) and antisymmetric stretching (ν_3) modes causes a “hot” low frequency shoulder on the band at room temperature, shifted by

the anharmonic coupling constant (x_{23}) between the two modes. The combination of the relatively low energy of the ν_2 bending mode ($\sim 3k_B T$), its twofold degeneracy (due to the $D_{\infty H}$ symmetry of CO_2), the narrowness of the ν_3 main band, and a mild increase in the ν_3 transition dipole moment with thermally populated bending mode allow the shoulder to readily be seen at room temperature. Population exchange between the ground and thermally excited states of the bending mode over the duration of the 2D-IR experiment generate dynamic cross-peaks on the 2D-IR spectrum, the kinetics of which give insight into the thermal population dynamics of the bending mode populations at room temperature. The appearance of both the low frequency shoulder and the dynamic cross-peaks depend on the rate of thermal population dynamics in a given condensed phase environment. When the rate of exchange is too fast (as is the case when CO_2 is dissolved in liquid water), the main band and shoulder coalesce, and only a single diagonal band is seen. When the dynamics are too slow, the shoulder can be resolved, but there are no cross-peaks over the 2D-IR experimental time window.

As implied above, in discussing the spectrum of CO_2 in liquid water, the intramolecular origin of the “hot” shoulder means that it will be present in any CO_2 ν_3 spectrum at or near room temperature.ⁱ Indeed, this shoulder has been previously seen in CO_2 dissolved in organic liquids²⁷³ and polymers,¹¹² although it was mis-attributed to a harmonically forbidden combination band (a three-quantum transition), rather than allowed single quantum transitions of the heterogeneous subensembles of CO_2 . Thus, 2D-IR spectroscopy of CO_2 's stretching mode gives a mechanism to access the dynamics of the CO_2 across a variety of condensed phase environments, which could potentially be important in understanding the reactivity of CO_2 , since most reactions to CO_2 require a nonlinear transition state of the molecule.

ⁱSince many gas phase experiments are performed at very cold temperatures, the shoulder would not complicate their spectra as it depends on thermal population of the bending mode ($\Delta E \approx 8 \text{ kJ mol}^{-1}$); however, it should in principle be present in gas phase spectra of CO_2 at room temperature, assuming that transitions of the bending mode are not too fast.

9.2 FIFTH-ORDER SIGNAL

The peaks from fifth-order signal result from up-pumping of the carbon dioxide during either of the first two pulses (which are significantly more intense than the probe pulse). Since a 2D-IR experiment only experimentally resolves two coherences, and there are three coherences that contribute to a fully-resolved fifth-order signal, peaks from individual double-sided Feynman diagrams can be split into multiple components on the 2D-IR spectrum (depending on the two vibrational frequencies that are resolved). Due to the phase matching condition for these pathways ($\vec{k}_1 - \vec{k}_1 + \vec{k}_1 - \vec{k}_2 + \vec{k}_3$ or $\vec{k}_1 - \vec{k}_2 + \vec{k}_2 - \vec{k}_2 + \vec{k}_3$ for non-rephasing pathways) these signals are always emitted in the direction of third-order signal $S^{(3)}$ ($\vec{k}_1 - \vec{k}_2 + \vec{k}_3$), regardless of the collection geometry used for the 2D-IR spectrometer. Unlike the CO₂ bending mode, this fifth-order contribution should be present on every 2D-IR spectrum; however, with a relatively weaker chromophore, it likely does not rise above the level of the noise of the spectrum.ⁱⁱ Nevertheless, for strong chromophores like CO₂, and for narrow lines, it could appear as a small set of features in a similar pattern to that seen in CO₂.

9.3 CO₂ AND THE IONIC LIQUID ENVIRONMENT

The average frequency of the carbon dioxide ν_3 transition gives insight into its local interactions with different ionic liquids. The center frequency of the line varies most strongly with the choice of the anion, red-shifting further from the gas phase value with harder anions. This finding is consistent with the previous attribution in the literature of a Lewis acid-base relationship¹¹³ between CO₂ and the anion, which is the most important component of the ionic liquid in determining CO₂ solubility.²⁵⁸ Quantum chemistry calculations suggest that small amounts of charge transfer from the anion to virtual orbitals on CO₂ (some of which leaks back onto the cation) is important in determining the equilibrium geometry of CO₂ in each ionic liquid, which is the principal driver of the difference in frequency between liquids.

ⁱⁱA back of the envelope calculation suggests that for a vibrational mode with $\varepsilon \approx 500 \text{ M}^{-1} \text{ cm}^{-1}$, compared with CO₂'s $\varepsilon \approx 1000 \text{ M}^{-1} \text{ cm}^{-1}$, the signal would only be around 2% of the main band. With any increase in linewidth over CO₂'s, this would be very difficult indeed to resolve.

Further quantum calculations, carried out in the development of spectroscopic map for CO₂ support this finding, but refine it. While charge transfer is important in determining the frequency shift between different ionic liquids, electrostatic and Pauli repulsion terms are the most important terms for determining the frequency shift in a single ionic liquid. Dispersion interactions, which are important in the overall interaction energy of CO₂ with the ionic liquid, are relatively consistent across geometries of CO₂, and do not contribute substantially to the overall frequency shift.¹⁰ This finding is important in understanding the sources of spectral diffusion within any individual ionic liquid in the context of the MD/spectroscopic map results. Fast motions, with small amplitudes, give rise to large amplitude changes in the CO₂ instantaneous frequency, due to the strong distance dependence of the repulsion. The relatively large amplitude frequency changes in a short (sub-100 fs) time contribute substantially to the narrowing of the line. Longer timescale motions relate to the changing electrostatic environment around CO₂, primarily caused by ion cage breakup and disruption of the CO₂-anion interaction.

As described above, the ν_3 vibrational line of carbon dioxide appears almost motionally narrowed in ionic liquids. Lineshape analysis, with careful attention paid to the dephasing time (T_2) of carbon dioxide, suggests that the instantaneous frequency distribution of carbon dioxide is reasonable broad (FWHM \approx 16 to 22 cm⁻¹, assuming a Gaussian lineshape); however, it is narrowed to less than half of that on the IR spectrum. Despite this narrowing, the slowly-relaxing ion shell around CO₂ causes ν_3 's two-dimensional spectrum to reflect information on local structural relaxation of the liquid. The frequency and rotational dynamics of carbon dioxide in ionic liquids are gated by the motions of the constituent ions of the ionic liquid. Across 1-*N*-alkyl-3-methylimidazolium ionic liquids studied, the timescale of relaxation of CO₂'s initial environment is correlated with the bulk viscosity of the ionic liquid. This relationship suggests that the timescale of microscopic solvent cage breakup for CO₂ in a pure ionic liquid may govern macroscopic properties of interest, such as the mass transport of CO₂. Such a relationship is consistent with previous computational studies,³ but has not been previously shown experimentally.

In order to gain both further experimental insight into the relationship between spectral and translational diffusion of CO₂, and to determine the effect of increasing alkyl chain length

on CO₂ dynamics, temperature-dependent studies were carried out on both thiocyanate and carbon dioxide dissolved in ionic liquids with varying alkyl chain lengths ([Im_{*n*,1}][Tf₂N], *n* = 2, 4, 6). Thiocyanate, which is a linear triatomic that is isoelectronic with CO₂, can be thought of as a charged analog of carbon dioxide, and should interact more strongly with the local ion network than the quadrupolar CO₂, due to its stronger Coulombic interactions. Both thiocyanate and carbon dioxide exhibited thermally activated behavior in their ultrafast dynamics. Given the aforementioned correlation of microscopic dynamics with bulk viscosity, and the Arrhenius behavior of glassy liquids (like ionic liquids) far from the glass transition,^{348,349} this might be expected, but it was nevertheless difficult to reconcile with random diffusion of a small molecule in solution causing spectral diffusion.

The timescale of spectral diffusion for a mode coupled to low frequency (classical) bath modes depends on the spectral density of the bath, which can be modeled with overdamped Brownian oscillators;¹⁹⁶ however, there is no explicit temperature-dependence of spectral diffusion in this model. Modeling of the low frequency spectral density as a three mode Brownian oscillator shows that a spectral density which blue shifts and broadens with increasing temperature reproduces the observed spectral diffusion. A microscopic picture of a random walk (in frequency space) on a rugged free energy surface suggests that changes in effective solvent friction with increasing temperature cause the observed spectral diffusion trend and calculated activation barriers.

The temperature-dependent timescales of dynamical relaxation for SCN⁻ are highly correlated with the bulk viscosity in each individual ionic liquid studied; however, there is a linear offset (in log scaling) in the trend line for τ_{corr} and η between [Im_{2,1}][Tf₂N] and the longer chain ionic liquids, attribute to easier rotational motions of the ions that do not contribute to viscosity but lower the correlation times. The observed activation barriers of spectral diffusion for thiocyanate in [Im_{4,1}][Tf₂N] correspond to those calculated and measured by NMR for translational self-diffusion of ions.³⁵⁴ An unexpected decrease in activation barrier at *n* = 6 is attributed to motions of nanoscopically ordered non-polar domains, which are not present in shorter chain ionic liquids.

The temperature-dependent timescales of dynamical relaxation for CO₂ are highly correlated with the bulk viscosity in all ionic liquids studied, falling on a single trend line (unlike

SCN⁻). CO₂ shows activation barrier that are larger than those of thiocyanate by approximately 0.5 kcal mol⁻¹ to 1 kcal mol⁻¹, despite its overall shorter correlation time. These activation barriers are larger than those from calculation or NMR experiment for CO₂ self-diffusion. The increase in barrier height in the presence of dilute CO₂ matches the prediction from MD simulations, but not from NMR measurements, which show a slight decrease.³⁵⁴

It is unclear if the increased energetic barrier to spectral diffusion of CO₂ (compared with SCN⁻) is due to systematic errors in the method of spectral analysis, or if there is some bias of the measurement towards charge dense regions of the ionic liquid.^{7,175,176} Ongoing MD simulations of CO₂ in [Im_{4,1}][PF₆] do suggest that CO₂ at equilibrium occupies a charge-ordered region of the ionic liquid, which helps to stabilize its quadrupole, and that the timescale of spectral diffusion is directly related to an ion cage lifetime. Therefore, it is plausible that CO₂ is sampling the dynamics in a charge-dense (and thus more slowly evolving) region of the ionic liquid. Future temperature-dependent molecular modeling may help to resolve this question.

Dynamics in ionic liquids are subtle, with numerous competing enthalpic and entropic factors driving factors. The body of this work has laid the foundations for future studies of both CO₂ in ionic liquids and other condensed phase systems such as polymers or metal-organic frameworks. In ionic liquids, CO₂ shows multiexponential frequency and rotational dynamics, the timescale of which varies with the ionic liquid in question. Future experimental work can further elucidate the liquid structure effects that vary with choice of anion and cation (including alkyl chain), and may be able to determine whether the heterogeneous dynamics (and their temperature-dependence) result from heterogeneous or homogeneous local environments. It may also be possible to directly probe the intramolecular interactions of carbon dioxide with the anion and cation through clever two-color 2D-IR experiments. Polarization controlled work is just at its beginning in these systems as well, and may illumine the microscopic dynamics across liquids and at different temperatures. Finally, ongoing computational collaboration is both useful and necessary, and should be encouraged and expanded, as it can both guide and be guided by experimental work, and offers the potential of resolving structures and dynamics that current experiments explicitly cannot. Continued experimental and computational work can, in time, advance the understanding we

have gained here, and reach a fuller picture of the relationship between observed microscopic dynamics and bulk properties, as well as the driving fundamental interactions on which all properties of these useful and complicated materials ultimately rest.

APPENDIX

SUPPORTING INFORMATION

A.1 ANION DEPENDENCE

A.1.1 Comparison of Global Fitting with Center Line Slope

For the center line slope method, we fit the signal size as a function of final frequency (ω_3) with two Gaussians with opposite signs for each initial frequency (ω_1) data point. The resolved positions of the Gaussians of the 0 to 1 transition peak are considered the center points. The center line slope is determined by fitting the center points linearly as a function of ω_1 . Estimated errors are propagated accordingly.

The resulting center line slope is fitted to a biexponential decay as a function of t_2

$$c_2 = \sum_{i=1}^2 a_i \exp(-t_2/\tau_i) \quad (.1)$$

with the resulting parameters for CO₂ ν_3 in [Im_{4,1}][TFA]: $a = 0.09 \pm 0.04$, $\tau_1 = 2.1 \pm 2.1$ ps, $b = 0.35 \pm 0.04$, $\tau_2 = 35 \pm 5$ ps.

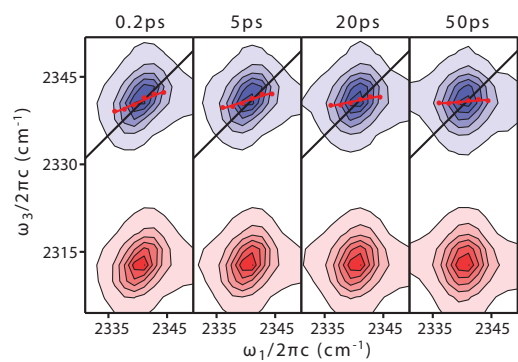


Figure 45: CLS overlaid on the 2D spectrum of CO₂ in [Im_{4,1}][TFA]

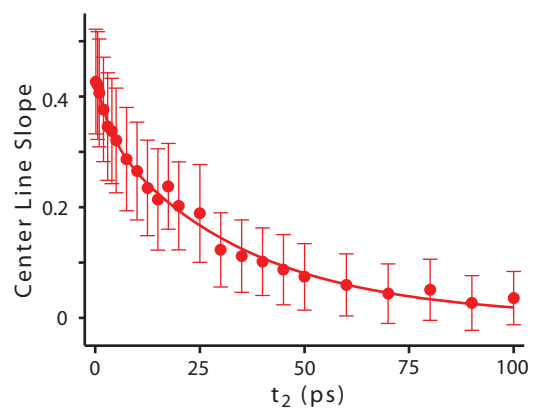


Figure 46: CLS fitting of CO₂ ν₃ 2D spectrum from [Im_{4,1}][TFA]

A.1.2 2D IR Spectra

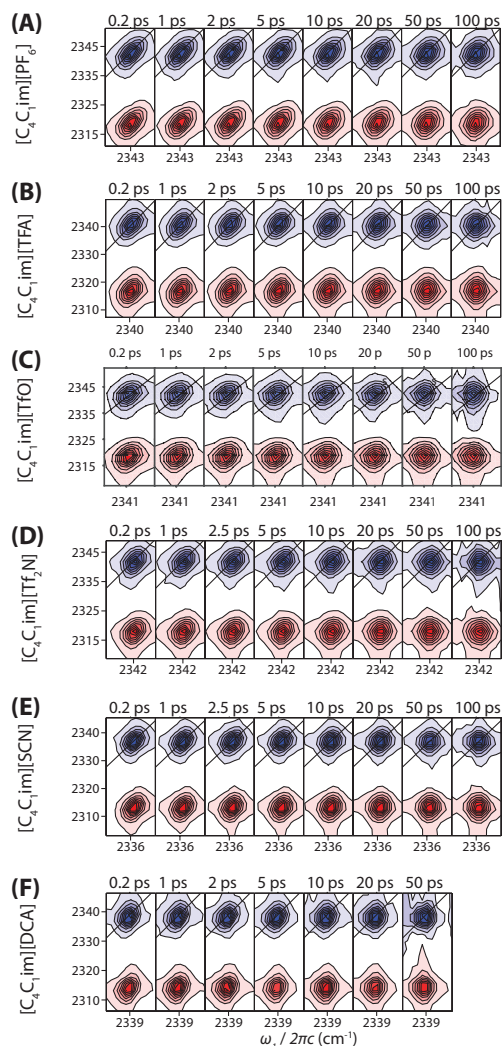


Figure 47: 2D-IR spectra of $\text{CO}_2 \nu_3$ in $[\text{Im}_{4,1}]^+$ (A) $[\text{PF}_6]^-$, (B) $[\text{Tf}_2\text{N}]^-$, and (C) $[\text{DCA}]^-$, showing the range of timescales for spectral diffusion in ν_3 .

A.1.3 Computational Results

' ν_1 ' is the frequency of the symmetric stretching mode of CO_2 , and ' ν_3 ' is the frequency of the antisymmetric stretching mode of CO_2 . α is the average of the two normal mode frequencies, $\alpha = (\omega_s + \omega_a)/2$. β is the coupling constant, or the difference of the two local mode frequencies, $\beta = (\omega_s - \omega_a)/2$.

‘CT: CO₂ to IL’ is the amount of charge transferred from the CO₂ into the ionic liquid components, ‘CT: IL to CO₂’ is the amount of charge transferred from the ionic liquid components into the CO₂, and ‘CT: net’ is the net charge transferred into the CO₂.

‘geom: angle’ is the CO₂ O–C–O angle, and ‘geom: θ ’ is the deviation of the angle from 180°. ‘geom: l_1 ’ and ‘geom: l_2 ’ are the bond lengths of the two C–O bonds, ‘geom: $l_2 - l_1$ ’ is the difference between the two bonds lengths, and ‘geom: L’ is the sum of the two bond lengths. ‘geom: O₁₂’ is the through-space oxygen-oxygen distance in CO₂.

Table 18: Geometries optimized allowing charge transfer.

	Free CO ₂	Cation	BF ₄	DCA	PF ₆	SCN	TFA	Tf ₂ N	TfO
ν_1 (cm ⁻¹)	1371.93	1372.12	1372.96	1370.71	1373.95	1370.35	1371.68	1372.88	1371.14
ν_3 (cm ⁻¹)	2436.1	2443.07	2434.71	2430.85	2437.48	2430.27	2429.81	2437.74	2433.89
β (cm ⁻¹)	-532.085	-535.475	-530.875	-530.07	-531.765	-529.96	-529.065	-532.43	-531.375
α (cm ⁻¹)	1904.015	1907.595	1903.835	1900.7	1905.715	1900.31	1900.745	1905.31	1902.515
CT:CO ₂ to IL (me)	0	2.251	1.264	2.259	1.012	1.323	1.618	1.603	2.339
CT:IL to CO ₂ (me)	0	0.079	4.558	3.376	3.336	3.317	5.131	2.493	3.009
CT: net (me)	0	-2.172	3.294	1.117	2.324	1.994	3.513	0.89	0.67
geom: angle (°)	179.96	179.93	175.49	175.01	176.21	175.65	174.78	177.36	175.99
geom: θ (°)	0.042	0.07	4.51	4.99	3.79	4.35	5.22	2.64	4.01
geom: $l_2 - l_1$ (Å)	1.9×10^{-7}	0.015	0.0087	0.011	0.0071	0.0089	0.0076	0.0076	0.011
geom: l_1 (Å)	1.169	1.176	1.174	1.175	1.173	1.165	1.173	1.165	1.175
geom: l_2 (Å)	1.169	1.161	1.165	1.164	1.165	1.174	1.166	1.173	1.164
geom:O ₁₂ (Å)	2.338	2.337	2.337	2.337	2.337	2.338	2.337	2.337	2.337
geom:L (Å)	2.338	2.337	2.338	2.339	2.338	2.339	2.339	2.338	2.339

A.2 NOVEL EUTECTIC IONIC LIQUID MIXTURE

A.2.1 Viscosity

Viscosity measurements were taken with a RheoSense microVISC viscometer, using the microVISC temperature controller to maintain the system at 50 °C. Each sample was melted and filtered through hot glass wool to remove any sediment before being loaded into a 400 μ L syringe. The syringe was placed into the viscometer before beginning temperature ramp to allow adequate equilibration time. Each sample was measured five consecutive times, and the average of these measurements is reported, along with error.

A.2.2 Density

Density measurements were obtained using a Micromeritics AccuPyc II 1340 gas pycnometer with an attached water bath to maintain a system temperature of 50 °C. A 1 cm insert was used in the 10 cm sample chamber to reduce the sample size required.

A.2.3 Water Content

Water content was determined using a Metrohm 860 Karl Fisher (KF) Thermoprep titration unit, equipped with an 831 KF Coulometer; IL samples which had undergone KF using an oven were treated as water-free samples. Viscosity measurements were made at ambient temperatures (50 °C) using a Rheosense Inc. μ Visc unit and 400 μ L pipettes.

A.2.4 DSC Melting Point

Differential scanning calorimetry (DSC) was conducted using a TA Instruments Q2000 DSC equipped with a liquid nitrogen cooling accessory. A standard DSC run was conducted with a heating and cooling rate of 10 °C min⁻¹, a temperature range of -100 °C to 150 °C, and three cycles to ensure repeatability of the results. Tzero aluminum hermetic pans were used with a sample size of approximately 10 mg. Additionally, modulated DSC was conducted using the same instrument with a heating and cooling rate of 2 °C min⁻¹, an amplitude of

0.318 °C and a period of 60 s. A heat cool heat cycle was performed and the data was taken from the second heat. The melting point was slightly lower compared to the 10 °C min⁻¹ DSC run by approximately 1 °C for the three samples tested, confirming that the 10 °C min⁻¹ DSC run was sufficient for measuring the final melting point.

A.2.5 DSC Heat Capacity

Differential scanning calorimetry (DSC) was conducted using a TA Instruments Q2000 DSC equipped with a liquid nitrogen cooling accessory. The heat capacity measurements for the samples were measured using Tzero aluminum hermetic pans. The Q2000 instrument was calibrated for Cp analysis using water at 50 °C. The heat capacity at 25 °C, 50 °C and 75 °C was measured using a sample size of approximately 10 mg. A Quasi-isothermal method using modulated DSC with a modulated temperature of ±1 °C, and a period of 120 s was used at each isothermal temperature. The temperature was kept constant for 10 min at each temperature for the signal to stabilize. Analysis of the DSC data was conducted using the reversing heat capacity signal and Universal Analysis 2000 software. The heat capacity reported was calculated by averaging the heat capacity over the last 2 min of each 10 min isotherm at each temperature.

A.2.6 Conductivity

Samples were heated to 50 °C for 10 min to melt the mixture and ensure homogeneity. The samples were withdrawn using a syringe and injected into a custom built conductivity cell. The custom built cell consisted of two 1.6 mm diameter platinum disc electrodes (BASi) in a ‘face-on’ configuration with a separation of 2 mm held within a PTFE tube of inner diameter 6 mm. The solution was injected through the side wall of the cell to fill the cavity with the PTFE wall creating a seal once the syringe was removed. The entire cell was placed into a fan circulated thermostatic oven and held at 50 °C for all impedance measurements. Samples were pretreated by holding at Over Current Protection (OCP) for 2 minutes before Electrochemical impedance spectroscopy (EIS) was carried out on each sample at OCP using 10, 20 and 50 mV perturbations sequentially over a frequency range of 0.1 to 100.000 Hz. Solution

resistance was measured at the point where the plot crossed the real axis (x axis), and was converted to a conductivity by using a measured cell constant. The cell constant was found by calibration with a $1413 \mu\text{Sv cm}^{-1}$ conductivity standard solution over the appropriate temperature range.

A.2.7 TGA Thermal Stability

Thermogravimetric analysis (TGA) was carried out using a TA Instruments Q500 with a standard furnace. The measurements were made using sample sizes of ~ 20 mg in platinum pans. Each sample was heated from room temperature to 900°C at $10^\circ\text{C min}^{-1}$, under a nitrogen flow of 60 mL min^{-1} . The onset, inflection, and end points were determined using TA Universal Analysis 2000 software.

A.2.8 IR Spectroscopy

CO_2 was loaded into each ionic liquid by exposure of a small volume of the rapidly-stirred ionic liquid to a pure CO_2 atmosphere at approximately 1 bar for 2 hours. Following this time, a $2 \mu\text{L}$ aliquot of the sample was placed between two CaF_2 windows (2 mm thickness) with a $25 \mu\text{m}$ spacer. In the case of $[\text{C}_1\text{C}_1\text{pyrr}]_{0.3}[\text{C}_1\text{pyr}]_{0.7}[\text{Tf}_2\text{N}]$, the sample was heated to $\sim 35^\circ\text{C}$ before loading, then allowed to supercool to room temperature before measuring. $[\text{Im}_{6,1}][\text{Tf}_2\text{N}]$ was loaded at room temperature. Optical density of CO_2 dissolved in $[\text{Im}_{6,1}][\text{Tf}_2\text{N}]$ was 0.3, while that dissolved in $[\text{C}_1\text{C}_1\text{pyrr}]_{0.3}[\text{C}_1\text{pyr}]_{0.7}[\text{Tf}_2\text{N}]$ was 0.1. Cells were assembled under ambient conditions. Water content of the ILs after assembly was estimated using absorbance of water stretching modes seen on FTIR. Mass fractions for $[\text{C}_1\text{C}_1\text{pyrr}]_{0.3}[\text{C}_1\text{pyr}]_{0.7}[\text{Tf}_2\text{N}]$ (0.0011) and $[\text{Im}_{6,1}][\text{Tf}_2\text{N}]$ (0.0012) were similar.

A commercial Ti:Sapphire laser source (Coherent Legend Elite) was used to pump an optical parametric amplifier (OPA) to generate mid-infrared pulses.²⁰⁴ These pulses were directed to a two-dimensional infrared (2D IR) spectrometer in a pump-probe geometry.²⁵³ The resulting signal was dispersed onto a 2×32 channel array MCT detector (Infrared Associates) using a single monochromator (150 line/mm grating) (Horiba iHR320).

Following spectral calibration, the spectra were globally fitted to a calculated spectrum,

which was based on a third-order nonlinear response function formalism¹⁹⁷ using a two point correlation function

$$c(t_2) = \frac{\delta(t_2)}{T_2} + \Delta^2 \exp\left(-\frac{t_2}{\tau_c}\right) \quad (.2)$$

where the first (Bloch) term represents molecular processes in the homogeneous (fast or motional narrowing) limit, and the second term corresponds to Kubo' s ansatz for a spectral diffusive process. The resulting lineshape function

$$g(t_2) = \frac{t_2}{T_2} + \Delta^2 \tau_c^2 \left(\exp\left(-\frac{t_2}{\tau_c}\right) + \frac{t_2}{\tau_c} - 1 \right) \quad (.3)$$

was substituted into the third-order response functions to generated a calculated 2D IR spectrum that depends on the correlation time (τ_c) and dephasing time (T_2) of the chromophore.

Following normalization of each 2D-IR spectra to the CO₂ antisymmetric stretch peak to remove the effects of vibrational relaxation on spectral intensity, a nonlinear least squares fitting algorithm was used to minimize the squared error between the series of calculated spectra and the experimental spectra, with parameters of homogeneous dephasing time (T_2), spectral diffusion time (τ_c), frequency range for spectral diffusion (Δ), anharmonicity, transition dipole moment for the 0 \rightarrow 1 and 1 \rightarrow 2 transitions, phase, and central frequency. When the value of the squared error for all spectra had converged, the fitting parameters were considered to be optimized.

In order to obtain confidence intervals for the fitting parameters, a bootstrapping procedure was employed.²⁵⁴ Briefly, the spectra were repeatedly fitted using a set of randomly selected points in the experimental and calculated spectra. The total number of data points chosen for each optimization was kept constant in order to preserve appropriate statistical weighting. The resulting parameters from 100 fits using random data points were used to generate a histogram of values for each fitting parameter, which were then analyzed to obtain confidence intervals for each parameter.

Table 20: TGA Data.

Sample	% [C ₁ pyr][Tf ₂ N]	% [C ₁ C ₁ pyrr][Tf ₂ N]	Onset (°C)	End (°C)	Inflect. (°C)	Weight (mg)	Weight (%)
AI 2-18	100	0	422.22	451.49	445.37	20.52	97.61
AI 2-24a	90	10	421.41	452.46	446.34	21.04	96.64
AI 2-24b	80	20	419.24	453.35	444.34	22.25	97.51
AI 2-24c	70	30	424.44	454.1	446.02	29.19	97.84
AI 2-24d	60	40	417.85	452.76	444.31	17.86	98.75
AI 2-24e	50	50	415.02	451.93	442.81	13.07	98.87
AI 2-24f	40	60	424.58	455.84	447.31	23.6	98.92
AI 2-24g	30	70	425.47	457.7	448.51	22.84	99.16
AI 2-24h	20	80	429.85	461.93	452.75	21.3	99.14
AI 2-24i	10	90	428.91	462.67	453.19	16.78	99.51
AI 2-19	0	100	430.55	462.87	453.79	18.11	99.62

A.2.9 Data

Table 21: MDSC Data (second heat at 2 °C min⁻¹)

Sample	% [C ₁ pyr][Tf ₂ N]	% [C ₁ C ₁ pyrr][Tf ₂ N]	T _m °C (peak)
AI 2-18	100	0	44
AI 2-24a	90	10	38
AI 2-24b	80	20	33

Table 22: **Water Content Data.** The water content of the three samples of most interest was measured using KF titration described in the water content section. Prior to the measurement the samples were sealed and stored in a Sanpla Dry Keeper vertical desiccator with a relative humidity of approximately 40%. The KF titration unit was checked for accuracy by measuring the water content of 4 Hydranol standards that contained a certified amount of 999 ppm of water. The average measurement for the water standards was 976 ppm giving an error of approximately 2.3%.

Sample	% [C ₁ pyr][Tf ₂ N]	% [C ₁ C ₁ pyrr][Tf ₂ N]	ppm H ₂ O
Al-2-24a	10	90	820 ± 50
Al-2-24b	20	80	3210 ± 50
Al-2-24c	30	70	680 ± 50

A.3 THIOCYANATE TEMPERATURE DEPENDENT 2D-IR

Table 23: Activation barrier heights and prefactors calculated from correlation times with (E_a and A) and without (E'_a and A') fast components in the correlation functions.

n	E_a (kcal/mol)	E'_a (kcal/mol)	A (fs ⁻¹)	A' (fs ⁻¹)
2	5.5	5.6	0.6	0.7
4	6.3	6.4	1.3	1.4
6	6.0	6.1	0.6	0.7

Table 24: Arrhenius fits for the intermediate and long time constants in each ionic liquid.

n	$E_a^{(2)}$ (kcal/mol)	$A^{(2)}$ (ps ⁻¹)	$E_a^{(3)}$ (kcal/mol)	$A^{(3)}$ (ps ⁻¹)
2	2.6 ± 1.2	8.7 ± 16.6	5.0 ± 1.1	92.8 ± 174.1
4	3.1 ± 1.0	13.0 ± 20.6	5.0 ± 0.9	50.1 ± 73.3
6	2.6 ± 0.9	5.5 ± 7.7	4.4 ± 0.5	18.2 ± 13.4

Table 25: Correlation times calculated for the total correlation function (τ_{corr}) and for the correlation function omitting the fast time component (τ'_{corr}). The amplitude is relatively insensitive to omission of the fast time component.

$n = 2$		
T (°C)	τ_{corr} (ps)	τ'_{corr} (ps)
6.8	32.3 ± 3.7	32.1 ± 3.7
22.6	18.0 ± 2.3	17.9 ± 2.3
39.6	11.2 ± 2.0	11.0 ± 2.0
58.2	6.9 ± 1.6	6.7 ± 1.6
75.9	4.5 ± 1.1	4.4 ± 1.1
$n = 4$		
T (°C)	τ_{corr} (ps)	τ'_{corr} (ps)
6.7	69.2 ± 10.2	68.9 ± 10.2
22.6	37.6 ± 5.3	37.3 ± 5.3
39.8	20.2 ± 4.5	20.0 ± 4.5
58.5	11.5 ± 3.5	11.3 ± 3.5
76.2	7.7 ± 3.1	7.5 ± 3.1
$n = 6$		
T (°C)	τ_{corr} (ps)	τ'_{corr} (ps)
4.9	84.5 ± 15.3	84.2 ± 15.3
22.0	48.4 ± 7.8	48.1 ± 7.8
39.4	26.1 ± 4.2	25.9 ± 4.2
58.7	15.1 ± 1.6	14.9 ± 1.6
76.6	9.1 ± 1.7	8.9 ± 1.7

BIBLIOGRAPHY

- [1] Bhowan, A. S.; Freeman, B. C. *Environ. Sci. Technol.* **2011**, *45*, 8624–8632.
- [2] Mota-Martinez, M. T.; Hallett, J. P.; Mac Dowell, N. *Sustain. Energy Fuels* **2017**, *1*, 2078–2090.
- [3] Zhang, Y.; Maginn, E. J. *J. Phys. Chem. Lett.* **2015**, *6*, 700–705.
- [4] Harris, K. R. *J. Phys. Chem. B* **2010**, *114*, 9572–9577.
- [5] Jin, H.; Li, X.; Maroncelli, M. *J. Phys. Chem. B* **2007**, *111*, 13473–13478.
- [6] Castner, E. W. J.; Margulis, C. J.; Maroncelli, M.; Wishart, J. F. *Annu. Rev. Phys. Chem.* **2011**, *62*, 85–105.
- [7] Araque, J. C.; Hettige, J. J.; Margulis, C. J. *J. Phys. Chem. B* **2015**, *119*, 12727–12740.
- [8] Kossmann, S.; Thar, J.; Kirchner, B.; Hunt, P. A.; Welton, T. *J. Chem. Phys.* **2006**, *124*, 174506.
- [9] Cremer, T.; Kolbeck, C.; Lovelock, K. R. J.; Paape, N.; Wölfel, R.; Schulz, P. S.; Wasserscheid, P.; Weber, H.; Thar, J.; Kirchner, B.; Maier, F.; Steinrück, H.-P. *Chemistry* **2010**, *16*, 9018–33.
- [10] Berquist, E. J.; Daly, C. A. J.; Brinzer, T.; Bullard, K. K.; Campbell, Z. M.; Corcelli, S. A.; Garrett-Roe, S.; Lambrecht, D. S. *J. Phys. Chem. B* **2017**, *121*, 208–220.
- [11] Hardacre, C.; Holbrey, J. D.; Mullan, C. L.; Youngs, T. G. A.; Bowron, D. T. *J. Chem. Phys.* **2010**, *133*, 74510.
- [12] Hollóczki, O.; Kelemen, Z.; Konczol, L.; Szieberth, D. D.; Nyulászi, L.; Stark, A.; Kirchner, B. *ChemPhysChem* **2013**, *14*, 315–320.
- [13] Hollóczki, O.; Malberg, F.; Welton, T.; Kirchner, B. *Phys. Chem. Chem. Phys.* **2014**, *16*, 16880–90.
- [14] Firaha, D. S.; Thomas, M.; Hollóczki, O.; Korth, M.; Kirchner, B. *J. Chem. Phys.* **2016**, *145*, 204502.

- [15] Cadena, C.; Anthony, J. L.; Shah, J. K.; Morrow, T. I.; Brennecke, J. F.; Maginn, E. J. *J. Am. Chem. Soc.* **2004**, *126*, 5300–5308.
- [16] Seo, S.; Quiroz-Guzman, M.; Desilva, M. A.; Lee, T. B.; Huang, Y.; Goodrich, B. F.; Schneider, W. F.; Brennecke, J. F. *J. Phys. Chem. B* **2014**, *118*, 5740–5751.
- [17] Karadas, F.; Atilhan, M.; Aparicio, S. *Energy & Fuels* **2010**, *24*, 5817–5828.
- [18] Corvo, M. C.; Sardinha, J.; Menezes, S. C.; Einloft, S.; Seferin, M.; Dupont, J.; Casimiro, T.; Cabrita, E. J. *Angew. Chem. Int. Ed. Engl.* **2013**, *52*, 13024–13027.
- [19] Sahu, K.; Kern, S. J.; Berg, M. A. *J. Phys. Chem. A* **2011**, *115*, 7984–7993.
- [20] Verma, S. D.; Corcelli, S. A.; Berg, M. A. *J. Phys. Chem. Lett.* **2016**, *7*, 504–508.
- [21] Woutersen, S.; Mu, Y.; Stock, G.; Hamm, P. *Chem. Phys.* **2001**, *266*, 137.
- [22] Zheng, J.; Kwak, K.; Asbury, J.; Chen, X.; Piletic, I. R.; Fayer, M. D. *Science* **2005**, *309*, 1338–1343.
- [23] Hamm, P.; Lim, M.; DeGrado, W. F.; Hochstrasser, R. M. *Proc. Natl. Acad. Sci. U.S.A.* **1999**, *96*, 2036–2041.
- [24] Zanni, M. T.; Asplund, M. C.; Hochstrasser, R. M. *J. Chem. Phys.* **2001**, *114*, 4579–4590.
- [25] Zanni, M. T.; Hochstrasser, R. M. *Curr. Opin. Struct. Biol.* **2001**, *11*, 516–522.
- [26] Hamm, P.; Hochstrasser, R. M. In *Ultrafast Infrared Raman Spectrosc.*; Fayer, M. D., Ed.; Marcel Dekker, Inc: New York, 2001; Vol. 26; pp 273–347.
- [27] Asplund, M. C.; Zanni, M. T.; Hochstrasser, R. M. *Proc. Natl. Acad. Sci. U.S.A.* **2000**, *97*, 8219–8224.
- [28] Ganim, Z.; Chung, H. S.; Smith, A. W.; DeFlores, L. P.; Jones, K. C.; Tokmakoff, A. *Acc. Chem. Res.* **2008**, *41*, 432–441.
- [29] Hamm, P.; Lim, M.; Hochstrasser, R. M. *Phys. Rev. Lett.* **1998**, *81*, 5326–5329.
- [30] Asbury, J. B.; Steinel, T.; Stromberg, C.; Gaffney, K. J.; Piletic, I. R.; Fayer, M. D. *J. Chem. Phys.* **2003**, *119*, 12981–12997.
- [31] Asbury, J. B.; Steinel, T.; Stromberg, C.; Gaffney, K. J.; Piletic, I. R.; Goun, A.; Fayer, M. D. *Phys. Rev. Lett.* **2003**, *91*, 237402.
- [32] Eaves, J. D.; Tokmakoff, A.; Geissler, P. L. *J. Phys. Chem. A* **2005**, *109*, 9424–9436.
- [33] Tokmakoff, A. *Science* **2007**, *317*, 54–55.

- [34] Zanni, M. T.; Ge, N. H.; Kim, Y. S.; Decatur, S. M.; Hochstrasser, R. M. *Biophys. J.* **2002**, *82*, 14A–14A.
- [35] Chung, H. S.; Khalil, M.; Tokmakoff, A. *J. Phys. Chem. B* **2004**, *108*, 15332–15342.
- [36] Chung, H. S.; Khalil, M.; Tokmakoff, A. *Biophys. J.* **2004**, *86*, 526A–526A.
- [37] Chung, H. S.; Khalil, M.; Smith, A. W.; Ganim, Z.; Tokmakoff, A. *Proc. Natl. Acad. Sci. U.S.A.* **2005**, *102*, 612–617.
- [38] Ganim, Z.; Tokmakoff, A. *Biophys. J.* **2006**, *91*, 2636–2646.
- [39] Smith, A. W.; Tokmakoff, A. *Angew. Chem. Int. Ed.* **2007**, *46*, 7984–7987.
- [40] Chung, H. S.; Shandiz, A.; Sosnick, T. R.; Tokmakoff, A. *Biochemistry* **2008**, *47*, 13870–13877.
- [41] Ishikawa, H.; Finkelstein, I. J.; Kim, S.; Kwak, K.; Chung, J. K.; Wakasugi, K.; Mas-sari, A. M.; Fayer, M. D. *Proc. Natl. Acad. Sci. U.S.A.* **2007**, *104*, 16116–16121.
- [42] Dunkelberger, E. B.; Grechko, M.; Zanni, M. T. *J. Phys. Chem. B* **2015**, *119*, 14065–14075.
- [43] Middleton, C. T.; Marek, P.; Cao, P.; Chiu, C.-c.; Singh, S.; Woys, A. M.; de Pa-blo, J. J.; Raleigh, D. P.; Zanni, M. T. *Nat. Chem.* **2012**, *4*, 355–360.
- [44] Backus, E. H. G.; Bloem, R.; Donaldson, P. M.; Ihalainen, J. A.; Pfister, R.; Paoli, B.; Caffisch, A.; Hamm, P. *J. Phys. Chem. B* **2010**, *114*, 3735–3740.
- [45] Buchli, B.; Waldauer, S. A.; Walser, R.; Donten, M. L.; Pfister, R.; Blöchliger, N.; Steiner, S.; Caffisch, A.; Zerbe, O.; Hamm, P. *Proc. Natl. Acad. Sci. U.S.A.* **2013**, *110*, 11725–30.
- [46] Bagchi, S.; Falvo, C.; Mukamel, S.; Hochstrasser, R. M. *J. Phys. Chem. B* **2009**, *113*, 11260–11273.
- [47] Merchant, K. A.; Noid, W. G.; Akiyama, R.; Finkelstein, I. J.; Goun, A.; McClain, B. L.; Loring, R. F.; Fayer, M. D. *J. Am. Chem. Soc.* **2003**, *125*, 13804–13818.
- [48] Finkelstein, I. J.; Goj, A.; McClain, B. L.; Massari, A. M.; Merchant, K. A.; Lo-ring, R. F.; Fayer, M. D. *J. Phys. Chem. B* **2005**, *109*, 16595–16966.
- [49] Remorino, A.; Korendovych, I. V.; Wu, Y.; DeGrado, W. F.; Hochstrasser, R. M. *Science* **2011**, *332*, 1206–1209.
- [50] Bandaria, J. N.; Dutta, S.; Hill, S. E.; Kohen, A.; Cheatum, C. M. *J. Am. Chem. Soc.* **2008**, *130*, 22–23.

- [51] Fang, C.; Bauman, J. D.; Das, K.; Remorino, A.; Arnold, E.; Hochstrasser, R. M. *Proc. Natl. Acad. Sci. U.S.A.* **2008**, *105*, 1472–1477.
- [52] Dutta, S.; Cook, R. J.; Houtman, J. C.; Kohen, A.; Cheatum, C. M. *Anal. Biochem.* **2010**, *407*, 241–246.
- [53] Bandaria, J. N.; Dutta, S.; Nydegger, M. W.; Rock, W.; Kohen, A.; Cheatum, C. M. *Proc. Natl. Acad. Sci. U.S.A.* **2010**, *107*, 17974–17979.
- [54] Dutta, S.; Li, Y.-L.; Rock, W.; Houtman, J. C. D.; Kohen, A.; Cheatum, C. M. *J. Phys. Chem. B* **2012**, *116*, 542–548.
- [55] Kuroda, D. G.; Bauman, J. D.; Challa, J. R.; Patel, D.; Troxler, T.; Das, K.; Arnold, E.; Hochstrasser, R. M. *Nat. Chem.* **2013**, *5*, 174–181.
- [56] Ghosh, A.; Wang, J.; Moroz, Y. S.; Korendovych, I. V.; Zanni, M.; DeGrado, W. F.; Gai, F.; Hochstrasser, R. M. *J. Chem. Phys.* **2014**, *140*, 235105.
- [57] Laage, D.; Stirnemann, G.; Hynes, J. T. *J. Phys. Chem. B* **2009**, *113*, 2428–2435.
- [58] Stenger, J.; Madsen, D.; Hamm, P.; Nibbering, E. T. J.; Elsaesser, T. *J. Phys. Chem. A* **2002**, *106*, 2341–2350.
- [59] Møller, K. B.; Rey, R.; Hynes, J. T. *J. Phys. Chem. A* **2004**, *108*, 1275–1289.
- [60] Rey, R.; Møller, K. B.; Hynes, J. T. *J. Phys. Chem. A* **2002**, *106*, 11993–11996.
- [61] Laage, D.; Hynes, J. T. *Chem. Phys. Lett.* **2006**, *433*, 80–85.
- [62] Ramasesha, K.; Roberts, S. T.; Nicodemus, R. A.; Mandal, A.; Tokmakoff, A. *J. Chem. Phys.* **2011**, *135*, 54509.
- [63] Nicodemus, R. A.; Ramasesha, K.; Roberts, S. T.; Tokmakoff, A. *J. Phys. Chem. Lett.* **2010**, *1*, 1068–1072.
- [64] Loparo, J. J.; Roberts, S. T.; Tokmakoff, A. *J. Chem. Phys.* **2006**, *125*, 194522.
- [65] Loparo, J. J.; Roberts, S. T.; Tokmakoff, A. *J. Chem. Phys.* **2006**, *125*, 194521.
- [66] Fecko, C. J.; Loparo, J. J.; Roberts, S. T.; Tokmakoff, A. *J. Chem. Phys.* **2005**, *122*, 54506.
- [67] Loparo, J. J.; Roberts, S. T.; Nicodemus, R. A.; Tokmakoff, A. *Chem. Phys.* **2007**, *341*, 218–229.
- [68] Steinel, T.; Asbury, J. B.; Corcelli, S. A.; Lawrence, C. P.; Skinner, J. L.; Fayer, M. D. *Chem. Phys. Lett.* **2004**, *386*, 295–300.

- [69] Asbury, J. B.; Steinel, T.; Stromberg, C.; Corcelli, S. A.; Lawrence, C. P.; Skinner, J. L.; Fayer, M. D. *J. Phys. Chem. A* **2004**, *108*, 1107–1119.
- [70] Schmidt, J. R.; Roberts, S. T.; Loparo, J. J.; Tokmakoff, A.; Fayer, M. D.; Skinner, J. L. *Chem. Phys.* **2007**, *341*, 143–157.
- [71] Garrett-Roe, S.; Hamm, P. *J. Chem. Phys.* **2009**, *130*, 164510.
- [72] Garrett-Roe, S.; Hamm, P. *Acc. Chem. Res.* **2009**, *42*, 1412–1422.
- [73] Garrett-Roe, S.; Perakis, F.; Rao, F.; Hamm, P. *J. Phys. Chem. B* **2011**, *115*, 6976–6984.
- [74] Savolainen, J.; Ahmed, S.; Hamm, P. *Proc. Natl. Acad. Sci. U.S.A.* **2013**, *110*, 20402–20407.
- [75] Kim, Y. S.; Hochstrasser, R. M. *Proc. Natl. Acad. Sci. U.S.A.* **2005**, *102*, 11185–11190.
- [76] Urbanek, D. C.; Vorobyev, D. Y.; Serrano, A. L.; Gai, F.; Hochstrasser, R. M. *J. Phys. Chem. Lett.* **2010**, *1*, 3311–3315.
- [77] Park, S.; Ji, M.; Gaffney, K. J. *J. Phys. Chem. B* **2010**, *114*, 6693–6702.
- [78] Ji, M.; Park, S.; Gaffney, K. J. *J. Phys. Chem. Lett.* **2010**, *1*, 1771–1775.
- [79] Sun, Z.; Zhang, W.; Ji, M.; Hartsock, R.; Gaffney, K. J. *J. Phys. Chem. B* **2013**, *117*, 15306–15312.
- [80] Sun, Z.; Zhang, W.; Ji, M.; Hartsock, R.; Gaffney, K. J. *J. Phys. Chem. B* **2013**, *117*, 12268–12275.
- [81] Ren, Z.; Ivanova, A. S.; Couchot-Vore, D.; Garrett-Roe, S. *J. Phys. Chem. Lett.* **2014**, *5*, 1541–1546.
- [82] Lim, M.; Hamm, P.; Hochstrasser, R. M. *Proc. Natl. Acad. Sci. U.S.A.* **1998**, *95*, 15315–15320.
- [83] Nydegger, M. W.; Dutta, S.; Cheatum, C. M. *J. Chem. Phys.* **2010**, *133*, 134506.
- [84] Dutta, S.; Ren, Z.; Brinzer, T.; Garrett-Roe, S. *Phys. Chem. Chem. Phys.* **2015**, *17*, 26575–26579.
- [85] Xu, Q.-H.; Fayer, M. D. *Laser Phys.* **2002**, *12*, 1104–1113.
- [86] Ross, M. R.; White, A. M.; Yu, F.; King, J. T.; Pecoraro, V. L.; Kubarych, K. J. *J. Am. Chem. Soc.* **2015**, *137*, 10164–10176.
- [87] Anna, J. M.; Kubarych, K. J. *J. Chem. Phys.* **2010**, *133*, 174506.

- [88] Zhang, X.; Zhang, X.; Dong, H.; Zhao, Z.; Zhang, S.; Huang, Y. *Energy Environ. Sci.* **2012**, *5*, 6668.
- [89] Miller, W. H. *J. Phys. Chem. A* **2001**, *105*, 2942–2955.
- [90] Sanda, F.; Mukamel, S. *J. Chem. Phys.* **2006**, *125*, 14507.
- [91] Miller, T. F.; Manolopoulos, D. E. *J. Chem. Phys.* **2005**, *123*, 154504.
- [92] Habershon, S.; Manolopoulos, D. E.; Markland, T. E.; Miller, T. F. *Annu. Rev. Phys. Chem.* **2013**, *64*, 387–413.
- [93] Petersilka, M.; Gossmann, U. J.; Gross, E. K. U. *Phys. Rev. Lett.* **1996**, *76*, 1212–1215.
- [94] Hayashi, T.; Zhuang, W.; Mukamel, S. *J. Phys. Chem. A* **2005**, *109*, 9747–9759.
- [95] Hayashi, T.; Zhuang, W.; Mukamel, S. Nonlinear vibrational response of the amide I, II, III and A bands of NMA: Simulation study based on an electrostatic DFT map. TRVS XII Conf. Proc. 2005.
- [96] Roy, S.; Lessing, J.; Meisl, G.; Ganim, Z.; Tokmakoff, A.; Knoester, J.; Jansen, T. L. C. *J. Chem. Phys.* **2011**, *135*, 234507.
- [97] Reppert, M.; Tokmakoff, A. *J. Chem. Phys.* **2015**, *143*, 061102.
- [98] Hayashi, T.; la Cour Jansen, T.; Zhuang, W.; Mukamel, S. *J. Phys. Chem. A* **2005**, *109*, 64–82.
- [99] Eaves, J. D.; Loparo, J. J.; Fecko, C. J.; Roberts, S. T.; Tokmakoff, A.; Geissler, P. L. *Proc. Natl. Acad. Sci. U.S.A.* **2005**, *102*, 13019–13022.
- [100] Li, S.; Schmidt, J. R.; Corcelli, S. A.; Lawrence, C. P.; Skinner, J. L. *J. Chem. Phys.* **2006**, *124*, 204110.
- [101] Oh, K.-I.; Choi, J.-H.; Lee, J.-H.; Han, J.-B.; Lee, H.; Cho, M. *J. Chem. Phys.* **2008**, *128*, 154504.
- [102] Choi, J.-H.; Oh, K.-I.; Lee, H.; Lee, C.; Cho, M. *J. Chem. Phys.* **2008**, *128*, 134506.
- [103] Lindquist, B. A.; Corcelli, S. A. *J. Phys. Chem. B* **2008**, *112*, 6301–6303.
- [104] Lindquist, B. A.; Haws, R. T.; Corcelli, S. A. *J. Phys. Chem. B* **2008**, *112*, 13991–14001.
- [105] Lindquist, B. A.; Furse, K. E.; Corcelli, S. A. *Phys. Chem. Chem. Phys.* **2009**, *11*, 8119–8132.
- [106] Błasiak, B.; Londergan, C. H.; Webb, L. J.; Cho, M. *Acc. Chem. Res.* **2017**, *50*, 968–976.

- [107] Daly, C. A. J.; Berquist, E. J.; Brinzer, T.; Garrett-Roe, S.; Lambrecht, D. S.; Corcelli, S. A. *J. Phys. Chem. B* **2016**, *120*, 12633–12642.
- [108] Jalenak, W.; Weston, R. E.; Sears, T. J.; Flynn, G. W. *J. Chem. Phys.* **1988**, *89*, 2015–2022.
- [109] Sedlacek, A. J.; Weston, R. E.; Flynn, G. W. *J. Chem. Phys.* **1991**, *94*, 6483–6490.
- [110] Michaels, C. A.; Mullin, A. S.; Park, J.; Chou, J. Z.; Flynn, G. W. *J. Chem. Phys.* **1998**, *108*, 2744–2755.
- [111] Johnson, C. J.; Poad, B. L. J.; Shen, B. B.; Continetti, R. E. *J. Chem. Phys.* **2011**, *134*, 171106.
- [112] Kazarian, S. G.; Vincent, M. F.; Bright, F. V.; Liotta, C. L.; Eckert, C. A. *J. Am. Chem. Soc.* **1996**, *118*, 1729–1736.
- [113] Kazarian, S. G.; Briscoe, B. J.; Welton, T. *Chem. Commun.* **2000**, 2047–2048.
- [114] Meredith, J. C.; Johnston, K. P.; Seminario, J. M.; Kazarian, S. G.; Eckert, C. A. *J. Phys. Chem.* **1996**, *100*, 10837–10848.
- [115] Hamm, P.; Lim, M.; Hochstrasser, R. M. Vibrational relaxation and dephasing of small molecules strongly interacting with water. Ultrafast Phenom. XI. BERLIN, 1998; pp 514–516.
- [116] Rosenthal, S. J.; Xie, X.; Du, M.; Fleming, G. R. *J. Chem. Phys.* **1991**, *95*, 4715.
- [117] Jimenez, R.; Fleming, G. R.; Kumar, P. V.; Maroncelli, M. *Nature* **1994**, *369*, 471–473.
- [118] Stratt, R. M.; Maroncelli, M. *J. Phys. Chem.* **1996**, *100*, 12981–12996.
- [119] Werner, S.; Haumann, M.; Wasserscheid, P. *Annu. Rev. Chem. Biomol. Eng.* **2010**, *1*, 203–230.
- [120] Hussey, C. L. *Pure Appl. Chem.* **1988**, *60*, 1763–1772.
- [121] Bates, E. D.; Mayton, R. D.; Ntai, I.; Davis, J. H. *J. Am. Chem. Soc.* **2002**, *124*, 926–927.
- [122] Bara, J. E.; Camper, D. E.; Gin, D. L.; Noble, R. D. *Acc. Chem. Res.* **2010**, *43*, 152–159.
- [123] Gurkan, B.; Goodrich, B. F.; Mindrup, E. M.; Ficke, L. E.; Massel, M.; Seo, S.; Senftle, T. P.; Wu, H.; Glaser, M. F.; Shah, J. K.; Maginn, E. J.; Brennecke, J. F.; Scheider, W. F. *J. Phys. Chem. Lett.* **2010**, *1*, 3494–3499.

- [124] Gurkan, B. E.; de la Fuente, J. C.; Mindrup, E. M.; Ficke, L. E.; Goodrich, B. F.; Price, E. A.; Schneider, W. F.; Brennecke, J. F. *J. Am. Chem. Soc.* **2010**, *132*, 2116–2117.
- [125] Ramdin, M.; de Loos, T. W.; Vlugt, T. J. H. *Ind. Eng. Chem. Res.* **2012**, *51*, 8149–8177.
- [126] Pinto, A. M.; Rodríguez, H.; Colo, Y. J.; Arce, A. J.; Soto, A. *Ind. Eng. Chem. Res.* **2013**, *52*, 5975–5984.
- [127] Patel, R.; Kumari, M.; Khan, A. B. *Appl. Biochem. Biotechnol.* **2014**, *172*, 3701–3720.
- [128] Buzzeo, M. C.; Evans, R. G.; Compton, R. G. *Chemphyschem* **2004**, *5*, 1106–1120.
- [129] Armand, M.; Endres, F.; MacFarlane, D. R.; Ohno, H.; Scrosati, B. *Nat. Mater.* **2009**, *8*, 621–9.
- [130] Macfarlane, D. R.; Forsyth, M.; Howlett, P. C.; Pringle, J. M.; Sun, J.; Annat, G.; Neil, W.; Izgorodina, E. I. *Acc. Chem. Res.* **2007**, *40*, 1165–1173.
- [131] van de Ven, E.; Chairuna, A.; Merle, G.; Benito, S. P.; Borneman, Z.; Nijmeijer, K. *J. Power Sources* **2013**, *222*, 202–209.
- [132] Yasuda, T.; Watanabe, M. *MRS Bull.* **2013**, *38*, 560–566.
- [133] Ketabi, S.; Decker, B.; Lian, K. *Solid State Ionics* **2016**, *298*, 73–79.
- [134] Welton, T. *Chem. Rev.* **1999**, *99*, 2071–2083.
- [135] Welton, T. *Coord. Chem. Rev.* **2004**, *248*, 2459–2477.
- [136] Martins, M. A. P.; Frizzo, C. P.; Moreira, D. N.; Zanatta, N.; Bonacorso, H. G. *Chem. Rev.* **2008**, *108*, 2015–2050.
- [137] Hallett, J. P.; Welton, T. *Chem. Rev.* **2011**, *111*, 3508–3576.
- [138] Wang, T.; Zhu, Y.; Getahun, Z.; Du, D.; Huang, C.-Y.; DeGrado, W. F.; Gai, F. *J. Phys. Chem. B* **2004**, *108*, 15301–15310.
- [139] Plechkova, N. V.; Seddon, K. R. *Chem. Soc. Rev.* **2008**, *37*, 123–150.
- [140] Zhou, F.; Liang, Y.; Liu, W. *Chem. Soc. Rev.* **2009**, *38*, 2590–2599.
- [141] Wishart, J. F. *Energy Environ. Sci.* **2009**, *2*, 956.
- [142] Brandt, A.; Gräsvik, J.; Hallett, J. P.; Welton, T. *Green Chem.* **2013**, *15*, 550–583.
- [143] Davis, J. H. *J. Chem. Lett.* **2004**, *33*, 1072–1077.
- [144] Davis, J. H. *Acc. Chem. Res.* **2005**, *38*, 49–56.

- [145] Bonhôte, P.; Dias, A.-P.; Papageorgiou, N.; Kalyanasundaram, K.; Grätzel, M. *Inorg. Chem.* **1996**, *35*, 1168–1178.
- [146] MacFarlane, D. R.; Forsyth, M.; Izgorodina, E. I.; Abbott, A. P.; Annat, G.; Fraser, K. *Phys. Chem. Chem. Phys.* **2009**, *11*, 4962–4967.
- [147] Ueno, K.; Tokuda, H.; Watanabe, M. *Phys. Chem. Chem. Phys.* **2010**, *12*, 1649–1658.
- [148] Every, H. A.; Bishop, A. G.; MacFarlane, D. R.; Orädd, G.; Forsyth, M. *Phys. Chem. Chem. Phys.* **2004**, *6*, 1758–1765.
- [149] Tokuda, H.; Tsuzuki, S.; Susan, M. A. B. H.; Hayamizu, K.; Watanabe, M. *J. Phys. Chem. B* **2006**, *110*, 19593–19600.
- [150] Katoh, R.; Hara, M.; Tsuzuki, S. *J. Phys. Chem. B* **2008**, *112*, 15426–15430.
- [151] Daguene, C.; Dyson, P. J.; Krossing, I.; Oleinikova, A.; Slattery, J.; Wakai, C.; Weingärtner, H. *J. Phys. Chem. B* **2006**, *110*, 12682–12688.
- [152] Weingärtner, H.; Sasisanker, P.; Daguene, C.; Dyson, P. J.; Krossing, I.; Slattery, J. M.; Schubert, T. *J. Phys. Chem. B* **2007**, *111*, 4775–4780.
- [153] Del Pópolo, M. G.; Voth, G. A. *J. Phys. Chem. B* **2004**, *108*, 1744–1752.
- [154] Hu, Z.; Margulis, C. J. *Proc. Natl. Acad. Sci. U.S.A.* **2006**, *103*, 831–836.
- [155] Araque, J. C.; Hettige, J. J.; Margulis, C. J. *J. Chem. Phys.* **2015**, *143*, 134505.
- [156] Kashyap, H. K.; Hettige, J. J.; Annapureddy, H. V. R.; Margulis, C. J. *Chem. Commun.* **2012**, *48*, 5103–5105.
- [157] Triolo, A.; Russina, O.; Bleif, H.-J.; Di Cola, E. *J. Phys. Chem. B* **2007**, *111*, 4641–4644.
- [158] Russina, O.; Triolo, A.; Gontrani, L.; Caminiti, R.; Xiao, D.; Hines, Jr., L. G.; Bartsch, R. A.; Quitevis, E. L.; Pleckhova, N.; Seddon, K. R. *J. Phys. Condens. Matter* **2009**, *21*, 424121.
- [159] Triolo, A.; Russina, O.; Caminiti, R.; Shirota, H.; Lee, H. Y.; Santos, C. S.; Murthy, N. S.; Castner, E. W. *J. Chem. Commun.* **2012**, *48*, 4959.
- [160] Kashyap, H. K.; Santos, C. S.; Annapureddy, H. V. R.; Murthy, N. S.; Margulis, C. J.; Castner, E. W. *J. Faraday Discuss.* **2012**, *154*, 133.
- [161] Hayes, R.; Warr, G. G.; Atkin, R. *Chem. Rev.* **2015**, *115*, 6357–6426.
- [162] Urahata, S. M.; Ribeiro, M. C. C. *J. Chem. Phys.* **2004**, *120*, 1855–1863.
- [163] Wang, Y.; Voth, G. A. *J. Am. Chem. Soc.* **2005**, *127*, 12192–12193.

- [164] Canongia Lopes, J. N. A.; Pádua, A. A. H. *J. Phys. Chem. B* **2006**, *110*, 3330–3335.
- [165] Turton, D. A.; Hunger, J.; Stoppa, A.; Hefter, G.; Thoman, A.; Walkther, M.; Buchner, R.; Wynne, K. *J. Am. Chem. Soc.* **2009**, *131*, 11140–11146.
- [166] Dougan, L.; Bates, S. P.; Hargreaves, R.; Fox, J. P.; Crain, J.; Finney, J. L.; Réat, V.; Soper, A. K. *J. Chem. Phys.* **2004**, *121*, 6456–6462.
- [167] Dixit, S.; Crain, J.; Poon, W. C. K.; Finney, J. L.; Soper, A. K. *Nature* **2002**, *416*, 829–832.
- [168] Takamuku, T.; Saisho, K.; Nozawa, S.; Yamaguchi, T. *J. Mol. Liq.* **2005**, *119*, 133–146.
- [169] Maginn, E. J. *J. Phys. Condens. Matter* **2009**, *21*, 373101.
- [170] Sonnleitner, T.; Turton, D. A.; Waselikowski, S.; Hunger, J.; Stoppa, A.; Walther, M.; Wynne, K.; Buchner, R. *J. Mol. Liq.* **2014**, *192*, 19–25.
- [171] Wendler, K.; Brehm, M.; Malberg, F.; Kirchner, B.; Delle Site, L. *J. Chem. Theory Comput.* **2012**, *8*, 1570–1579.
- [172] Huang, X.; Margulis, C. J.; Li, Y.; Berne, B. J. *J. Am. Chem. Soc.* **2005**, *127*, 17842–17851.
- [173] Kerlé, D.; Ludwig, R.; Geiger, A.; Paschek, D. *J. Phys. Chem. B* **2009**, *113*, 12727–35.
- [174] Kaintz, A.; Baker, G.; Benesi, A.; Maroncelli, M. *J. Phys. Chem. B* **2013**, *117*, 11697–708.
- [175] Araque, J. C.; Daly, R. P.; Margulis, C. J. *J. Chem. Phys.* **2016**, *144*, 204504.
- [176] Araque, J. C.; Yadav, S. K.; Shadeck, M.; Maroncelli, M.; Margulis, C. J. *J. Phys. Chem. B* **2015**, *119*, 7015–7029.
- [177] Ito, N.; Arzhantsev, S.; Heitz, M.; Maroncelli, M. *J. Phys. Chem. B* **2004**, *108*, 5771–5777.
- [178] Zhang, X.-X.; Liang, M.; Ernsting, N. P.; Maroncelli, M. *J. Phys. Chem. B* **2013**, *117*, 4291–4304.
- [179] Terranova, Z. L.; Corcelli, S. A. *J. Phys. Chem. B* **2013**, *117*, 15659–15666.
- [180] Aki, S. N. V. K.; Mellein, B. R.; Saurer, E. M.; Brennecke, J. F. *J. Phys. Chem. B* **2004**, *108*, 20355–20365.
- [181] Scovazzo, P.; Camper, D.; Kieft, J.; Poshusta, J.; Koval, C.; Noble, R. *Ind. Eng. Chem. Res.* **2004**, *43*, 6855–6860.
- [182] Carvalho, P. J.; Coutinho, J. A. P. *J. Phys. Chem. Lett.* **2010**, *1*, 774–780.

- [183] Torralba-Calleja, E.; Skinner, J.; Gutiérrez-Tauste, D. *J. Chem.* **2013**, *2013*.
- [184] Shim, Y.; Kim, H. J. *J. Phys. Chem. B* **2010**, *114*, 10160–10170.
- [185] Bhargava, B. L.; Balasubramanian, S. *Chem. Phys. Lett.* **2007**, *444*, 242–246.
- [186] Cabço, M. I.; Besnard, M.; Danten, Y.; Coutinho, J. A. P. *J. Phys. Chem. A* **2012**, *116*, 1605–1620.
- [187] Andanson, J.-M.; Jutz, F.; Baiker, A. *J. Phys. Chem. B* **2009**, *113*, 10249–10254.
- [188] Yokozeki, A.; Shiflett, M. B.; Junk, C. P.; Grieco, L. M.; Foo, T. *J. Phys. Chem. B* **2008**, *112*, 16654–63.
- [189] Indarto, A.; Palgunadi, J. *Ionics (Kiel)*. **2011**, *18*, 143–150.
- [190] Shin, E.-K.; Lee, B.-C. *J. Chem. Eng. Data* **2008**, *53*, 2728–2734.
- [191] Anderson, J. L.; Dixon, J. K.; Brennecke, J. F. *Acc. Chem. Res.* **2007**, *40*, 1208–16.
- [192] Carlisle, T. K.; Bara, J. E.; Gabriel, C. J.; Noble, R. D.; Gin, D. L. *Ind. Eng. Chem. Res.* **2008**, *47*, 7005–7012.
- [193] Reichert, W. M.; Eucker, W.; Trulove, P. C.; Urban, J. J.; De Long, H. C. *ECS Trans.* **2009**, *16*, 151–163.
- [194] Anthony, J. L.; Maginn, E. J.; Brennecke, J. F. *J. Phys. Chem. B* **2002**, *106*, 7315–7320.
- [195] Carvalho, P. J.; Alvarez, V. H.; Schröder, B.; Gil, A. M.; Marrucho, I. M.; Aznar, M.; Santos, L. M. N. B. F.; Coutinho, J. A. P. *J. Phys. Chem. B* **2009**, *113*, 6803–6812.
- [196] Mukamel, S. *Principles of Nonlinear Optical Spectroscopy*; Oxford University Press: New York, 1995.
- [197] Hamm, P.; Zanni, M. T. *Concepts and Methods of {2D} Infrared Spectroscopy*; Cambridge University Press, 2011.
- [198] Feynman, R. P.; Leighton, R. B.; Sands, M. *The Feynman Lectures of Physics. Volume I: Mainly Mechanics, Radiation, and Heat*; Addison-Wesley Pub. Co.: Reading, Mass., 1963.
- [199] Kubo, R. In *Adv. Chem. Phys. Stoch. Process. Chem. Phys.*; Shuler, K. E., Ed.; John Wiley & Sons, Inc.: Hoboken, NJ, USA, 1969; Chapter 6, pp 101–127.
- [200] Rivera, C. A.; Souna, A. J.; Bender, J. S.; Manfred, K.; Fourkas, J. T. *J. Phys. Chem. B* **2013**, *117*, 15875–15885.

- [201] Kramer, P. L.; Nishida, J.; Giammanco, C. H.; Tamimi, A.; Fayer, M. D. *J. Chem. Phys.* **2015**, *142*, 184505.
- [202] Kramer, P. L.; Nishida, J.; Fayer, M. D. *J. Chem. Phys.* **2015**, *143*, 124505.
- [203] Ren, Z.; Garrett-Roe, S. *J. Chem. Phys.* **2017**, *147*, 144504.
- [204] Hamm, P.; Kaindl, R. A.; Stenger, J. *Opt. Lett.* **2000**, *25*, 1798–1800.
- [205] Helbing, J.; Hamm, P. *J. Opt. Soc. Am. B* **2011**, *28*, 171.
- [206] Welty, J. R.; Rorrer, G. L.; Foster, D. G. In *Fundamentals of Momentum, Heat, and Mass Transfer*, 6th ed.; Sayre, D., Ed.; John Wiley & Sons, Inc.: Hoboken, NJ, USA, 2015.
- [207] Roberts, S. T.; Loparo, J. J.; Tokmakoff, A. *J. Chem. Phys.* **2006**, *125*, 84502.
- [208] Lazonder, K.; Pshenichnikov, M. S.; Wiersma, D. A. *Opt. Lett.* **2006**, *31*, 3354–3356.
- [209] Kwak, K.; Park, S.; Finkelstein, I. J.; Fayer, M. D. *J. Chem. Phys.* **2007**, *127*, 124503.
- [210] Kwak, K.; Rosenfeld, D. E.; Fayer, M. D. *J. Chem. Phys.* **2008**, *128*, 204505.
- [211] Fenn, E. E.; Fayer, M. D. *J. Chem. Phys.* **2011**, *135*, 074502.
- [212] Ingle, J. D.; Crouch, S. R. *Spectrochemical Analysis*; Prentice Hall: Englewood Cliffs, N.J., 1988.
- [213] Millward, A. R.; Yaghi, O. M. *J. Am. Chem. Soc.* **2005**, *127*, 17998–17999.
- [214] Sumida, K.; Rogow, D. L.; Mason, J. A.; McDonald, T. M.; Bloch, E. D.; Herm, Z. R.; Bae, T.-h.; Long, J. R. *Chem. Rev.* **2012**, *112*, 724–781.
- [215] Du, N.; Park, H. B.; Robertson, G. P.; Dal-Cin, M. M.; Visser, T.; Scoles, L.; Guiver, M. D. *Nat. Mater.* **2011**, *10*, 372–375.
- [216] Dawson, R.; Stöckel, E.; Holst, J. R.; Adams, D. J.; Cooper, A. I. *Energy Environ. Sci.* **2011**, *4*, 4239.
- [217] Holbrey, J. D.; Seddon, K. R. *Clean Technol. Environ. Policy* **1999**, *1*, 223–236.
- [218] Bara, J. E.; Carlisle, T. K.; Gabriel, C. J.; Camper, D.; Finotello, A.; Gin, D. L.; Noble, R. D. *Ind. Eng. Chem. Res.* **2009**, *48*, 2739–2751.
- [219] Cadena, C.; Anthony, J. L.; Shah, J. K.; Morrow, T. I.; Brennecke, J. F.; Maginn, E. J. *J. Am. Chem. Soc.* **2004**, *126*, 5300–5308.
- [220] Seo, S.; Quiroz-Guzman, M.; Desilva, M. A.; Lee, T. B.; Huang, Y.; Goodrich, B. F.; Schneider, W. F.; Brennecke, J. F. *J. Phys. Chem. B* **2014**, *118*, 5740–5751.

- [221] Wang, C.; Luo, X.; Luo, H.; Jiang, D.-e.; Li, H.; Dai, S. *Angew. Chem. Int. Ed. Engl.* **2011**, *50*, 4918–4922.
- [222] Wang, C.; Luo, H.; Jiang, D.-e.; Li, H.; Dai, S. *Angew. Chemie* **2010**, *122*, 6114–6117.
- [223] Zhang, Y.; Zhang, S.; Lu, X.; Zhou, Q.; Fan, W.; Zhang, X. *Chemistry* **2009**, *15*, 3003–3011.
- [224] Paduszyński, K.; Domańska, U. *J. Chem. Inf. Model.* **2014**, *54*, 1311–1324.
- [225] Yan, F.; Lartey, M.; Jariwala, K.; Bowser, S.; Damodaran, K.; Albenze, E.; Luebke, D. R.; Nulwala, H. B.; Smit, B.; Haranczyk, M. *J. Phys. Chem. B* **2014**, *118*, 13609–13620.
- [226] Chatel, G.; Pereira, J. F. B.; Debbeti, V.; Wang, H.; Rogers, R. D. *Green Chem.* **2014**, *16*, 2051–2083.
- [227] Maximo, G. J.; Santos, R. J. B. N.; Brandão, P.; Esperança, J. M. S. S.; Costa, M. C.; Meirelles, A. J. A.; Freire, M. G.; Coutinho, J. A. P. *Cryst. Growth Des.* **2014**, *14*, 4270.
- [228] Romanos, G. E.; Zubeir, L. F.; Likodimos, V.; Falaras, P.; Kroon, M. C.; Iliev, B.; Adamova, G.; Schubert, T. J. S. *J. Phys. Chem. B* **2013**, *117*, 12234–12251.
- [229] Camper, D.; Bara, J. E.; Gin, D. L.; Noble, R. D. *Ind. Eng. Chem. Res.* **2008**, *47*, 8496–8498.
- [230] Yu, G.; Zhang, S.; Yao, X.; Zhang, J.; Dong, K.; Dai, W.; Mori, R. *Ind. Eng. Chem. Res.* **2006**, *45*, 2875–2880.
- [231] Gonzalez-Miquel, M.; Talreja, M.; Ethier, A. L.; Flack, K.; Switzer, J. R.; Biddinger, E. J.; Pollet, P.; Palomar, J.; Rodriguez, F.; Eckert, C. A.; Liotta, C. L. *Ind. Eng. Chem. Res.* **2012**, *51*, 16066–16073.
- [232] Steckel, J. A. *J. Phys. Chem. A* **2012**, *116*, 11643–11650.
- [233] Palomar, J.; Gonzalez-Miquel, M.; Polo, A.; Rodriguez, F. *Ind. Eng. Chem. Res.* **2011**, *50*, 3452–3463.
- [234] Shi, W.; Sorescu, D. C.; Luebke, D. R.; Keller, M. J.; Wickramanayake, S. *J. Phys. Chem. B* **2010**, *114*, 6531–6541.
- [235] Shi, W.; Thompson, R. L.; Albenze, E.; Steckel, J. A.; Nulwala, H. B.; Luebke, D. R. *J. Phys. Chem. B* **2014**, *118*, 7383–7394.
- [236] Shah, J. K.; Brennecke, J. F.; Maginn, E. J. *Green Chem.* **2002**, *4*, 112–118.
- [237] Kerlé, D.; Ludwig, R.; Paschek, D. *Zeitschrift für Phys. Chemie* **2013**, *227*, 167–176.

- [238] Ghobadi, A. F.; Taghikhani, V.; Elliott, J. R. *J. Phys. Chem. B* **2011**, *115*, 13599–13607.
- [239] Khalil, M.; Demirdöven, N.; Tokmakoff, A. *J. Phys. Chem. A* **2003**, *107*, 5258–5279.
- [240] Cho, M. *Chem. Rev.* **2008**, *108*, 1331–1418.
- [241] Wong, D. B.; Giammanco, C. H.; Fenn, E. E.; Fayer, M. D. *J. Phys. Chem. B* **2013**, *117*, 623–635.
- [242] Woutersen, S.; Mu, Y.; Stock, G.; Hamm, P. *Proc. Natl. Acad. Sci. U.S.A.* **2001**, *98*, 11254–11258.
- [243] Cabaço, M. I.; Besnard, M.; Danten, Y.; Coutinho, J. A. P. *J. Phys. Chem. B* **2011**, *115*, 3538–3550.
- [244] Dahl, K.; Sando, G. M.; Fox, D. M.; Sutto, T. E.; Owrutsky, J. C. *J. Chem. Phys.* **2005**, *123*, 084504.
- [245] Maroncelli, M.; Zhang, X.-X.; Liang, M.; Roy, D.; Ernsting, N. P. *Faraday Discuss.* **2012**, *154*, 409.
- [246] Xiao, D.; Hines Jr., L. G.; Bartsch, R. A.; Quitevis, E. L. *J. Phys. Chem. B* **2009**, *113*, 4544–4548.
- [247] Bardak, F.; Xiao, D.; Hines, L. G. J.; Son, P.; Bartsch, R. A.; Quitevis, E. L.; Yang, P.; Voth, G. A. *ChemPhysChem* **2012**, *13*, 1687–1700.
- [248] Turton, D. A.; Sonnleitner, T.; Ortner, A.; Walther, M.; Hefter, G.; Seddon, K. R.; Stana, S.; Plechkova, N. V.; Buchner, R.; Wynne, K. *Faraday Discuss.* **2012**, *154*, 145.
- [249] Castner, E. W. J.; Wishart, J. F.; Shirota, H. *Acc. Chem. Res.* **2007**, *40*, 1217–1227.
- [250] Hamm, P.; Lim, M.; Hochstrasser, R. M. Vibrational relaxation and dephasing of small molecules strongly interacting with water. Ultrafast Phenom. XI Proc. 11th Int. Conf. 1998; pp 514–516.
- [251] Garrett-Roe, S.; Hamm, P. *J. Chem. Phys.* **2009**, *130*, 164510.
- [252] Giernoth, R.; Bankmann, D. *European J. Org. Chem.* **2008**, 2881–2886.
- [253] Helbing, J.; Hamm, P. *J. Opt. Soc. Am. B* **2010**, *28*, 171–178.
- [254] Press, W. H.; Teukolsky, S. A.; Vetterlin, W. T.; Flannery, B. P. *Numerical Recipes in C*, 2nd ed.; Cambridge University Press: New York, 1992.
- [255] Shao, Y. *et al. Mol. Phys.* **2015**, *113*, 184–215.
- [256] Merrick, J. P.; Moran, D.; Radom, L. *J. Phys. Chem. A* **2007**, *111*, 11683–11700.

- [257] Khaliullin, R. Z.; Head-Gordon, M.; Bell, A. T. *J. Chem. Phys.* **2006**, *124*, 204105.
- [258] Anthony, J. L.; Anderson, J. L.; Maginn, E. J.; Brennecke, J. F. *J. Phys. Chem. B* **2005**, *109*, 6366–6374.
- [259] Khaliullin, R. Z.; Cobar, E. A.; Lochan, R. C.; Bell, A. T.; Head-Gordon, M. *J. Phys. Chem. A* **2007**, *111*, 8753–8765.
- [260] Khaliullin, R. Z.; Bell, A. T.; Head-Gordon, M. *J. Chem. Phys.* **2008**, *128*, 184112.
- [261] Ramos-Cordoba, E.; Lambrecht, D. S.; Head-Gordon, M. *Faraday Discuss.* **2011**, *150*, 345.
- [262] Bakowies, D.; Thiel, W. *J. Phys. Chem.* **1996**, *100*, 10580–10594.
- [263] Hu, L.; Söderhjelm, P.; Ryde, U. *J. Chem. Theory Comput.* **2011**, *7*, 761–777.
- [264] Breen, K. J.; DeBlase, A. F.; Guasco, T. L.; Voora, V. K.; Jordan, K. D.; Nagata, T.; Johnson, M. A. *J. Phys. Chem. A* **2012**, *116*, 903–912.
- [265] Muraoka, A.; Inokuchi, Y.; Hammer, N. I.; Shin, J.-w.; Johnson, M. A.; Nagata, T. *J. Phys. Chem. A* **2009**, *113*, 8942–8948.
- [266] Lee, A. J.; Rick, S. W. *J. Chem. Phys.* **2011**, *134*, 184507.
- [267] Khaliullin, R. Z.; Bell, A. T.; Head-Gordon, M. *Chem. - A Eur. J.* **2009**, *15*, 851–855.
- [268] Hochstrasser, R. M. *Chem. Phys.* **2001**, *266*, 273–284.
- [269] Botan, V.; Hamm, P. *J. Chem. Phys.* **2008**, *129*, 164506.
- [270] Taylor, P. R.; Lee, J. M. L. *Chem. Phys. Lett.* **1993**, *205*, 535–542.
- [271] Dressier, S.; Thiel, W. *Chem. Phys. Lett.* **1997**, *273*, 71–78.
- [272] Culp, J. T.; Goodman, A. L.; Chirdon, D.; Sankar, S. G.; Matranga, C. *J. Phys. Chem. C* **2010**, *114*, 2184–2191.
- [273] Cunliffe-Jones, D. B. *Spectrochim. Acta Part A* **1969**, *25*, 779.
- [274] Dobrowolski, J. C.; Jamróz, M. H. *J. Mol. Struct.* **1992**, *275*, 211–219.
- [275] Giammanco, C. H.; Kramer, P. L.; Yamada, S. A.; Nishida, J.; Tamimi, A.; Fayer, M. D. *J. Chem. Phys.* **2016**, *144*, 104506.
- [276] Kaintz, A.; Baker, G.; Benesi, A.; Maroncelli, M. *J. Phys. Chem. B* **2014**, *118*, 5615–5615.
- [277] Li, W.; Zhang, Z.; Han, B.; Hu, S.; Xie, Y.; Yang, G. *J. Phys. Chem. B* **2007**, *111*, 6452–6456.

- [278] Tokuda, H.; Tsuzuki, S.; Susan, M. A. B. H.; Hayamizu, K.; Watanabe, M. *J. Phys. Chem. B* **2006**, *110*, 19593–19600.
- [279] Domańska, U.; Królikowska, M. *J. Solution Chem.* **2012**, *41*, 1422–1445.
- [280] Sánchez, L. G.; Espel, J. R.; Onink, F.; Meindersma, G. W.; de Haan, A. B. *J. Chem. Eng. Data* **2009**, *54*, 2803–2812.
- [281] Asbury, J. B.; Steinel, T.; Stromberg, C.; Corcelli, S. A.; Lawrence, C. P.; Skinner, J. L.; Fayer, M. D. *J. Phys. Chem. A* **2004**, *108*, 1107–1119.
- [282] Corcelli, S. A.; Lawrence, C. P.; Asbury, J. B.; Steinel, T.; Fayer, M. D.; Skinner, J. L. *J. Chem. Phys.* **2004**, *121*, 8897–8900.
- [283] Li, S.; Schmidt, J. R.; Piryatinski, A.; Lawrence, C. P.; Skinner, J. L. *J. Phys. Chem. B* **2006**, *110*, 18933–18938.
- [284] Li, S.; Schmidt, J. R.; Corcelli, S. A.; Lawrence, C. P.; Skinner, J. L. *J. Chem. Phys.* **2006**, *124*, 204110.
- [285] Terranova, Z. L.; Corcelli, S. A. *J. Phys. Chem. B* **2014**, *118*, 8264–8272.
- [286] Wasserscheid, P.; Keim, W. *Angew. Chem. Int. Ed. Engl.* **2000**, *39*, 3772–3789.
- [287] Brennecke, J. F.; Gurkan, B. E. *J. Phys. Chem. Lett.* **2010**, *1*, 3459–3464.
- [288] Nulwala, H. B.; Tang, C. N.; Kail, B. W.; Damodaran, K.; Kaur, P.; Wickramanayake, S.; Shi, W.; Luebke, D. R. *Green Chem.* **2011**, *13*, 3345.
- [289] Cui, G.; Zheng, J.; Luo, X.; Lin, W.; Ding, F.; Li, H.; Wang, C. *Angew. Chemie* **2013**, *125*, 10814–10818.
- [290] Fukumoto, K.; Yoshizawa, M.; Ohno, H. *J. Am. Chem. Soc.* **2005**, *127*, 2398–2399.
- [291] Ogihara, W.; Yoshizawa, M.; Ohno, H. *Chem. Lett.* **2004**, *33*, 1022–1023.
- [292] Luo, X.; Guo, Y.; Ding, F.; Zhao, H.; Cui, G.; Li, H.; Wang, C. *Angew. Chemie Int. Ed.* **2014**, *53*, 7053–7057.
- [293] Fletcher, K. A.; Baker, S. N.; Baker, G. A.; Pandey, S. *New J. Chem.* **2003**, *27*, 1706.
- [294] Bayley, P. M.; Best, A. S.; MacFarlane, D. R.; Forsyth, M. *ChemPhysChem* **2011**, *12*, 823–827.
- [295] Castejón, H. J.; Lashock, R. J. *J. Mol. Liq.* **2012**, *167*, 1–4.
- [296] Niedermeyer, H.; Hallett, J. P.; Villar-Garcia, I. J.; Hunt, P. A.; Welton, T. *Chem. Soc. Rev.* **2012**, *41*, 7780–7802.

- [297] Crosthwaite, J. M.; Muldoon, M. J.; Dixon, J. K.; Anderson, J. L.; Brennecke, J. F. *J. Chem. Thermodyn.* **2005**, *37*, 559–568.
- [298] Canongia Lopes, J. N.; Pádua, A. A. H.; Shimizu, K. *J. Phys. Chem. B* **2008**, *112*, 5039–5046.
- [299] Widegren, J. A.; Magee, J. W. *J. Chem. Eng. Data* **2007**, *52*, 2331–2338.
- [300] Schreiner, C.; Zugmann, S.; Hartl, R.; Gores, H. J. *J. Chem. Eng. Data* **2010**, *55*, 4372–4377.
- [301] Chen, Y.; Ke, F.; Wang, H.; Zhang, Y.; Liang, D. *ChemPhysChem* **2012**, *13*, 160–167.
- [302] Canongia Lopes, J. N.; Pádua, A. A. H. *J. Phys. Chem. B* **2006**, *110*, 19586–19592.
- [303] Hu, Y.-F.; Liu, Z.-C.; Xu, C.-M.; Zhang, X.-M. *Chem. Soc. Rev.* **2011**, *40*, 3802.
- [304] Pringle, J. M.; Howlett, P. C.; MacFarlane, D. R.; Forsyth, M. *J. Mater. Chem.* **2010**, *20*, 2056.
- [305] Gordon, C. M.; Holbrey, J. D.; Kennedy, A. R.; Seddon, K. R. *J. Mater. Chem.* **1998**, *8*, 2627–2636.
- [306] Marsh, K. N.; Brennecke, J. F.; Chirico, R. D.; Frenkel, M.; Heintz, A.; Magee, J. W.; Peters, C. J.; Rebelo, L. P. N.; Seddon, K. R. *Pure Appl. Chem.* **2009**, *81*, 781–790.
- [307] Chirico, R. D.; Diky, V.; Magee, J. W.; Frenkel, M.; Marsh, K. N. *Pure Appl. Chem.* **2009**, *81*, 791–828.
- [308] Muldoon, M. J.; Aki, S. N. V. K.; Anderson, J. L.; Dixon, J. K.; Brennecke, J. F. *J. Phys. Chem. B* **2007**, *111*, 9001–9009.
- [309] Shiflett, M. B.; Yokozeki, A. *J. Phys. Chem. B* **2007**, *111*, 2070–2074.
- [310] Seduraman, A.; Klähn, M.; Wu, P. *Calphad* **2009**, *33*, 605–613.
- [311] Brinzer, T.; Berquist, E. J.; Ren, Z.; Dutta, S.; Johnson, C. A.; Krisher, C. S.; Lambrecht, D. S.; Garrett-Roe, S. *J. Chem. Phys.* **2015**, *142*, 212425.
- [312] D’Alessandro, D. M.; Smit, B.; Long, J. R. *Angew. Chemie - Int. Ed.* **2010**, *49*, 6058–6082.
- [313] Liu, H.; Huang, J.; Pendleton, P. *Recent Adv. Post-Combustion CO₂ Capture Chem.*; ACS Symposium Series 1097; American Chemical Society, 2012; Vol. 1097; pp 153–175.
- [314] Blanchard, L. A.; Hancu, D.; Beckman, E. J.; Brennecke, J. F. *Nature* **1999**, *399*, 28–29.

- [315] Cornils, B., Herrmann, W. A., Horvth, I. T., Leitner, W., Mecking, S., Olivier-Bourbigou, H., Vogt, D., Eds. *Multiphase Homogeneous Catalysis*; Wiley-VCH Verlag GmbH: Weinheim, Germany, 2005.
- [316] Jutz, F.; Andanson, J.-M.; Baiker, A. *Chem. Rev.* **2011**, *111*, 322–353.
- [317] Lei, Z.; Dai, C.; Chen, B. *Chem. Rev.* **2013**, *114*, 1289–1326.
- [318] Carvalho, P. J.; Regueira, T.; Santos, L. M. N. B. F.; Fernandez, J.; Coutinho, J. A. P. *J. Chem. Eng. Data* **2010**, *55*, 645–652.
- [319] Corvo, M. C.; Sardinha, J.; Casimiro, T.; Marin, G.; Seferin, M.; Einloft, S.; Menezes, S. C.; Dupont, J.; Cabrita, E. J. *ChemSusChem* **2015**, *8*, 1935–1946.
- [320] Giammanco, C. H.; Kramer, P. L.; Yamada, S. A.; Nishida, J.; Tamimi, A.; Fayer, M. D. *J. Chem. Phys.* **2016**, *144*, 104506.
- [321] Seo, S.; DeSilva, M. A.; Brennecke, J. F. *J. Phys. Chem. B* **2014**, *118*, 14870–14879.
- [322] Ivanova, A. S.; Brinzer, T.; Roth, E. A.; Kusuma, V. A.; Watkins, J. D.; Zhou, X.; Luebke, D.; Hopkinson, D.; Washburn, N. R.; Garrett-Roe, S.; Nulwala, H. B. *RSC Adv.* **2015**, *5*, 51407–51412.
- [323] Hollóczki, O.; Firaha, D. S.; Friedrich, J.; Brehm, M.; Cybik, R.; Wild, M.; Stark, A.; Kirchner, B. *J. Phys. Chem. B* **2013**, *117*, 5898–5907.
- [324] Bhargava, B. L.; Balasubramanian, S. *J. Phys. Chem. B* **2007**, *111*, 4477–4487.
- [325] Firaha, D. S.; Kirchner, B. *J. Chem. Eng. Data* **2014**, *59*, 3098–3104.
- [326] Cang, H.; Li, J.; Fayer, M. D. *J. Chem. Phys.* **2003**, *119*, 13017.
- [327] Skinner, J. L.; Auer, B. M.; Lin, Y.-S. In *Adv. Chem. Phys.*; Rice, S. A., Ed.; John Wiley & Sons, Inc.: Hoboken, NJ, USA, 2009; Vol. 142; pp 59–103.
- [328] Gruenbaum, S. M.; Tainter, C. J.; Shi, L.; Ni, Y.; Skinner, J. L. *J. Chem. Theory Comput.* **2013**, *9*, 3109–3117.
- [329] Reppert, M.; Tokmakoff, A. *Annu. Rev. Phys. Chem.* **2016**, *67*, 359–386.
- [330] Edington, S. C.; Flanagan, J. C.; Baiz, C. R. *J. Phys. Chem. A* **2016**, *120*, 3888–3896.
- [331] Terranova, Z. L.; Corcelli, S. A. *J. Phys. Chem. B* **2014**, *118*, 8264–8272.
- [332] Plimpton, S. *J. Comput. Phys.* **1995**, *117*, 1–19.
- [333] Schmidt, J. R.; Corcelli, S. A. *J. Chem. Phys.* **2008**, *128*, 184504.

- [334] Brinzer, T.; Berquist, E. J.; Dutta, S.; Johnson, C. A.; Krisher, C. S.; Lambrecht, D. S.; Garrett-Roe, S.; Ren, Z. *J. Chem. Phys.* **2017**, *147*, 049901.
- [335] Giammanco, C. H.; Kramer, P. L.; Wong, D. B.; Fayer, M. D. *J. Phys. Chem. B* **2016**, *120*, 11523–11538.
- [336] Ren, Z.; Brinzer, T.; Dutta, S.; Garrett-Roe, S. *J. Phys. Chem. B* **2015**, *119*, 4699–4712.
- [337] Tamimi, A.; Bailey, H. E.; Fayer, M. D. *J. Phys. Chem. B* **2016**, *120*, 7488–7501.
- [338] Hoffman, D. J.; Sokolowsky, K. P.; Fayer, M. D. *J. Chem. Phys.* **2017**, *146*, 124505.
- [339] Andrews, S. S.; Boxer, S. G. *J. Phys. Chem. A* **2000**, *104*, 11853–11863.
- [340] Andrews, S. S.; Boxer, S. G. *J. Phys. Chem. A* **2002**, *106*, 469–477.
- [341] Perakis, F.; Hamm, P. *J. Phys. Chem. B* **2011**, *115*, 5289–5293.
- [342] Russina, O.; Triolo, A.; Gontriani, L.; Caminiti, R. *J. Phys. Chem. B* **2011**, *3*, 27–33.
- [343] Santos, C. S.; Annapureddy, H. V. R.; Murthy, N. S.; Kashyap, H. K.; Castner, E. W.; Margulis, C. J. *J. Chem. Phys.* **2011**, *134*, 064501.
- [344] Hayes, R.; Imberti, S.; Warr, G. G.; Atkin, R. *J. Phys. Chem. C* **2014**, *118*, 13998–14008.
- [345] Dhungana, K. B.; Faria, L. F. O.; Wu, B.; Liang, M.; Ribeiro, M. C. C.; Margulis, C. J.; Castner, E. W. *J. Chem. Phys.* **2016**, *145*, 024503.
- [346] Hu, Z.; Margulis, C. J. *Acc. Chem. Res.* **2007**, *40*, 1097–1105.
- [347] Kashyap, H. K.; Annapureddy, H. V. R.; Raineri, F. O.; Margulis, C. J. *J. Phys. Chem. B* **2011**, *115*, 13212–13221.
- [348] Angell, C. A. *Science* **1995**, *267*, 1924–1935.
- [349] Ediger, M. D.; Angell, C. A.; Nagel, S. R. *J. Phys. Chem.* **1996**, *100*, 13200–13212.
- [350] Ferrer, M. L.; Sakai, H.; Kivelson, D.; Alba-Simionesco, C. *J. Phys. Chem. B* **1999**, *103*, 4191–4196.
- [351] Mirigian, S.; Schweizer, K. S. *J. Phys. Chem. Lett.* **2013**, *4*, 3648–3653.
- [352] Chandler, D.; Garrahan, J. P. *Annu. Rev. Phys. Chem.* **2010**, *61*, 191–217.
- [353] Tokuda, H.; Hayamizu, K.; Ishii, K.; Susan, M. A. B. H.; Watanabe, M. *J. Phys. Chem. B* **2005**, *109*, 6103–6110.

- [354] Hazelbaker, E. D.; Budhathoki, S.; Katihar, A.; Shah, J. K.; Maginn, E. J.; Vasenkov, S. *J. Phys. Chem. B* **2012**, *116*, 9141–9151.
- [355] Waldeck, D. H. *Chem. Rev.* **1991**, *91*, 415–436.
- [356] Hamm, P.; Shalit, A. *J. Chem. Phys.* **2017**, *146*, 130901.